Gravitational Waves in Boson Star Mergers

Ge, Bo-Xuan

Awarding institution:
King's College London

Gravitational Waves in Boson Star Mergers

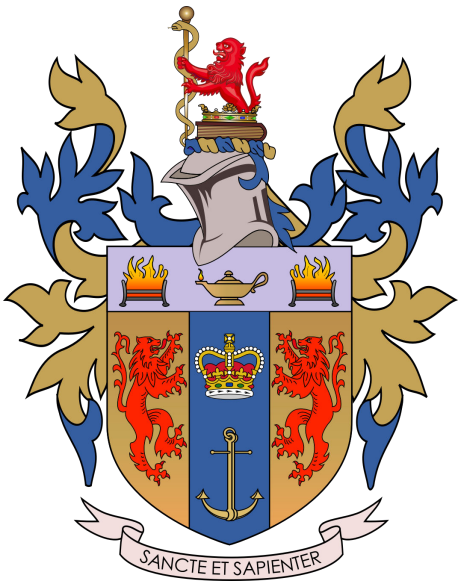

Bo-Xuan Ge

Supervisor: Prof. Eugene A. Lim

The Department of Physics
King's College London

This dissertation is submitted for the degree of
Doctor of Philosophy

October 2024

You *Crucify* freedom upon the altar of *Coercion* and *Perfidy*,
yet the essence of the human spirit soars,
unshackled and eternal.

Acknowledgements

Not until the very moment I was informed I had passed my PhD defense did the profound significance of earning a doctorate truly descend upon me. The odyssey had been long and meandering, at times feeling utterly surreal, as though I were traversing the chapters of a narrative I could scarcely believe belonged to me.

My undergraduate days unfolded within the familiar confines of ordinariness, four years passing in uneventful monotony. Yet somewhere amidst the routine, a spark was kindled—a fervent yearning to delve deeper, to unravel the intricate tapestry of theoretical physics. The allure of deciphering the universe's enigmas ignited a passion far surpassing any contentment found in charting maps at a desk. Thus, I embarked upon a solitary journey, self-instructing in the fundamentals of this vast and mysterious domain. This insatiable curiosity propelled me toward a master's degree in physics, and as that chapter drew to a close, I dared to ask myself: might I venture further still?

Fate whispered its assent when I received an offer from King's College London. For this, I am profoundly indebted to my PhD supervisor, Prof. Eugene Lim, who bestowed his trust upon me—a student whose credentials, on paper, were scarcely remarkable. This opportunity is a gift I shall treasure eternally. Yet what I hold dearest are not the accolades, but the indelible lessons gleaned in the ensuing years: the meticulous discipline required in research, the unwavering perseverance to carry a project to its fruition. Indeed, these lessons may well eclipse the doctorate itself in worth.

Relocating to London heralded my first sojourn beyond the bounds of Peking, the city that had sculpted nearly the entirety of my existence. London, with its labyrinthine streets and unfamiliar faces, was at first an intimidating expanse. Yet fortune graced me with the friendship of Dr. Josu Aurrekoetxea, who, though then yet to attain his own doctorate, was the first among our circle to extend a welcoming hand. Through his kindness, I discovered that the vastness of a new city need not be overwhelming.

I owe Josu a debt beyond the reach of words—not merely for his academic guidance, but for his quiet wisdom in navigating life's subtleties. His approach to research has etched an indelible imprint upon my own.

Then, without forewarning, the world shifted. COVID-19 swept in like a tempest, upending plans and suspending life as we knew it. The abrupt cessation of in-person

interactions and the city's lockdown left me adrift, anxious, and uncertain. In those trying times, Dr. Thomas Helfer emerged as a steadfast anchor. I shall forever cherish our daily two-hour conversations, during which he patiently initiated me—a complete novice—into the intricacies of programming. His unwavering support and encouragement not only helped me overcome technical challenges but also provided much-needed morale during those isolating times. The skills he imparted became the very bedrock of my subsequent research, and his kindness and generosity left a lasting impact on both my professional and personal growth. For this, I am eternally grateful.

I am also profoundly grateful to my fellow group members: Eloy, Liina, Matthew, Michelle, Nicole, and Panos. Their insights during our meetings expanded my comprehension of myriad concepts. A special note of gratitude is reserved for Eloy, whose generosity in sharing his code laid the foundation for the concluding work of my PhD journey.

To the TPPC group, I extend my heartfelt thanks for cultivating an atmosphere of warmth and camaraderie within the office. I was fortunate to share that space with colleagues who became dear friends: Angelo, Ansh, Carlos, Charlie, Damon, Drew, Giuseppe, Katarina, Louis, Nikos, Silvia, Wenyuan, and other members of TPPC. To friends from other groups, such as Joana and Lu, I also express my deepest gratitude.

Being part of the GRChombo team was an honor beyond words, and I am grateful to have contributed to such an extraordinary endeavor. My gratitude extends especially to the Cambridge team—Miren, Robin, Tamara, and Prof. Ulrich Sperhake—who so generously shared their expertise with me.

Finally, I am profoundly and irrevocably grateful to my family and friends, especially my mother. Her unwavering support has been a beacon of light, guiding me through the stormy seas of my academic voyage. Time and again, she has reminded me of a simple yet profound truth: no matter the trials we face, kindness must always prevail.

Looking back, my years in London were perhaps the happiest of my life. The path to a PhD was not without its challenges, but it was also replete with discovery and anticipation. I remain forever thankful to Prof. Eugene Lim, not only for granting me the chance to study at King's, but for his invaluable mentorship. And to King's College London, I am deeply grateful for the intellectual freedom and space it provided—a haven where curiosity was nurtured and inquiry allowed to flourish.

Abstract

Gravitational wave physics has experienced a significant advancement, particularly with the GW150914 detection [2] and numerous subsequent compact binary events [5, 10, 11]. First predicted by Einstein in 1916, the recent detection of gravitational waves by LIGO and Virgo has opened a new window to the Universe, offering insights into black holes and numerous astrophysical phenomena, and challenging our understanding of stellar evolution and binary populations [2, 4, 12, 1].

Moreover, gravitational waves hold the exciting potential to illuminate the nature of dark matter. Gravitational interactions are essential for probing dark matter's fundamental properties, such as mass, spin, and self-interactions, especially as weakly interacting massive particles (WIMPs) remain elusive in direct detection experiments. This has led to a resurgence in interest in other dark matter candidates, notably low-mass ($m \leq$ eV) bosonic particles like QCD axions, axion-like particles (ALPs), and "dark photons" [28, 90, 155, 220, 132, 30, 183, 235, 173, 232]. Gravitational wave physics also connects with other fields, particularly particle/high-energy physics and the exploration of the dark sector [65, 35]. A key aspect of this connection is the interaction of fundamental fields with compact objects through superradiance [58] and the formation of distinct compact objects like boson stars [233]. Gravitational wave observations now systematically search for boson star populations, heavily relying on accurate gravitational wave signal predictions, a topic central to our work using numerical relativity techniques [37].

This thesis primarily focuses on the collision behavior of binary boson stars using numerical relativity, exploring their initial conditions, the afterglow phenomenon, and the regularities of gravitational wave energy emission. Specifically, the structure of this thesis is as follows.

Chapter 1 offers a concise overview of the fundamental concepts of General Relativity, along with the basic theory related to gravitational waves.

Chapter 2 explores the fundamental principles of numerical relativity, including its theoretical foundations and mathematical tools. In particular, it offers a detailed discussion of the evolution methods in numerical relativity, as well as the approaches for computing initial data and selecting gauges.

Chapter 3 is dedicated to the discussion of boson stars and also briefly introduces relevant background information.

Chapter 4 focuses on two main areas. ***The first section*** examines numerical simulations of boson-star head-on collisions, particularly the quality of binary initial data from single-star spacetime superposition. We find that using only superposition for boosted boson-star spacetimes leads to significant unphysical results. This issue can be addressed by modifying the initial data as suggested in [110] for oscillaton collisions. Our focus is on massive complex scalar field boson star models with a 6th-order-polynomial potential, but we believe this issue is common in various exotic compact systems, meriting further research [113]. ***The second section*** explores the lasting gravitational wave signature after a boson-star binary coalescence. We fully use numerical relativity to simulate the post-merger phase and observe the extended gravitational afterglow. Recent advancements in binary initial data have been applied, reducing false initial scalar field excitations and including a metric for angular momentum to track the total momentum of the spatial volume, including curvature effects. A key finding is the persistence of the afterglow beyond the spin-down timescale, emitting a unique gravitational wave signal that could distinguish it from other astrophysical phenomena [77].

Chapter 5 examines the behavior of binary solitons in head-on collisions. We examine a two-dimensional hypersurface of the parameter space spanned by σ and the boson star compactness, controlled through the central scalar-field amplitude. A novel superposition method for initial conditions, as discussed in Chapter 4, was employed. Additionally, this research utilized a more efficient two-dimensional code, which significantly enhanced the speed of the evolution process compared to the previous three-dimensional approach. Our results reveal that the patterns of gravitational wave energy exhibit complex structures, which are closely related to the stability of the solitons.

Table of contents

List of figures

List of tables

Chapter 1

General Relativity

Conventions and Notation

This chapter primarily draws on references [231, 144]. The specific conventions and notations employed are as follows.

Conventions

This thesis employs both abstract index notation and concrete index notation to represent tensors. For instance, v^a represents a vector, where the Latin letter a, known as an abstract index, functions similarly to the arrow in the commonly used notation $\vec{v}$. It is important not to interpret v^a as the ath component of v^a. When referring to components, Greek letters are used as indices (called component or concrete indices); for example, v^μ represents the μth component of the vector v^a.

There is one exception: in a 4-dimensional spacetime, a vector v^a has three spatial components, which are conventionally denoted by v^i (where $i = 1,2,3$) to represent the ith component of v^a. Although this deviates from the rule of using Latin letters for abstract indices, it offers significant convenience. To differentiate from abstract indices $a,b,c,d,e,\ldots$, only Latin letters starting from i (typically i,j,k) are used as labels for the spatial components.

This thesis adopts the $-+++$ signature convention for the metric in 4-dimensional spacetime. Various conventions exist in the literature for defining the Riemann tensor $R_{abc}{}^d$ and the Ricci tensor R_{ab}. The conventions followed here are those established in Robert Wald's textbook, *General Relativity* [231].

Notation List

$\{\}$	Set. E.g., $X = \{1,3,9\}$ stands for the set formed by the real numbers 1, 3, and 9.
$\mathbb{R}$	The set of real numbers.
$\mathbb{N}$	The set of natural numbers.
$\forall x$	For all x.
$\exists$	There exists.
$\in$	Belongs to. E.g., $x \in X$ stands for "x belongs to the set X", i.e., x is an element of X.
$\notin$	Does not belong to.
$\subset$	Contained in. E.g., $A \subset X$ stands for "A is contained in the set X", i.e., A is a subset of X.
$\subsetneq$	Contained in but not equal to. E.g., $A \subset X$ stands for "A is contained in but not equal to the set X", i.e., A is a proper subset of X.
$\cup$	Union.
$\cap$	Intersection.
$\varnothing$	Empty set.
:=	Defined as.
$\equiv$	Identical to or denoted by. E.g., $A \equiv B \cup C$ means "denote $B \cup C$ by A".
$\cong$	Approximately equal to.
$\Rightarrow$	Implies (if ... then), e.g., $A \Rightarrow B$ stands for "if A then B".
$\Leftrightarrow$	Equivalent to (if and only if).
$\times$	Cartesian product.
$\square$	Quod Erat Demonstrandum (Denotes the end of a proof, aligned to the right.)
$\mathbb{R}^n$	The set of n-tuples $\left(x^1,\ldots,x^n\right)$ of real numbers, i.e., $\mathbb{R}^n = \mathbb{R} \times \cdots \times \mathbb{R}$ (n factors in total).
$\otimes$	Tensor product.
$:\!\rightarrow$	Map. E.g., $f : X \rightarrow Y$ stands for "the map from X to Y".
e_μ or $\left(e_\mu\right)^a$	The μth basis vector in the chosen basis $\left\{\left(e_\mu\right)^a\right\}$.
$e^{\mu *}$ or $\left(e^\mu\right)_a$	The μth dual basis vector of the basis $\left\{\left(e_\mu\right)^a\right\}$.
$\frac{\partial}{\partial x^\mu}$ or $\left(\frac{\partial}{\partial x^\mu}\right)^a$	The μth coordinate basis vector field.
$\mathrm{d}x^\mu$ or $\left(\mathrm{d}x^\mu\right)_a$	The μth dual coordinate basis vector field.

$f[A]$	Suppose $f : X \to Y, A \subset X$, then the image of A under the action of f is denoted by $f[A]$ in order to distinguish it from the image $f(x)$ of $x \in X$ under f.
$\circ$	Composite map. E.g., $\phi \circ \psi$ stands for the composite map of ϕ and ψ(ψ after ϕ).
C^r	The first r derivatives exist and are continuous.
C^∞	Smooth (derivatives of all orders exist and are continuous).
$\dim V$	The dimension of V.
V^*	The dual space of the vector space V.
V_p	The tangent space at a point p in the manifold.
V_p^*	The dual space of the vector space V_p.
$\vec{E}$	3-dimensional (spatial) vector E.
$\mathscr{T}_V(k,l)$	The set of all the tensors of type (k,l) on a vector field V.
$\mathscr{F}_M$ or $\mathscr{F}$	The set of all the smooth functions on a manifold M.
$\mathscr{F}_M(k,l)$	The set of all the smooth tensor fields of type (k,l) on a manifold M.
$[u,v]$	The commutator of the vector fields u and v.
δ or δ_{ab}	Euclidean metric.
η or η_{ab}	Minkowski metric.
$\delta^a{}_b$	Identity map.
$g(u,v)$	The result of acting the metric tensor g on u and v. Same as $g_{ab}u^a v^b$.
$T_{(abc)}$	The total symmetrization over the indices a,b,c.
$T_{[abc]}$	The total antisymmetrization over the indices a,b,c.
∇_a	Derivative operator.
∂_a	The ordinary derivative operator in a coordinate system. In special relativity it refers to the ordinary derivative operator in an inertial coordinate system, satisfying $\partial_a \eta_{bc} = 0$.
$\Gamma^a{}_{bc}$	The Christoffel symbol of a derivative operator in a coordinate system.
$\Gamma^\mu{}_{\nu\sigma}$	The components of the Christoffel symbol $\Gamma^a{}_{bc}$ in a coordinate system.
ϕ^*	The pullback map induced by the map ϕ.
ϕ_*	The pushforward map induced by the map ϕ.
$\mathscr{L}_v T^{\cdots}{}_{\cdots}$	The Lie derivative of the tensor field $T^{\cdots}{}_{\cdots}$ along a vector field v^a.

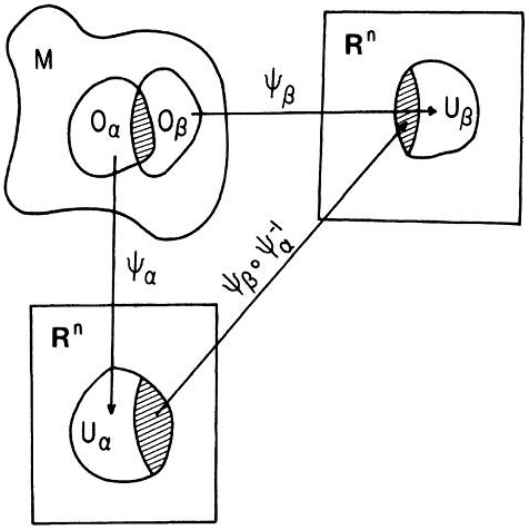

Fig. 1.1 An illustration of the map $\psi_\beta \circ \psi_\alpha^{-1}$ arising when two coordinate systems overlap. [231].

1.1 Differential Geometry

Differential Manifold

Physics is inherently connected to background space. For instance, Newtonian mechanics and electrodynamics are based on three-dimensional space, denoted as $\mathbb{R}^3$. Similarly, statistical physics and Hamiltonian theory often use phase space. In special relativity, the background is four-dimensional spacetime, represented as $\mathbb{R}^4$. Generally, these "**spaces**" are continuous rather than discrete. The spacetime in general relativity is also depicted as continuous. Locally, it resembles $\mathbb{R}^4$, but globally, it may deviate from the structure of $\mathbb{R}^4$ [144].

A differential manifold is a type of topological space endowed with a differential structure. The definition is as follows.

Definition: A topological space M is called an n-dimensional **Differentiable Manifold**, or n-dimensional manifold for short, if M has an open cover $\{O_\alpha\}$, i.e., $M = \bigcup_\alpha O_\alpha$, satisfying

(a) for each $O_\alpha \exists$ a homeomorphism $\psi_\alpha : O_\alpha \to V_\alpha$ (V_α is an open subset of $\mathbb{R}^n$ measured by the usual topology);

(b) If $O_\alpha \cap O_\beta \neq \varnothing$, then the composite map $\psi_\beta \circ \psi_\alpha^{-1}$ (see Figure 1.1) is C^∞ (smooth).

Scalar Field

Before introducing the scalar field, we will first discuss the concepts of C^r class mappings and diffeomorphisms.

Definition: $f : M \to M'$ is called a C^r map if $\forall p \in M$, the n' functions of n variables corresponding to the map $\psi'_\beta \circ f \circ \psi_\alpha^{-1}$ are of class C^r.

Definition: Differential manifolds M and M' are said to be diffeomorphic to each other if $\exists f : M \to M'$ satisfying

(a) f is one-to-one and onto;

(b) f and f^{-1} are C^∞.

Such an f is called a diffeomorphism from M to M'.

Next, we introduce the concept of the scalar field.

Definition: $f : M \to \mathbb{R}$ is called a **Function** on M or a **Scalar Field** on M. If f is C^∞, then it is called a smooth function on M. The collection of all smooth functions on M is denoted by $\mathscr{F}_M$, abbreviated with $\mathscr{F}$ when there is no confusion. From now on, functions will refer to smooth functions unless stated otherwise.

Vector Field

Definition: A vector space over the field of real numbers is a set V together with two maps, namely $V \times V \to V$ (called addition) and $\mathbb{R} \times V \to V$ (called scalar multiplication), satisfying the following conditions:

(a) $v_1 + v_2 = v_2 + v_1, \quad \forall v_1, v_2 \in V,$

(b) $(v_1 + v_2) + v_3 = v_1 + (v_2 + v_3), \quad \forall v_1, v_2, v_3 \in V,$

(c) $\exists$ a zero element $\underline{0} \in V$ such that $\underline{0} + v = v, \quad \forall v \in V,$

(d) $\alpha_1(\alpha_2 v) = (\alpha_1 \alpha_2)v, \quad \forall v \in V, \quad \alpha_1, \alpha_2 \in \mathbb{R},$

(e) $(\alpha_1 + \alpha_2)v = \alpha_1 v + \alpha_2 v, \quad \forall v \in V, \quad \alpha_1, \alpha_2 \in \mathbb{R},$

(f) $\alpha(v_1 + v_2) = \alpha v_1 + \alpha v_2, \quad \forall v_1, v_2 \in V, \quad \alpha \in \mathbb{R},$

(g) $1 \cdot v = v, \quad 0 \cdot v = \underline{0}, \quad \forall v \in V.$

Now that the definition of a differential manifold is in place, we can introduce the concept of a vector.

Definition: A map $v : \mathscr{F}_M \to \mathbb{R}$ is called a **Vector** at a point $p \in M$ if $\forall f, g \in \mathscr{F}_M, \alpha, \beta \in \mathbb{R}$ we have

(a) (Linearity) $v(\alpha f + \beta g) = \alpha v(f) + \beta v(g)$,

(b) (Leibniz rule) $v(fg) = f|_p v(g) + g|_p v(f)$, where $f|_p$ stands for the value of the function f at p, which can also be denoted by $f(p)$.

The transformation between two coordinate systems follows the rule:

$$v'^{\nu} = \left.\frac{\partial x'^{\nu}}{\partial x^{\mu}}\right|_p v^{\mu}. \tag{1.1}$$

Here, v'^{ν} and v^{μ} represent the coordinate component values in the coordinates $\{x'^{\nu}\}$ and $\{x^{\mu}\}$, respectively.

With the concept of a vector established, we can now construct the idea of a vector field. Essentially, a vector field is a tangent field, v, on a manifold M. It assigns a tangent vector, denoted as $v|_p \in V_p$, to each point $p \in M$. The specific details are as follows:

Definition: Suppose A is a subset of M. If we assign a vector to each point of A, we obtain a **Vector Field** defined on A.

Dual Vector Field

The counterparts to the vector and vector field are the dual vector and dual vector field, respectively.

Definition: Suppose V is a finite dimensional vector space on $\mathbb{R}$. A linear map $\omega : V \to \mathbb{R}$ is called a **Dual Vector** on V. The collection of all the dual vectors on V is called the dual vector space of V, denoted by V^*.

Since V possesses addition and scalar multiplication properties, ω needs to satisfy the following conditions:

$$\omega(\alpha v+\beta u)=\alpha\omega(v)+\beta\omega(u),\quad \forall v,u\in V,\quad \alpha,\beta\in\mathbb{R}. \tag{1.2}$$

Now we get back to a manifold M. Since $p\in M$ has a vector space V_p, it also has a V_p^*. If we assign a dual vector at each point of M, we obtain a **Dual Vector Field** on M. A dual vector field ω on M is said to be smooth if $\omega(v)\in\mathscr{F}_M\forall$ smooth vector fields v.

Finally, we will examine the transformation relationships in different coordinate systems. Under a coordinate transformation, the components of the dual vector transform as follows:

$$\omega'_\nu=\left.\frac{\partial x^\mu}{\partial x'^\nu}\right|_p\omega_\mu. \tag{1.3}$$

Tensor Field

By extending this concept further, we can introduce various types of tensors.

Definition: A tensor of type (k,l) on a vector space V is a multilinear map

$$T:\underbrace{V^*\times\cdots\times V^*}_{k\text{ terms}}\times\underbrace{V\times\cdots\times V}_{l\text{ terms}}\to\mathbb{R}.$$

The concept is quite accessible. A (k,l) tensor can map k dual vectors and l vectors to a real number.

Now, we will introduce the concept of the tensor product.

Definition: The tensor product $T\otimes T'$ of a tensor T of type (k,l) and a tensor T' of type (k',l') on V is a tensor of type $(k+k',l+l')$ defined as follows:

$$\begin{aligned}&T\otimes T'\left(\omega^1,\ldots,\omega^k,\omega^{k+1},\ldots,\omega^{k+k'};v_1,\ldots,v_l,v_{l+1},\ldots,v_{l+l'}\right)\\:=&T\left(\omega^1,\ldots,\omega^k;v_1,\ldots,v_l\right)T'\left(\omega^{k+1},\ldots,\omega^{k+k'};v_{l+1},\ldots,v_{l+l'}\right).\end{aligned}$$

The components of a (k,l) tensor T transform as follows:

$$T'^{\mu_1\cdots\mu_k}{}_{\nu_1\cdots\nu_l}=\frac{\partial x'^{\mu_1}}{\partial x^{\rho_1}}\cdots\frac{\partial x^{\sigma_l}}{\partial x'^{\nu_l}}T^{\rho_1\cdots\rho_k}{}_{\sigma_1\cdots\sigma_l}. \tag{1.4}$$

Metric

We now introduce the concept of a metric. Intuitively, a metric is meant to convey the "infinitesimal squared distance" associated with an "infinitesimal displacement". The intuitive idea of an "infinitesimal displacement" is accurately encapsulated by the notion of a tangent vector. Given that the "infinitesimal squared distance" should exhibit a quadratic relationship with the displacement, the metric can be defined as follows:

Definition: A **Metric** g on a vector space V is a symmetric, non-degenerate tensor of type $(0,2)$ on V. Symmetric means $g(v,u) = g(u,v) \quad \forall v,u \in V$, and non-degenerate means $g(v,u) = 0 \quad \forall u \in V \Rightarrow v = 0 \in V$.

With the established metric, the length can now be defined as follows:

$$\mathrm{d}l := \sqrt{\left| g_{\mu\nu} \mathrm{d}x^{\mu} \mathrm{d}x^{\nu} \right|}. \tag{1.5}$$

The notation often used is: $\mathrm{d}s^2 \equiv g_{\mu\nu}\mathrm{d}x^{\mu}\mathrm{d}x^{\nu}$, where $\mathrm{d}s^2$ is referred to as the line element.

Given the signature $(-,+,+,+)$,

$$\begin{aligned} ds^2 < 0 \quad & \text{Timelike}, \\ ds^2 = 0 \quad & \text{Null}, \\ ds^2 > 0 \quad & \text{Spacelike}. \end{aligned} \tag{1.6}$$

The Abstract Index Notation

> *I recall that when I first learned general relativity, I was told that mastering the core of relativity lies in understanding the "absolute aspects" rather than the "relative aspects".*

In much of the literature, tensors are represented in the following manner: $T^{\mu_1 \cdots \mu_k}{}_{\nu_1 \ldots \nu_l}$. However, this method has a significant drawback: sometimes, by choosing a particular basis, we obtain simpler component equations, which are valid only for that special basis and hence do not represent tensor equations. We aim to discern which equations represent tensor equations and which do not, yet this distinction is difficult to make with the aforementioned notation. Therefore, we need to resort to Penrose's **Abstract Index Notation** to overcome this difficulty.

Below, we briefly outline the key points of this notation.

1. A (k,l) type tensor is represented by a letter with k upper indices and l lower indices, where the indices are ***lowercase*** **Latin** letters, only representing the type of tensor, and thus it is referred to as the **Abstract Index**.

2. Repeated upper and lower abstract indices signify taking the "contraction" over these two indices.

3. The tensor product notation is omitted.

4. The letters representing tensors, carrying their own abstract index, can be interchanged.

5. When involving the components of tensors, the corresponding indices use lowercase Greek letters, referred to as **Component Indices** or **Concrete Indices**.

Specifically, the expansion of a tensor in a basis can be written as:

$$T^{ab}{}_{c} = T^{\mu\nu}{}_{\sigma} \left(e_{\mu}\right)^{a} \left(e_{v}\right)^{b} \left(e^{\sigma}\right)_{c}. \tag{1.7}$$

The components are given by:

$$T^{\mu\nu}{}_{\sigma} = T^{ab}{}_{c} \left(e^{\mu}\right)_{a} \left(e^{v}\right)_{b} \left(e_{\sigma}\right)^{c}. \tag{1.8}$$

In the abstract index notation, a coordinate basis vector is denoted by $(\partial/\partial x^{\mu})^{a}$, and a dual coordinate basis vector is denoted by $(\mathrm{d}x^{\mu})_{a}$. Using a metric g_{ab} and its inverse g^{ab} to raise and lower their indices, respectively, we obtain a dual vector $g_{ab}\,(\partial/\partial x^{\mu})^{b}$ and a vector $g^{ab}\,(\,\mathrm{d}x^{\mu})_{b}$. Denote the $g_{ab}\,(\partial/\partial x^{\mu})^{b}$ by ω_{a} for short and expand it using the dual coordinate basis as $g_{ab}\,(\partial/\partial x^{\mu})^{b} = \omega_{\nu}\,(\mathrm{d}x^{\nu})_{a}$. Applying both sides to $(\partial/\partial x^{\sigma})^{a}$ yields $g_{\sigma\mu} = \omega_{\sigma}$. Hence,

$$g_{ab}\,(\partial/\partial x^{\mu})^{b} = g_{\mu\nu}\,(\mathrm{d}x^{\nu})_{a}. \tag{1.9}$$

Thus, in general $g^{ab}\,(\,\mathrm{d}x^{\mu})_{b}$ does not equal $(\mathrm{d}x^{\mu})_{a}$. Similarly, we have

$$g^{ab}\,(\,\mathrm{d}x^{\mu})_{b} = g^{\mu\nu}\,(\partial/\partial x^{\nu})^{a}. \tag{1.10}$$

Derivative Operators

In Euclidean space, derivative operators such as $\vec{\nabla}$ can be used to compute the gradient $\vec{\nabla} f$ and divergence $\vec{\nabla}\cdot\vec{v}$. Given that Euclidean space is equipped with the metric δ_{ab}, one can identify a vector and its corresponding dual vector, i.e., $v_{a} = \delta_{ab}v^{b}$. We now aim to extend these derivative operators to any manifold.

Definition: A **Derivative Operator** ∇ (covariant derivative) on a manifold M is a map which takes each smooth tensor field of type (k,l) to a smooth tensor field of type $(k,l+1)$ and satisfies the five properties listed below.

1. Linearity.
2. Leibnitz rule.
3. Commutativity with contraction.
4. $v(f) = v^a \nabla_a f, \quad \forall f \in \mathscr{F}_M, \quad v \in \mathscr{F}_M(1,0).$
5. Torsion free.

Utilizing property 4, we obtain:

$$\nabla_a f = (\mathrm{d}f)_a, \quad \forall f \in \mathscr{F}_M. \tag{1.11}$$

Note that the derivative operator is not unique. Considering two derivative operators, ∇_a and $\tilde{\nabla}_a$, Equation (1.11) leads to the result:

$$\nabla_a f = \tilde{\nabla}_a f = (\mathrm{d}f)_a, \quad \forall f \in \mathscr{F}_M. \tag{1.12}$$

Equation (1.12) implies that the distinction between these two derivative operators can only be discerned in higher-type tensors, not in $(0,0)$ type tensors.

For dual vectors, we have

$$\nabla_a \omega_b = \tilde{\nabla}_a \omega_b - C^c{}_{ab}\omega_c, \quad \forall \omega_b \in \mathscr{F}(0,1), \tag{1.13}$$

where $C^c{}_{ab}$ is a $(1,2)$ type tensor satisfying the property $C^c{}_{ab} = C^c{}_{ba}$. Using the property $\nabla_a\left(\omega_b v^b\right) = \tilde{\nabla}_a\left(\omega_b v^b\right)$, one can find the rule for the vector:

$$\nabla_a v^b = \tilde{\nabla}_a v^b + C^b_{ac} v^c. \tag{1.14}$$

Extending this to a general tensor, the transformation rule is given by

$$\nabla_a T_1^{b_1\cdots b_k} c_1 \cdots c_l = \tilde{\nabla}_a T^{b_1\cdots b_k} c_1 \cdots c_l + \sum_i C^{b_i}_{ad} T^{b_1\cdots d\cdots b_k} c_1 \cdots c_l - \sum_j C^d_{ac_j} T_1^{b_1\cdots b_k} c_1 \cdots d \cdots c_l. \tag{1.15}$$

Theorem: Let g_{ab} be a metric. Then there exists a ***unique*** derivative operator ∇_a satisfying $\nabla_a g_{bc} = 0$.

An important derivative operator, known as the **Ordinary Derivative**, merits mention. Given a manifold M with coordinates denoted by $\{x^\mu\}$, the corresponding coordinate basis is represented by $\{(\partial/\partial x^\mu)^a\}$ and $\{(\mathrm{d}x^\mu)_a\}$. We define a map $\partial_a : \mathscr{F}_O(k,l) \to \mathscr{F}_O(k,l+1)$ as follows:

$$\partial_a T^b{}_c := (\mathrm{d}x^\mu)_a (\partial/\partial x^\nu)^b (\mathrm{d}x^\sigma)_c \, \partial_\mu T^\nu{}_\sigma. \tag{1.16}$$

It can be demonstrated that this derivative operator adheres to properties 1- 5 previously outlined. Furthermore, when selecting the ordinary derivative as $\tilde{\nabla}_a$, the corresponding $C^c{}_{ab}$ is referred to as the **Christoffel Symbol**, denoted by $\Gamma^b{}_{ac}$.

Parallel Transport

Given a specific ∇_a, the notion of parallel transport of a vector along a curve C with a tangent t^a can be defined.

Definition: A vector v^a given at each point on the curve is said to be ***parallelly*** transported as one moves along the curve if the equation

$$t^a \nabla_a v^b = 0 \tag{1.17}$$

is satisfied along the curve.

For other types of tensors, the condition for **Parallel Transport** is given by:

$$t^a \nabla_a T^{b_1 \cdots b_k}{}_{c_1 \cdots c_l} = 0. \tag{1.18}$$

Given a coordinate system, Equation (1.17) can be elucidated further as:

$$t^a \partial_a v^b + t^a \Gamma^b{}_{ac} v^c = 0. \tag{1.19}$$

Theorem: A point $C(t_0)$ on a curve and a vector at this point uniquely defines a vector field that is parallelly transported along the curve.

Suppose p and q are points in the manifold M. Then, V_p and V_q are two distinct vector spaces, and their elements cannot be directly compared. However, if there exists a curve $C(t)$ that connects p and q, we can define a map from V_p to V_q as follows: for any $v^a \in V_p$, this theorem guarantees the existence of a unique vector field that is parallelly transported along $C(t)$, with the vector field at p being v^a. The value of this vector field at q is then

considered the image of v^a. It is important to note that this map is curve-dependent, meaning that for a different curve connecting p and q, the resulting vector v^a at q could differ. Nevertheless, the existence of the connection ∇_a, although dependent on the curve, provides a way to relate the two vector spaces V_p and V_q, which were previously unrelated. This is why ∇_a is also referred to as a **Connection**.

Geodesic

On a related note, the concept of a geodesic can be introduced.

Definition: Given a derivative operator, ∇_a, we define a **Geodesic** to be a curve whose tangent vector is parallel propagated along itself, i.e. a curve whose tangent, T^a, satisfies the equation

$$T^a \nabla_a T^b = 0. \tag{1.20}$$

We can observe that a necessary and sufficient condition for a curve to be a geodesic is that its tangent vector field is parallelly transported along the curve. The equation $T^a \nabla_a T^b = 0$ is known as the **Geodesic Equation**. If a metric field g_{ab} exists on a manifold M, then the geodesics of (M, g_{ab}) are the geodesics of (M, ∇_a), where ∇_a is the connection associated with g_{ab}.

For a vector field T^a, we have:

$$T^a = \left(\frac{\partial}{\partial t}\right)^a = \left(\frac{\partial}{\partial t'}\right)^a \frac{\mathrm{d}t'}{\mathrm{d}t} = \frac{\mathrm{d}t'}{\mathrm{d}t} T'^a. \tag{1.21}$$

The condition for geodesic equation is given by:

$$\begin{aligned} 0 &= T^b \nabla_b T^a \\ &= \frac{\mathrm{d}t'}{\mathrm{d}t} T'^b \nabla_b \left(\frac{\mathrm{d}t'}{\mathrm{d}t} T'^a\right) \\ &= \left(\frac{\mathrm{d}t'}{\mathrm{d}t}\right)^2 T'^b \nabla_b T'^a + T'^a \frac{\mathrm{d}t'}{\mathrm{d}t} T'^b \nabla_b \left(\frac{\mathrm{d}t'}{\mathrm{d}t}\right) \\ &= \left(\frac{\mathrm{d}t'}{\mathrm{d}t}\right)^2 T'^b \nabla_b T'^a + T'^a \frac{\mathrm{d}t'}{\mathrm{d}t} \frac{\mathrm{d}}{\mathrm{d}t'} \left(\frac{\mathrm{d}t'}{\mathrm{d}t}\right) \\ &= \left(\frac{\mathrm{d}t'}{\mathrm{d}t}\right)^2 T'^b \nabla_b T'^a + T'^a \frac{\mathrm{d}^2 t'}{\mathrm{d}t^2}. \end{aligned} \tag{1.22}$$

Hence, we obtain:

$$T'^b \nabla_b T'^a = -\left(\frac{\mathrm{d}t'}{\mathrm{d}t}\right)^2 \frac{\mathrm{d}^2 t'}{\mathrm{d}t^2} T'^a. \tag{1.23}$$

Define:

$$\alpha \equiv -\left(\frac{\mathrm{d}t'}{\mathrm{d}t}\right)^2 \frac{\mathrm{d}^2 t'}{\mathrm{d}t^2}. \tag{1.24}$$

Thus, we can write:

$$T'^b \nabla_b T'^a = \alpha T'^a. \tag{1.25}$$

Theorem: Suppose $\gamma(t)$ is a geodesic, then the tangent vector field T'^a of its reparametrization $\gamma'(t')[=\gamma(t)]$ satisfies

$$T'^b \nabla_b T'^a = \alpha T'^a \quad [\alpha \text{ is a function defined on } \gamma(t)]. \tag{1.26}$$

Theorem: Suppose the tangent vector field T^a of a curve $\gamma(t)$ satisfies $T^b \nabla_b T^a = \alpha T^a [\alpha$ is a function on $\gamma(t)]$, then there exists a $t' = t'(t)$ such that $\gamma'(t')[=\gamma(t)]$ is a geodesic.

Definition: A parameter which makes a curve become a geodesic is called an ***affine*** parameter of this curve.

Sometimes a curve that satisfies $T^b \nabla_b T^a = \alpha T^a$ is also called a geodesic. Nonetheless, in order to avoid confusion, a better way to call it is a ***non-affinely parametrized*** geodesic.

Theorem: If t is an affine parameter of a geodesic, then the necessary and sufficient condition of any parameter t' of this curve to be an affine parameter is $t' = at + b$ (where a, b are constants and $a \neq 0$).

Finally, we introduce the concept of the geodesic congruences, which will be mentioned in later section. We refer to the definition of a reference frame provided in [190].

Definition: A reference frame R on a spacetime M is a vector field each of whose integral curves is an observer.

If the worldlines of all observers are geodesics, such a reference frame is physically referred to as a **Geodesic Congruence**.

Riemann Curvature

The concept of Torsion free was touched upon in Section 1.1, which ensures that

$$(\nabla_a \nabla_b - \nabla_b \nabla_a) f = 0, \tag{1.27}$$

meaning $\nabla_a \nabla_b f$ is a symmetric (0,2) type tensor. The operator $(\nabla_a \nabla_b - \nabla_b \nabla_a)$ is termed as the commutator of ∇_a. Although the result vanishes when the commutator acts on a (0,0) type tensor (scalar), it does not assure that the result remains null for other types of tensors.

Definition: The **Riemann Curvature** tensor field ${R_{abc}}^d$ of a derivative operator ∇_a is defined by the following equation

$$(\nabla_a \nabla_b - \nabla_b \nabla_a) \omega_c = {R_{abc}}^d \omega_d, \quad \forall \omega_c \in \mathscr{F}(0,1). \tag{1.28}$$

For $\forall \omega_c \in \mathscr{F}(0,1)$, we have $v^c \omega_c \in \mathscr{F}$. From the torsion-free condition, it follows that

$$\begin{aligned} 0 &= (\nabla_a \nabla_b - \nabla_b \nabla_a)(v^c \omega_c) \\ &= \nabla_a (v^c \nabla_b \omega_c + \omega_c \nabla_b v^c) - \nabla_b (v^c \nabla_a \omega_c + \omega_c \nabla_a v^c) \\ &= v^c \nabla_a \nabla_b \omega_c + \omega_c \nabla_a \nabla_b v^c - v^c \nabla_b \nabla_a \omega_c - \omega_c \nabla_b \nabla_a v^c. \end{aligned} \tag{1.29}$$

Thus, we obtain

$$\begin{aligned} & \omega_c (\nabla_a \nabla_b - \nabla_b \nabla_a) v^c \\ =& - v^c (\nabla_a \nabla_b - \nabla_b \nabla_a) \omega_c \\ =& - v^c {R_{abc}}^d \omega_d \\ =& - \omega_c {R_{abd}}^c v^d. \end{aligned} \tag{1.30}$$

Therefore, we have

Theorem:

$$(\nabla_a \nabla_b - \nabla_b \nabla_a) v^c = -{R_{abd}}^c v^d \quad \forall v^c \in \mathscr{F}(1,0). \tag{1.31}$$

If a metric field g_{ab} exists on M and satisfies $\nabla_a g_{bc} = 0$, then we can define[1]:

$$R_{abcd} \equiv g_{de} R_{abc}{}^{e},$$

$$\textbf{Ricci Tensor:} \quad R_{ac} \equiv g^{bd} R_{abcd}, \tag{1.32}$$

$$\textbf{Scalar Curvature:} \quad R \equiv g^{ac} R_{ac}.$$

The Riemann tensor field reflects the non-commutativity of a derivative operator and describes the intrinsic properties of (M, ∇_a). Once a derivative operator is chosen, its corresponding Riemann tensor can be defined. Additionally, we can discuss the Riemann tensor of a generalized Riemannian space (M, g_{ab}), often referred to as the Riemann tensor of g_{ab}. This is also known as the Riemann tensor field associated with the derivative operator ∇_a corresponding to g_{ab}. A metric with a vanishing Riemann tensor field is called a ***flat*** metric.

The Riemann curvature tensor possesses the following properties:

1. $R_{abc}{}^{d} = -R_{bac}{}^{d}$,
2. $R_{[abc]}{}^{d} = 0$,
3. $\nabla_{[a} R_{bc]d}{}^{e} = 0$,
4. $R_{abcd} = -R_{abdc}$,
5. $R_{abcd} = R_{cdab}$.

The second property, $R_{\lceil abc\rceil}{}^{d} = 0$, is known as the **Cyclic Identity**. This can be easily proven as follows:

$$\begin{aligned}
\nabla_a (\nabla_b \omega_c) &= \partial_a (\nabla_b \omega_c) - \Gamma^{d}{}_{ab} \nabla_d \omega_c - \Gamma^{d}{}_{ac} \nabla_b \omega_d \\
&= \partial_a (\partial_b \omega_c - \Gamma^{e}{}_{bc} \omega_e) - \Gamma^{d}{}_{ab} \nabla_d \omega_c - \Gamma^{d}{}_{ac} \nabla_b \omega_d \\
&= (\partial_a \partial_b \omega_c - \Gamma^{e}{}_{bc} \partial_a \omega_e - \omega_e \partial_a \Gamma^{e}{}_{bc}) - \Gamma^{d}{}_{ab} \nabla_d \omega_c - \Gamma^{d}{}_{ac} \nabla_b \omega_d.
\end{aligned} \tag{1.33}$$

Therefore, we have

$$\nabla_{[a} \nabla_b \omega_{c]} = \partial_{[a} \partial_b \omega_{c]} - \Gamma^{e}{}_{[bc} \partial_{a]} \omega_e - \omega_e \partial_{[a} \Gamma^{e}{}_{bc]} - \Gamma^{d}{}_{[ab} \nabla_{|d|} \omega_{c]} - \Gamma^{d}{}_{[ac} \nabla_{b]} \omega_d. \tag{1.34}$$

[1]The definition of the Ricci tensor is not unique; in this thesis, we adhere to the approach outlined in [231].

Noting that $\partial_a\partial_b\omega_c = \partial_b\partial_a\omega_c$ and $\Gamma^e{}_{bc} = \Gamma^e{}_{cb}$, each term on the right-hand side of the above equation vanishes. Now, considering

$$R_{[abc]}{}^d\omega_d = \nabla_{[a}\nabla_b\omega_{c]} - \nabla_{[b}\nabla_a\omega_{c]} = 2\nabla_{[a}\nabla_b\omega_{c]}, \tag{1.35}$$

we finally obtain $R_{[abc]}{}^d = 0$.

The third property, $\nabla_{[a}R_{bc]d}{}^e = 0$, is known as the **Bianchi Identity**, which was published by L. Bianchi in 1902.

To prove this identity, we need to show that $\omega_e\nabla_{[a}R_{bc]d}{}^e = 0\ \forall\omega_e \in \mathscr{F}(0,1)$. Since

$$\begin{aligned}\omega_e\nabla_a R_{bcd}{}^e &= \nabla_a\left(R_{bcd}{}^e\omega_e\right) - R_{bcd}{}^e\nabla_a\omega_e \\ &= \nabla_a\left(\nabla_b\nabla_c\omega_d - \nabla_c\nabla_b\omega_d\right) - R_{bcd}{}^e\nabla_a\omega_e,\end{aligned} \tag{1.36}$$

we have

$$\begin{aligned}\omega_e\nabla_{[a}R_{bc]d}{}^e &= \nabla_{[a}\nabla_b\nabla_{c]}\omega_d - \nabla_{[a}\nabla_c\nabla_{b]}\omega_d - R_{[bc|d|}{}^e\nabla_{a]}\omega_e \\ &= \nabla_{[a}\nabla_b\nabla_{c]}\omega_d - \nabla_{[b}\nabla_a\nabla_{c]}\omega_d - R_{[bc|d|}{}^e\nabla_{a]}\omega_e.\end{aligned} \tag{1.37}$$

To derive the sum of the first two terms on the right-hand side, we first write out the expression without the square bracket

$$\nabla_a\nabla_b\nabla_c\omega_d - \nabla_b\nabla_a\nabla_c\omega_d = \left(\nabla_a\nabla_b - \nabla_b\nabla_a\right)\nabla_c\omega_d = R_{abc}{}^e\nabla_e\omega_d + R_{abd}{}^e\nabla_c\omega_e. \tag{1.38}$$

Antisymmetrizing the lower indices a, b, and c, and using the **Cyclic Identity**, we obtain

$$\nabla_{[a}\nabla_b\nabla_{c]}\omega_d - \nabla_{[b}\nabla_a\nabla_{c]}\omega_d = R_{[ab|d|}{}^e\nabla_{c]}\omega_e = R_{[bc|d|}{}^e\nabla_{a]}\omega_e, \tag{1.39}$$

which implies that the right-hand side of Equation (1.37) vanishes. Therefore, $\omega_e\nabla_{[a}R_{bc]d}{}^e = 0$.

The trace free part of the Riemann curvature tensor is referred to as the **Weyl Tensor**, which can be defined for manifolds of dimension $n \geq 3$ by the equation

$$C_{abcd} := R_{abcd} - \frac{2}{n-2}\left(g_{a[c}R_{d]b} - g_{b[c}R_{d]a}\right) + \frac{2}{(n-1)(n-2)}Rg_{a[c}g_{d]b}. \tag{1.40}$$

Lie Derivative

Until now, our discussion has been confined to a single manifold. We will now extend our consideration to multiple manifolds. Let M and N be two distinct manifolds, and let $\phi : M \to N$ be a smooth map. We denote the sets of smooth functions on M and N as $\mathscr{F}_M$ and $\mathscr{F}_N$, respectively. The tensors $\mathscr{F}_M(k,l)$ and $\mathscr{F}_N(k,l)$ correspond to type (k,l) tensors on these manifolds.

Definition: The **Pullback Map** $\phi^* : \mathscr{F}_N \to \mathscr{F}_M$ is defined as

$$(\phi^* f)|_p := f|_{\phi(p)}, \quad \forall f \in \mathscr{F}_N, p \in M, \tag{1.41}$$

i.e., $\phi^* f = f \circ \phi$.

One can show that:

1. $\phi^* : \mathscr{F}_N \to \mathscr{F}_M$ is a linear map, i.e.,
   $\phi^*(\alpha f + \beta g) = \alpha\phi^*(f) + \beta\phi^*(g), \quad \forall f, g \in \mathscr{F}_N, \quad \alpha, \beta \in \mathbb{R}.$
2. $\phi^*(fg) = \phi^*(f)\phi^*(g), \quad \forall f, g \in \mathscr{F}_N.$

Definition: For any point in M one can define the **Pushforward Map** $\phi_* : V_p \to V_{\phi(p)}$ as follows: $\forall v^a \in V_p$, define its image $\phi_* v^a \in V_{\phi(p)}$ as

$$(\phi_* v)(f) := v(\phi^* f), \quad \forall f \in \mathscr{F}_N. \tag{1.42}$$

The map $\phi_* : V_p \to V_{\phi(p)}$ is linear, i.e., $\phi_*(\alpha u^a + \beta v^a) = \alpha\phi_* u^a + \beta\phi_* v^a, \forall u^a, v^a \in V_p$, $\alpha, \beta \in \mathbb{R}$.

For higher-rank tensors, we have $\phi^* : \mathscr{F}_N(0,l) \to \mathscr{F}_M(0,l)$ in the following way: $\forall T \in \mathscr{F}_N(0,l)$ define $\phi^* T \in \mathscr{F}_M(0,l)$ as

$$\begin{aligned} &(\phi^* T)_{a_1 \cdots a_l}\Big|_p (v_1)^{a_1} \cdots (v_l)^{a_l} := T_{a_1 \cdots a_l}|_{\phi(p)} (\phi_* v_1)^{a_1} \cdots (\phi_* v_l)^{a_l}, \\ &\forall p \in M, \quad v_1, \ldots, v_l \in V_p. \end{aligned} \tag{1.43}$$

$\forall p \in M$ the pushforward map can be extended to $\phi_* : \mathscr{T}_{V_p}(k,0) \to \mathscr{T}_{V_{\phi(p)}}(k,0)$ in the following manner [namely, ϕ_* is a map that turns a tensor of type $(k,0)$ at p into a tensor of the same type at $\phi(p)$]: $\forall T \in \mathscr{T}_{V_p}(k,0)$ its image $\phi_* T \in \mathscr{T}_{V_{\phi(p)}}(k,0)$ is defined by the following equation:

$$\begin{aligned} (\phi_* T)^{a_1 \cdots a_k} \left(\omega^1\right)_{a_1} \cdots \left(\omega^k\right)_{a_k} &:= T^{a_1 \cdots a_k} \left(\phi^* \omega^1\right)_{a_1} \cdots \left(\phi^* \omega^k\right)_{a_k}, \\ &\forall \omega_1, \ldots, \omega_k \in V^*_{\phi(p)}, \end{aligned} \tag{1.44}$$

where $(\phi^* \omega)_a$ is defined as $(\phi^* \omega)_a v^a := \omega_a (\phi_* v)^a \quad \forall v^a \in V_p$.

Note: In the definition of the pullback, the map operates between two fields, whereas in the definition of the pushforward, the map operates between two vector spaces. This implies that if ϕ is merely a *smooth* map, it cannot push forward fields. However, by adopting a more relaxed approach and assuming ϕ to be a ***diffeomorphism***, the process becomes simpler.

In this case, we obtain $\phi_* : \mathscr{F}_M(k,0) \to \mathscr{F}_N(k,0)$.

With the concepts of pullback and pushforward maps introduced, we can now define the Lie derivative:

Definition:

$$\mathscr{L}_v T^{a_1\cdots a_k}{}_{b_1\cdots b_l} := \lim_{t\to 0} \frac{1}{t}\left(\phi_t^* T^{a_1\cdots a_k}{}_{b_1\cdots b_l} - T^{a_1\cdots a_k}{}_{b_1\cdots b_l}\right) \tag{1.45}$$

is called the **Lie Derivative** of a tensor field $T^{a_1\cdots a_k}{}_{b_1\cdots b_l}$ along a vector field v^a.

Here are several highly useful theorems that we may use later.

Theorem:

$$\mathscr{L}_v f = v(f), \quad \forall f \in \mathscr{F}. \tag{1.46}$$

Theorem:

$$\mathscr{L}_v u^a = [v,u]^a, \quad \forall u^a, v^a \in \mathscr{F}(1,0), \tag{1.47}$$

i.e.

$$\mathscr{L}_v u^a = v^b \nabla_b u^a - u^b \nabla_b v^a, \tag{1.48}$$

where ∇_a is an arbitrary torsion-free derivative operator.

Theorem:

$$\mathscr{L}_v \omega_a = v^b \nabla_b \omega_a + \omega_b \nabla_a v^b, \quad \forall v^a \in \mathscr{F}(1,0), \omega_a \in \mathscr{F}(0,1), \tag{1.49}$$

where ∇_a is an arbitrary torsion-free derivative operator.

Next, we introduce a crucial concept: a vector field ξ^a on (M, g_{ab}) is called a **Killing Vector Field** if

$$\mathscr{L}_\xi g_{ab} = 0. \tag{1.50}$$

Hypersurfaces

"I could be bounded in a nutshell and count myself a king of infinite space."

— William Shakespeare, *"Hamlet"*.

In numerical relativity, hypersurfaces and the spatial physical quantities defined on them are frequently employed. As such, it is essential to introduce hypersurfaces within this context.

First, we will introduce the concept of embedding.

Definition: Suppose M and S are manifolds, $\dim S \leqslant \dim M \equiv n$. A map $\phi : S \to M$ is called an **Embedding** if ϕ is one-to-one and C^∞, and $\forall p \in S$, the pushforward map $\phi_* : V_p \to V_{\phi(p)}$ is non-degenerate [$V_{\phi(p)}$ is the tangent space at the point $\phi(p)$ in M], i.e., $\phi_* v^a = 0 \Rightarrow v^a = 0$.

Now, with the help of embedding, we introduce hypersurfaces.

Definition: An embedding $\phi : S \to M$ is called an embedded submanifold of M, or a **Submanifold** of M for short. The image $\phi[S]$ is also often called an embedded submanifold. If $\dim S = n-1$, then $\phi[S] \subset M$ is called a **Hypersurface** of M.

When discussing a hypersurface, it is intuitive to consider its normal vectors. Assume $\phi[S]$ represents a hypersurface, and $q \in \phi[S]$, then a normal vector n^a at point q is defined as a vector orthogonal to all vectors tangent to $\phi[S]$. Yet, the notion of orthogonality holds meaning only once a metric is assigned. In the absence of a metric on M, defining a normal vector n^a is not feasible, but it is possible to define a "normal covector" n_a. A covector is alternatively referred to as a dual vector. Given that a dual vector yields a real number upon acting on a vector (without the need for a metric), a normal covector can be defined as follows:

Definition: Suppose $\phi[S]$ is a hypersurface, $q \in \phi[S]$. A nonzero dual vector $n_a \in V_q^*$ is called a **Normal Covector** of $\phi[S]$ at q if $n_a w^a = 0, \forall w^a \in W_q$.

Suppose n_a is a normal covector of $\phi[S]$ at the point q. If a metric g_{ab} exists on M, then the vector $n^a \equiv g^{ab} n_b \in V_q$ is orthogonal to all tangent vectors at q on $\phi[S]$ (since $g_{ab} n^a w^b = n_b w^b = 0$ for all $w^b \in W_q$). Therefore, n^a is referred to as the normal vector of the hypersurface $\phi[S]$ at q.

Using n^a, we can classify hypersurfaces into three types.

Definition: A hypersurface is said to be ***spacelike*** if its normal vectors are everywhere ***timelike*** ($n^a n_a < 0$); a hypersurface is said to be ***timelike*** if its normal vectors are everywhere ***spacelike*** ($n^a n_a > 0$); a hypersurface is said to be ***null*** or ***lightlike*** if its normal vectors are everywhere ***null*** $(n^a n_a = 0)$.

Furthermore, we will discuss the induced metric.

Definition: Suppose $\phi[S]$ is an embedding submanifold (not necessarily a hypersurface) in M. Let W_q be the tangent space at an arbitrary point $q \in \phi[S]$ that is tangent to $\phi[S]$. A tensor γ_{ab} on W_q is called the **Induced Metric** derived from the metric g_{ab} on V_q if

$$\gamma_{ab} w_1^a w_2^b = g_{ab} w_1^a w_2^b, \quad \forall w_1^a, w_2^b \in W_q. \tag{1.51}$$

The induced metric, denoted as γ_{ab}, essentially arises from restricting the target action of g_{ab} on V_q to W_q. Being defined pointwise on $\phi[S]$, it consequently generates an induced metric field on $\phi[S]$. When $\phi[S]$ represents a timelike or spacelike hypersurface, the induced metric can be succinctly expressed using the normalized normal vector, denoted by $(n^a n_a = \pm 1)$, as follows:

$$\gamma_{ab} \equiv g_{ab} \mp n_a n_b, \tag{1.52}$$

where the sign "$-$" is chosen for $n^a n_a = +1$, and the sign "$+$" is chosen for $n^a n_a = -1$. It is important to note that there is no induced metric on the null hypersurface, as it is degenerate.

Additionally, we would like to mention the projection map:

$$\gamma^a{}_b \equiv g^{ac} \gamma_{cb} = \delta^a{}_b \mp n^a n_b, \tag{1.53}$$

where sometimes the notation $h^a{}_b$ is used instead of $\gamma^a{}_b$.

Spatial Derivative

Next, we introduce a derivative operator that plays a crucial role in numerical relativity.

Let Σ be a spacelike hypersurface in (M, g_{ab}), where γ_{ab} is the induced metric of g_{ab} on Σ. [Σ can either be any Σ_t from the family of spacelike hypersurfaces $\{\Sigma_t\}$, or an isolated spacelike hypersurface unrelated to the $3+1$ decomposition.] Then, (Σ, γ_{ab}) forms a 3-dimensional Riemannian space, and there exists a unique derivative operator compatible with γ_{ab}, denoted as D_c, such that $\mathrm{D}_c \gamma_{ab} = 0$. This operator D_c can be obtained through the compatible derivative operator ∇_a of g_{ab}.

Definition: The **Spatial Derivative** of a spatial tensor field $T^{a_1 \cdots a_k}{}_{b_1 \cdots b_l}$ is defined as:

$$\mathrm{D}_c T^{a_1 \cdots a_k}{}_{b_1 \cdots b_l} := \gamma^{a_1}{}_{d_1} \cdots \gamma^{a_k}{}_{d_k} h_{b_1}{}^{e_1} \cdots \gamma_{b_l}{}^{e_l} \gamma_c{}^f \nabla_f T^{d_1 \cdots d_k}{}_{e_1 \cdots e_l}. \tag{1.54}$$

Extrinsic Curvature

Here, we introduce the extrinsic curvature, which is defined by how the normal vector changes as it is parallel transported from one point on the hypersurface to another.

Definition: The definition of **Extrinsic Curvature** is related to the induced metric and normal covector mentioned earlier:

$$K_{ab} := \gamma^c{}_a \gamma^d{}_b \nabla_c n_d, \tag{1.55}$$

where $\gamma^a{}_b$ is the induced metric, and n_d is the normal covector.

Humans can perceive objects externally; we perceive a plane as flat and a spherical surface as curved. In reality, we are considering objects in a higher-dimensional space. An *ant* living in a 1-dimensional world cannot distinguish a circle, as it only knows front and back. We perceive something as flat or curved because we live in a 3-dimensional world. The question arises: for a given n-dimensional manifold, can we discuss curvature? The answer is ***YES***, and that's where Extrinsic curvature comes into play. However, we need to first embed this n-dimensional manifold into an $(n+1)$-dimensional manifold [144].

In contrast, the Riemann curvature tensor does not require an additional dimensional manifold for embedding. It represents intrinsic curvature, shedding light on certain properties of the manifold:

1. The non-commutativity, i.e., $(\nabla_a \nabla_b - \nabla_b \nabla_a)\, \omega_c = R_{abc}{}^d \omega_d$,

2. The path dependence of parallel transport,

3. Existence of geodesics that are initially parallel but do not remain parallel later on.

1.2 The Einstein Field Equations

Prelude

Two significant factors prompted Einstein to establish **General Relativity**: **Universality** and **Mach's Principle**.

The Universality of Newtonian gravity includes two aspects:

1. Every object within a gravitational field is affected by gravity.
2. Within a gravitational field, any two objects, regardless of their mass and composition, will have identical positions and velocities at every subsequent moment, provided their initial states are the same and they are not subjected to any other forces besides gravity.

As for Mach's Principle, we believe it indeed influenced Einstein at the outset, but it seems that once general relativity matured, few people continued to emphasize this principle. Therefore, we humbly choose not to discuss it here.

When establishing general relativity, Einstein proposed the following **Principle of General Covariance**, asserting that the mathematical expressions of physical laws remain invariant under any coordinate transformations. A more precise articulation comes from R. Wald: ***The metric, and quantities derivable from it are the only spacetime quantities that can appear in the equations of physics [231].***

Equivalence principle

> *In a society flourishing with health, it is not merely a singular echo that should resound.*

We will start with the well-known example of Einstein's elevator. Suppose an elevator near the ground is in free fall due to a broken cable, the stationary observer inside it (a freely falling observer with no self-rotation) will experience a sense of weightlessness, a result already known in Newtonian mechanics. If he releases an apple from his hand, he will find that it does not fall as usual, but remains in a state of equilibrium. The reason is straightforward: the elevator observer G experiences a gravitational acceleration $\vec{g}$ relative to the inertial frame (Earth), classifying him as a non-inertial observer from the perspective of Newtonian mechanics, whereas the opposite is true in general relativity. Therefore,

he perceives two forces acting on the apple; one is the gravitational force $m_G\vec{g}$ (m_G is the gravitational mass of the apple), and the other is the inertial force $-m_I\vec{g}$ ($-m_I$ is the inertial mass of the apple). Since $m_G = m_I$, the net force is zero, hence the apple is in equilibrium or said to be in a state of weightlessness. If he were an astronaut, he would find this apple behaving similarly to an apple inside an inertial spaceship far away from any planet (where spacetime is approximately flat). Extending this further, due to $m_G = m_I$, according to Newtonian mechanics, all (non-gravitational) mechanical experiments within Einstein's elevator would yield the same results as corresponding experiments inside an inertial spaceship far from any planet. This is precisely why $m_G = m_I$ is referred to as the equivalence principle.

In the process of conceptualizing general relativity, Einstein hypothetically extended this principle from mechanical experiments to all physical experiments, implying that all (non-gravitational) physical experiments within a freely falling elevator would yield identical results as corresponding experiments inside an inertial spaceship far from any planet (in flat spacetime). Successors referred to the principle associated with $m_G = m_I$ as the **Weak Equivalence Principle (WEP)**, and the extended principle postulated by Einstein as the **Einstein Equivalence Principle (EEP)**. Additionally, there is the **Strong Equivalence Principle (SEP)**, which we will not discuss here.

It is worth noting that different scholars have varying interpretations regarding the meaning, status, and role of the equivalence principle. Some consider it to be of great significance [144].

For example, Misner et al. [158] p.386 said that "The principle of equivalence has great power. With it one can generalize all the special relativistic laws of physics to curved spacetime." They also said (p.207) "The vehicle that carries one from classical mechanics to quantum mechanics is the correspondence principle. Similarly, the vehicle between flat spacetime and curved spacetime is the equivalence principle."

On the other hand, J.L.Synge showed disdain for the equivalence principle. He wrote in the preface of Synge [221] that: "I have never been able to understand this principle. ..... Does it mean that the effects of a gravitational field are indistinguishable from the effects of an observer's acceleration? If so, it is false. In Einstein's theory, either there is a gravitational field or there is none, according as the Riemann tensor does not or does vanish. This is an absolute property; it has nothing to do wiany observer's world line. Spacetime is either flat or curved, and in several places in this book I have been at considerable pains to separate truly gravitational effects due to curvature of spacetime from those due to curvature of the observer's world line (in most ordinary cases the latter predominate). The principle of equivalence performed the essential office of midwife at the birth of general relativity, ... I suggest that the midwife be now buried with appropriate honors and the facts of absolute spacetime be faced."

Tidal Forces and Geodesic Deviation Equation

Using Newtonian gravitational theory, we will consider the case of an Einstein elevator near the Earth, without loss of generality. Suppose there are small balls placed everywhere inside the elevator (see Figure (1.2)). Let $\vec{r}(t)$ and $\vec{r}(t)+\vec{w}(t)$ represent the position vectors of two closely packed balls 1 and 2 relative to the origin o of the Cartesian coordinate system, respectively. Therefore, $\vec{w}(t)$ is the position of ball 2 relative to ball 1, hence $\mathrm{d}^2\vec{w}/\mathrm{d}t^2$ is the acceleration of ball 2 relative to ball 1 (tidal acceleration). The expression is as follows:

$$\frac{\mathrm{d}^2 w^i}{\mathrm{d}t^2} = -\left.\frac{\partial^2\phi}{\partial x^i \partial x^j}\right|_{\vec{r}} w^j, \quad i=1,2,3. \tag{1.56}$$

Next, we will examine tidal phenomena from the perspective of general relativity. In general relativity, tidal effects arise due to the curvature of spacetime and are an inevitable manifestation of the intrinsic curvature within spacetime. We will continue to use Figure (1.2) as an example. Each small ball can be regarded as a freely falling observer, and their world lines are timelike geodesics with proper time τ as the affine parameter. These geodesics form a geodesic congruence in some open region of spacetime (physically corresponding to a freely falling reference frame), with the tangent vector $Z^a \equiv (\partial/\partial\tau)^a$ being a timelike vector field on U. Let $\mu_0(s)$ be a smooth transverse curve (transverse means that the tangent vector at any point on $\mu_0(s)$ does not coincide with the geodesic passing through that point), then each geodesic $\gamma(\tau)$ intersecting with $\mu_0(s)$ can be denoted by s, i.e., $\gamma_s(\tau)$ where s is the value of s at the intersection point of the geodesic with $\mu_0(s)$. If we let $w^a \equiv (\partial/\partial s)^a$, the following conclusions can be drawn.

Claim: The tidal acceleration measured in any reference geodesic $\gamma_0(\tau)$ within a single-parameter timelike geodesic congruence is related to the curvature tensor of spacetime expressed through the following equation, commonly known as the **Geodesic Deviation Equation**,

$$a^c = -R_{abd}{}^c Z^a w^b Z^d. \tag{1.57}$$

The geodesic deviation equation reflects the close relationship between a^c and the spacetime curvature tensor $R_{abd}{}^c$, for flat spacetime ($R_{abd}{}^c = 0$), a^c must be zero, thus initially parallel geodesics remain parallel. However, as long as $R_{abd}{}^c \neq 0$, there exists such a single-parameter geodesic family whose geodesic deviation is non-zero, which can be interpreted as initially parallel geodesics becoming non-parallel later on. Therefore, a non-zero curvature tensor's equivalent expression is the existence of geodesics that are initially parallel but become non-parallel later on.

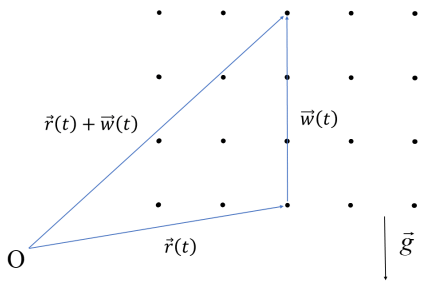

Fig. 1.2 Small balls placed everywhere inside the Einstein elevator

The Christoffel symbols $\Gamma^{\sigma}{}_{\mu\nu}$ depend on the coordinate system; choosing an inertial coordinate system of free-falling, non-rotating observers can make the Christoffel symbols zero along the observer's worldline, thereby explaining the weightlessness felt by the observer in the Einstein elevator. However, the tidal acceleration a^c is directly associated with the Riemann tensor $R_{abc}{}^{d}$, and as a tensor (note that we are using abstract index notation here), the latter cannot be made zero by choosing a coordinate system. Therefore, tidal acceleration cannot be eliminated by coordinate transformation. Although the observer in the Einstein elevator does not feel gravity, he still feels the tidal forces.

The Einstein Field Equations

Since material distribution gives rise to gravity, and gravity manifests as spacetime curvature, a natural conjecture is that the curvature of spacetime should be influenced by the distribution of matter. The distribution of matter is described by the energy-momentum tensor T_{ab}, thus there should be an equation that relates spacetime curvature to T_{ab}. Considering that Newtonian gravity should be the weak-field, low-speed approximation of general relativity, the comparison between the geodesic deviation equation (1.57) and the expression for tidal forces in Newtonian gravity (1.56) provides important clues for seeking (or conjecturing) this equation. Let $\{x^i\}$ be the Cartesian coordinate system of a 3-dimensional Euclidean space, then Equation (1.56) can be written as:

$$\begin{aligned} a^c &= a^i \left(\frac{\partial}{\partial x^i}\right)^c = \left(\frac{\partial}{\partial x^i}\right)^c \frac{\mathrm{d}^2 w^i}{\mathrm{d}t^2} = -\left(\frac{\partial}{\partial x^i}\right)^c w^j \frac{\partial}{\partial x^j}\left(\frac{\partial \phi}{\partial x^i}\right) \\ &= -\left(\frac{\partial}{\partial x^i}\right)^c w^b \partial_b \left(\frac{\partial \phi}{\partial x^i}\right) = -w^b \partial_b \left[\left(\frac{\partial}{\partial x^i}\right)^c \left(\frac{\partial \phi}{\partial x^i}\right)\right] \\ &= -w^b \partial_b \partial^c \phi. \end{aligned} \tag{1.58}$$

The tidal acceleration obtained above according to Newton's theory of gravity should be an approximation of a^c derived from general relativity. Hence, the comparison between

the above expression and Equation (1.57) suggests the following correspondence:

$$R_{abd}{}^{c}Z^{a}Z^{d} \leftrightarrow \partial_b\partial^c\phi. \tag{1.59}$$

Contracting the upper index c with the lower index b yields

$$R_{abd}{}^{b}Z^{a}Z^{d} \leftrightarrow \partial_b\partial^b\phi = \nabla^2\phi = 4\pi\rho = 4\pi T_{ad}Z^{a}Z^{d}, \tag{1.60}$$

where $\nabla^2\phi = 4\pi\rho$ is the Poisson equation in Newtonian gravity. This correspondence leads us to hope that the following equation holds:

$$R_{ad}Z^{a}Z^{d} = 4\pi T_{ad}Z^{a}Z^{d}, \tag{1.61}$$

The simplest assumption that satisfies the above equation is

$$R_{ab} = 4\pi T_{ab}. \tag{1.62}$$

In fact, this was the assumption initially made and publicly proposed by Einstein.

However, we know that $\nabla^a T_{ab} = 0$, hence this would lead to:

$$\nabla^a R_{ab} = 0. \tag{1.63}$$

This would lead to a physically unacceptable inference. By the Bianchi identity $\nabla_{[a}R_{bc]d}{}^{e} = 0$, contracting yields $\nabla_{[a}R_{bc]d}{}^{a} = 0$, therefore

$$0 = \nabla_a R_{bcd}{}^{a} + \nabla_c R_{abd}{}^{a} + \nabla_b R_{cad}{}^{a} = \nabla_a R_{bcd}{}^{a} - \nabla_c R_{bd} + \nabla_b R_{cd}, \tag{1.64}$$

by raising the index d using the metric and contracting with index b we get

$$0 = \nabla_a R^{a}_{c} - \nabla_c R + \nabla_b R^{b}_{c} = 2\nabla^a R_{ca} - \nabla_c R, \tag{1.65}$$

thus, the Equation (1.63) requires

$$\nabla_c R = 0. \tag{1.66}$$

This is an additional condition imposed on R_{ab} by the Equation (1.63). To illustrate the unacceptability of this condition, let $T \equiv g^{ab}T_{ab}$, by raising the index b of Equation (1.62) using the metric and contracting with index a we get $R = 4\pi T$. Hence, Equation (1.66) leads to $\nabla_c T = 0$, meaning T is constant throughout the material field. And this contradicts what we know.

The issue arises from $\nabla^a T_{ab} = 0$ while $\nabla^a R_{ab}$ should not be zero. If we could find a symmetric tensor G_{ab} of type $(0,2)$, that both automatically satisfies $\nabla^a G_{ab} = 0$, and still

leads to Equation (1.61) when written in an equation similar to Equation (1.62) replacing R_{ab}, the problem could be overcome. Einstein indeed found such a tensor, namely

$$G_{ab} \equiv R_{ab} - \frac{1}{2} R g_{ab}, \quad \nabla^a G_{ab} = 0. \tag{1.67}$$

He replaced Equation (1.62) with $G_{ab} = 8\pi T_{ab}$, that is to assume

$$R_{ab} - \frac{1}{2} R g_{ab} = 8\pi T_{ab}. \tag{1.68}$$

Einstein presented Equation (1.68) as the equation describing the relationship between spacetime curvature and the matter field, and published it in November 1915. It was later referred to as the **Einstein Field Equations**, and is a fundamental assumption of general relativity.

1.3 Gravitational Waves

The existence of wave solutions to the Einstein field equations, propagating at the speed of light, has been known since shortly after the inception of general relativity. However, the reality of gravitational waves remained a subject of skepticism for quite some time. In 1922, A. S. Eddington raised the question of whether gravitational wave solutions might merely represent fluctuations in spacetime coordinates, thus having no observable effects. The situation began to change in the 1950s. H. Bondi and others demonstrated, using methods independent of coordinate systems, that gravitational waves indeed carry energy and momentum, and the mass of a system must decrease as it emits gravitational waves. This breakthrough led to the gradual acceptance of the physical reality and observability of gravitational radiation [144].

Especially, on September 14, 2015, the LIGO gravitational wave detectors located in Hanford and Louisiana captured the gravitational waves from a black hole merger event occurring 410 Mpc away, an event now known as GW150914. This merger involved two black holes, initially 29 and 36 times the mass of the sun, spiraling into each other and eventually merging into a single black hole with a mass of 62 times that of the sun. Additionally, it can be inferred that the resultant black hole is rotating. This type of rotating black hole was initially deduced theoretically by mathematician Roy Kerr in 1963 and is known as a Kerr black hole. This event provided valuable scientific data to the scientific community, unveiling the mysterious veil of gravitational waves in the universe. Furthermore, Rainer Weiss, Barry C. Barish, and Kip S. Thorne were awarded the Nobel Prize in 2017 for their contributions to the detection of gravitational waves.

In this section, we will provide a brief introduction to the fundamental theory of gravitational waves, primarily referencing [215, 149, 19]. Furthermore, to ensure clarity and directness, we will use ***concrete*** indices throughout this section.

Gravitational Waves in the Linear Approximation

The nonlinearity of the Einstein field equations introduces significant difficulties in solving them and in the entirety of general relativity. In most cases, the gravitational field is weak, allowing us to use approximations to convert the field equations into linear equations, thereby greatly simplifying the problem. In this situation, the metric is just a small deviation from the Minkowski metric, i.e.,

$$g_{\alpha\beta} = \eta_{\alpha\beta} + h_{\alpha\beta}, \tag{1.69}$$

where $h_{\alpha\beta} = \mathscr{O}(\varepsilon) \ll 1$ represents the perturbations.

The inverse physical metric $g^{\alpha\beta}$ is given by an as yet unknown perturbation of the inverse background metric $\eta^{\alpha\beta}$,

$$g^{\alpha\beta} = \eta^{\alpha\beta} + k^{\alpha\beta}, \quad \text{where} \quad k^{\alpha\beta} = \mathscr{O}(\varepsilon), \tag{1.70}$$

and is defined by the condition $g^{\alpha\mu} g_{\mu\beta} = \delta^{\alpha}{}_{\beta}$. At linear order this gives us

$$g^{\alpha\mu} g_{\mu\beta} = (\eta^{\alpha\mu} + k^{\alpha\mu})\left(\eta_{\mu\beta} + h_{\mu\beta}\right) = \eta^{\alpha\mu}\eta_{\mu\beta} + \eta^{\alpha\mu} h_{\mu\beta} + k^{\alpha\mu}\eta_{\mu\beta} + \mathscr{O}\left(\varepsilon^2\right) = \delta^{\alpha}{}_{\beta}. \tag{1.71}$$

Applying $\eta^{\gamma\beta}$ to the above equation, we obtain

$$k^{\alpha\gamma} = -\eta^{\gamma\beta}\eta^{\alpha\mu} h_{\mu\beta} =: -h^{\alpha\gamma}. \tag{1.72}$$

Here, we introduced the convention of raising and lowering indices using the background metric. In this context, we treat the tensor field $h_{\mu\nu}$ as a tensor field on the Minkowski background.

By neglecting all $\mathscr{O}\left(\varepsilon^2\right)$ and other higher-order terms, we can obtain the following derived quantities of the physical metric,

$$\begin{aligned}
\Gamma^{\mu}{}_{\nu\rho} &= \frac{1}{2}\eta^{\mu\sigma}\left(\partial_\rho h_{\sigma\nu} + \partial_\nu h_{\rho\sigma} - \partial_\sigma h_{\nu\rho}\right), \\
R_{\mu\nu\rho\sigma} &= \frac{1}{2}\left(\partial_\rho\partial_\nu h_{\mu\sigma} + \partial_\sigma\partial_\mu h_{\nu\rho} - \partial_\rho\partial_\mu h_{\nu\sigma} - \partial_\sigma\partial_\nu h_{\mu\rho}\right), \\
R_{\mu\nu} &= \partial^\rho\partial_{(\mu} h_{\nu)\rho} - \frac{1}{2}\partial^\rho\partial_\rho h_{\mu\nu} - \frac{1}{2}\partial_\mu\partial_\nu h, \\
G_{\mu\nu} &= \partial^\rho\partial_{(\mu} h_{\nu)\rho} - \frac{1}{2}\partial^\rho\partial_\rho h_{\mu\nu} - \partial_\mu\partial_\nu h - \frac{1}{2}\eta_{\mu\nu}\left(\partial^\rho\partial^\sigma h_{\rho\sigma} - \partial^\rho\partial_\rho h\right),
\end{aligned} \tag{1.73}$$

where $h := h^{\mu}{}_{\mu}$.

Note that in the expression for the Ricci tensor, there are mixed derivative terms in addition to the d'Alembert operator. Next, we eliminate all these mixed derivative terms, leaving only the d'Alembert operator. This simplification allows us to obtain hyperbolic partial differential equations directly, which are much easier to solve.

Definition: The trace-reversed metric perturbation is defined as:

$$\bar{h}_{\mu\nu} := h_{\mu\nu} - \frac{1}{2} h\eta_{\mu\nu}. \tag{1.74}$$

According to $\bar{h} = \bar{h}^{\mu}{}_{\mu} = -h$, we obtain $h_{\mu\nu} = \bar{h}_{\mu\nu} - \frac{1}{2}\bar{h}\eta_{\mu\nu}$.

Using the above equations, the Einstein tensor (1.73) can be simplified to the following form:

$$\begin{aligned}
G_{\mu\nu} =& \partial^\rho \partial_\mu (\bar{h}_{\nu\rho} - \frac{1}{2}\bar{h}\eta_{\nu\rho}) + \partial^\rho \partial_\nu (\bar{h}_{\mu\rho} - \frac{1}{2}\bar{h}\eta_{\mu\rho}) - \frac{1}{2}\partial^\rho \partial_\rho (\bar{h}_{\mu\nu} - \frac{1}{2}\bar{h}\eta_{\mu\nu}) \\
&+ \partial_\mu \partial_\nu \bar{h} - \left[\frac{1}{2}\eta_{\mu\nu}\partial^\rho \partial^\alpha \bar{h}_{\rho\alpha} - \frac{1}{4}\eta_{\mu\nu}\partial_\alpha \partial^\alpha \bar{h} + \frac{1}{2}\eta_{\mu\nu}\partial^\rho \partial_\rho \bar{h} \right] \\
=& \partial^\rho \partial_\mu \bar{h}_{\nu\rho} - \frac{1}{2}\partial_\nu \partial_\mu \bar{h} + \partial^\rho \partial_\nu \bar{h}_{\mu\rho} - \frac{1}{2}\partial_\mu \partial_\nu \bar{h} - \frac{1}{2}\partial^\rho \partial_\rho \bar{h}_{\mu\nu} + \frac{1}{4}\eta_{\mu\nu}\partial^\rho \partial_\rho \bar{h} \\
&+ \partial_\mu \partial_\nu \bar{h} - \frac{1}{2}\eta_{\mu\nu}\partial^\rho \partial^\alpha \bar{h}_{\rho\alpha} + \frac{1}{4}\eta_{\mu\nu}\partial_\alpha \partial^\alpha \bar{h} - \frac{1}{2}\eta_{\mu\nu}\partial^\rho \partial_\rho \bar{h} \\
=& -\frac{1}{2}\partial^\rho \partial_\rho \bar{h}_{\mu\nu} + \partial^\rho \partial_{(\mu}\bar{h}_{\nu)\rho} - \frac{1}{2}\eta_{\mu\nu}\partial^\rho \partial^\sigma \bar{h}_{\rho\sigma}.
\end{aligned} \tag{1.75}$$

We can achieve further simplification by changing to a more suitable set of coordinates. In this process, however, we aim to preserve the background metric and thus consider coordinate transformations at the perturbative level.

By introducing $\xi^\mu = \mathscr{O}(\varepsilon)$, we perform the following coordinate transformation:

$$\tilde{x}^\alpha = x^\alpha - \xi^\alpha, \qquad x^\alpha = \tilde{x}^\alpha + \xi^\alpha. \tag{1.76}$$

The metric in the new coordinate system becomes

$$\begin{aligned}
\tilde{g}_{\alpha\beta} &= \frac{\partial x^\mu}{\partial \tilde{x}^\alpha}\frac{\partial x^\nu}{\partial \tilde{x}^\beta} g_{\mu\nu} \\
&= g_{\alpha\beta} + \partial_\alpha \xi^\mu \delta^\nu{}_\beta g_{\mu\nu} + \partial_\beta \xi^\nu \delta^\mu{}_\alpha g_{\mu\nu} + \mathscr{O}\left(\varepsilon^2\right) \\
&= \eta_{\alpha\beta} + h_{\alpha\beta} + \partial_\alpha \xi_\beta + \partial_\beta \xi_\alpha + \mathscr{O}\left(\varepsilon^2\right),
\end{aligned} \tag{1.77}$$

so that the perturbation transforms according to

$$\begin{aligned}
\tilde{h}_{\alpha\beta} &= h_{\alpha\beta} + \partial_\alpha \xi_\beta + \partial_\beta \xi_\alpha, \\
\tilde{h} &= h + 2\eta^{\mu\nu}\partial_\mu \xi_\nu, \\
\bar{\tilde{h}}_{\alpha\beta} &:= \tilde{h}_{\alpha\beta} - \frac{1}{2}\tilde{h}\eta_{\alpha\beta} = \bar{h}_{\alpha\beta} + \partial_\alpha \xi_\beta + \partial_\beta \xi_\alpha - \partial^\mu \xi_\mu \eta_{\alpha\beta}.
\end{aligned} \tag{1.78}$$

From this, we can derive

$$\partial^\nu \bar{\bar{h}}_{\mu\nu} = \partial^\nu \left[\bar{h}_{\mu\nu} + \partial_\mu \xi_\nu + \partial_\nu \xi_\mu - \partial^\rho \xi_\rho \eta_{\mu\nu}\right] = \partial^\nu \bar{h}_{\mu\nu} + \partial^\nu \partial_\nu \xi_\mu. \tag{1.79}$$

By choosing

$$\partial^\rho \partial_\rho \xi_\mu = -\partial^\rho \bar{h}_{\mu\rho}, \tag{1.80}$$

the Lorenz gauge condition can then be satisfied. This simplifies the linearized Einstein equations to

$$G_{\mu\nu} = \Box \bar{h}_{\mu\nu} = \partial^\rho \partial_\rho \bar{h}_{\mu\nu} = -16\pi T_{\mu\nu}. \tag{1.81}$$

Gravitational waves are ripples in spacetime created by strong-field sources and then spread outwards. Far from the source, their amplitude decreases enough that we can treat them as perturbations of the Minkowski metric. Additionally, we assume the area where the gravitational waves travel is a vacuum. Therefore, in Lorenz gauge, gravitational waves follow Equation (1.81) with $T_{\mu\nu} = 0$, which is the wave equation for flat-space

$$\Box \bar{h}_{\mu\nu} = \left(-\partial_t^2 + \vec{\nabla}^2\right) \bar{h}_{\mu\nu} = 0. \tag{1.82}$$

Plane-wave solutions to this equation are readily obtained as follows

$$\bar{h}_{\mu\nu} = H_{\mu\nu} e^{\mathrm{i} k_\rho x^\rho}, \tag{1.83}$$

where k_ρ denotes the 4-wave vector and $H_{\mu\nu}$ is a constant. Substituting this solution into Equation (1.82), we obtain $k^\alpha k_\alpha = 0$, which means that gravitational waves propagate at the speed of light. Furthermore, from the Lorenz gauge condition $\partial^\nu \bar{h}_{\mu\nu} = 0$, we obtain

$$k^\mu H_{\mu\nu} = 0, \tag{1.84}$$

which means that these waves propagate transverse to the direction of propagation. For example, for a gravitational wave propagating along the z-axis, $k_\mu = \omega(-1,0,0,1)$, it follows that $H_{\mu 0} + H_{\mu 3} = 0$.

Substituting solution (1.83) into Equation (1.80) and considering the condition given by Equation (1.84), we find that

$$\partial^\rho \partial_\rho \xi_\mu = 0. \tag{1.85}$$

This is another wave equation, and thus we can immediately write its solution as

$$\xi_\mu = X_\mu e^{\mathrm{i} k_\rho x^\rho}. \tag{1.86}$$

This implies that the Lorenz gauge does not uniquely determine $\bar{h}_{\mu\nu}$. One can show that there exists a choice for X_μ such that

$$H_{0\mu} = 0, \qquad H^{\mu}{}_{\mu} = 0. \tag{1.87}$$

This specific gauge is commonly referred to as the **Transverse-Traceless Gauge**.

Next, we will see two benefits of this gauge. First, in this gauge, $h = 0$, which means the trace-reversed perturbation is equal to the original metric perturbation, i.e., $\bar{h}_{\mu\nu} = h_{\mu\nu}$. Another benefit is that for a plane wave propagating along the z-axis, we have $H_{0\mu} = H_{3\mu} = H^{\mu}{}_{\mu} = 0$. This means we can write $H_{\mu\nu}$ in the following form

$$H_{\mu\nu} = \begin{pmatrix} 0 & 0 & 0 & 0 \\ 0 & H_+ & H_\times & 0 \\ 0 & H_\times & -H_+ & 0 \\ 0 & 0 & 0 & 0 \end{pmatrix} \tag{1.88}$$

where H_+ and $H_\times$ are the two polarization modes.

To clearly understand the physical meaning of these two polarization modes, we can consider a simple example. Suppose a particle is initially at rest in a background inertial frame, i.e., with 4-velocity $u^\alpha = (1,0,0,0)$. The geodesic equation at the initial time is given by

$$\frac{\mathrm{d}}{\mathrm{d}\tau}u^\alpha + \Gamma^\alpha{}_{\mu\nu}u^\mu u^\nu = \dot{u}^\alpha + \Gamma^\alpha{}_{00} = 0. \tag{1.89}$$

Here, $\Gamma^\alpha{}_{00} = \frac{1}{2}\eta^{\alpha\mu}\left(\partial_0 h_{\mu 0} + \partial_0 h_{0\mu} - \partial_\mu h_{00}\right) = 0$ since $H_{0\mu} = 0$. This means $u^\alpha = (1,0,0,0)$ at all times is the unique solution of the geodesic equation, and the particle remains at a fixed coordinate position x^μ as the gravitational wave passes through.

Physical experiments, however, measure the proper distance, which is obtained from

$$\mathrm{d}s^2 = -\mathrm{d}t^2 + (1+h_+)\,\mathrm{d}x^2 + (1-h_+)\,\mathrm{d}y^2 + 2h_\times \mathrm{d}x\,\mathrm{d}y + \mathrm{d}z^2 \tag{1.90}$$

where $h_{+,\times} = H_{+,\times}e^{ik_\rho x^\rho}$.

For the case where $H_\times = 0$ and $H_+ \neq 0$, h_+ oscillates, as shown in Figure 1.3a.

2 particles at $(-\delta,0,0),(\delta,0,0)$ have $\mathrm{d}s^2 = (1+h_+)4\delta^2$.

2 particles at $(0,-\delta,0),(0,\delta,0)$ have $\mathrm{d}s^2 = (1-h_+)4\delta^2$.

For the case where $H_+ = 0$ and $H_\times \neq 0$, $h_\times$ oscillates, as shown in Figure 1.3b.

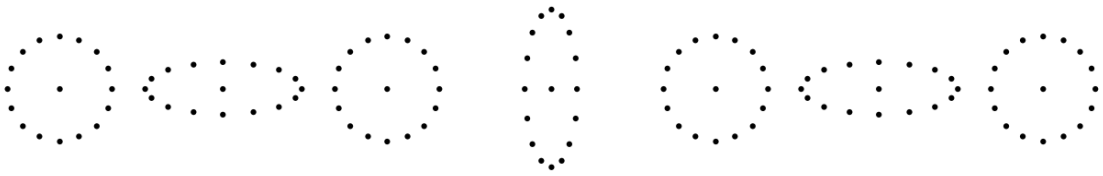

(a) The evolution of the + mode gravitational wave. Time moves from left to right in the figure, and the circle's deformation oscillates like a + sign [149].

(b) The evolution of the × mode gravitational wave. Time moves from left to right in the figure, and the circle's deformation oscillates like a × sign [149].

Fig. 1.3 The figures illustrate the motion of the test particles as the gravitational wave generates the oscillating perturbations H_+ and $H_\times$.

2 particles at $(-\delta,-\delta,0)/\sqrt{2},(\delta,\delta,0)/\sqrt{2}$ have $\mathrm{d}s^2 = (1+h_\times)4\delta^2$.

2 particles at $(\delta,-\delta,0)/\sqrt{2},(-\delta,\delta,0)/\sqrt{2}$ have $\mathrm{d}s^2 = (1-h_\times)4\delta^2$.

The Newman–Penrose Formalism

Besides the coordinate basis method and the orthonormal tetrad method, another frequently used method in relativity for computing curvature is the **Null Tetrad Method** proposed by Newman and Penrose [165]. This method can be viewed as a variant of the tetrad method, but instead of using an orthonormal tetrad, it employs a complex null tetrad. Suppose p is a point in a 4-dimensional spacetime, and $\left\{e^\mu_{(0)}, e^\mu_{(1)}, e^\mu_{(2)}, e^\mu_{(3)}\right\}$ is an orthonormal tetrad at p. Define four special vectors at p as follows:

$$\begin{aligned} l^\mu &= \frac{1}{\sqrt{2}}\left(e^\mu_{(0)} + e^\mu_{(1)}\right), \\ k^\mu &= \frac{1}{\sqrt{2}}\left(e^\mu_{(0)} - e^\mu_{(1)}\right), \\ m^\mu &= \frac{1}{\sqrt{2}}\left(e^\mu_{(2)} + ie^\mu_{(3)}\right), \\ \bar{m}^\mu &= \frac{1}{\sqrt{2}}\left(e^\mu_{(2)} - ie^\mu_{(3)}\right). \end{aligned} \tag{1.91}$$

These four null vectors satisfy the following relations:

$$\begin{aligned} l_\mu l^\mu = k_\mu k^\mu = m_\mu m^\mu = \bar{m}_\mu \bar{m}^\mu = 0, \\ l_\mu m^\mu = l_\mu \bar{m}^\mu = k_\mu m^\mu = k_\mu \bar{m}^\mu = 0, \\ l_\mu k^\mu = -m_\mu \bar{m}^\mu = -1. \end{aligned} \tag{1.92}$$

In practice, we usually choose the vector $e^\mu_{(0)}$ as the unit normal to the spatial hypersurfaces, i.e., $e^\mu_{(0)} = n^\mu$, and $e^\mu_{(1)}$ as the unit radial vector in spherical coordinates, i.e., $e^\mu_{(1)} = e^\mu_r$. The vectors $\left(e^\mu_{(2)}, e^\mu_{(3)}\right)$ are chosen as unit vectors in the angular directions [2].

Weyl Scalars

By using the Newman–Penrose formalism, the Weyl tensor (1.40) can be conveniently represented by five complex scalar quantities known as the Weyl scalars, defined as follows:

$$\begin{aligned} \Psi_0 &:= C_{(1)(3)(1)(3)} = C_{\alpha\beta\mu\nu} l^\alpha m^\beta l^\mu m^\nu, \\ \Psi_1 &:= C_{(1)(2)(1)(3)} = C_{\alpha\beta\mu\nu} l^\alpha k^\beta l^\mu m^\nu, \\ \Psi_2 &:= C_{(1)(3)(4)(2)} = C_{\alpha\beta\mu\nu} l^\alpha m^\beta \bar{m}^\mu k^\nu, \\ \Psi_3 &:= C_{(1)(2)(4)(2)} = C_{\alpha\beta\mu\nu} l^\alpha k^\beta \bar{m}^\mu k^\nu, \\ \Psi_4 &:= C_{(2)(4)(2)(4)} = C_{\alpha\beta\mu\nu} k^\alpha \bar{m}^\beta k^\mu \bar{m}^\nu. \end{aligned} \tag{1.93}$$

Among the five Weyl scalars mentioned above, we are particularly interested in Ψ_4. This is because, far from the source of the gravitational waves, for plane waves in the transverse-traceless gauge traveling along the r direction, the Weyl scalars become:

$$\begin{aligned} &\Psi_1 = \Psi_2 = \Psi_3 = 0, \\ &\Psi_0 = -\frac{1}{4}\left(\partial_t^2 h_+ + 2\partial_t\partial_r h_+ + \partial_r^2 h_+\right) - \frac{i}{4}\left(\partial_t^2 h_\times + 2\partial_t\partial_r h_\times + \partial_r^2 h_\times\right), \\ &\Psi_4 = -\frac{1}{4}\left(\partial_t^2 h_+ - 2\partial_t\partial_r h_+ + \partial_r^2 h_+\right) + \frac{i}{4}\left(\partial_t^2 h_\times - 2\partial_t\partial_r h_\times + \partial_r^2 h_\times\right). \end{aligned} \tag{1.94}$$

[2] Note that even in flat space, the coordinate vectors e^μ_θ and e^μ_φ are not unit vectors, so they need to be normalized.

Furthermore, for outgoing waves we have $h = h(r-t)$, so that $\partial_r h = -\partial_t h$. The Weyl scalars then reduce to

$$\begin{aligned} &\Psi_0 = \Psi_1 = \Psi_2 = \Psi_3 = 0, \\ &\Psi_4 = -\ddot{h}_+ + i\ddot{h}_\times. \end{aligned} \tag{1.95}$$

It should be mentioned that in the above derivation, we have assumed the null tetrad is obtained from the standard spherical coordinates in flat space. This is reasonable because, in practical work, we are always extracting the gravitational waveform at a great distance from the source.

The Multipolar Decomposition of Ψ_4

Though these expressions are quite general, it is convenient to rewrite them in terms of multipole expansions. This method is also used in practice.

Given a gravitational wave signal Ψ_4 extracted on a sphere of constant extraction radius $R_{\rm ex}$, we obtain the individual multipoles of indices $l = 2,3,\ldots$ and $m = -l, -l+1, \ldots, l$ by projecting Ψ_4 onto spherical harmonics Y^{-2}_{lm} of spin-weight -2,

$$\psi_{lm} := \left(Y^{-2}_{lm}, \Psi_4\right) := \int_0^{2\pi}\int_0^{\pi} \Psi_4 \bar{Y}^{-2}_{lm} \sin\theta \mathrm{d}\theta \mathrm{d}\phi, \tag{1.96}$$

$$\Psi_4(t,\theta,\phi) = \sum_{l=2}^{\infty}\sum_{m=-l}^{l} \psi_{lm}(t) Y^{-2}_{lm}(\theta,\phi). \tag{1.97}$$

Ideally, we hope $R_{\rm ex}$ can be taken to infinity, but in practice, we can only choose sufficiently large finite values. Furthermore, within a given simulation domain, selecting $R_{\rm ex}$ closer to the boundary is not necessarily better, as feedback effects from the boundary may worsen the results. Therefore, selecting an appropriate $R_{\rm ex}$ is crucial in gravitational wave signal analysis.

Here, we present an example for $l = 2$, which is of primary interest in our practical work:

$$
\begin{aligned}
Y_{22}^{-2}(\theta,\phi) &= \sqrt{\frac{5}{64\pi}}(1+\cos\theta)^2 e^{2\mathrm{i}\phi}, \\
Y_{21}^{-2}(\theta,\phi) &= \sqrt{\frac{5}{16\pi}}\sin\theta(1+\cos\theta)e^{\mathrm{i}\phi}, \\
Y_{20}^{-2}(\theta,\phi) &= \sqrt{\frac{15}{32\pi}}\sin^2\theta, \\
Y_{2-1}^{-2}(\theta,\phi) &= \sqrt{\frac{5}{16\pi}}\sin\theta(1-\cos\theta)e^{-\mathrm{i}\phi}, \\
Y_{2-2}^{-2}(\theta,\phi) &= \sqrt{\frac{5}{64\pi}}(1-\cos\theta)^2 e^{-2\mathrm{i}\phi}.
\end{aligned}
\tag{1.98}
$$

The spherical harmonics form a complete orthonormal basis, so that

$$
\left(Y_{lm}^{-2}, \bar{Y}_{l'm'}^{-2}\right) = \left(\bar{Y}_{lm}^{-2}, Y_{l'm'}^{-2}\right) = \delta_{ll'}\delta_{mm'}. \tag{1.99}
$$

Energy and Momentum of Gravitational Waves

Although the energy and momentum carried by gravitational waves cannot be precisely localized and only have physical meaning in a finite region [19], they can be computed from the averaged stress-energy tensor for the effective energy contained in high-frequency gravitational waves, first calculated by Isaacson [118, 119].

In terms of the trace-reversed first-order perturbation, the Isaacson stress-energy tensor is given by

$$
t_{\mu\nu} = \frac{1}{32\pi}\left\langle \partial_\mu \bar{h}_{\rho\sigma}\partial_\nu \bar{h}^{\rho\sigma} - \frac{1}{2}\partial_\mu \bar{h}\partial_\nu \bar{h} - 2\partial_\sigma \bar{h}^{\rho\sigma}\partial_{(\mu}\bar{h}_{\nu)\rho} \right\rangle, \tag{1.100}
$$

where $\langle\cdots\rangle$ denotes the average over volumes.

It is also not difficult to show that $t_{\mu\nu}$ is, in fact, gauge invariant. In the transverse-traceless gauge, $t_{\mu\nu}$ reduces to

$$
t_{\mu\nu}^{\mathrm{TT}} = \frac{1}{32\pi}\left\langle \partial_\mu h_{ij}\partial_\nu h^{ij} \right\rangle, \tag{1.101}
$$

where "TT" stands for transverse-traceless gauge.

Consider the flux of energy along the direction i, which is generally given by t^{0i}. The energy flux along the radial direction for gravitational waves will then be given in locally

Cartesian coordinates by

$$\frac{dE}{dtdA} = t^{0r} = \frac{1}{16\pi}\,\mathrm{Re}\left\langle \partial^0 H \partial^r \bar{H}\right\rangle = -\frac{1}{16\pi}\,\mathrm{Re}\left\langle \partial_t H \partial_r \bar{H}\right\rangle \tag{1.102}$$

where $H = h_+ - ih_\times$, "Re" denotes the real part, and dA is the area element orthogonal to the radial direction.

For outgoing waves, we have

$$\frac{dE}{dtdA} = \frac{1}{16\pi}\langle \dot{H}\dot{\bar{H}}\rangle = \frac{1}{16\pi}\left\langle |\dot{H}|^2\right\rangle. \tag{1.103}$$

By integrating the above equation, we obtain the total energy flux

$$\frac{dE}{dt} = \lim_{r\to\infty}\frac{r^2}{16\pi}\oint |\dot{H}|^2 d\Omega = \lim_{r\to\infty}\frac{r^2}{16\pi}\oint \left|\int_{-\infty}^{t}\Psi_4 dt'\right|^2 d\Omega, \tag{1.104}$$

here, we have taken $dA = r^2 d\Omega$, with Ω being the standard solid angle element, and the limit of infinite radius has been introduced since the Isaacson stress-energy tensor is only valid in the weak field approximation.

Next, consider the flux of momentum, which corresponds to the spatial components of the stress-energy tensor t_{ij}. The flux of momentum i along the radial direction will then be given by

$$\frac{dP_i}{dtdA} = t_{ir} = \frac{1}{16\pi}\,\mathrm{Re}\left\langle \partial_i H \partial_r \bar{H}\right\rangle. \tag{1.105}$$

For regions sufficiently far from the source, gravitational waves can be considered plane waves. In this case, we can approximate $\partial_i H \simeq (x_i/r)\,\partial_r H$. Thus, for outgoing waves, the above equation can be simplified to

$$\frac{dP_i}{dtdA} \simeq \frac{1}{16\pi} l_i \left\langle |\dot{H}|^2\right\rangle, \tag{1.106}$$

where $\vec{l} = (\sin\theta\cos\varphi, \sin\theta\sin\varphi, \cos\theta)$ is the unit radial vector in flat spacetime.

Similarly, by integrating the above equation, we obtain the total momentum flux

$$\frac{dP_i}{dt} = \lim_{r\to\infty}\frac{r^2}{16\pi}\oint l_i |\dot{H}|^2 d\Omega = \lim_{r\to\infty}\frac{r^2}{16\pi}\oint l_i \left|\int_{-\infty}^{t}\Psi_4 dt'\right|^2 d\Omega. \tag{1.107}$$

Chapter 2

Numerical Relativity

2.1 Spacetime Foliation

In learning basic physics, people often regard time and space as simple concepts, assuming that events occurring simultaneously is a straightforward matter. But relativity shakes up this view from the start, showing that only spacetime is the real deal, not affected by human bias, while space and time are flexible ideas that come alive when we choose a specific frame of reference and break down spacetime into a "$3+1$" mix. Minkowski was the first to see the made-up nature of space and time, and the solid reality of spacetime, saying back in 1908: "From now on, space by itself, and time by itself, are set to fade into mere shadows, and only a blend of the two will hold onto a real identity." Penrose noted: "It might be said that the big takeaway from relativity is that space and time cannot be seen as solo acts, they have to join forces to paint a 4D picture of what's happening: a story told in the language of spacetime." Synge, in a paper explaining the broad strokes of relativity [222], penned: "We engage with events... All events craft a 4D stretch, named spacetime. This is a singular idea, not a mash-up of two distinct space and time ideas... We've got to firmly say no to treating space and time as pre-cooked concepts. If you aim to use them in a certain way, you need to clarify that way upfront." This does not reject the use of space and time concepts but calls for a clear definition of their meaning before proceeding.

Next, we will introduce the 3+1 decomposition from the perspective of numerical relativity. The 3+1 decomposition is a framework where the roles of space and time are distinctly separated. In this scheme, the entire spacetime is foliated into a series of three-dimensional spacelike slices. Each of these foliations is characterized by varying values of the parameter t, which serves as a general time function. Through this decomposition, a

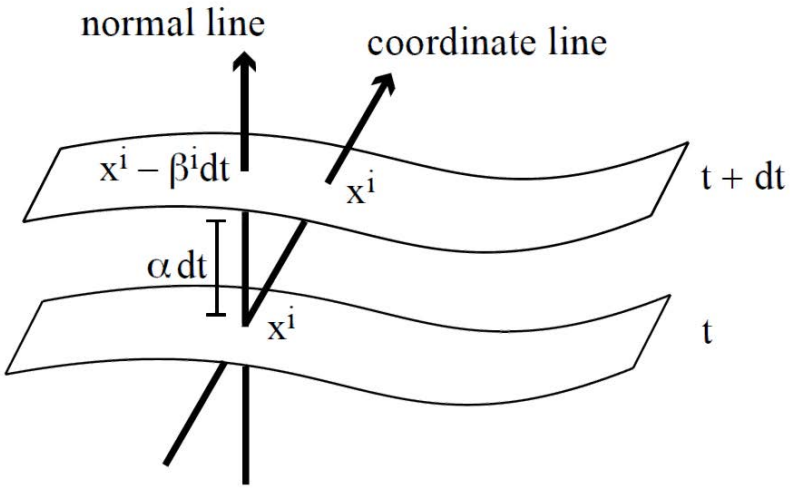

Fig. 2.1 This figure shows the definitions of the lapse function α and the shift vector β^i [223].

clear demarcation between spatial and temporal aspects is achieved, facilitating a structured examination of spacetime dynamics [144].

Now consider a specific foliation, and take two adjacent hypersurfaces, Σ_t and Σ_{t+dt}. The geometry of the spacetime region contained between these two hypersurfaces can be determined from the following three fundamental components:

1. $ds^2 = \gamma_{ij} dx^i dx^j$ — The proper distances within the hypersurface,
2. $d\tau = \alpha(t, x^i) dt$ — α lapse function,
3. $x^i_{t+dt} = x^i_t - \beta^i(t, x^i) dt$ — β^i shift vector field,

where γ_{ij} is the induced metric introduced in Chapter 1. The functions α and β are designated as **Gauge Functions**, exhibiting non-uniqueness due to their reliance on the coordinate system. Their selection, as will be elucidated subsequently, is paramount for attaining numerically stable solutions. By pursuing a geometric rationale with the vectors illustrated in Figure 2.1, it can be demonstrated that the line element is expressed through these functions as

$$ds^2 = -\alpha^2 dt^2 + \gamma_{ij}(\beta^i dt + dx^i)(\beta^j dt + dx^j) \tag{2.1}$$

and the reciprocal of the metric is expressed as

$$g^{\mu\nu} = \begin{pmatrix} -1/\alpha^2 & \beta^i/\alpha^2 \\ \beta^j/\alpha^2 & \gamma^{ij} - \beta^i\beta^j/\alpha^2 \end{pmatrix}. \tag{2.2}$$

We are now in a position to define the normal covector to the hypersurface as

$$n_\mu = (-\alpha, 0). \tag{2.3}$$

Utilizing the metric, we can obtain the normal vector to the hypersurface as

$$n^\mu = \left(1/\alpha, -\beta^i/\alpha\right). \tag{2.4}$$

By virtue of the definition of the induced metric, the induced metric on each hypersurface can be articulated as

$$\gamma_{\mu\nu} = g_{\mu\nu} + n_\mu n_\nu. \tag{2.5}$$

Consider the **Global Time Function** t (where $t : M \to \mathbb{R}$ defines a function such that each constant t surface, Σ_t, is a *spacelike* hypersurface) associated with the foliation. The lapse function is defined as

$$\alpha = (-\nabla t \cdot \nabla t)^{-1/2}. \tag{2.6}$$

Subsequently, the unit normal vector can be re-expressed in terms of α and $\nabla_\mu t$ as

$$n^\mu = -\alpha \nabla^\mu t, \tag{2.7}$$

accompanied by

$$g^{\mu\nu}\nabla_\mu t \nabla_\nu t \equiv \frac{-1}{\alpha^2}. \tag{2.8}$$

The negative sign in Equation (2.7) is opted for such that n^μ points in the direction of increasing t as depicted in Figure 2.1. It is straightforward to demonstrate that n^μ is timelike,

$$n^\mu n_\mu = g_{\mu\nu} n^\mu n^\nu = \alpha^2 g_{\mu\nu} \nabla^\mu t \nabla^\nu t = \alpha^2 \left(\frac{-1}{\alpha^2}\right) = -1. \tag{2.9}$$

A pivotal element is the delineation of the time vector using n^μ and β^μ:

$$t^\mu = \alpha n^\mu + \beta^\mu, \tag{2.10}$$

which is tangent to time lines. It proves beneficial to select t^μ as the congruence along which the spatial coordinate grid is propagated from one time slice to the ensuing one. In essence, t^μ links points sharing identical spatial coordinates on adjacent time slices (thus, in general, $t^\mu \neq \nabla^\mu t$). The shift vector gauges the extent to which the spatial coordinates are translated within a slice relative to the normal vector. Consequently, the gauge functions are instrumental in determining the temporal evolution of the coordinates.

Utilizing the projection operator, the extrinsic curvature can be reformulated as

$$K_{\mu\nu} = -\gamma^{\alpha}{}_{\mu}\gamma^{\beta}{}_{\nu}\nabla_{\alpha}n_{\beta} = -(\delta^{\alpha}{}_{\mu} + n^{\alpha}n_{\mu})(\delta^{\beta}{}_{\nu} + n^{\beta}n_{\nu})\nabla_{\alpha}n_{\beta} = -(\nabla_{\mu}n_{\nu} + n_{\mu}n^{\alpha}\nabla_{\alpha}n_{\nu}), \tag{2.11}$$

given that

$$n^{\beta}n_{\beta} = -1 \Longrightarrow n^{\beta}\nabla_{\alpha}n_{\beta} = 0. \tag{2.12}$$

According to the definition of $K_{\mu\nu}$, it is evident that it is symmetric and purely spatial,

$$n^{\mu}K_{\mu\nu} = -(n^{\mu}\nabla_{\mu}n_{\nu} + n^{\mu}n_{\mu}n^{\alpha}\nabla_{\alpha}n_{\nu}) = -(n^{\mu}\nabla_{\mu}n_{\nu} - n^{\alpha}\nabla_{\alpha}n_{\nu}) = 0. \tag{2.13}$$

This implies that, in an adapted coordinate system, it is feasible to solely consider the spatial components of the extrinsic curvature tensor K_{ij}, where i, j can assume values from 1 to 3 [19].

Utilizing the definition of the Lie derivative, the expression for $K_{\mu\nu}$ can be elegantly reformulated. Initiating from

$$\begin{aligned}
\pounds_{\vec{n}}\gamma_{\mu\nu} &= n^{\alpha}\nabla_{\alpha}\gamma_{\mu\nu} + \gamma_{\mu\alpha}\nabla_{\nu}n^{\alpha} + \gamma_{\nu\alpha}\nabla_{\mu}n^{\alpha} \\
&= n^{\alpha}\nabla_{\alpha}(g_{\mu\nu} + n_{\mu}n_{\nu}) + (g_{\mu\alpha} + n_{\mu}n_{\alpha})\nabla_{\nu}n^{\alpha} + (g_{\nu\alpha} + n_{\nu}n_{\alpha})\nabla_{\mu}n^{\alpha} \\
&= n^{\alpha}\nabla_{\alpha}(n_{\mu}n_{\nu}) + g_{\mu\alpha}\nabla_{\nu}n^{\alpha} + g_{\nu\alpha}\nabla_{\mu}n^{\alpha} \\
&= n^{\alpha}n_{\nu}\nabla_{\alpha}n_{\mu} + n^{\alpha}n_{\mu}\nabla_{\alpha}n_{\nu} + \nabla_{\nu}n_{\mu} + \nabla_{\mu}n_{\nu} = -K_{\mu\nu} - K_{\nu\mu} \\
&= -2K_{\mu\nu},
\end{aligned} \tag{2.14}$$

where the symmetry properties of $K_{\mu\nu}$, $\nabla_{\alpha}g_{\mu\nu} = 0$, and again $n^{\alpha}\nabla_{\mu}n_{\alpha} = 0$ have been employed. Consequently, the extrinsic curvature tensor can be expressed in a compact form as

$$K_{\mu\nu} = -\frac{1}{2}\pounds_{\vec{n}}\gamma_{\mu\nu}. \tag{2.15}$$

Following the definition of the time vector (2.10) and properties of the Lie derivatives[1], this result can be bifurcated into two components, one associated with the time vector $\vec{t}$ and the other with the shift vector $\vec{\beta}$,

$$\begin{aligned}
K_{\mu\nu} = -\frac{1}{2\alpha}\pounds_{\alpha\vec{n}}\gamma_{\mu\nu} &= -\frac{1}{2\alpha}(\pounds_{\vec{t}} - \pounds_{\vec{\beta}})\gamma_{\mu\nu} \\
\Longrightarrow \pounds_{\vec{t}}\gamma_{\mu\nu} &= -2\alpha K_{\mu\nu} + \pounds_{\vec{\beta}}\gamma_{\mu\nu}.
\end{aligned}$$

[1] $\pounds_{\vec{v}} = (1/k)\pounds_{k\vec{v}}$

2.2 Constraints

First, we review the source-free Maxwell's equations.

The Maxwell's equations describe the evolution of source-free electromagnetic fields:

$$\partial^{\mu} F_{\mu\nu} = 0, \quad \partial_{[\mu} F_{\nu\sigma]} = 0, \tag{2.16}$$

where $F_{\mu\nu}$ is electromagnetic field tensor.

After selecting a standard $3+1$ decomposition of Minkowski spacetime, Maxwell's equations can be expressed in a three-dimensional form:

$$\dot{\vec{E}} \equiv \frac{\partial \vec{E}}{\partial t} = \vec{\nabla} \times \vec{B}, \quad \dot{\vec{B}} \equiv \frac{\partial \vec{B}}{\partial t} = -\vec{\nabla} \times \vec{E}, \tag{2.17}$$

and

$$\vec{\nabla} \cdot \vec{E} = 0, \quad \vec{\nabla} \cdot \vec{B} = 0. \tag{2.18}$$

Broadly speaking, Equation (2.17) can be referred to as the evolution equation of the electromagnetic field. However, a closer look should also be taken at the difference between Equation (2.17) and Equation (2.18). Equation (2.18) does not contain time derivatives, and therefore is unrelated to evolution. It merely reflects the conditions that the spatial vector fields $\vec{E}(t)$ and $\vec{B}(t)$ must satisfy at any given moment (on any spacelike hypersurface Σ_t in the standard $3+1$ decomposition): the divergence of both must be zero. This indicates that only spatial vector fields with zero divergence can act as electric and magnetic fields. This kind of restriction imposed by the theory itself on the instantaneous values of the field quantities is called a constraint. Constraints are also known as instantaneous laws, to distinguish them from evolution laws, which are described by evolution equations. In general relativity, the roles analogous to those in the electromagnetic field scenario are played by the Hamiltonian constraint and the momentum constraint.

Hamiltonian Constraint

Using the Gauss-Codazzi equation (see Appendix A for details),

$$\gamma_{\alpha}{}^{\delta} \gamma_{\beta}{}^{\kappa} \gamma_{\mu}{}^{\lambda} \gamma_{\nu}{}^{\sigma} R_{\delta\kappa\lambda\sigma} = {}^{(3)}R_{\alpha\beta\mu\nu} + K_{\alpha\mu} K_{\beta\nu} - K_{\alpha\nu} K_{\beta\mu}, \tag{2.19}$$

we define ${}^{(3)}R$ as follows:

$$\begin{aligned}
{}^{(3)}R &\equiv \gamma^{\alpha\mu}\gamma^{\beta\nu}{}^{(3)}R_{\alpha\beta\mu\nu} \\
&= \gamma^{\alpha\mu}\gamma^{\beta\nu}\left[\gamma_\alpha{}^\delta\gamma_\beta{}^\kappa\gamma_\mu{}^\lambda\gamma_\nu{}^\sigma R_{\delta\kappa\lambda\sigma} - \left(K_{\mu\alpha}K_{\beta\nu} - K_{\mu\beta}K_{\alpha\nu}\right)\right] \\
&= \gamma^{\delta\lambda}\gamma^{\kappa\sigma}R_{\delta\kappa\lambda\sigma} - K^2 + K^{\alpha\beta}K_{\alpha\beta} \\
&= \left(g^{\delta\lambda} + n^\delta n^\lambda\right)\left(g^{\kappa\sigma} + n^\kappa n^\sigma\right)R_{\delta\kappa\lambda\sigma} - K^2 + K^{\alpha\beta}K_{\alpha\beta} \\
&= R + n^\kappa n^\sigma R_{\kappa\sigma} + n^\delta n^\lambda R_{\delta\lambda} - K^2 + K^{\alpha\beta}K_{\alpha\beta} \\
&= 2n^\alpha n^\beta\left(R_{\alpha\beta} - \frac{1}{2}Rg_{\alpha\beta}\right) - K^2 + K^{\alpha\beta}K_{\alpha\beta} \\
&= 2n^\alpha n^\beta \times 8\pi T_{\alpha\beta} - K^2 + K^{\alpha\beta}K_{\alpha\beta} \\
&= 16\pi\rho - K^2 + K^{\alpha\beta}K_{\alpha\beta},
\end{aligned} \tag{2.20}$$

where $\rho \equiv n^\alpha n^\beta T_{\alpha\beta}$.

Finally, we rearrange the terms and obtain the expression for the **Hamiltonian Constraint**:

$$R + K^2 - K_{ij}K^{ij} = 16\pi\rho. \tag{2.21}$$

Momentum Constraint

First, we introduce an important equation - the Codazzi-Mainardi equation (See Appendix A for details),

$$\gamma^\delta{}_\alpha\gamma^\kappa{}_\beta\gamma^\lambda{}_\mu n^\nu R_{\delta\kappa\lambda\nu} = D_\beta K_{\alpha\mu} - D_\alpha K_{\beta\mu}. \tag{2.22}$$

We apply $\gamma^{\alpha\mu}$ to both sides of the Codazzi-Mainardi equation,

$$\gamma^{\alpha\mu}\left(\gamma_\alpha{}^\delta\gamma_\beta{}^\kappa\gamma_\mu{}^\lambda n^\nu R_{\delta\kappa\lambda\nu}\right) = \gamma^{\alpha\mu}\left(D_\beta K_{\alpha\mu} - D_\alpha K_{\beta\mu}\right). \tag{2.23}$$

Thus,

$$\gamma^{\delta\lambda}\gamma_\beta{}^\kappa n^\nu R_{\delta\kappa\lambda\nu} = D_\beta K - D_\alpha K_\beta{}^\alpha. \tag{2.24}$$

Utilizing the definition of the induced metric, we obtain:

$$\begin{aligned}\left(g^{\delta\lambda}+n^{\delta}n^{\lambda}\right)\left(\gamma_{\beta}{}^{\kappa}n^{\nu}R_{\delta\kappa\lambda\nu}\right) &= D_{\beta}K-D_{\alpha}K_{\beta}{}^{\alpha},\\ g^{\delta\lambda}\gamma_{\beta}{}^{\kappa}n^{\nu}R_{\delta\kappa\lambda\nu} &= D_{\beta}K-D_{\alpha}K_{\beta}{}^{\alpha},\\ \gamma_{\alpha}{}^{\mu}n^{\nu}R_{\mu\nu} &= D_{\alpha}K-D_{\mu}K_{\alpha}{}^{\mu}.\end{aligned} \tag{2.25}$$

On the other hand, we apply $\gamma_{\alpha}{}^{\mu}n^{\nu}$ to the Einstein equations,

$$\begin{aligned}\gamma_{\alpha}{}^{\mu}n^{\nu}G_{\mu\nu} &= \gamma_{\alpha}{}^{\mu}n^{\nu}8\pi T_{\mu\nu},\\ \gamma_{\alpha}{}^{\mu}n^{\nu}\left(R_{\mu\nu}-\frac{1}{2}Rg_{\mu\nu}\right) &= \gamma_{\alpha}{}^{\mu}n^{\nu}8\pi T_{\mu\nu},\\ \gamma_{\alpha}{}^{\mu}n^{\nu}R_{\mu\nu} &= \gamma_{\alpha}{}^{\mu}n^{\nu}8\pi T_{\mu\nu}.\end{aligned} \tag{2.26}$$

Comparing Equation (2.26) with Equation (2.25), we obtain:

$$D_{\alpha}K-D_{\mu}K_{\alpha}{}^{\mu}=\gamma_{\alpha}{}^{\mu}n^{\nu}8\pi T_{\mu\nu}=-8\pi j_{\alpha} \tag{2.27}$$

where $j_{\alpha}\equiv-\gamma_{\alpha}{}^{\mu}n^{\nu}T_{\mu\nu}$.

Lastly, through spacetime foliation, we obtain the **Momentum Constraint**:

$$D_{j}K_{i}{}^{j}-D_{i}K=8\pi j_{i} \tag{2.28}$$

where $j_{i}\equiv-\gamma_{i}{}^{\mu}n^{\nu}T_{\mu\nu}$.

It can be shown that the time derivatives of the Hamiltonian constraint and the momentum constraint are equal to zero. This illustrates that as long as the initial values $\gamma_{\mu\nu}$ and $K_{\mu\nu}$ specified on the initial value surface Σ satisfy the constraint equations, they will satisfy the constraint equations at any moment during the evolution process [19].

2.3 ADM Formalism

The primary objective of numerical relativity is to elucidate the nonlinear dynamics of various spacetimes by numerically solving Einstein's equations. To accomplish this, we treat Einstein's equations as an initial-value problem. This approach starts by reformulating the equations into a form that enables the feasible evolution of geometric quantities over time.

The most widely used method for deriving an initial-value formalism of general relativity is based on the **Arnowitt–Deser–Misner (ADM) Formalism** [29]. This approach explicitly decomposes time and space, providing a clear geometric interpretation of spacetime foliation. In this formalism, spacelike hypersurfaces are sequentially chosen to fill the spacetime, allowing the unambiguous evolution of geometric quantities on each hypersurface over time. Moreover, this method fully preserves the freedom of gauge choice, which is intrinsically linked to the general covariance in general relativity.

The ADM formalism consists of the Hamiltonian constraint, the momentum constraint, and the evolution equations for K_{ij} and γ_{ij}. We have derived the Hamiltonian constraint and momentum constraint in the previous section, now, we will derive the evolution equations for K_{ij} and γ_{ij}.

The Evolution Equation for K_{ij}

First, we will examine the evolution equation for K_{ij}. Applying $\gamma^{\beta\nu}$ to the Gauss-Codazzi equation, we obtain:

$$\begin{aligned} \gamma^{\beta\nu}\left(\gamma_\alpha{}^\delta\gamma_\beta{}^\kappa\gamma_\mu{}^\lambda\gamma_\nu{}^\sigma R_{\delta\kappa\lambda\sigma}\right) &= \gamma^{\beta\nu}\left({}^{(3)}R_{\alpha\beta\mu\nu}+K_{\alpha\mu}K_{\beta\nu}-K_{\alpha\nu}K_{\beta\mu}\right), \\ \gamma^{\kappa\sigma}\gamma_\alpha{}^\delta\gamma_\mu{}^\lambda R_{\delta\kappa\lambda\sigma} &= {}^{(3)}R_{\alpha\mu}+KK_{\alpha\mu}-K_{\alpha\lambda}K_\mu{}^\lambda. \end{aligned} \tag{2.29}$$

By relabelling $\mu\to\nu$, $\alpha\to\mu$ on both sides and exchanging $\kappa\leftrightarrow\lambda$ on the left side,we obtain:

$$\begin{aligned} \gamma^{\lambda\sigma}\gamma_\mu{}^\delta\gamma_\nu{}^\kappa R_{\delta\lambda\kappa\sigma} &= {}^{(3)}R_{\mu\nu}+KK_{\mu\nu}-K_{\mu\lambda}K_\nu{}^\lambda, \\ \left(n^\lambda n^\sigma+g^{\lambda\sigma}\right)\gamma_\mu{}^\delta\gamma_\nu{}^\kappa R_{\delta\lambda\kappa\sigma} &= {}^{(3)}R_{\mu\nu}+KK_{\mu\nu}-K_{\mu\lambda}K_\nu{}^\lambda, \\ \gamma_\mu{}^\delta\gamma_\nu{}^\kappa\left(n^\lambda n^\sigma R_{\delta\lambda\kappa\sigma}+R_{\delta\kappa}\right) &= {}^{(3)}R_{\mu\nu}+KK_{\mu\nu}-K_{\mu\lambda}K_\nu{}^\lambda. \end{aligned} \tag{2.30}$$

Now, we introduce the Ricci equation (See Appendix A for details):

$$\gamma_\mu{}^\delta\gamma_\nu{}^\kappa n^\lambda n^\sigma R_{\delta\lambda\kappa\sigma} = \mathscr{L}_{\vec{n}}K_{\mu\nu}+K_{\mu\lambda}K_\nu{}^\lambda+\frac{1}{\alpha}D_\mu D_\nu\alpha. \tag{2.31}$$

By applying the Ricci equation to Equation (2.30), we obtain

$$\mathscr{L}_{\vec{n}}K_{\mu\nu}+K_{\mu\lambda}K_{\nu}{}^{\lambda}+\frac{1}{\alpha}D_{\mu}D_{\nu}\alpha+\gamma_{\mu}{}^{\delta}\gamma_{\nu}{}^{\kappa}R_{\delta\kappa}={}^{(3)}R_{\mu\nu}+KK_{\mu\nu}-K_{\mu\lambda}K_{\nu}{}^{\lambda}, \tag{2.32}$$

i.e.,

$$\mathscr{L}_{\vec{t}}K_{\mu\nu}-\mathscr{L}_{\vec{\beta}}K_{\mu\nu}=-D_{\mu}D_{\nu}\alpha+\alpha\left(-\gamma_{\mu}{}^{\delta}\gamma_{\nu}{}^{\kappa}R_{\delta\kappa}+{}^{(3)}R_{\mu\nu}+KK_{\mu\nu}-2K_{\mu\lambda}K_{\nu}{}^{\lambda}\right). \tag{2.33}$$

Utilizing $R_{\mu\nu}=8\pi\left(T_{\mu\nu}-\frac{1}{2}Tg_{\mu\nu}\right)$, we can obtain

$$-\gamma_{\mu}{}^{\delta}\gamma_{\nu}{}^{\kappa}R_{\delta\kappa}=4\pi\left[\gamma_{\mu\nu}(S-\rho)-2S_{\mu\nu}\right] \tag{2.34}$$

where $S_{\mu\nu}:=\gamma_{\mu}{}^{\alpha}\gamma_{\nu}{}^{\beta}T_{\alpha\beta}$ and $S:=S^{\mu}_{\mu}$ (see Appendix A for details). Substituting Equation (2.34) into Equation (2.33), we obtain

$$\mathscr{L}_{\vec{t}}K_{\mu\nu}-\mathscr{L}_{\vec{\beta}}K_{\mu\nu}=-D_{\mu}D_{\nu}\alpha+\alpha\left({}^{(3)}R_{\mu\nu}+KK_{\mu\nu}-2K_{\mu\lambda}K_{\nu}{}^{\lambda}\right)+4\pi\alpha\left[\gamma_{\mu\nu}(S-\rho)-2S_{\mu\nu}\right]. \tag{2.35}$$

Lastly, taking into account our Spacetime Foliation and $\mathscr{L}_{\vec{t}}=\partial_t$, $\mathscr{L}_{\vec{\beta}}K_{ij}=\beta^k\partial_k K_{ij}+K_{ik}\partial_j\beta^k+K_{kj}\partial_i\beta^k$, we obtain the final expression:

$$\begin{aligned}\partial_t K_{ij}=&\beta^k\partial_k K_{ij}+K_{ik}\partial_j\beta^k+K_{kj}\partial_i\beta^k-D_iD_j\alpha+\alpha\left({}^{(3)}R_{ij}+KK_{ij}-2K_{ik}K_j{}^k\right)\\&+4\pi\alpha\left[\gamma_{ij}(S-\rho)-2S_{ij}\right].\end{aligned} \tag{2.36}$$

The Evolution Equation for γ_{ij}

At the end of Section 2.1, the following expression was derived:

$$\pounds_{\vec{t}}\gamma_{\mu\nu}=-2\alpha K_{\mu\nu}+\pounds_{\vec{\beta}}\gamma_{\mu\nu}. \tag{2.37}$$

In a adapted coordinate system, $\pounds_{\vec{t}}=\partial_t$, leading to

$$\partial_t\gamma_{ij}=-2\alpha K_{ij}+\pounds_{\vec{\beta}}\gamma_{ij}. \tag{2.38}$$

We find that

$$\mathscr{L}_{\vec{\beta}}\gamma_{ij}=\beta^k D_k\gamma_{ij}+\gamma_{kj}D_i\beta^k+\gamma_{ik}D_j\beta^k=D_i\beta_j+D_j\beta_i. \tag{2.39}$$

Consequently, Equation (2.38) is refined to:

$$\partial_t\gamma_{ij}=-2\alpha K_{ij}+D_i\beta_j+D_j\beta_i. \tag{2.40}$$

Summary

Hamiltonian Constraint

$$R + K^2 - K_{ij}K^{ij} = 16\pi\rho \tag{2.41}$$

where $\rho \equiv n^\alpha n^\beta T_{\alpha\beta}$.

Momentum Constraint

$$D_j K_i{}^j - D_i K = 8\pi j_i \tag{2.42}$$

where $j_i \equiv -\gamma_i{}^\mu n^\nu T_{\mu\nu}$.

The Evolution Equation for γ_{ij}

$$\partial_t \gamma_{ij} = -2\alpha K_{ij} + D_i\beta_j + D_j\beta_i. \tag{2.43}$$

The Evolution Equation for K_{ij}

$$\begin{aligned}\partial_t K_{ij} =& \beta^k \partial_k K_{ij} + K_{ik}\partial_j\beta^k + K_{kj}\partial_i\beta^k - D_i D_j\alpha + \alpha\left({}^{(3)}R_{ij} + KK_{ij} - 2K_{ik}K_j{}^k\right) \\ &+ 4\pi\alpha\left[\gamma_{ij}(S-\rho) - 2S_{ij}\right].\end{aligned} \tag{2.44}$$

The evolution equations referenced above are commonly known in the numerical relativity community as the ADM equations or formalism. However, these equations do not match the form originally derived by Arnowitt, Deser, and Misner in [29]. Instead, they represent a significant reformulation introduced by York [238]. It is important to note that the primary contribution of ADM lies in the Hamiltonian formulation of general relativity. This Hamiltonian approach, however, is not utilized in numerical relativity, which instead proceeds by integrating the ADM Equations (2.41) - (2.44) [99]. These equations, notably, predate the ADM formalism, with the recognition of the extrinsic curvature K as a fundamental 3+1 variable having already been established by Darmois in 1927 [80].

The ADM formulation of the Einstein equations was employed for most 3+1 simulations well into the 1990s, despite the pervasive instabilities encountered in these simulations. Over time, the community began to recognize that these issues might stem from inherent properties of the ADM equations themselves, rather than from the numerical algorithms used for their evolution. This realization emerged gradually throughout the 1990s, driven by a combination of empirical observation and growing suspicion. The weakly hyperbolic nature of the ADM equations, however, was not fully understood until the early 2000s.

To overcome this difficulty, it is essential to ensure the following two points:

- The momentum constraints must be identically satisfied.
- Either the densitized lapse $\tilde{\alpha}$ is assumed to be a known function of spacetime (rather than the lapse itself), or a slicing condition from the Bona-Masso family[2] is employed.

While adopting a slicing condition of the Bona-Masso type is straightforward, ensuring that the momentum constraints are identically satisfied is a far more complex issue [19]. Numerically, the constraints will inevitably be violated; even if they are perfectly satisfied in the initial data, numerical evolution will introduce errors. This makes it effectively impossible for the ADM formalism to remain viable.

[2]We will discuss this in Section 2.7

2.4 BSSN Formalism

In Section 2.3, we recognized that the ADM equations lack the necessary stability properties for long-term numerical simulations, a limitation now understood to be related to their weakly hyperbolic nature [19]. In this section, however, we will introduce a specific reformulation that has proven particularly robust in the numerical evolution of a wide variety of spacetimes, both with and without matter.

In 1987, Nakamura, Oohara, and Kojima introduced a revised version of the ADM evolution equations using a conformal transformation, which showed improved stability compared to the original ADM [163]. Although this approach developed over the years, it remained largely unnoticed by most researchers in numerical relativity until 1998, when Baumgarte and Shapiro systematically compared it with ADM across various spacetimes. Their analysis revealed that the new formalism had significantly better stability in all the scenarios they examined [36]. This discovery led to the reformulation gaining broader recognition, and today it is utilized in some form by most major three-dimensional numerical relativity codes. Although often called **Conformal ADM**, this name is somewhat misleading because it does not emphasize the most critical distinction between the new formulation and ADM. A more appropriate name might be **Conformal Γ Formulation**, as the key feature of the BSSN formulation is the modification of the evolution equation for $\tilde{\Gamma}^i$ using momentum constraints—a method now widely adopted in all mainstream formalisms [19].

The most widely used version of this formalism is based on the work of Shibata and Nakamura [203] as well as Baumgarte and Shapiro [36], and is commonly known as the **Baumgarte-Shapiro-Shibata-Nakamura (BSSN) Formalism**. The contributions of Ken-Ichi Oohara and Yasufumi Kojima should also be acknowledged, as the development of humanity's understanding of the universe is built upon the knowledge passed down through generations.

Given that the BSSN formalism is currently one of the most widely used methods, and that many subsequent approaches share significant similarities with it, we will present the detailed derivation process here as thoroughly as possible. Any overly redundant derivations will be included in the Appendix A.

Conformal Transformations

To introduce the BSSN formalism, we first consider a conformal rescaling of the spatial metric in the following form:

$$\widetilde{\gamma}_{ij} := \psi^{-4}\gamma_{ij} \tag{2.45}$$

where ψ is conformal factor. In the BSSN formalism, the conformal factor is selected such that the conformal metric $\widetilde{\gamma}_{ij}$ possesses a unit determinant, i.e.,

$$\psi^4 = \gamma^{1/3} \quad \Rightarrow \quad \psi = \gamma^{1/12} \tag{2.46}$$

where γ is the determinant of γ_{ij}. In practice, it is common to work with

$$\phi = \ln(\psi) = \frac{1}{12}\ln(\gamma), \tag{2.47}$$

such that:

$$\widetilde{\gamma}_{ij} = e^{-4\phi}\gamma_{ij}. \tag{2.48}$$

The BSSN formalism also decomposes the extrinsic curvature into its trace K and its trace-free part, denoted as

$$A_{ij} = K_{ij} - \frac{1}{3}\gamma_{ij}K. \tag{2.49}$$

Furthermore, we apply a conformal rescaling to the traceless extrinsic curvature, expressed as

$$\widetilde{A}_{ij} = \psi^{-4}A_{ij} = e^{-4\phi}A_{ij}. \tag{2.50}$$

A pivotal aspect is that the BSSN formalism also introduces three auxiliary variables, termed as the conformal connection functions, defined by

$$\widetilde{\Gamma}^i := \widetilde{\gamma}^{jk}\widetilde{\Gamma}^i{}_{jk} = -\partial_j\widetilde{\gamma}^{ij} \tag{2.51}$$

where $\widetilde{\Gamma}^i{}_{jk}$ are the Christoffel symbols associated with the conformal metric, and the second equality arises from the definition of the Christoffel symbols, particularly when the determinant $\widetilde{\gamma}$ is equal to 1 (a condition ensured by construction).

The Evolution Equation for ϕ

Applying γ^{ij} to Equation (2.40), we obtain

$$\gamma^{ij}\partial_t\gamma_{ij} = \gamma^{ij}\left(-2\alpha K_{ij} + D_i\beta_j + D_j\beta_i\right). \tag{2.52}$$

Utilizing

$$\frac{\partial g}{\partial x^\alpha} = g\cdot g^{\mu\nu}\frac{\partial g_{\mu\nu}}{\partial x^\alpha} = -g\cdot g_{\mu\nu}\frac{\partial g^{\mu\nu}}{\partial x^\alpha}, \tag{2.53}$$

we can derive the following result,

$$\begin{aligned}\partial_t \ln\gamma &= -2\alpha K + D_i\beta^i + D_j\beta^j,\\ \partial_t\gamma &= -2\gamma\left(\alpha K - D_i\beta^i\right)\\ &= -2\gamma\left(\alpha K - \partial_i\beta^i\right) + \beta^i\partial_i\gamma.\end{aligned} \tag{2.54}$$

Noting that

$$\phi = \ln\psi = \frac{1}{12}\ln\gamma, \tag{2.55}$$

we express the evolution of ϕ as follows:

$$\begin{aligned}\partial_t\psi^{12} &= -2\psi^{12}\left(\alpha K - \partial_i\beta^i\right) + \beta^i\partial_i\psi^{12},\\ \partial_t\psi &= -\frac{1}{6}\psi\left(\alpha K - \partial_i\beta^i\right) + \beta^i\partial_i\psi,\\ \partial_t e^{\phi} &= -\frac{1}{6}e^{\phi}\left(\alpha K - \partial_i\beta^i\right) + \beta^i\partial_i e^{\phi},\\ \partial_t\phi &= -\frac{1}{6}\left(\alpha K - \partial_i\beta^i\right) + \beta^i\partial_i\phi.\end{aligned} \tag{2.56}$$

The Evolution Equation for $\widetilde{\gamma}_{ij}$

We rewrite Equation (2.38) using $\widetilde{\gamma}_{ij}$,

$$\begin{aligned}\partial_t(\psi^4\widetilde{\gamma}_{ij}) - \mathscr{L}_{\vec{\beta}}(\psi^4\widetilde{\gamma}_{ij}) &= -2\alpha K_{ij},\\ \psi^4(\partial_t - \mathscr{L}_{\vec{\beta}})\widetilde{\gamma}_{ij} + \widetilde{\gamma}_{ij}(\partial_t - \mathscr{L}_{\vec{\beta}})\psi^4 &= -2\alpha K_{ij},\\ \psi^4(\partial_t - \mathscr{L}_{\vec{\beta}})\widetilde{\gamma}_{ij} + \widetilde{\gamma}_{ij}\psi^4(\partial_t - \mathscr{L}_{\vec{\beta}})\ln\psi^4 &= -2\alpha(\psi^4\widetilde{A}_{ij} + \frac{1}{3}\psi^4\widetilde{\gamma}_{ij}K),\\ (\partial_t - \mathscr{L}_{\vec{\beta}})\widetilde{\gamma}_{ij} &= -2\alpha\widetilde{A}_{ij} - \frac{2}{3}[\alpha K + 6(\partial_t - \mathscr{L}_{\vec{\beta}})\ln\psi]\widetilde{\gamma}_{ij}.\end{aligned}$$

By applying $\widetilde{\gamma}^{ij}$ to the above equation and noting that the determinant $\widetilde{\gamma}$ equals 1, we obtain

$$0 = \widetilde{\gamma}^{ij}\left(\partial_t - \mathscr{L}_{\vec{\beta}}\right)\widetilde{\gamma}_{ij} = -2\left[\alpha K + 6\left(\partial_t - \mathscr{L}_{\vec{\beta}}\right)\ln\psi\right]. \tag{2.57}$$

This implies that $\alpha K + 6\left(\partial_t - \mathscr{L}_{\vec{\beta}}\right)\ln\psi = 0$, thus

$$\left(\partial_t - \mathscr{L}_{\vec{\beta}}\right)\widetilde{\gamma}_{ij} = -2\alpha\widetilde{A}_{ij}. \tag{2.58}$$

Here, $\mathscr{L}_{\hat{\beta}}\widetilde{\gamma}_{ij}$ can be expressed as [3]

$$\mathscr{L}_{\widetilde{\beta}}\widetilde{\gamma}_{ij} = \beta^k\partial_k\widetilde{\gamma}_{ij} + \widetilde{\gamma}_{ik}\partial_j\beta^k + \widetilde{\gamma}_{jk}\partial_i\beta^k - \frac{2}{3}\widetilde{\gamma}_{ij}\partial_k\beta^k. \tag{2.59}$$

Thus, the final evolution equation for $\widetilde{\gamma}_{ij}$ is

$$\left(\partial_t - \beta^k\partial_k\right)\widetilde{\gamma}_{ij} = -2\alpha\widetilde{A}_{ij} + \widetilde{\gamma}_{ik}\partial_j\beta^k + \widetilde{\gamma}_{jk}\partial_i\beta^k - \frac{2}{3}\widetilde{\gamma}_{ij}\partial_k\beta^k. \tag{2.60}$$

The Evolution Equation for K

We first apply $\partial_t - \mathscr{L}_{\vec{\beta}}$ to K, obtaining:

$$\left(\partial_t - \mathscr{L}_{\vec{\beta}}\right)K = \left(\partial_t - \mathscr{L}_{\vec{\beta}}\right)\gamma^{ij}K_{ij} = \gamma^{ij}\left(\partial_t - \mathscr{L}_{\vec{\beta}}\right)K_{ij} + K_{ij}\left(\partial_t - \mathscr{L}_{\vec{\beta}}\right)\gamma^{ij}. \tag{2.61}$$

On the other hand, using the Leibniz rule and $\gamma_{ik}\gamma^{kj} = \delta_i{}^j$, we have

$$\gamma^{kj}\left(\partial_t - \mathscr{L}_{\vec{\beta}}\right)\gamma_{ik} + \gamma_{ik}\left(\partial_t - \mathscr{L}_{\vec{\beta}}\right)\gamma^{kj} = 0. \tag{2.62}$$

We relabel the index i with l, and apply γ^{il}, yielding

$$\gamma^{il}\gamma_{lk}(\partial_t - \mathscr{L}_{\vec{\beta}})\gamma^{kj} + \gamma^{il}\gamma^{kj}(\partial_t - \mathscr{L}_{\vec{\beta}})\gamma_{lk} = 0. \tag{2.63}$$

Using Equation (2.37),

$$(\partial_t - \mathscr{L}_{\vec{\beta}})\gamma^{ij} = -\gamma^{il}\gamma^{kj}(\partial_t - \mathscr{L}_{\vec{\beta}})\gamma_{kl} = \gamma^{il}\gamma^{kj}2\alpha K_{lk} = 2\alpha K^{ij}. \tag{2.64}$$

Substituting the above expression into Equation (2.61), we obtain a useful expression:

$$\gamma^{ij}(\partial_t - \mathscr{L}_{\vec{\beta}})K_{ij} = (\partial_t - \mathscr{L}_{\vec{\beta}})K - 2\alpha K_{ij}K^{ij}. \tag{2.65}$$

[3] It is crucial to account for the computation of Lie derivatives with respect to $\vec{\beta}$ of tensor densities. These are tensors multiplied by powers of the determinant of the metric γ. When an object is represented as a tensor times $\gamma^{w/2}$, it is termed as a tensor density of weight w. The Lie derivative of a tensor density of weight w is expressed as

$$\mathscr{L}_{\vec{\beta}}T = \left[\mathscr{L}_{\vec{\beta}}T\right]_{w=0} + wT\partial_i\beta^i,$$

where the first term represents the Lie derivative assuming $w = 0$, and the second term signifies the additional contribution due to the density factor. Given that $\psi = e^{\phi} = \gamma^{1/12}$, it is evident that the density weight is $1/6$. Hence, the weight of $\widetilde{\gamma}_{ij}$ and $\widetilde{A}_{ij}$ is $-2/3$, and the weight of $\widetilde{\gamma}^{ij}$ is $2/3$ [19].

Applying $\widetilde{\gamma}_{ij}$ to Equation (2.44) yields:

$$\begin{aligned}\gamma^{ij}(\partial_t - \mathscr{L}_{\vec{\beta}})K_{ij} &= \gamma^{ij}\{-D_iD_j\alpha + \alpha[{}^{(3)}R_{ij} + KK_{ij} - 2K_{ik}K^k{}_j] + 4\pi\alpha[\gamma_{ij}(S-\rho) - 2S_{ij}]\} \\ &= -D_iD^i\alpha + \alpha[{}^{(3)}R + K^2 - 2K_{ik}K^{ik}] + 4\pi\alpha(S-3\rho).\end{aligned}$$

Thus, by combining Equations (2.66) and (2.65), we obtain

$$(\partial_t - \mathscr{L}_{\vec{\beta}})K = -D_iD^i\alpha + \alpha({}^{(3)}R + K^2) + 4\pi\alpha(S-3\rho). \tag{2.66}$$

Lastly, by utilizing the Hamiltonian constraint (2.21) and

$$K_{ij}K^{ij} = (A_{ij} + \frac{1}{3}K\gamma_{ij})(A^{ij} + \frac{1}{3}K\gamma^{ij}) = \widetilde{A}_{ij}\widetilde{A}^{ij} + \frac{1}{3}K^2, \tag{2.67}$$

we obtain the evolution equation for K:

$$(\partial_t - \beta^i\partial_i)K = -D_iD^i\alpha + \alpha(\widetilde{A}_{ij}\widetilde{A}^{ij} + \frac{1}{3}K^2) + 4\pi\alpha(\rho + S). \tag{2.68}$$

The Evolution Equation for $\widetilde{A}_{ij}$

Because $\widetilde{A}_{ij}$ is closely related to K_{ij}, we apply $\partial_t - \mathscr{L}_{\vec{\beta}}$ to K_{ij}:

$$\begin{aligned}(\partial_t - \mathscr{L}_{\vec{\beta}})K_{ij} &= (\partial_t - \mathscr{L}_{\vec{\beta}})(A_{ij} + \frac{1}{3}K\gamma_{ij}) \\ &= (\partial_t - \mathscr{L}_{\vec{\beta}})A_{ij} + \frac{1}{3}K(\partial_t - \mathscr{L}_{\vec{\beta}})\gamma_{ij} + \frac{1}{3}\gamma_{ij}(\partial_t - \mathscr{L}_{\vec{\beta}})K.\end{aligned}$$

Combining the above equation with Equations (2.66) and (2.44) yields:

$$\begin{aligned}&-D_iD_j\alpha + \alpha[{}^{(3)}R_{ij} + KK_{ij} - 2K_{ik}K^k{}_j] + 4\pi\alpha[\gamma_{ij}(S-\rho) - 2S_{ij}] \\ &= (\partial_t - \mathscr{L}_{\vec{\beta}})A_{ij} - \frac{2}{3}\alpha KK_{ij} + \frac{1}{3}\gamma_{ij}[-D_iD^i\alpha + \alpha({}^{(3)}R + K^2) + 4\pi\alpha(S-3\rho)].\end{aligned}$$

Further, we obtain

$$\begin{aligned}(\partial_t - \mathscr{L}_{\vec{\beta}})A_{ij} = &-D_iD_j\alpha + \alpha[{}^{(3)}R_{ij} + \frac{5}{3}KK_{ij} - 2K_{ik}K^k{}_j] - 8\pi\alpha(S_{ij} - \frac{1}{3}S\gamma_{ij}) \\ &+ \frac{1}{3}\gamma_{ij}[D_kD^k\alpha - \alpha({}^{(3)}R + K^2)].\end{aligned} \tag{2.69}$$

In the above expression, the three terms $\frac{5}{3}KK_{ij}$, $2K_{ik}K^k{}_j$, and $\frac{1}{3}K^2\gamma_{ij}$ can be further combined to form:

$$\begin{aligned}&\frac{5}{3}KK_{ij}-2K_{ik}K^k{}_j-\frac{1}{3}K^2\gamma_{ij}\\&=\frac{5}{3}K(A_{ij}+\frac{1}{3}K\gamma_{ij})-2(A_{ik}+\frac{1}{3}K\gamma_{ik})(A^k{}_j+\frac{1}{3}K\delta^k{}_j)=\frac{1}{3}KA_{ij}-2A_{ik}A^k{}_j.\end{aligned}$$

Therefore, Equation (2.69) can also be written in the following form:

$$\begin{aligned}&(\partial_t-\mathscr{L}_{\vec{\beta}})A_{ij}\\&=-D_iD_j\alpha+\alpha[{}^{(3)}R_{ij}+\frac{1}{3}KA_{ij}-2A_{ik}A^k{}_j]-8\pi\alpha(S_{ij}-\frac{1}{3}S\gamma_{ij})+\frac{1}{3}\gamma_{ij}[D_kD^k\alpha-\alpha^{(3)}R].\end{aligned}\tag{2.70}$$

What we want to determine is the evolution equation for $\widetilde{A}_{ij}$, so it is natural to apply $\widetilde{A}_{ij}$ instead of A_{ij}. The left-hand side of Equation (2.70) can be written as follows:

$$\begin{aligned}(\partial_t-\mathscr{L}_{\vec{\beta}})A_{ij}&=(\partial_t-\mathscr{L}_{\vec{\beta}})(\psi^4\widetilde{A}_{ij})=\psi^4(\partial_t-\mathscr{L}_{\vec{\beta}})\widetilde{A}_{ij}+\widetilde{A}_{ij}(\partial_t-\mathscr{L}_{\vec{\beta}})\psi^4\\&=\psi^4(\partial_t-\mathscr{L}_{\vec{\beta}})\widetilde{A}_{ij}+4\psi^4\widetilde{A}_{ij}(\partial_t-\mathscr{L}_{\vec{\beta}})\ln\psi\\&=\psi^4[(\partial_t-\mathscr{L}_{\vec{\beta}})\widetilde{A}_{ij}-\frac{2}{3}\alpha K\widetilde{A}_{ij}].\end{aligned}$$

Note that

$$-2A_{ik}A^k{}_j=-2\psi^4\widetilde{A}_{ik}\widetilde{A}^k{}_j,\tag{2.71}$$

thus, Equation (2.70) can be written as follows:

$$\begin{aligned}&\psi^4[(\partial_t-\mathscr{L}_{\vec{\beta}})\widetilde{A}_{ij}-\frac{2}{3}\alpha K\widetilde{A}_{ij}]\\&=(-D_iD_j\alpha+\frac{1}{3}\gamma_{ij}D_kD^k\alpha)+(\alpha^{(3)}R_{ij}-\frac{1}{3}\alpha^{(3)}R\gamma_{ij})-8\pi\alpha(S_{ij}-\frac{1}{3}S\gamma_{ij})+\frac{1}{3}\alpha K\psi^4\widetilde{A}_{ij}\\&\quad-2\alpha\psi^4\widetilde{A}_{ik}\widetilde{A}^k{}_j\\&=-(D_iD_j\alpha)^{TF}+\alpha^{(3)}R^{TF}_{ij}-8\pi\alpha S^{TF}_{ij}+\frac{1}{3}\alpha K\psi^4\widetilde{A}_{ij}-2\alpha\psi^4\widetilde{A}_{ik}\widetilde{A}^k{}_j,\end{aligned}\tag{2.72}$$

where the meaning of TF is ***trace-free***, i.e.,

$$(D_iD_j\alpha)^{TF}\equiv D_iD_j\alpha-\frac{1}{3}\gamma_{ij}D_kD^k\alpha,$$

$${}^{(3)}R^{TF}_{ij}\equiv{}^{(3)}R_{ij}-\frac{1}{3}\gamma_{ij}{}^{(3)}R,$$

$$S_{ij}^{TF} \equiv S_{ij} - \frac{1}{3}\gamma_{ij}S.$$

Similar to Equation (2.59), we have a similar Lie derivative result for $\widetilde{A}_{ij}$:

$$\mathscr{L}_{\vec{\beta}}\widetilde{A}_{ij} = \beta^k\partial_k\widetilde{A}_{ij} + \widetilde{A}_{ik}\partial_j\beta^k + \widetilde{A}_{jk}\partial_i\beta^k - \frac{2}{3}\widetilde{A}_{ij}\partial_k\beta^k. \tag{2.73}$$

Thus, substituting the above expression into Equation (2.72), we obtain the evolution equation for $\widetilde{A}_{ij}$:

$$\begin{aligned}(\partial_t - \beta^k\partial_k)\widetilde{A}_{ij} = \psi^{-4}[-D_iD_j\alpha + \alpha^{(3)}R_{ij} - 8\pi\alpha S_{ij}]^{TF} + \alpha(K\widetilde{A}_{ij} - 2\widetilde{A}_{ik}\widetilde{A}^k{}_j) + \widetilde{A}_{ik}\partial_j\beta^k \\ + \widetilde{A}_{jk}\partial_i\beta^k - \frac{2}{3}\widetilde{A}_{ij}\partial_k\beta^k.\end{aligned} \tag{2.74}$$

The Evolution Equation for $\widetilde{\Gamma}^i$

Up until now, numerous types of metrics have appeared, leading to the existence of various types of Christoffel symbols. To prevent confusion, we will clarify the different Christoffel symbols here,

$$\Gamma^k{}_{ij} : D_i \to \partial_i, \qquad \widetilde{\Gamma}^k{}_{ij} : \widetilde{D}_i \to \partial_i, \qquad C^k{}_{ij} : D_k \to \widetilde{D}_k \tag{2.75}$$

and

$$C^k{}_{ij} = \Gamma^k{}_{ij} - \widetilde{\Gamma}^k{}_{ij}. \tag{2.76}$$

We now aim to find the specific expressions connecting $\Gamma^k{}_{ij}$ with $\widetilde{\Gamma}^k{}_{ij}$. We will start with the expression for $C^k{}_{ij}$:

$$C^k{}_{ij} = \frac{1}{2}\gamma^{kl}(\widetilde{D}_i\gamma_{lj} + \widetilde{D}_j\gamma_{il} - \widetilde{D}_l\gamma_{ij}). \tag{2.77}$$

Next, we will rewrite the expression using $\widetilde{\gamma}_{ij} = \psi^{-4}\gamma_{ij}$ and $\widetilde{\gamma}^{ij} = \psi^4\gamma^{ij}$,

$$\begin{aligned}C^k{}_{ij} &= \frac{1}{2}\psi^{-4}\widetilde{\gamma}^{kl}[\widetilde{D}_i(\psi^4\widetilde{\gamma}_{lj}) + \widetilde{D}_j(\psi^4\widetilde{\gamma}_{il}) - \widetilde{D}_l(\psi^4\widetilde{\gamma}_{ij})] \\ &= \frac{1}{2}\psi^{-4}(\delta^k{}_j\widetilde{D}_i\psi^4 + \delta^k{}_i\widetilde{D}_j\psi^4 - \widetilde{\gamma}^{kl}\widetilde{\gamma}_{ij}\widetilde{D}_l\psi^4) \\ &= \frac{1}{2}\psi^{-4}(\delta^k{}_j\partial_i\psi^4 + \delta^k{}_i\partial_j\psi^4 - \gamma^{kl}\gamma_{ij}\partial_l\psi^4).\end{aligned}$$

Noting that $\psi = e^{\phi}$, we then have:

$$\begin{aligned}\widetilde{\Gamma}^{k}{}_{ij} &= \Gamma^{k}{}_{ij} - \frac{1}{2}e^{-4\phi}(\delta^{k}{}_{i}\partial_j e^{4\phi} + \delta^{k}{}_{j}\partial_i e^{4\phi} - \gamma^{kl}\gamma_{ij}\partial_l e^{4\phi}) \\ &= \Gamma^{k}{}_{ij} - 2(\delta^{k}{}_{i}\partial_j\phi + \delta^{k}{}_{j}\partial_i\phi - \gamma_{ij}\gamma^{kl}\partial_l\phi).\end{aligned}$$

Following the choices made in Section 2.4 i.e.,

$$\partial_i\phi = \frac{1}{12}\partial_i \ln\gamma = \frac{1}{6}\times\frac{1}{2\gamma}\partial_i\gamma = \frac{1}{6}\times\frac{1}{\sqrt{\gamma}}\partial_i\sqrt{\gamma} = \frac{1}{6}\Gamma^{m}{}_{im}, \tag{2.78}$$

we have

$$\widetilde{\Gamma}^{k}{}_{ij} = \Gamma^{k}{}_{ij} - \frac{1}{3}(\delta^{k}{}_{i}\Gamma^{m}{}_{jm} + \delta^{k}{}_{j}\Gamma^{m}{}_{im} - \gamma_{ij}\gamma^{kl}\Gamma^{m}{}_{lm}). \tag{2.79}$$

This also implies that $C^{k}{}_{ij}$ equals

$$C^{k}{}_{ij} = \frac{1}{3}(\delta^{k}{}_{i}\Gamma^{m}{}_{jm} + \delta^{k}{}_{j}\Gamma^{m}{}_{im} - \gamma_{ij}\gamma^{kl}\Gamma^{m}{}_{lm}). \tag{2.80}$$

Now, we can write down the expression for the **Conformal Connection Functions**:

$$\begin{aligned}\widetilde{\Gamma}^{i} \equiv \widetilde{\gamma}^{jk}\widetilde{\Gamma}^{i}{}_{jk} &= \widetilde{\gamma}^{jk}\frac{1}{2}\widetilde{\gamma}^{il}\left(\partial_j\widetilde{\gamma}_{kl} + \partial_k\widetilde{\gamma}_{jl} - \partial_l\widetilde{\gamma}_{jk}\right) \\ &= \frac{1}{2}\left[\widetilde{\gamma}^{jk}\left(-\widetilde{\gamma}_{kl}\partial_j\widetilde{\gamma}^{l}\right) + \widetilde{\gamma}^{jk}\left(-\widetilde{\gamma}_{jl}\partial_k\widetilde{\gamma}^{l}\right) - \widetilde{\gamma}^{l}\partial_l\ln\widetilde{\gamma}\right] \\ &= \frac{1}{2}\left(-\delta_{l}{}^{j}\partial_j\widetilde{\gamma}^{il} - \delta_{l}{}^{k}\partial_k\widetilde{\gamma}^{l}\right) \\ &= -\partial_j\widetilde{\gamma}^{ij}.\end{aligned} \tag{2.81}$$

On the other hand, similar to Equation (2.58), we have (see Appendix A for a detailed proof)

$$\partial_t\widetilde{\gamma}^{ij} - \mathscr{L}_{\vec{\beta}}\widetilde{\gamma}^{ij} = 2\alpha\widetilde{A}^{ij}. \tag{2.82}$$

Combining Equations (2.81) and (2.82), we obtain

$$\begin{aligned}\partial_t\widetilde{\Gamma}^{i} &= \partial_t(-\partial_j\widetilde{\gamma}^{ij}) \\ &= -\partial_j\partial_t\widetilde{\gamma}^{ij} \\ &= -\partial_j(\mathscr{L}_{\vec{\beta}}\widetilde{\gamma}^{ij} + 2\alpha\widetilde{A}^{ij}) \\ &= -\partial_j(\mathscr{L}_{\vec{\beta}}\widetilde{\gamma}^{ij}) - 2(\alpha\partial_j\widetilde{A}^{ij} + \widetilde{A}^{ij}\partial_j\alpha),\end{aligned} \tag{2.83}$$

in which, the term $-\partial_j\left(\mathscr{L}_{\vec{\beta}}\tilde{\gamma}^{ij}\right)$ in the above equation can be further expressed as

$$\begin{aligned}
-\partial_j(\mathscr{L}_{\vec{\beta}}\tilde{\gamma}^{ij}) &= \partial_j(-\beta^k\partial_k\tilde{\gamma}^{ij}+\tilde{\gamma}^{kj}\partial_k\beta^i+\tilde{\gamma}^{ik}\partial_k\beta^j-\frac{2}{3}\tilde{\gamma}^{ij}\partial_k\beta^k)\\
&= [-\beta^k\partial_j\partial_k\tilde{\gamma}^{ij}-(\partial_j\beta^k)\partial_k\tilde{\gamma}^{ij}]+[\tilde{\gamma}^{kj}\partial_j\partial_k\beta^i+(\partial_j\tilde{\gamma}^{kj})\partial_k\beta^i]\\
&\quad+[\tilde{\gamma}^{ik}\partial_j\partial_k\beta^j+(\partial_j\tilde{\gamma}^{ik})\partial_k\beta^j]-\frac{2}{3}\tilde{\gamma}^{ij}\partial_j\partial_k\beta^k-\frac{2}{3}(\partial_j\tilde{\gamma}^{ij})\partial_k\beta^k\\
&= -\beta^k\partial_j\partial_k\tilde{\gamma}^{ij}+\tilde{\gamma}^{kj}\partial_j\partial_k\beta^i+(\partial_j\tilde{\gamma}^{kj})\partial_k\beta^i+\frac{1}{3}\tilde{\gamma}^{ij}\partial_j\partial_k\beta^k-\frac{2}{3}(\partial_j\tilde{\gamma}^{ij})\partial_k\beta^k\\
&= \tilde{\gamma}^{kj}\partial_j\partial_k\beta^i+\frac{1}{3}\tilde{\gamma}^{ij}\partial_j\partial_k\beta^k-\beta^j\partial_j\partial_k\tilde{\gamma}^{ik}+(\partial_k\tilde{\gamma}^{jk})\partial_j\beta^i-\frac{2}{3}(\partial_k\tilde{\gamma}^{ik})\partial_j\beta^j\\
&= \tilde{\gamma}^{jk}\partial_j\partial_k\beta^i+\frac{1}{3}\tilde{\gamma}^{ij}\partial_j\partial_k\beta^k+\beta^j\partial_j\tilde{\Gamma}^i-\tilde{\Gamma}^j\partial_j\beta^i+\frac{2}{3}\tilde{\Gamma}^i\partial_j\beta^j.
\end{aligned}$$

Then, we obtained the preliminary expression for $\tilde{\Gamma}^i$:

$$\partial_t\tilde{\Gamma}^i=\tilde{\gamma}^{jk}\partial_j\partial_k\beta^i+\frac{1}{3}\tilde{\gamma}^{ij}\partial_j\partial_k\beta^k+\beta^j\partial_j\tilde{\Gamma}^i-\tilde{\Gamma}^j\partial_j\beta^i+\frac{2}{3}\tilde{\Gamma}^i\partial_j\beta^j-2(\alpha\partial_j\tilde{A}^{ij}+\tilde{A}^{ij}\partial_j\alpha). \tag{2.84}$$

Finally, with the help of the momentum constraints written out in terms of conformally transformed quantities:

$$\partial_j\tilde{A}^{ij}+\tilde{\Gamma}^i{}_{jk}\tilde{A}^{jk}+6\tilde{A}^{ij}\partial_j\phi-\frac{2}{3}\tilde{\gamma}^{ij}\partial_jK=8\pi\tilde{j}^i, \tag{2.85}$$

where $\tilde{j}^i\equiv e^{4\phi}j^i$. We can obtain the final expression:

$$\begin{aligned}
(\partial_t-\beta^j\partial_j)\tilde{\Gamma}^i =& -2\tilde{A}^{ij}\partial_j\alpha+2\alpha(\tilde{\Gamma}^i{}_{jk}\tilde{A}^{jk}+6\tilde{A}^{ij}\partial_j\phi-\frac{2}{3}\tilde{\gamma}^{ij}\partial_jK-8\pi\tilde{j}^i)\\
&-\tilde{\Gamma}^j\partial_j\beta^i+\frac{2}{3}\tilde{\Gamma}^i\partial_j\beta^j+\frac{1}{3}\tilde{\gamma}^{ij}\partial_j\partial_k\beta^k+\tilde{\gamma}^{jk}\partial_j\partial_k\beta^i.
\end{aligned}$$

It is important to note that the final step of applying the momentum constraints is *crucial*. This step enables the entire evolution system to transition from **weakly hyperbolic** to **strongly hyperbolic**, ensuring that the evolution can proceed *stably*.

The Effective Ricci Tensor Expression in BSSN

In the evolution equation for $\tilde{A}_{ij}$, we also need to compute the Ricci tensor associated with the physical metric. This tensor can be decomposed into two contributions as follows:

$$R_{ij}=\tilde{R}_{ij}+R^{\phi}_{ij}. \tag{2.86}$$

The first term on the right-hand side, $\widetilde{R}_{ij}$, can be directly obtained through its corresponding metric and Christoffel symbols (See Appendix A for details),

$$\widetilde{R}_{ij} = -\frac{1}{2}\widetilde{\gamma}^{lm}\partial_l\partial_m\widetilde{\gamma}_{ij} + \widetilde{\gamma}_{k(i}\partial_{j)}\widetilde{\Gamma}^k + \widetilde{\Gamma}^k\widetilde{\Gamma}_{(ij)k} + \widetilde{\gamma}^{lm}(2\widetilde{\Gamma}^k{}_{l(i}\widetilde{\Gamma}_{j)km} + \widetilde{\Gamma}^k{}_{im}\widetilde{\Gamma}_{klj}). \tag{2.87}$$

For R^{ϕ}_{ij}, we start from $R_{ij} - \widetilde{R}_{ij}$. By definition, we have

$$\left(D_iD_j - D_jD_i\right)v^k = -R_{ijl}{}^k v^l, \tag{2.88}$$

and

$$\left(D_jD_i - D_iD_j\right)v^j = R_{ij}v^j. \tag{2.89}$$

Similarly,

$$\left(\widetilde{D}_j\widetilde{D}_i - \widetilde{D}_i\widetilde{D}_j\right)v^j = \widetilde{R}_{ij}v^j. \tag{2.90}$$

We start with $R_{ij}v^j$ and using the Christoffel symbols C_{ijk} introduced earlier, we obtain:

$$\begin{aligned}
R_{ij}v^j &= D_jD_iv^j - D_iD_jv^j \\
&= \left[\widetilde{D}_j(D_iv^j) + C^j{}_{jk}D_iv^k - C^k{}_{ji}D_kv^j\right] - \widetilde{D}_i(D_jv^j) \\
&= \left[\widetilde{D}_j(\widetilde{D}_iv^j + C^j{}_{ik}v^k) + C^j{}_{jk}(\widetilde{D}_iv^k + C^k{}_{il}v^l) - C^k{}_{ji}(\widetilde{D}_kv^j + C^j{}_{kl}v^l)\right] - \widetilde{D}_i(\widetilde{D}_jv^j + C^j{}_{jk}v^l) \\
&= (\widetilde{D}_j\widetilde{D}_iv^j + v^k\widetilde{D}_jC^j{}_{ik} + C^j{}_{ik}\widetilde{D}_jv^k) + (C^j{}_{jk}\widetilde{D}_iv^k + C^j{}_{jk}C^k{}_{il}v^l) - (C^k{}_{ji}\widetilde{D}_kv^j + C^k{}_{ji}C^j{}_{kl}v^l) \\
&\quad - (\widetilde{D}_i\widetilde{D}_jv^j + v^k\widetilde{D}_iC^j{}_{jk} + C^j{}_{jk}\widetilde{D}_iv^k) \\
&= \widetilde{D}_j\widetilde{D}_iv^j - \widetilde{D}_i\widetilde{D}_jv^j + v^k\widetilde{D}_jC^j{}_{ik} - C^k{}_{ji}C^j{}_{kl}v^l + C^j{}_{jk}C^k{}_{il}v^l - v^k\widetilde{D}_iC^j{}_{jk} \\
&= \widetilde{R}_{ij}v^j + v^j\widetilde{D}_kC^k{}_{ij} - v^j\widetilde{D}_iC^k{}_{kj} + C^l{}_{lk}C^k{}_{ij}v^j - C^k{}_{li}C^l{}_{kj}v^j.
\end{aligned}$$

From this, it is evident that

$$R_{ij} = \widetilde{R}_{ij} + \widetilde{D}_kC^k{}_{ij} - \widetilde{D}_iC^k{}_{kj} + C^l{}_{lk}C^k{}_{ij} - C^k{}_{il}C^l{}_{kj}. \tag{2.91}$$

Using Equation (2.80), we obtain

$$C^k{}_{ki} = 2(\delta^k{}_i\widetilde{D}_k\phi + \delta^k{}_k\widetilde{D}_i\phi - \widetilde{\gamma}_{ik}\widetilde{D}^k\phi) = 6\widetilde{D}_i\phi, \tag{2.92}$$

and

$$\widetilde{D}_k C^k{}_{ij} = 2\widetilde{D}_k(\delta^k{}_i\widetilde{D}_j\phi + \delta^k{}_j\widetilde{D}_i\phi - \widetilde{\gamma}_{ij}\widetilde{D}^k\phi) = 4\widetilde{D}_i\widetilde{D}_j\phi - 2\widetilde{\gamma}_{ij}\widetilde{D}_k\widetilde{D}^k\phi. \tag{2.93}$$

Substituting Equations (2.80), (2.92), and (2.93) into (2.91), we obtain

$$\begin{aligned}
R_{ij} &= \widetilde{R}_{ij} + (4\widetilde{D}_i\widetilde{D}_j\phi - 2\widetilde{\gamma}_{ij}\widetilde{D}_k\widetilde{D}^k\phi) - 6\widetilde{D}_i\widetilde{D}_j\phi + 6\widetilde{D}_k\phi \times 2(\delta^k{}_i\widetilde{D}_j\phi + \delta^k{}_j\widetilde{D}_i\phi - \widetilde{\gamma}_{ij}\widetilde{D}^k\phi) \\
&\quad - 2(\delta^k{}_i\widetilde{D}_l\phi + \delta^k{}_l\widetilde{D}_i\phi - \widetilde{\gamma}_{il}\widetilde{D}^k\phi) \times 2(\delta^l{}_k\widetilde{D}_j\phi + \delta^l{}_j\widetilde{D}_k\phi - \widetilde{\gamma}_{kj}\widetilde{D}^l\phi) \\
&= \widetilde{R}_{ij} + (4\widetilde{D}_i\widetilde{D}_j\phi - 2\widetilde{\gamma}_{ij}\widetilde{D}_k\widetilde{D}^k\phi) - 6\widetilde{D}_i\widetilde{D}_j\phi + [12(\widetilde{D}_i\phi)\widetilde{D}_j\phi + 12(\widetilde{D}_j\phi)\widetilde{D}_i\phi \\
&\quad - 12\widetilde{\gamma}_{ij}(\widetilde{D}_k\phi)\widetilde{D}^k\phi] + [-4(\widetilde{D}_i\phi)\widetilde{D}_j\phi - 4(\widetilde{D}_i\phi)\widetilde{D}_j\phi + 4\widetilde{\gamma}_{ij}(\widetilde{D}_l\phi)\widetilde{D}^l\phi] + [-12(\widetilde{D}_i\phi)\widetilde{D}_j\phi \\
&\quad - 4(\widetilde{D}_i\phi)\widetilde{D}_j\phi + 4\widetilde{\gamma}_{lj}(\widetilde{D}_i\phi)\widetilde{D}^l\phi] + [4(\widetilde{D}_i\phi)\widetilde{D}_j\phi + 4\widetilde{\gamma}_{ij}(\widetilde{D}^k\phi)\widetilde{D}_k\phi - 4(\widetilde{D}_j\phi)\widetilde{D}_i\phi] \\
&= \widetilde{R}_{ij} - 2\widetilde{D}_i\widetilde{D}_j\phi - 2\widetilde{\gamma}_{ij}\widetilde{D}_k\widetilde{D}^k\phi + 4(\widetilde{D}_i\phi)\widetilde{D}_j\phi - 4\widetilde{\gamma}_{ij}(\widetilde{D}_k\phi)\widetilde{D}^k\phi.
\end{aligned}$$

Therefore, the expression for R^{ϕ}_{ij} is as follows:

$$R^{\phi}_{ij} = -2\widetilde{D}_i\widetilde{D}_j\phi - 2\widetilde{\gamma}_{ij}\widetilde{D}_k\widetilde{D}^k\phi + 4(\widetilde{D}_i\phi)\widetilde{D}_j\phi - 4\widetilde{\gamma}_{ij}(\widetilde{D}_k\phi)\widetilde{D}^k\phi. \tag{2.94}$$

Finally, we obtain the expression for R_{ij} in the BSSN formalism as

$$\begin{aligned}
R_{ij} &= \widetilde{R}_{ij} + R^{\phi}_{ij} \\
&= -\frac{1}{2}\widetilde{\gamma}^{lm}\partial_l\partial_m\widetilde{\gamma}_{ij} + \widetilde{\gamma}_{k(i}\partial_{j)}\widetilde{\Gamma}^k + \widetilde{\Gamma}^k\widetilde{\Gamma}_{(ij)k} + \widetilde{\gamma}^{lm}(2\widetilde{\Gamma}^k{}_{l(i}\widetilde{\Gamma}_{j)km} + \widetilde{\Gamma}^k{}_{im}\widetilde{\Gamma}_{klj}) \\
&\quad - 2\widetilde{D}_i\widetilde{D}_j\phi - 2\widetilde{\gamma}_{ij}\widetilde{D}_k\widetilde{D}^k\phi + 4(\widetilde{D}_i\phi)\widetilde{D}_j\phi - 4\widetilde{\gamma}_{ij}(\widetilde{D}_k\phi)\widetilde{D}^k\phi.
\end{aligned} \tag{2.95}$$

Summary

The Evolution Equation for ϕ

$$(\partial_t - \beta^i \partial_i)\phi = -\frac{1}{6}\alpha K + \frac{1}{6}\partial_i \beta^i. \tag{2.96}$$

The Evolution Equation for $\widetilde{\gamma}_{ij}$

$$(\partial_t - \beta^k \partial_k)\widetilde{\gamma}_{ij} = -2\alpha \widetilde{A}_{ij} + \widetilde{\gamma}_{ik}\partial_j \beta^k + \widetilde{\gamma}_{jk}\partial_i \beta^k - \frac{2}{3}\widetilde{\gamma}_{ij}\partial_k \beta^k. \tag{2.97}$$

The Evolution Equation for K

$$(\partial_t - \beta^i \partial_i)K = -D_i D^i \alpha + \alpha(\widetilde{A}_{ij}\widetilde{A}^{ij} + \frac{1}{3}K^2) + 4\pi\alpha(\rho + S). \tag{2.98}$$

The Evolution Equation for $\widetilde{A}_{ij}$

$$\begin{aligned}(\partial_t - \beta^k \partial_k)\widetilde{A}_{ij} = \psi^{-4}[-D_i D_j \alpha + \alpha^{(3)}R_{ij} - 8\pi\alpha S_{ij}]^{TF} + \alpha(K\widetilde{A}_{ij} - 2\widetilde{A}_{ik}\widetilde{A}^k{}_j) + \widetilde{A}_{ik}\partial_j \beta^k \\ + \widetilde{A}_{jk}\partial_i \beta^k - \frac{2}{3}\widetilde{A}_{ij}\partial_k \beta^k.\end{aligned}$$

The Evolution Equation for $\widetilde{\Gamma}^i$

$$\begin{aligned}(\partial_t - \beta^j \partial_j)\widetilde{\Gamma}^i = &-2\widetilde{A}^{ij}\partial_j \alpha + 2\alpha(\widetilde{\Gamma}^i{}_{jk}\widetilde{A}^{jk} + 6\widetilde{A}^{ij}\partial_j \phi - \frac{2}{3}\widetilde{\gamma}^{ij}\partial_j K - 8\pi \widetilde{j}^i) \\ &- \widetilde{\Gamma}^j \partial_j \beta^i + \frac{2}{3}\widetilde{\Gamma}^i \partial_j \beta^j + \frac{1}{3}\widetilde{\gamma}^{ij}\partial_j \partial_k \beta^k + \widetilde{\gamma}^{jk}\partial_j \partial_k \beta^i.\end{aligned}$$

The Effective Ricci Tensor Expression

$$\begin{aligned}R_{ij} &= \widetilde{R}_{ij} + R^{\phi}_{ij} \\ &= -\frac{1}{2}\widetilde{\gamma}^{lm}\partial_l \partial_m \widetilde{\gamma}_{ij} + \widetilde{\gamma}_{k(i}\partial_{j)}\widetilde{\Gamma}^k + \widetilde{\Gamma}^k \widetilde{\Gamma}_{(ij)k} + \widetilde{\gamma}^{lm}(2\widetilde{\Gamma}^k{}_{l(i}\widetilde{\Gamma}_{j)km} + \widetilde{\Gamma}^k{}_{im}\widetilde{\Gamma}_{klj}) \\ &\quad - 2\widetilde{D}_i \widetilde{D}_j \phi - 2\widetilde{\gamma}_{ij}\widetilde{D}_k \widetilde{D}^k \phi + 4(\widetilde{D}_i \phi)\widetilde{D}_j \phi - 4\widetilde{\gamma}_{ij}(\widetilde{D}_k \phi)\widetilde{D}^k \phi.\end{aligned} \tag{2.99}$$

This new formalism not only avoids the violent instability previously mentioned, but it also proves to be far more stable than ADM in all cases studied to date. This was first demonstrated empirically through direct comparison of numerical simulations by Baumgarte and Shapiro [36], and was later substantiated by Alcubierre et al. [20] through the analysis of linear perturbations of flat space.

It is important to recognize that the search for well-posed formulations is not confined to the BSSN formalism. Numerous other formalisms have been studied and implemented in numerical codes, including the **Kidder-Scheel-Teukolsky (KST) Formalism** [131], the **Nagy-Ortiz-Reula (NOR) Formalism** [162], the generalized harmonic formalism [96, 180, 179, 150], and the Z4-based formalisms [48, 103, 38, 25, 115]. In fact, the first black hole binary inspiral and merger simulations by Pretorius [179] were accomplished using the generalized harmonic (GH) formulation. These results were followed and confirmed about six months later by the so-called moving puncture breakthroughs from the Brownsville (Texas U., Brownsville) [63] and Goddard (NASA) [33] groups, who employed the BSSN formalism. In recent years, Z4-based formalisms have become a particularly popular alternative to the BSSN formalism, which will be discussed in the next Section 2.5.

2.5 CCZ4 Formalism

Besides BSSN, another popular method is the **Generalized Harmonic (GH) Formalism** [96, 180, 179, 150]. The GH formalism employs a 4D version of the Einstein equations in harmonic-like coordinates. Unlike BSSN, the GH formalism uses a generalized harmonic gauge that cannot manage the physical singularity inside the apparent horizon. This means it needs special techniques to handle certain areas in simulations.

One benefit of the GH formalism is its capacity to incorporate damping terms, as proposed by [103], which are used to control and reduce constraint violations, resulting in more accurate solutions of the Einstein equations.

It would be very useful to have a formalism of the Einstein equations that combines the strengths of both the BSSN and GH formalism. One of the first works to be noted is the **Z4 Covariant Formalism** [4] proposed by C. Bona et al. in 2003 [48]. This formalism is considered a covariant extension of Einstein field equations. The basic variables include the metric tensor and an additional four-vector Z_μ. Einstein's solutions are recovered when this additional four-vector vanishes. The extended field equations can be supplemented with appropriate coordinate conditions to yield symmetric hyperbolic evolution systems.

In subsequent years, the Z4 formalism has been further developed in works such as Gundlach et al. [103], Bernuzzi and Hilditch [38], Alic et al. [25], and Hilditch et al. [115]. Among these, the **Covariant and Conformal Z4 (CCZ4) Formalism** [25] and **Conformal Z4 (Z4c) Formalism** [115] have gained popularity due to their robustness in simulations of inspiraling neutron-star binaries.

The names CCZ4 and Z4c clearly indicate that the latter lacks a "**C**", representing general covariance. However, as long as the constraint violation remains small throughout, the impact of the violation will be similarly minimal. Conversely, if the violation becomes significant, using this formulation could be problematic [202].

Since the GRCHOMBO code employs the CCZ4 formalism, we will provide a brief introduction to CCZ4.

The starting point is the Z4-damped, modified version of the Einstein equations,

$$R_{\mu\nu} + \nabla_\mu Z_\nu + \nabla_\nu Z_\mu - \kappa_1 \left[n_\mu Z_\nu + n_\nu Z_\mu - (1+\kappa_2)\, g_{\mu\nu} n_\sigma Z^\sigma \right] = 8\pi \left(T_{\mu\nu} - \frac{1}{2} g_{\mu\nu} T \right). \tag{2.100}$$

where Z^μ is a vector field and n_μ is the timelike unit normal form. Note that when $Z^\mu = 0$, Equation (2.100) reduces to the Einstein equations. In addition, κ_1 and κ_2 are additional damping parameters.

[4] **Z4 Covariant Formalism** abbreviated as Z4, to distinguish it from the Z4c formalism discussed later.

We also need to consider the decomposition of the four-vector Z^μ. Therefore, we define the time and spatial projections of the Z^μ vector as

$$\Theta := -n_\alpha Z^\alpha, \quad \Theta^i := \gamma^i{}_\alpha Z^\alpha, \tag{2.101}$$

i.e.,

$$Z^\mu = \Theta n^\mu + \Theta^\mu. \tag{2.102}$$

If we consider the terms related to Z^μ as an additional stress-energy tensor, i.e.,

$$\begin{aligned} 8\pi T_{\mu\nu} \to 8\pi T_{\mu\nu} &- \left(\nabla_\mu Z_\nu + \nabla_\nu Z_\mu - g_{\mu\nu}\nabla_\sigma Z^\sigma\right) \\ &+\kappa_1 \left(n_\mu Z_\nu + n_\nu Z_\mu + \kappa_2 g_{\mu\nu} n_\sigma Z^\sigma\right). \end{aligned} \tag{2.103}$$

Then the corresponding ρ, j_μ, and $S_{\mu\nu}$ should be modified accordingly as

$$\begin{aligned} 8\pi\rho \to& 8\pi\rho + n^\mu \nabla_\mu \Theta + K\Theta - D_\mu \Theta^\mu + \Theta^\mu D_\mu \ln\alpha + \kappa_1 (2+\kappa_2)\Theta \\ 8\pi j_\mu \to& 8\pi j_\mu + \Theta D_\mu \ln\alpha - D_\mu\Theta + \gamma^\sigma{}_\mu n^\nu \nabla_\nu \Theta_\sigma + K_{\mu\nu}\Theta^\nu - \kappa_1 \Theta_\mu \\ 8\pi S_{\mu\nu} \to& 8\pi S_{\mu\nu} + 2K_{\mu\nu}\Theta - \left(D_\mu\Theta_\nu + D_\nu\Theta_\mu - \gamma_{\mu\nu} D_\sigma \Theta^\sigma\right) \\ &+ \gamma_{\mu\nu}\left(-K\Theta + n^\sigma \nabla_\sigma \Theta + \Theta^\sigma D_\sigma \ln\alpha\right) - \kappa_1\kappa_2\Theta\gamma_{\mu\nu}. \end{aligned} \tag{2.104}$$

With the introduction of new variables, it is essential to consider their impact on the original evolution equations, as well as the evolution of these variables themselves. The evolution equations for the new variables, within the context of the ADM formalism, are as follows:

$$\begin{aligned} \partial_t \Theta = \beta^m \partial_m \Theta + \frac{\alpha}{2}[&R + K(K-2\Theta) - K_{mn}K^{mn} - 2\gamma^{jj}\Theta_i \frac{\partial_j \alpha}{\alpha} \\ &-\kappa_1\Theta(4+2\kappa_2) + 2D^m\Theta_m - 16\pi\rho], \end{aligned} \tag{2.105}$$

and

$$\partial_t \Theta_i = \beta^m \partial_m \Theta_i + \Theta_m \partial_i \beta^m + \alpha\left(D_m K^m{}_i - D_i K - 2K_{im}\Theta^m + D_i\Theta - \Theta\frac{\partial_i\alpha}{\alpha} - \kappa_1\Theta_i - 8\pi j_i\right). \tag{2.106}$$

The evolution equation for γ_{ij} remains unchanged; however, the evolution of K_{ij} is modified by the introduction of the new variables and is now expressed as follows:

$$\begin{aligned}\partial_t K_{ij} =& \beta^m \partial_m K_{ij} + K_{mj}\partial_i \beta^m + K_{im}\partial_j \beta^m - D_i \partial_j \alpha \\ &+ \alpha \Bigg\{ R_{ij} + K_{ij}(K - 2\Theta) - 2K_{im}K^m{}_j \\ &+ D_i \Theta_j + D_j \Theta_i - \kappa_1 (1+\kappa_2)\gamma_{ij}\Theta - 8\pi \left[S_{ij} - \gamma_{ij}\frac{S-\rho}{2} \right] \Bigg\}. \end{aligned} \tag{2.107}$$

The CCZ4 formalism can be understood as a BSSN-like approach based on the Z4 formalism, with the addition of damping terms. Unlike the ADM version of the Z4 formalism mentioned above, in the evolution equations of the CCZ4 formalism, the variable Θ^i does not evolve explicitly due to the redefinition of the conformal connection,

$$\hat{\Gamma}^i := \tilde{\Gamma}^i + 2\tilde{\gamma}^{jk}\Theta_k = \tilde{\Gamma}^i + 2\frac{\Theta^i}{\chi}. \tag{2.108}$$

Instead, Θ^i is indirectly determined by

$$\Theta^i = \frac{\chi}{2}\left(\hat{\Gamma}^i - \tilde{\Gamma}^i\right), \tag{2.109}$$

where χ denotes the conformal factor, i.e., ψ^{-4}.

Therefore, the evolution variables of CCZ4 include only

$$\left\{\chi, \tilde{\gamma}_{ij}, K, \tilde{A}_{ij}, \Theta, \hat{\Gamma}^i\right\} \tag{2.110}$$

and do not include Θ^i.

In addition, CCZ4 introduce the modified Ricci tensor R^Z_{ij} which is the only form in which the spatial Ricci tensor appears. It is defined by

$$R^Z_{ij} := R_{ij} + 2D_{(i}\Theta_{j)} = \hat{R}_{ij} + \frac{1}{\chi}\left(R^\chi_{ij} + R^\Theta_{ij}\right) \tag{2.111}$$

with the components given by

$$\begin{aligned}
\hat{R}_{ij} &= -\frac{1}{2}\tilde{\gamma}^{kl}\partial_k\partial_l\tilde{\gamma}_{ij} + \tilde{\gamma}_{k(i}\partial_{j)}\hat{\Gamma}^k + \hat{\Gamma}^k\partial_k\tilde{\gamma}_{ij} + \tilde{\gamma}^{lm}\left(\tilde{\Gamma}^k{}_{li}\tilde{\Gamma}_{jkm} + \tilde{\Gamma}^k{}_{lj}\tilde{\Gamma}_{ikm} + \tilde{\Gamma}^k{}_{im}\tilde{\Gamma}_{klj}\right), \\
R^{\chi}_{ij} &= \frac{1}{2}\left[\tilde{D}_i\tilde{D}_j\chi + \tilde{\gamma}_{ij}\tilde{\gamma}^{kl}\tilde{D}_k\tilde{D}_l\chi\right] - \frac{1}{4\chi}\left[\partial_i\chi\partial_j\chi + 3\tilde{\gamma}_{ij}\tilde{\gamma}^{kl}\partial_k\chi\partial_l\chi\right], \\
R^{\Theta}_{ij} &= \frac{\Theta^k}{\chi}\left(\tilde{\gamma}_{ik}\partial_j\chi + \tilde{\gamma}_{jk}\partial_i\chi - \tilde{\gamma}_{ij}\partial_k\chi\right).
\end{aligned} \tag{2.112}$$

Using the redefined variables mentioned above, the complete evolution equations of CCZ4 can be expressed in the following form.

The Evolution Equation for χ

$$\partial_t \chi = \beta^k \partial_k \chi + \frac{2}{3}\chi\left(\alpha K - \partial_k \beta^k\right). \tag{2.113}$$

The Evolution Equation for $\tilde{\gamma}_{ij}$

$$\partial_t \tilde{\gamma}_{ij} = \beta^k \partial_k \tilde{\gamma}_{ij} + \tilde{\gamma}_{ki}\partial_j \beta^k + \tilde{\gamma}_{kj}\partial_i \beta^k - 2\alpha \tilde{A}_{ij} - \frac{2}{3}\tilde{\gamma}_{ij}\partial_k \beta^k. \tag{2.114}$$

The Evolution Equation for K

$$\partial_t K = \beta^k \partial_k K + \alpha\left[R^Z + K(K-2\Theta)\right] - 3\alpha\kappa_1(1+\kappa_2)\Theta - \gamma^{kl} D_k D_l \alpha + 4\pi\alpha(S-3\rho). \tag{2.115}$$

The Evolution Equation for $\tilde{A}_{ij}$

$$\begin{aligned}\partial_t \tilde{A}_{ij} = {} & \beta^k \partial_k \tilde{A}_{ij} + \chi\left[-D_i D_j \alpha + \alpha\left(R^Z_{ij} - 8\pi S_{ij}\right)\right]^{\mathrm{TF}} \\ & + \tilde{A}_{ij}\left[\alpha(K-2\Theta) - \frac{2}{3}\partial_k \beta^k\right] + 2\tilde{A}_{k(i}\partial_{j)}\beta^k - 2\alpha\tilde{\gamma}^{kl}\tilde{A}_{ik}\tilde{A}_{lj}.\end{aligned} \tag{2.116}$$

The Evolution Equation for Θ

$$\begin{aligned}\partial_t \Theta = {} & \beta^k \partial_k \Theta + \frac{1}{2}\alpha\left(R^Z - \tilde{A}_{kl}\tilde{A}^{kl} + \frac{2}{3}K^2 - 2\Theta K\right) - \alpha\kappa_1\Theta(2+\kappa_2) \\ & - \Theta^k \partial_k \alpha - 8\pi\alpha\rho.\end{aligned} \tag{2.117}$$

The Evolution Equation for $\hat{\Gamma}^i$

$$\begin{aligned}\partial_t \hat{\Gamma}^i = {} & \beta^k \partial_k \hat{\Gamma}^i + \frac{2}{3}\left[\partial_k \beta^k\left(\tilde{\Gamma}^i + 2\kappa_3\frac{\Theta^i}{\chi}\right) - 2\alpha K\frac{\Theta^i}{\chi}\right] - 2\alpha\kappa_1\frac{\Theta^i}{\chi} \\ & + 2\tilde{\gamma}^{ik}\left(\alpha\partial_k\Theta - \Theta\partial_k\alpha\right) - 2\tilde{A}^{ik}\partial_k\alpha + 2\alpha\tilde{\Gamma}^i{}_{kl}\tilde{A}^{kl} \\ & - \alpha\left[\frac{4}{3}\tilde{\gamma}^{ik}\partial_k K + 3\tilde{A}^{ik}\frac{\partial_k\chi}{\chi}\right] - \left(\tilde{\Gamma}^k + 2\kappa_3\frac{\Theta^k}{\chi}\right)\partial_k\beta^i \\ & + \tilde{\gamma}^{kl}\partial_k\partial_l\beta^i + \frac{1}{3}\tilde{\gamma}^{ik}\partial_l\partial_k\beta^l - 16\pi\alpha\tilde{\gamma}^{ik}j_k.\end{aligned} \tag{2.118}$$

where κ_3 is an additional parameter.

The parameter κ_3 was introduced by Alic et al. [25], who discovered that instability occurs during black hole evolution regardless of whether damping is applied (i.e., $\kappa_3 = 1, \kappa_1 \neq 0$) or not (i.e., $\kappa_3 = 1, \kappa_1 = 0$). Furthermore, they found that to achieve stable black hole evolution, κ_3 must be set to a value different from 1 (typically $\kappa_3 < 1$), though this comes at the expense of covariance.

It was later realized that even while keeping κ_3 equal to 1, redefining $\alpha\kappa_1$ as κ_1' allows both covariance and numerical stability to be maintained [26]. Specifically, the following parameter combination can be chosen

$$\begin{aligned} \kappa_1' &:= \alpha\kappa_1, \\ \kappa_1' &= 0.1, \\ \kappa_2 &= 0, \\ \kappa_3 &= 1. \end{aligned} \tag{2.119}$$

This choice is also the default setting in GRCHOMBO.

2.6 Initial Conditions

The initial value problem is a significant topic for physical theories. If a physical theory lacks a good initial value formulation, it has no predictive power. The initial value problem of general relativity attracts considerable attention not only because, as a physical theory, it must pass this test, but also because many physical understandings of general relativity depend on the existence of a good initial value formulation.

In Section 2.2, we have already discussed similar issues using the Maxwell equations as an example.

However, general relativity fundamentally differs from other field theories in terms of initial value problems: other field theories already presuppose a spacetime background (such as Minkowski space for the aforementioned Maxwell's theory) before discussing initial value problems, whereas the subject of the initial value problem in general relativity is spacetime itself. This seems peculiar: how can one specify initial values on a spacelike Cauchy surface Σ_0 when spacetime has not yet been defined? (Without a metric, the spacelikeness of a hypersurface is undefined.) The answer, though seemingly surprising, is quite clever: one first specifies "initial values" on an abstract 3-dimensional manifold Σ, namely a positive definite metric field $\overset{0}{\gamma}_{ab}$ and a symmetric $(0,2)$-tensor field $\overset{0}{K}_{ab}$, (subject to certain constraints). It is then shown that there exists a 4-dimensional spacetime (M, g_{ab}) (where g_{ab} satisfies Einstein's equations) which, upon appropriate $3+1$ decomposition, has each spacelike hypersurface Σ_t differentiably homeomorphic to Σ, with one such surface (denoted as Σ_0) having its induced metric γ_{ab} and extrinsic curvature K_{ab} exactly corresponding to $\overset{0}{\gamma}_{ab}$ and $\overset{0}{K}_{ab}$. Thus, Σ_0 and its (γ_{ab}, K_{ab}) can be interpreted as the initial values on the initial spacelike hypersurface Σ_0, and (M, g_{ab}) as the outcome of the evolution of these initial values. It is evident that in general relativity, terms like **initial surface**, **initial values**, and **time evolution** only acquire meaning after the solution to the **initial value problem** is obtained [143].

Next, we introduce a widely used method for obtaining initial data—the conformal decomposition of York and Lichnerowicz [145, 236, 237]. In this section, we apply a new conformal transformation method as follows:

$$\widetilde{\gamma}_{ij} = \psi^{-4}\gamma_{ij}, \qquad \widetilde{\gamma}^{ij} = \psi^{4}\gamma^{ij}, \tag{2.120}$$

$$\widetilde{A}^{ij} = \psi^{10}A^{ij}, \qquad \widetilde{A}_{ij} = \widetilde{\gamma}_{ik}\widetilde{\gamma}_{il}\widetilde{A}^{kl} = \psi^{2}A_{ij}. \tag{2.121}$$

Rewrite the Hamiltonian Constraint.

We apply $\widetilde{\gamma}_{ij}$ to Equation (2.94):

$$\begin{aligned}\psi^4 R &= \widetilde{R} - 2\left(\widetilde{D}^2 \ln\psi + 3\widetilde{D}^2 \ln\psi\right) + 4\left[\left(\widetilde{D}_i \ln\psi\right)\left(\widetilde{D}^i \ln\psi\right) - 3\left(\widetilde{D}_l \ln\psi\right)\left(\widetilde{D}^l \ln\psi\right)\right] \\ &= \widetilde{R} - 8\widetilde{D}^2 \ln\psi - 8\left(\widetilde{D}_i \ln\psi\right)\left(\widetilde{D}^i \ln\psi\right)\end{aligned} \tag{2.122}$$

where,

$$\widetilde{D}^i \widetilde{D}_i \ln\psi = -\psi^{-2}\left(\widetilde{D}^i\psi\right)\left(\widetilde{D}_i\psi\right) + \psi^{-1}\widetilde{D}^i\widetilde{D}_i\psi. \tag{2.123}$$

Thus,

$$\begin{aligned}\psi^4 R &= \widetilde{R} - 8\left[-\psi^{-2}\left(\widetilde{D}^i\psi\right)\left(\widetilde{D}_i\psi\right) + \psi^{-1}\widetilde{D}^i\widetilde{D}_i\psi\right] - 8\left(\widetilde{D}_i \ln\psi\right)\left(\widetilde{D}^i \ln\psi\right) \\ &= \widetilde{R} - 8\psi^{-1}\widetilde{D}^i\widetilde{D}_i\psi\end{aligned} \tag{2.124}$$

i.e.,

$$R = \psi^{-4}\widetilde{R} - 8\psi^{-5}\widetilde{D}^i\widetilde{D}_i\psi. \tag{2.125}$$

By utilizing the previously derived Equation (2.125) and substituting it into the Hamiltonian constraint (2.21), we obtain:

$$8\widetilde{D}^2\psi - \psi\widetilde{R} - \psi^5 K^2 + \psi^5 K_{ij}K^{ij} = -16\pi\psi^5\rho. \tag{2.126}$$

Note that:

$$K_{ij}K^{ij} = \left(A^{ij} + \frac{1}{3}\gamma^{ij}K\right)\left(A_{ij} + \frac{1}{3}\gamma_{ij}K\right) = A^{ij}A_{ij} + \frac{1}{3}K^2. \tag{2.127}$$

Finally, we arrive at the following reformulated Hamiltonian constraint:

$$8\widetilde{D}^2\psi - \widetilde{R}\psi + \psi^5\left[A^{ij}A_{ij} - \frac{2}{3}K^2\right] + 16\pi\psi^5\rho = 0. \tag{2.128}$$

Rewrite the Momentum Constraints.

Using A^{ij} and K to rewrite the momentum constraints yields:

$$D_j A^{ij} - \frac{2}{3} D^i K - 8\pi j^i = 0 \tag{2.129}$$

where

$$\begin{aligned} D_j A^{ij} =& \widetilde{D}_j A^{ij} + C^i{}_{jk} A^{kj} + C^j{}_{jk} A^{ik} \\ =& \widetilde{D}_j A^{ij} + 2\left(\delta_j{}^i \widetilde{D}_k (\ln\psi) + \delta_k{}^i \widetilde{D}_j \ln\psi - \widetilde{D}^i \ln\psi \widetilde{\gamma}_{jk}\right) A^{kj} + 6\widetilde{D}_k (\ln\psi) A^{ik} \\ =& \widetilde{D}_j A^{ij} + 10 A^{ij} \widetilde{D}_j \ln\psi - 2\widetilde{D}^i (\ln\psi) \widetilde{\gamma}_{jk} A^{jk}, \end{aligned} \tag{2.130}$$

i.e.,

$$D_j A^{ij} = \widetilde{D}_j A^{ij} + 10 A^{ij} \widetilde{D}_j \ln\psi. \tag{2.131}$$

Note that:

$$\begin{aligned} & \psi^{-10} \widetilde{D}_j \left(\psi^{10} A^{ij}\right) \\ =& \psi^{-10} \psi^{10} \widetilde{D}_j A^{ij} + \psi^{-10} A^{ij} \widetilde{D}_j \psi^{10} \\ =& \widetilde{D}_j A^{ij} + 10 A^{ij} \widetilde{D}_j \ln\psi. \end{aligned} \tag{2.132}$$

Thus,

$$D_j A^{ij} = \psi^{-10} \widetilde{D}_j \left(\psi^{10} A^{ij}\right). \tag{2.133}$$

Using Equation (2.121), we can further derive:

$$\widetilde{D}_j \widetilde{A}^{ij} - \frac{2}{3} \psi^{10} D^i K - 8\pi \psi^{10} j^i = 0, \tag{2.134}$$

where the second term on the left side can be written as:

$$\psi^{10} \gamma^{ij} D_j K = \psi^{10} \psi^{-4} \widetilde{\gamma}^{ij} \widetilde{D}_j K = \psi^6 \widetilde{D}^i K. \tag{2.135}$$

This means that

$$\widetilde{D}_j \widetilde{A}^{ij} - \frac{2}{3} \psi^6 \widetilde{D}^i K - 8\pi \psi^{10} j^i = 0. \tag{2.136}$$

A symmetric, ***trace-free*** tensor S^{ij} can be decomposed in the following manner [19],

$$S^{ij} = S_*^{ij} + (\widetilde{\mathbf{L}} W)^{ij}. \tag{2.137}$$

Here, S_*^{ij} is a ***symmetric***, ***traceless***, and ***transverse*** tensor, meaning $D_j S_*^{ij} = 0$. The term W^i represents a vector, while L signifies an operator, defined as:

$$(\widetilde{\mathbf{L}}W)^{ij} := D^i W^j + D^j W^i - \frac{2}{3}\gamma^{ij} D_k W^k. \tag{2.138}$$

The expression $(\widetilde{\mathbf{L}}W)^{ij}$ is recognized as the **Conformal Killing Form** linked to the vector W^i, and it constitutes the longitudinal component of S^{ij}. In scenarios where the conformal Killing form is nullified, the vector W^i is identified as a conformal Killing vector.

Similarly, we can decompose $\widetilde{A}^{ij}$ in the following form:

$$\widetilde{A}^{ij} = \widetilde{A}_*^{ij} + (\widetilde{\mathbf{L}}\widetilde{W})^{ij}. \tag{2.139}$$

Utilizing the above expression, we can further rewrite Equation (2.136) as follows:

$$\widetilde{D}_j \widetilde{A}_*^{ij} + \widetilde{D}_j (\widetilde{\mathbf{L}}\widetilde{W})^{ij} - \frac{2}{3}\psi^6 \widetilde{D}^i K - 8\pi\psi^{10} j^i = 0. \tag{2.140}$$

Here, we introduce a new definition [5]:

$$\widetilde{\Delta}_{\widetilde{\mathbf{L}}}\widetilde{W}^i := \widetilde{D}_j (\widetilde{\mathbf{L}}\widetilde{W})^{ij}. \tag{2.144}$$

Thus,

$$\widetilde{D}_j \widetilde{A}_*^{ij} + \widetilde{\Delta}_{\widetilde{\mathbf{L}}}\widetilde{W}^i - \frac{2}{3}\psi^6 \widetilde{D}^i K - 8\pi\psi^{10} j^i = 0. \tag{2.145}$$

Noting the transverse condition, hence $\widetilde{D}_j \widetilde{A}_*^{ij} = 0$, we have,

$$\widetilde{\Delta}_{\widetilde{\mathbf{L}}}\widetilde{W}^i - \frac{2}{3}\psi^6 \widetilde{D}^i K - 8\pi\psi^{10} j^i = 0. \tag{2.146}$$

Consider the following scenario: We are given the conformal metric $\widetilde{\gamma}_{ij}$, the trace of the extrinsic curvature K, and the transverse-traceless component of the conformal extrinsic

[5]

$$\begin{aligned}
\widetilde{\Delta}_{\widetilde{\mathbf{L}}}\widetilde{W}^i &:= \widetilde{D}_j (\widetilde{\mathbf{L}}\widetilde{W})^{ij} \\
&= \widetilde{D}_j \left[\widetilde{D}^i \widetilde{W}^j + \widetilde{D}^j \widetilde{W}^i - \frac{2}{3}\widetilde{\gamma}^{ij} \widetilde{D}_k \widetilde{W}^k \right] \\
&= \widetilde{D}_j \widetilde{D}^i \widetilde{W}^j + \widetilde{D}^2 \widetilde{W}^i - \frac{2}{3}\widetilde{\gamma}^{ij} \widetilde{D}_j \widetilde{D}_k \widetilde{W}^k.
\end{aligned} \tag{2.141}$$

Note that:

$$\widetilde{D}_j \widetilde{D}^i \widetilde{W}^j = \widetilde{D}^i \widetilde{D}_j \widetilde{W}^j + \widetilde{R}^i_j \widetilde{W}^j. \tag{2.142}$$

Thus:

$$\widetilde{\Delta}_{\widetilde{\mathbf{L}}}\widetilde{W}^i = \frac{1}{3}\widetilde{D}^i \widetilde{D}_j \widetilde{W}^j + \widetilde{R}^i_j \widetilde{W}^j + \widetilde{D}^2 \widetilde{W}^i. \tag{2.143}$$

curvature $\widetilde{A}^{ij}_*$. By utilizing the Hamiltonian constraint and momentum constraints, we can determine the conformal factor ψ and the vector $\widetilde{W}^i$. This allows us to reconstruct the physical metric γ_{ij} and the extrinsic curvature K_{ij}. However, an essential consideration remains. While finding a symmetric-tracefree tensor may be straightforward, constructing a transverse tensor presents a more complex challenge [19]. To achieve this, we must begin with an arbitrary symmetric-tracefree tensor M_{ij}, which may not inherently possess transverse properties.

The transverse component of a given tensor can be succinctly represented as follows:

$$\widetilde{M}^{ij}_* = \widetilde{M}^{ij} - (\widetilde{\mathbf{L}}\widetilde{Y})^{ij} \tag{2.147}$$

where the vector $\widetilde{Y}^i$ is yet to be determined. Applying $\widetilde{D}_j$ to the above equation and noting that $\widetilde{M}^{ij}_*$ is transverse (i.e., $\widetilde{D}_j\widetilde{M}^{ij}_* = 0$), we can obtain the following result:

$$\widetilde{\Delta}_{\widetilde{\mathbf{L}}}\widetilde{Y}^i = \widetilde{D}_j\widetilde{M}^{ij}. \tag{2.148}$$

Given $\widetilde{M}^{ij}$, this equation must be solved to find the vector $\widetilde{Y}^i$, which will in turn allow us to construct the transverse tensor $\widetilde{M}^{ij}_*$. The above procedure can in fact be incorporated into the solution of the constraints. Taking $\widetilde{A}^{ij}_* = \widetilde{M}^{ij}_*$ and note that $\widetilde{\mathbf{L}}$ is a linear operator, we obtain

$$\begin{aligned}
\widetilde{A}^{ij} &= \widetilde{A}^{ij}_* + (\widetilde{\mathbf{L}}\widetilde{W})^{ij} \\
&= \widetilde{M}^{ij}_* + (\widetilde{\mathbf{L}}\widetilde{W})^{ij} \\
&= \widetilde{M}^{ij} - (\widetilde{\mathbf{L}}\widetilde{Y})^{ij} + (\widetilde{\mathbf{L}}\widetilde{W})^{ij} \\
&= \widetilde{M}^{ij} + (\widetilde{\mathbf{L}}\widetilde{V})^{ij},
\end{aligned} \tag{2.149}$$

where, $\widetilde{V}^i := \widetilde{W}^i - \widetilde{Y}^i$. It is clear from the above equation that

$$\widetilde{A}^{ij} = \widetilde{M}^{ij}_* + (\widetilde{\mathbf{L}}\widetilde{W})^{ij} = \widetilde{M}^{ij} + (\widetilde{\mathbf{L}}\widetilde{V})^{ij}. \tag{2.150}$$

Utilizing the definition (2.144), we obtain,

$$\begin{aligned}
\widetilde{D}_j(\widetilde{\mathbf{L}}\widetilde{W})^{ij} &= \widetilde{D}_j\widetilde{M}^{ij} + \widetilde{D}_j(\widetilde{\mathbf{L}}\widetilde{V})^{ij} \\
\Rightarrow \widetilde{\Delta}_{\widetilde{\mathbf{L}}}\widetilde{W}^i &= \widetilde{D}_j\widetilde{M}^{ij} + \widetilde{\Delta}_{\widetilde{\mathbf{L}}}\widetilde{V}^i.
\end{aligned} \tag{2.151}$$

Ultimately, we can rewrite the momentum constraints in the following form:

$$D_j\widetilde{M}^{ij} + \widetilde{\Delta}_{\widetilde{\mathbf{L}}}\widetilde{V}^i - \frac{2}{3}\psi^6\widetilde{D}^iK - 8\pi\psi^{10}j^i = 0. \tag{2.152}$$

To solve for ψ and $\widetilde{V}^i$, we employ Equations (2.128) and (2.152), using as free data the conformal metric $\widetilde{\gamma}_{ij}$, a symmetric-tracefree tensor $\widetilde{M}^{ij}$, the trace of the extrinsic curvature K, and the energy and momentum densities $\widetilde{\rho}$ and $\widetilde{j}^i$. The physical quantities are reconstructed accordingly:

$$\begin{aligned} \gamma_{ij} &= \psi^4 \widetilde{\gamma}_{ij}, \\ K^{ij} &= \psi^{-10} \widetilde{A}^{ij} + \frac{1}{3} \gamma^{ij} K, \\ \widetilde{A}^{ij} &= (\widetilde{\mathbf{L}} \widetilde{V})^{ij} + \widetilde{M}^{ij}. \end{aligned} \tag{2.153}$$

The equations we have derived represent the predominant formulation of constraints in the York–Lichnerowicz approach.

2.7 Gauge Conditions

To numerically solve the Einstein field equations, a coordinate system must be selected. In the analytical sense, due to the differential invariance of general relativity, the choice of coordinates is entirely arbitrary, and the coordinates themselves have no intrinsic physical significance. From the perspective of differential manifolds, a spacetime manifold often requires multiple coordinate systems to cover it. The coordinate systems are connected through diffeomorphic transformations in their overlapping regions [231, 144]. At the numerical computation aspect, the impact of coordinate singularities on the stability of numerical calculations is similar to that of physical singularities. Therefore, at the boundaries of the domain of definition of a coordinate system, numerical calculations are not feasible. A natural idea is to switch to another coordinate system through a diffeomorphic transformation before the time evolution reaches the boundary of the coordinate domain. However, two reasons make this impractical in actual operation. One reason is that it is not possible to distinguish between coordinate singularities [6] and physical singularities in numerical calculations. Therefore, it is not possible to predict when one is approaching the boundary of the coordinate domain. The second reason is that the results of numerical calculations are discrete. It is difficult to calculate the Jacobian matrix required for the diffeomorphic transformation based on discrete metric functions [64].

In terms of the choice of coordinates, the current approach taken by numerical relativists is to use a coordinate system that covers the spacetime region of physical interest as much as possible. Taking the problem of binary black hole merger as an example, the spacetime region of physical interest includes the space outside the black hole's apparent horizon and the time range from the inspiral to the basic end of the ringdown. But the actual problem is how to set coordinate conditions so that the corresponding coordinates can cover the entire aforementioned spacetime region [19, 223]. In this section, we will introduce several slicing and gauge conditions.

[6] The first manifestation of a coordinate singularity is the divergence of coordinate values. The second manifestation is the tangency of coordinate lines of different dimensions. The third manifestation is the intersection of coordinate lines of the same dimension.

Assuming at a coordinate singularity the x^1 coordinate diverges, then the other $\left(\frac{\partial}{\partial x^\mu}\right)^a, \mu \neq 1$ at that point become zero, and thus can no longer serve as a coordinate basis. If at the coordinate singularity the x^1 and x^2 coordinate lines are tangent, then $\left(\frac{\partial}{\partial x^1}\right)^a$ and $\left(\frac{\partial}{\partial x^2}\right)^a$ are parallel, i.e., linearly related, and therefore can no longer serve as a coordinate basis. If at the coordinate singularity two x^1 coordinate lines intersect, then the $\left(\frac{\partial}{\partial x^1}\right)^a$ at that point cannot be determined, thus making the coordinate basis nonexistent.

Geodesic Slicing

The simplest coordinate choice is $\alpha = 1, \beta^i = 0$. In this case, we have ${\Gamma^\mu}_{00} = 0$ and $a_\mu = D_\mu \ln \alpha = 0$, indicating that the time coordinate lines are exactly geodesics. Therefore, this coordinate choice is referred to as **Geodesic Coordinates**, or **Gaussian Normal Coordinates**, and it was, in fact, used in the pioneering work of Hahn and Lindquist in the mid-1960s [106].

Under the geodesic coordinate system, the evolution equations give us

$$\begin{aligned} &\partial_t K = -D^2\alpha + \alpha\left(K_{ij}K^{ij} + 4\pi(\rho + S)\right) + \beta^i D_i K = K_{ij}K^{ij} + 4\pi(\rho + S) \geq 0, \\ &\partial_t \ln\sqrt{\gamma} = -\alpha K + D_i\beta^i = -K \leq 0. \end{aligned} \tag{2.154}$$

This means that the volume of the coordinate element monotonically decreases over time. Physically, this is because the time coordinate lines correspond to geodesics, which under the influence of gravity, approach each other over time and eventually collide. This forms what we previously discussed as the second type of coordinate singularity. For a spherical star or black hole, all spatial coordinates converge towards the center.

Maximal Slicing

Based on the experience of the above coordinate selection, we intuitively require that the time coordinate lines maintain a fixed distance, that is, the volume of the coordinate unit does not change over time. Based on this idea, a coordinate choice with $K = 0$ has been proposed. In Riemannian geometry, a Riemannian surface with $K = 0$ is the surface with the maximum volume among surfaces with the same area. Therefore, such a coordinate choice is referred to as the **Maximal Slicing Coordinate**.

The maximal slicing condition is expressed as

$$K = 0. \tag{2.155}$$

Utilizing Equation (2.66), we obtain

$$D^2\alpha = -\partial_t K + \alpha[K_{ij}K^{ij} + 4\pi(\rho + S)] + \beta^i D_i K. \tag{2.156}$$

Considering maximal slicing coordinate $K = 0$ and $\partial_t K = 0$, we obtain an elliptic equation:

$$D^2\alpha = \alpha[K_{ij}K^{ij} + 4\pi(\rho + S)]. \tag{2.157}$$

Utilizing the decomposition method of the extrinsic curvature that we previously discussed, i.e.,

$$K_{ij}K^{ij} = \widetilde{A}_{ij}\widetilde{A}^{ij} + \frac{1}{3}K^2 = \widetilde{A}_{ij}\widetilde{A}^{ij}, \tag{2.158}$$

we arrive at the final expression:

$$D^2\alpha = \alpha[\widetilde{A}_{ij}\widetilde{A}^{ij} + 4\pi(\rho + S)]. \tag{2.159}$$

Maximal slicing was originally proposed by Lichnerowicz [145] and was discussed in the classic papers of Smarr and York [211]. Over the years, it has been employed in numerous numerical simulations across various systems, including black holes, and remains in use today. Maximal slicing offers several advantageous properties, most notably its singularity-avoidance feature. For instance, maximal slices in Schwarzschild spacetime successfully circumvent the spacetime singularity at the areal radius $R = 0$. In areas where gravitational fields are strong, the maximal-slicing condition causes the lapse function to approach near-zero values — a phenomenon known as the lapse's collapse. As a result, slices are effectively "***held back***" from advancing in proper time within these regions, even while coordinate time $t \to \infty$. However, this approach has drawbacks, including the issue of grid stretching. Near a black hole, for example, metric coefficients can exhibit variations across numerous orders of magnitude, complicating the task of adequately resolving these regions with a sufficient number of grid points in numerical simulations.

Harmonic Slicing

Harmonic coordinate conditions possess the significant property of enabling the Einstein field equations to be expressed as a series of wave equations, with nonlinear source terms, for the metric coefficients $g_{\mu\nu}$. Consequently, these conditions have been widely used in analytical studies of the properties of the Einstein equations.

The harmonic coordinates condition is formulated as

$$\Box_g x^\sigma = g^{\mu\nu}\nabla_\mu\nabla_\nu x^\sigma = 0. \tag{2.160}$$

Here we will consider a variation of this condition, called **Harmonic Slicing**, in which we set to zero for $\sigma = 0$ component ($x^0 = t$),

$$\Box_g t \equiv \nabla_\mu\nabla^\mu t = 0. \tag{2.161}$$

Utilizing

$$\nabla_\mu v^\mu = \frac{1}{\sqrt{|g|}}\frac{\partial}{\partial x^\mu}\left(\sqrt{|g|}v^\mu\right), \tag{2.162}$$

we obtain

$$\frac{1}{\sqrt{-g}}\partial_\mu(\sqrt{-g}g^{\mu\nu}\partial_\nu t)=0. \tag{2.163}$$

Note that $g^{\mu\nu}\partial_\nu t = g^{\mu t}$ and $\sqrt{-g}=\alpha\sqrt{\gamma}$,

$$\partial_t(\alpha\sqrt{\gamma}g^{tt})+\partial_i(\alpha\sqrt{\gamma}g^{it})=0. \tag{2.164}$$

Given that $g^{tt}=-\frac{1}{\alpha^2}$ and $g^{it}=\frac{\beta^i}{\alpha^2}$, and multiplying both sides of Equation(2.164) by $\frac{\alpha^2}{\sqrt{\gamma}}$, we obtain

$$\partial_t\alpha-\beta^i\partial_i\alpha-\alpha[\frac{1}{\sqrt{\gamma}}\partial_t\sqrt{\gamma}-\frac{1}{\sqrt{\gamma}}\partial_i(\beta^i\sqrt{\gamma})]=0. \tag{2.165}$$

The expression inside the square brackets in the equation above is equal to $-\alpha K$, i.e. [7],

$$\frac{1}{\sqrt{\gamma}}\partial_t\sqrt{\gamma}-\frac{1}{\sqrt{\gamma}}\partial_i(\beta^i\sqrt{\gamma})=-\alpha K. \tag{2.166}$$

Thus, (2.165) yields an evolution equation for α under the harmonic slicing condition:

$$(\partial_t-\beta^i\partial_i)\alpha=-\alpha^2K. \tag{2.167}$$

The harmonic slicing condition facilitates a significantly more stable numerical evolution than geodesic slicing. It avoids focusing coordinate observers and, in some instances, permits extended time evolutions. However, it is important to note that harmonic slicing does not universally ensure well-behaved coordinates in more complex scenarios. Additionally, it has been observed that the singularity avoidance capabilities of harmonic slicing are ***less*** effective compared to those of maximal slicing.

[7] Using γ^{ij} on Equation (2.43), we obtain:

$$\gamma^{ij}(\partial_t\gamma_{ij})=\gamma^{ij}(-2\alpha K_{ij}+D_i\beta_j+D_j\beta_i),$$

$$\partial_t\ln\gamma=-2\alpha K+2D_i\beta^i,$$

$$\frac{1}{\sqrt{\gamma}}\partial_t\sqrt{\gamma}=-\alpha K+D_i\beta^i,$$

$$\frac{1}{\sqrt{\gamma}}\partial_t\sqrt{\gamma}=-\alpha K+\frac{1}{\sqrt{\gamma}}\partial_i(\beta^i\sqrt{\gamma}).$$

1+log Slicing

The harmonic slicing condition can be generalized to the form:

$$(\partial_t - \beta^i \partial_i)\alpha = -\alpha^2 f(\alpha) K, \quad f(\alpha) > 0, \tag{2.168}$$

where $f(\alpha)$ is an arbitrary function, known as the **Bona-Masso Condition** [49]. Considering the case where $\beta^i = 0$, and using the relationship between K and $\sqrt{\gamma}$, i.e.,

$$\frac{1}{\sqrt{\gamma}}\partial_t \sqrt{\gamma} = -\alpha K + \frac{1}{\sqrt{\gamma}}\partial_i(\beta^i \sqrt{\gamma}), \tag{2.169}$$

the Bona-Masso condition can be rewritten as:

$$\partial_t \ln \sqrt{\gamma} = \frac{\partial_t \alpha}{\alpha f(\alpha)}. \tag{2.170}$$

We now consider the behavior of the lapse function as the volume elements $\gamma^{1/2}$ approach zero. One scenario is for the lapse α to remain finite as $\gamma^{1/2}$ vanishes, indicating that coordinate time remains finite at the singularity, thereby not avoiding the singularity.

Given that the lapse cannot remain finite at a singularity, we are left with two alternatives: Either the lapse becomes zero at the singularity or it becomes zero before reaching the singularity. The latter case implies that the time slices will cease progressing a finite coordinate time before encountering the singularity, a phenomenon we refer to as strong singularity avoidance. Conversely, if the lapse becomes zero precisely at the singularity, the integrated coordinate time could be either finite or infinite, depending on how rapidly α approaches zero. We define a slicing as marginally singularity avoiding if the singularity is reached only after an infinite amount of coordinate time.

To determine the conditions under which strong or marginal singularity avoidance can occur, we need to examine the behavior of the function $f(\alpha)$ as we approach the singularity. For this analysis, we assume that as α approaches zero, the function $f(\alpha)$ follows a power law:

$$f(\alpha) = A\alpha^n \tag{2.171}$$

where $A > 0$ and n are constants.

For $n = 0$,

$$\int \frac{\partial_t \alpha}{\alpha f(\alpha)} = \ln \alpha^{1/A}. \tag{2.172}$$

This implies the following relationship:

$$\sqrt{\gamma} \sim \alpha^{1/A} \Rightarrow \alpha \sim \gamma^{A/2}. \tag{2.173}$$

It becomes evident that, in this case, both α and $\gamma^{1/2}$ vanish simultaneously.

For $n \neq 0$,

$$\int \frac{\partial_t \alpha}{\alpha f(\alpha)} = -\frac{1}{nA\alpha^n}. \tag{2.174}$$

This leads to the expression:

$$\gamma^{1/2} \sim \exp\left(-\frac{1}{nA\alpha^n}\right). \tag{2.175}$$

From this, we can infer that for $n < 0$, the volume elements remain finite as the lapse approaches zero, indicating strong singularity avoidance for this scenario. Notably, the $1+\log$ family of slicing conditions $f(\alpha) = N/\alpha$ corresponds to $n = -1$, suggesting that it is singularity avoiding in a strong sense. This explains its practical resemblance to maximal slicing. Conversely, if $n > 0$, both the lapse and the volume elements vanish simultaneously, implying that at best, we can achieve only marginal singularity avoidance.

The precise implementation of the $1+\log$ slicing condition in our work is achieved by selecting $f(\alpha) = \frac{2}{\alpha}$, as demonstrated in

$$(\partial_t - \beta^i \partial_i)\alpha = -2\alpha K. \tag{2.176}$$

Applying (2.166) and setting $\beta^i = 0$, the equation simplifies to

$$\partial_t \alpha = \partial_t \ln \gamma. \tag{2.177}$$

Integrating (2.177) yields

$$\alpha = \ln \gamma + C, \tag{2.178}$$

where C is an integration constant. By setting $C = 1$, we obtain

$$\alpha = 1 + \ln \gamma. \tag{2.179}$$

The **1+log Slicing**, as an **Algebraic Slicing Condition** [223], possesses the advantages of being exceptionally simple to implement and rapid to solve. Additionally, it has been demonstrated to exhibit ***stronger*** singularity avoidance properties compared to harmonic slicing.

Minimal Distortion Shift Condition

The distortion tensor, denoted as Σ_{ij}, is formally defined by the equation:

$$\Sigma_{ij} \equiv \partial_t \gamma_{ij} - \frac{1}{3}(\gamma^{kl}\partial_t \gamma_{kl})\gamma_{ij}. \tag{2.180}$$

This tensor specifically quantifies the shear change in volume elements.

We will now proceed to decompose the tensor into two distinct components: a ***longitudinal*** part and a ***transverse-traceless (TT)*** part.

$$\Sigma_{ij} = (LX)_{ij} + \Sigma_{ij}^{TT}, \tag{2.181}$$

where Σ_{ij}^{TT} represents the transverse-traceless component, satisfying $D^j\Sigma_{ij}^{TT} = 0$, and

$$(LX)_{ij} \equiv D_i X_j + D_j X_i - \frac{2}{3} D_k X^k \gamma_{ij}. \tag{2.182}$$

The vector field X is intrinsically linked to the divergence of the tensor Σ_{ij}, as expressed by the equation $D^j(LX)_{ij} = D^j\Sigma_{ij}$. This connection allows for the interpretation of the transverse-traceless (TT) part as being directly associated with the dynamics of the gravitational field. Conversely, the longitudinal part, attributable to the variation in the metric tensor γ_{ij}, emerges due to coordinate changes from the hypersurface Σ_t to $\Sigma_{t+\delta t}$.

This longitudinal component encapsulates three degrees of freedom, represented by the three components of the vector X. By employing a strategic choice of coordinates, denoted as $\left(x^i\right)$, it is possible to set this longitudinal part to zero. A coordinate system in which the condition $X = 0$ is satisfied is referred to as **Minimal Distortion Coordinates**, a concept introduced by Smarr and York in 1978 [211, 212].

By imposing the condition $X = 0$, we arrive at the following significant result:

$$D^j\Sigma_{ij} = 0. \tag{2.183}$$

A straightforward computation yields:

$$\begin{aligned}
\Sigma_{ij} &\equiv \partial_t \gamma_{ij} - \frac{1}{3}(\gamma^{kl}\partial_t \gamma_{kl})\gamma_{ij} \\
&= (-2\alpha K_{ij} + D_i\beta_j + D_j\beta_i) - \frac{2}{3}(D_k\beta^k - \alpha K)\gamma_{ij} \\
&= -2\alpha(A_{ij} + \frac{1}{3}K\gamma_{ij}) + D_i\beta_j + D_j\beta_i - \frac{2}{3}(D_k\beta^k - \alpha K)\gamma_{ij} \\
&= -2\alpha A_{ij} + (L\beta)_{ij}
\end{aligned}$$

which implies:

$$\Sigma^{ij} = -2\alpha A^{ij} + (L\beta)^{ij}. \tag{2.184}$$

Combining Equations (2.183) and (2.184), we derive:

$$-2\alpha D_j A^{ij} - 2A^{ij} D_j \alpha + D_j (L\beta)^{ij} = 0. \tag{2.185}$$

Considering the momentum constraint:

$$D_j(K^{ij} - \gamma^{ij}K) = 8\pi j^i,$$

$$D_j(A^{ij} + \frac{1}{3}K\gamma^{ij} - \gamma^{ij}K) = 8\pi j^i,$$

$$D_j A^{ij} = 8\pi j^i + \frac{2}{3}D^i K,$$

and

$$D_j(L\beta)^{ij} = D_j D^j \beta^i + \frac{1}{3}D^i D_j \beta^j + R^i{}_j \beta^j, \tag{2.186}$$

we ultimately obtain:

$$D_j D^j \beta^i + \frac{1}{3}D^i D_j \beta^j + R^i{}_j \beta^j = 16\pi\alpha j^i + \frac{4}{3}\alpha D^i K + 2A^{ij} D_j \alpha. \tag{2.187}$$

This represents the elliptic equation governing the shift vector, which must be solved to ensure the enforcement of minimal distortion.

Moving Puncture Gauge

Elevating the shift vector β^i to the status of an evolution variable offers a more computationally efficient approach than solving a set of elliptic partial differential equations (PDEs). A common strategy is to transform the elliptic PDEs governing β^i into hyperbolic equations. This is achieved by adding a second-order time derivative term $\partial_t^2 \beta^i$ and an artificial damping term, parameterized by η. Consequently, this modified equation takes the form of a damped wave equation, which is designed to eliminate any component of β^i that fails to satisfy $D^j \Sigma_{ij} = 0$. Here, we introduce an effective approach known as the **Gamma-Driver** [24].

Here, we adopt the form from [182],

$$\begin{aligned} \partial_t \beta^i &= b_1 \beta^k \partial_k \beta^i + b_2 B^i, \\ \partial_t B^i &= b_1 \left(\beta^k \partial_k B^i - \beta^k \partial_k \tilde{\Gamma}^i \right) + \partial_t \tilde{\Gamma}^i - \eta B^i, \end{aligned} \tag{2.188}$$

where B^i represents an auxiliary vector field and b_1, b_2 and η are specifiable parameters. For the CCZ4 formalism the $\tilde{\Gamma}^i$ should be replaced by $\hat{\Gamma}^i$.

Next, we will discuss the choice of parameters.

For b_1

For the advection parameter, setting $b_1 = 0$ disables the advection terms, resulting in a non-shifting shift, while $b_1 = 1$ includes them, leading to a shifting shift. A linear mode analysis comparing different variants of the Gamma driver shift condition was conducted by van Meter, Baker, Koppitz, and Choi [227], who found that $b_1 = 1$ was the better option. However, in practice, there is little difference between the variants, so we typically choose $b_1 = 1$.

For b_2

For b_2, the conventional choice is $b_2 = 3/4$, which appears to originate from [24], as this value makes the longitudinal speed of the shift equal to the speed of light when $\alpha = 1$. In the Z4 formulation [25] notes that $b_2 = 3/4$ can lead to weak hyperbolicity when $\alpha \sim 1$; thus, [38] suggests using $b_2 = 1$. However, $b_2 = 3/4$ generally works well in practice for CCZ4, and this is the value we will use.

For η

Examining the form in Equation (2.188), we see that the final term acts as a damping term, meaning that η controls the decay timescale. Dimensional analysis reveals that $[\eta] = L^{-1}$. Typically, for a spacetime with ADM mass M, we choose $\eta \sim 1/M$. However, in some scenarios, such as black hole binaries with small mass ratios, it can be advantageous to allow η to vary in space and time [185]. After the gauge has settled, the coordinate size of the black hole horizon tends to increase as η increases, as shown in [60]. Empirically, for

comparable mass black-hole binaries, simulations are reasonably robust against variations in η within an order of magnitude. However, if η is chosen too small, much less than $1/M$, the simulation can become unstable. Conversely, if η is too large, much greater than $1/M$, slice-stretching effects can occur.

In numerous numerical simulations, the combination of the 1+log slicing condition for the lapse and a Gamma-driver condition for the shift has been extensively employed. This setup, commonly referred to as the **Moving-Puncture Gauge**, is highly favored for its remarkable effectiveness.

In 2006, the moving puncture gauge enabled the first successful simulation of a black-hole binary [63] in the BSSN formalism without the use of excision. In 2012, the first simulations of black-hole binaries using constraint damping schemes in the moving puncture gauge, such as CCZ4 [25] and Z4c [115], were achieved. We have also adopted this method in our forthcoming research focused on boson stars.

Chapter 3

Overview of Boson Stars

3.1 Introduction

The idea of bosonic stars dates back to Wheeler's 1955 study of gravitational-electromagnetic entities or **Geons** [233]. By generalising from real to complex-valued fundamental fields, it is even possible to obtain genuinely stationary solutions to the Einstein-matter equations. First established for spin 0 or scalar fields [89, 129, 189], this idea has more recently been extended to spin 1 or vector (aka **Proca** [1]) fields [56] as well as wider classes of scalar boson stars [21, 67]. In the wake of the dramatic progress of numerical relativity in the simulations of black holes [179, 63, 33] (see [214] for a review), the modelling of boson stars and binary systems involving boson stars has rapidly gathered pace.

The first boson star models computed in the 1960s consisted of a massive but non-interacting complex scalar field φ. This class of stationary boson stars, commonly referred to as **Mini-Boson Stars**, consists of a one parameter family of ground-state solutions characterised by the central scalar-field amplitude that reveals a stability structure analogous to that of Tolman-Oppenheimer-Volkoff [224, 167] stars: a stable and an unstable branch of ground-state solutions are separated by the configuration with maximal mass [54, 98, 196]. For each ground-state model, there furthermore exists a countable hierarchy of excited states with $n > 0$ nodes in the scalar profile [140, 124, 147]. Numerical evolutions of these excited boson stars demonstrate their unstable character, but also reveal significant variation in the instability time scales [34].

Whereas mini-boson star models are limited in terms of their maximum compactness, self-interacting scalar fields can result in significantly more compact stars, even denser than neutron stars [72, 138, 195, 108]. This raises the intriguing question whether com-

[1] Even though the term boson star generally applies to compact objects formed of any bosonic fields, it is often used to specifically denote stars made up of a **Scalar** field. Stars composed of vector fields, in contrast, are most commonly referred to as **Proca** stars. Unless specified otherwise, we shall accordingly assume the term boson star to imply scalar-field matter.

pact boson star binaries may reveal themselves through characteristic gravitational wave emission analogous to that from black holes or neutron stars [62]. Recent studies conclude that this may well be within the grasp of next-generation gravitational wave detectors and, in the case of favourable events, even with advanced LIGO [200, 82, 225].

3.2 Formalism

The boson stars under consideration consist of a complex Klein-Gordon scalar field, denoted as φ, which is minimally coupled to gravity. The associated action combines the Einstein-Hilbert action for the vacuum and the matter action in curved spacetime:

$$S = \int_M [\mathscr{L}_{EH} + \mathscr{L}_M] \sqrt{-g}\, d^4x, \tag{3.1}$$

where

$$\mathscr{L}_{EH} = \frac{c^4}{16\pi G} R \tag{3.2}$$

represents the Einstein-Hilbert vacuum action, and

$$\mathscr{L}_M = -\frac{1}{2} g^{\mu\nu} \nabla_\mu \bar{\varphi} \nabla_\nu \varphi - \frac{1}{2} V(|\varphi|^2) \tag{3.3}$$

is the matter action. Here, $\bar{\varphi}$ denotes the complex conjugate of the complex scalar field φ, and $V(|\varphi|^2)$ is the potential, which depends solely on the magnitude of the scalar field, reflecting the $U(1)$ symmetry of the field in the complex plane.

Varying the action with respect to the metric and the scalar field yields the Einstein field equations and the Klein-Gordon equation in curved spacetime, respectively.

$$R_{\mu\nu} - \frac{1}{2} R g_{\mu\nu} = \frac{8\pi G}{c^4} T_{\mu\nu}, \tag{3.4}$$

$$g^{\mu\nu} \nabla_\mu \nabla_\nu \varphi = \frac{\partial V}{\partial |\varphi|^2} \varphi, \tag{3.5}$$

where

$$T_{\mu\nu} = \frac{1}{2} \nabla_\mu \bar{\varphi} \nabla_\nu \varphi + \frac{1}{2} \nabla_\nu \bar{\varphi} \nabla_\mu \varphi - \frac{1}{2} g_{\mu\nu} \left[g^{\alpha\beta} \nabla_\alpha \bar{\varphi} \nabla_\beta \varphi + V \right]. \tag{3.6}$$

By applying $g^{\mu\nu}$ to equation (3.4), the following formula can be derived:

$$R_{\mu\nu} = 8\pi G \left(T_{\mu\nu} - \frac{1}{2} g_{\mu\nu} T \right) \tag{3.7}$$

where $T \equiv g^{\mu\nu} T_{\mu\nu}$.

In BSSN/CCZ4 formalism, the corresponding ρ, j_α, $S_{\alpha\beta}$ are:

$$\rho = T_{\mu\nu} n^\mu n^\nu, \quad j_\alpha = -\gamma^\nu{}_\alpha T_{\mu\nu} n^\mu, \quad S_{\alpha\beta} = \gamma^\mu{}_\alpha \gamma^\nu{}_\beta T_{\mu\nu}, \quad \gamma^\mu{}_\alpha = \delta^\mu{}_\alpha + n^\mu n_\alpha. \tag{3.8}$$

Defining, in analogy to the extrinsic curvature,

$$\Pi = -\frac{1}{2\alpha} (\partial_t \varphi - \beta^m \partial_m \varphi) \quad \Leftrightarrow \quad \partial_t \varphi = \beta^m \partial_m \varphi - 2\alpha \Pi, \tag{3.9}$$

we obtain

$$\rho = 2\Pi\bar{\Pi} + \frac{1}{2}\partial^m\bar{\varphi}\,\partial_m\varphi + \frac{1}{2}V\,, \quad S + \rho = 8\bar{\Pi}\Pi - V\,,$$

$$j_i = \bar{\Pi}\partial_i\varphi + \Pi\partial_i\bar{\varphi}\,,$$

$$S_{ij} = \partial_{(i}\bar{\varphi}\partial_{j)}\varphi - \frac{1}{2}\gamma_{ij}\left(\gamma^{mn}\partial_m\bar{\varphi}\,\partial_n\varphi - 4\bar{\Pi}\Pi + V\right).$$

The evolution of the scalar field according to Equation (3.5) in terms of our 3+1 variables is given by Equation (3.9) and

$$\partial_t\Pi = \beta^m\partial_m\Pi + \alpha\left[\Pi K + \frac{1}{2}V'\varphi + \frac{1}{4}\tilde{\gamma}^{mn}\left(\partial_m\varphi\partial_n\chi - 2\chi\tilde{D}_m\tilde{D}_n\varphi\right)\right] - \frac{1}{2}\chi\tilde{\gamma}^{mn}\partial_m\varphi\partial_n\alpha\,, \tag{3.10}$$

where $V' = \mathrm{d}V/\mathrm{d}\left(|\varphi|^2\right)$.

Finally, we evolve the gauge variables α and β^i using the 1+log slicing and the Γ-driver condition, commonly known as the moving puncture conditions,

$$\partial_t\alpha = \beta^m\partial_m\alpha - 2\alpha K\,, \quad \partial_t\beta^i = \beta^m\partial_m\beta^i + \frac{3}{4}B^i\,, \quad \partial_t B^i = \beta^m\partial_m B^i + \partial_t\tilde{\Gamma}^i - \eta B^i\,, \tag{3.11}$$

where η is a constant we typically set to $M\eta \approx 1$ in units of the ADM mass M.

Additionally to the BSSN/CCZ4 evolution equations, the Einstein equations also imply four equations that do not contain time derivatives, the Hamiltonian and momentum constraints. While the constraints are preserved under time evolution in the continuum limit, some level of violations is inevitable due to numerical noise or imperfections of the initial data.

3.3 Mini-Boson Stars

The potential for **Mini-Boson Stars** is given by

$$V_{\min} = \mu^2 |\varphi|^2 \,, \tag{3.12}$$

where μ denotes the mass of the scalar field.

The initial data for our time evolution are based on single stationary boson star solutions in spherical symmetry. Using spherical polar coordinates, areal radius and polar slicing, the line element can be written as

$$\mathrm{d}s^2 = -e^{2\Phi}\mathrm{d}t^2 + \left(1 - \frac{2m}{r}\right)^{-1} \mathrm{d}r^2 + r^2 \left(\mathrm{d}\theta^2 + \sin^2\theta \mathrm{d}\phi^2\right) \tag{3.13}$$

where Φ and m are functions of r only. It turns out convenient to express the complex scalar field in terms of amplitude and frequency,

$$\varphi(t,r) = A(r)e^{\mathrm{i}\omega t}, \tag{3.14}$$

where $\omega = \mathrm{const} \in \mathbb{R}$.

At this point, our configurations are characterised by two scales, the scalar mass μ and the gravitational constant[2] G. In the following, we absorb μ and G by rescaling all dimensional variables according to

$$\hat{t} = \mu t \,, \quad \hat{r} = \mu r \,, \quad \hat{m} = \mu m \,, \quad \hat{A} = \sqrt{G} A \,, \quad \hat{\omega} = \omega/\mu \,; \tag{3.15}$$

note that μ has the dimension of a frequency or wave number and $\sqrt{G}$ is an inverse mass. Using the Planck mass $M_{\mathrm{Pl}} = 1/\sqrt{G} = 1.221 \times 10^{19}\,\mathrm{GeV}$, we can restore SI units from the dimensionless numerical variables according to

$$r = \hat{r} \times \left(\frac{\mu}{1.937 \times 10^{-10}\,\mathrm{eV}}\right)^{-1} \mathrm{km} \,, \quad \omega = \hat{\omega} \times \frac{\mu}{6.582 \times 10^{-16}\,\mathrm{eV}}\,\mathrm{Hz} \,, \quad A = \hat{A} M_{\mathrm{Pl}} \,,$$

and likewise for other variables. The rescaled version of the potential (3.12) is given by $\hat{V}_{\min} = \hat{A}^2$. Next, we aim to reduce these equations to a first-order system by introducing

$$\hat{\eta} \equiv \left(1 - \frac{2\hat{m}}{\hat{r}}\right)^{1/2} \partial_{\hat{r}} \hat{A}. \tag{3.16}$$

[2] Or, equivalently, the Planck mass $M_{\mathrm{Pl}} = \sqrt{\hbar c/G} = 1/\sqrt{G}$ for $\hbar = c = 1$.

In terms of the rescaled variables, the Einstein-Klein-Gordon equations in spherical symmetry become

$$\begin{aligned}
\partial_{\hat{r}}\Phi &= \frac{\hat{m}}{\hat{r}(\hat{r}-2\hat{m})} + 2\pi\hat{r}\left(\hat{\eta}^2 + \hat{\omega}^2 e^{-2\Phi}\hat{A}^2 - \hat{V}\right), \\
\partial_{\hat{r}}\hat{m} &= 2\pi\hat{r}^2\left(\hat{\eta}^2 + \hat{\omega}^2 e^{-2\Phi}\hat{A}^2 + \hat{V}\right), \\
\partial_{\hat{r}}\hat{A} &= \left(1 - \frac{2\hat{m}}{\hat{r}}\right)^{-1/2}\hat{\eta}, \\
\partial_{\hat{r}}\hat{\eta} &= -2\frac{\hat{\eta}}{\hat{r}} - \hat{\eta}\,\partial_{\hat{r}}\Phi + \left(1 - \frac{2\hat{m}}{\hat{r}}\right)^{-1/2}\left(\hat{V}' - \hat{\omega}^2 e^{-2\Phi}\right)\hat{A} \quad \text{with } \hat{V}' = \frac{\mathrm{d}\hat{V}}{\mathrm{d}(\hat{A})^2}.
\end{aligned} \tag{3.17}$$

By regularity, we have the following boundary conditions at the origin $\hat{r} = 0$ and at infinity,

$$\hat{A}(0) = \hat{A}_{\mathrm{ctr}} \in \mathbb{R}^+, \quad \hat{m}(0) = 0, \quad \hat{\eta}(0) = 0, \quad \Phi(\infty) = 0, \quad \hat{A}(\infty) = 0. \tag{3.18}$$

This two-point-boundary-value problem has two free parameters, the central amplitude $\hat{A}_{\mathrm{ctr}}$ and the frequency $\hat{\omega}$. For a given value $\hat{A}_{\mathrm{ctr}}$, however, only a discrete (albeit infinite) number of frequency values $\hat{\omega}$ will result in models with $\hat{A}(\infty) = 0$; all other frequencies lead to an exponentially divergent scalar field as $r \to \infty$. We obtain these solutions through a shooting algorithm, starting with the integration of Equations (3.17) outwards for $\hat{A}(0) = \hat{A}_{\mathrm{ctr}}$ specified, $\Phi(0) = 1$, and our *initial guess* $\hat{\omega} = 1$ [113].

Unlike other celestial bodies with well-defined boundaries, a boson star does not have a clear boundary. Therefore, it is necessary to define a mass and radius for a boson star.

In this thesis, we define the radius of a boson star using the areal radius $\hat{r}_{99}$, which contains 99% of the ADM mass. The 99% ADM mass contained within this radius is defined as the mass of the boson star. Using the radius and mass, we can further define the compactness as follows:

$$C \equiv \frac{GM}{R}. \tag{3.19}$$

Figures 3.1 and 3.2 present numerical solutions for mini-boson stars. In Figure 3.1, the x-axis represents the central amplitude, and the y-axis represents the mass, with the maximum mass reaching approximately $0.633\ M_{\mathrm{Pl}}^2 m^{-1}$ at a central amplitude of around $0.075\ M_{\mathrm{Pl}}$. In Figure 3.2, the x-axis denotes the radius, and the y-axis denotes the mass, showing a maximum mass of about $0.633\ M_{\mathrm{Pl}}^2 m^{-1}$ at a radius of approximately $7.953\ m^{-1}$.

We will further demonstrate that when the σ value of a soliton is large, the results tend to converge with those of mini-boson stars.

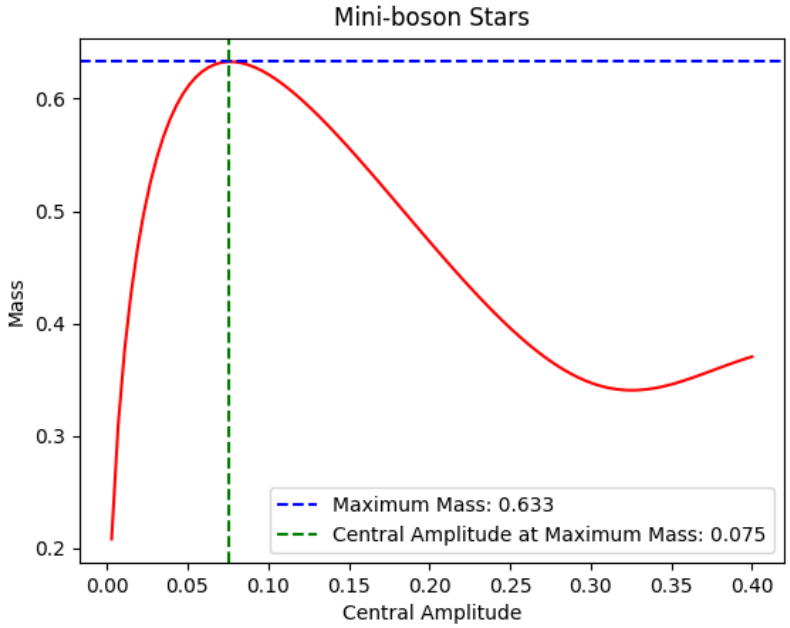

Fig. 3.1 This graph shows the numerical solution for mini-boson stars. In the graph, the x-axis represents the central amplitude and the y-axis represents mass. According to the results, the maximum mass is about 0.633 $M_{\mathrm{Pl}}^2 m^{-1}$, occurring at a central amplitude of approximately 0.075 M_{Pl}.

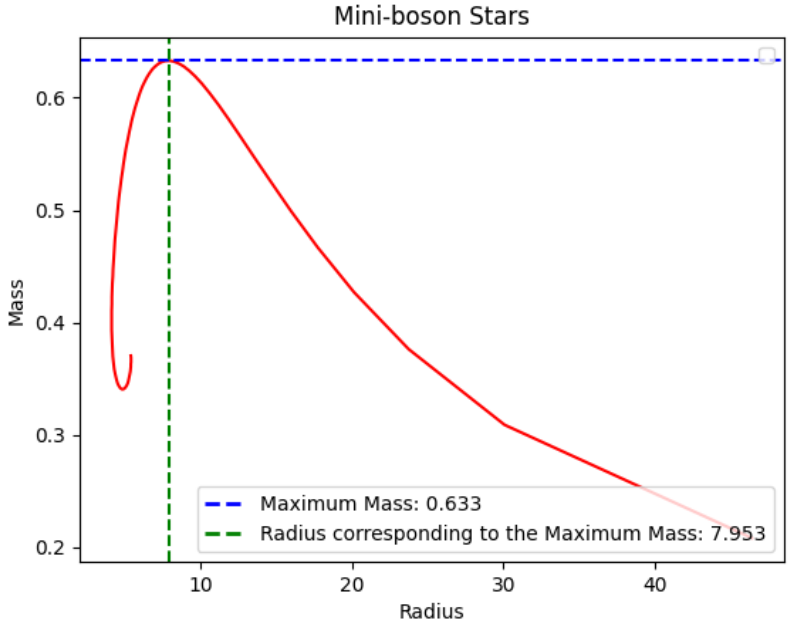

Fig. 3.2 This diagram represents the numerical solution for mini-boson stars. In the diagram, the x-axis indicates the radius, and the y-axis indicates mass. The results show that the maximum mass is approximately 0.633 $M_{\mathrm{Pl}}^2 m^{-1}$, corresponding to a radius of about 7.953 m^{-1}.

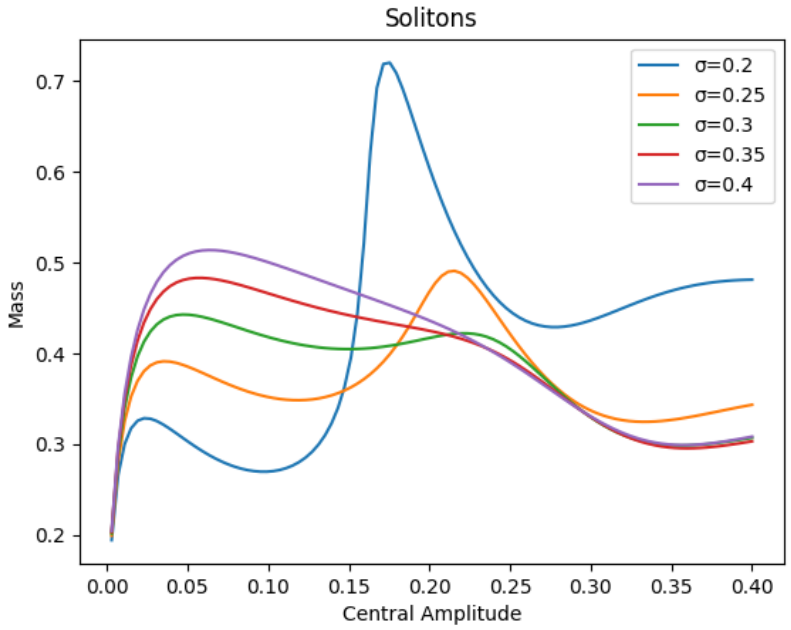

Fig. 3.3 This diagram illustrates the relationship between the mass of solitons and their central amplitude. There are five curves representing different values of $\sigma/M_{\rm Pl}$: 0.20 (blue), 0.25 (orange), 0.30 (green), 0.35 (red), and 0.40 (purple).

3.4 Solitonic Boson Stars

Solitonic Boson Stars (Solitons) represent solutions in the presence of gravity with the potential given by

$$V_{\rm sol} = \mu^2|\varphi|^2\left(1-2\frac{|\varphi|^2}{\sigma^2}\right)^2. \tag{3.20}$$

Here, μ denotes the mass of the scalar field, and σ describes the self-interaction in the solitonic potential, which can result in highly compact stars [138]. Note that $V_{\rm sol} \to V_{\rm min}$ in the limit $\sigma \to \infty$. Using the methods mentioned above, we can obtain a numerical solution for solitonic boson stars.

We begin by focusing on the ***low*** σ case [3], where $\sigma/M_{\rm Pl} \leq 0.4$. Figure 3.3 shows the relationship between the central amplitude (x-axis) and the mass (y-axis) of solitons. The range of central amplitude goes from 0.01 $M_{\rm Pl}$ to 0.40 $M_{\rm Pl}$. The figure displays five distinct curves, each representing solitons with different σ values, distinguished by colors. Furthermore, each curve exhibits unique behavior, suggesting that the mass of solitons changes non-linearly with their central amplitude and this variation depends on the σ value. Typically, the curves show that for a given σ, as the central amplitude increases, the mass of the soliton initially increases to a peak and then decreases, with peak masses varying

[3] σ is measured in units of $M_{\rm Pl}$.

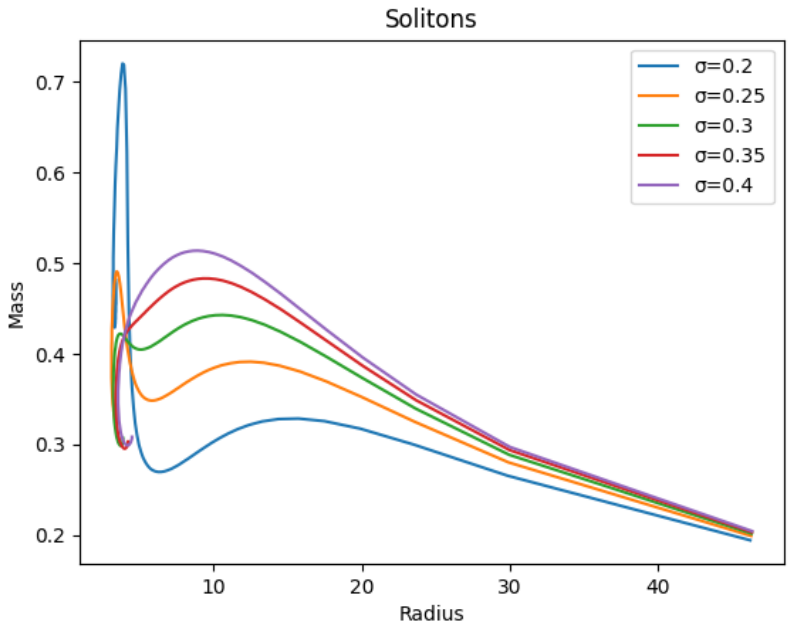

Fig. 3.4 The graph depicts the relationship between the mass of solitons and their radius R. There are five curves representing different values of $\sigma/M_{\rm Pl}$: 0.20 (blue), 0.25 (orange), 0.30 (green), 0.35 (red), and 0.40 (purple).

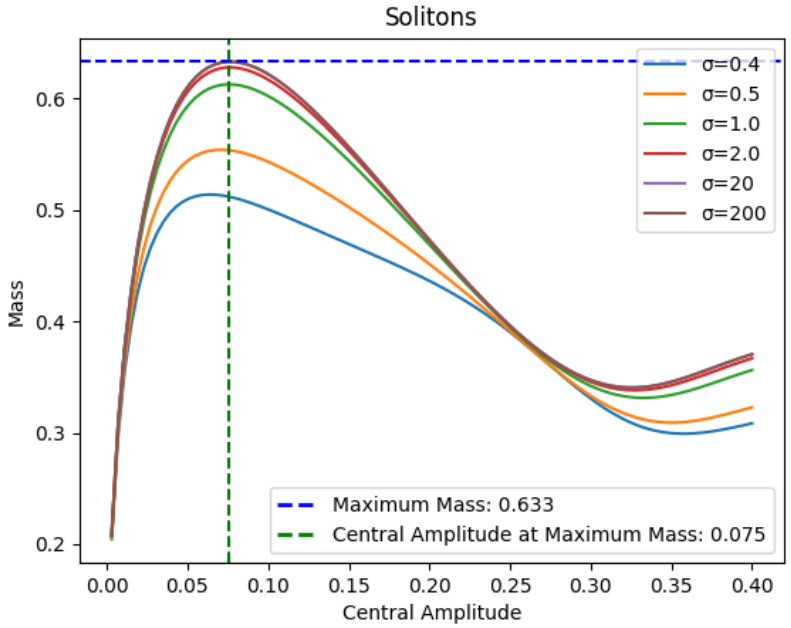

Fig. 3.5 This diagram illustrates the relationship between the mass of solitons and their central amplitude. There are five curves representing different ***higher*** values of $\sigma/M_{\rm Pl}$: 0.4 (blue), 0.5 (orange), 1.0 (green), 2.0 (red), 20 (purple) and 200 (brown).

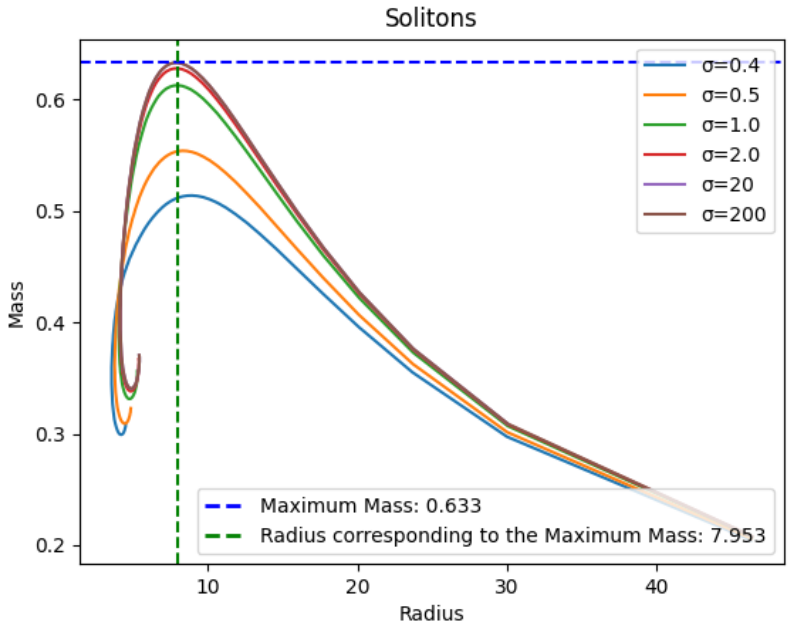

Fig. 3.6 The graph depicts the relationship between the mass of solitons and their radius R. There are five curves representing different ***higher*** values of $\sigma/M_{\rm Pl}$: 0.4 (blue), 0.5 (orange), 1.0 (green), 2.0 (red), 20 (purple) and 200 (brown).

for different σ values, and for $\sigma/M_{\rm Pl} = 0.30, 0.25$, and 0.20, we can see that there are two bumps. Moreover, as σ decreases, the second bump (corresponding to the larger central amplitude) becomes larger, especially the blue curve ($\sigma/M_{\rm Pl} = 0.20$), which has a higher and more pronounced peak. A similar Figure 3.4 shows the relationship between the radius (x-axis) and the mass (y-axis) of solitons. Each curve displays the unique behavior of the soliton mass as the radius changes. For lower σ values ($\sigma/M_{\rm Pl} = 0.20, 0.25, 0.30$), the curves begin with the mass rising rapidly to a peak, after which the mass decreases as the radius increases. The blue curve ($\sigma/M_{\rm Pl} = 0.20$) rises to a very high peak at a small radius and then the mass drops sharply, and it also has the largest mass peak. The peaks of the other curves are more gradual and occur at different radii.

Figures 3.5 and 3.6 demonstrate the cases for ***higher*** σ values. As previously mentioned, for high σ solitons, their behavior begins to closely resemble that of mini-boson Stars. Particularly for $\sigma/M_{\rm Pl} = 200$, a comparison between Figures 3.5 and 3.1 reveals that the maximum mass is the same at 0.633 $M_{\rm Pl}^2 m^{-1}$, to three decimal places, and the corresponding central amplitude is 0.075 $M_{\rm Pl}$. Similarly, comparing Figures 3.6 and 3.2, we observe the same mass (to three decimal places) and they both correspond to the same radius (to three decimal places).

Here, we have not discussed the issue of stability, which does not mean that stability is not important. On the contrary, stability plays a very important role in our subsequent research, so we will discuss it in a more appropriate chapter later on.

3.5 Oscillatons

For a ***real*** scalar field, although there are no time-independent solutions, non-singular, time-dependent solutions can still be found if the time-independent condition is relaxed. These solutions are known as **Oscillatons** [198].

We consider the Einstein-Klein-Gordon system and set the ansatz for the metric in the following form

$$ds^2 = -\alpha^2 dt^2 + a^2 dr^2 + r^2\left(d\theta^2 + \sin^2(\theta) d\varphi^2\right) \tag{3.21}$$

where $\alpha(r,t)$ is the lapse function and $a(r,t)$ is the radial metric function. To find equilibrium configurations, we expand both metric components:

$$A(r,t) \equiv a^2, \qquad C(r,t) \equiv (a/\alpha)^2 \tag{3.22}$$

and the ***real*** scalar field $\phi(r,t)$ as a truncated Fourier series

$$\begin{aligned} \phi(r,t) &= \sum_{j=1}^{j_{\max}} \phi_{2j-1}(r)\cos([2j-1]\omega t), \\ A(r,t) &= \sum_{j=0}^{j_{\max}} A_{2j}(r)\cos(2j\omega t), \\ C(r,t) &= \sum_{j=0}^{j_{\max}} C_{2j}(r)\cos(2j\omega t), \end{aligned} \tag{3.23}$$

where ω is the fundamental frequency and $j_{\max}$ is the mode at which the Fourier series are truncated.

According to the research [226, 22], the scalar field consists only of odd components, while the metric terms consist only of even ones. Solutions are obtained by substituting the expansions above into the Einstein-Klein-Gordon system. By matching terms of the same frequency, the system of equations reduces to a set of coupled ODEs. The boundary conditions require regularity at the origin and asymptotic flatness at large radii. These form an eigenvalue problem for the coefficients $\phi_{2j-1}(r=0)$, $A_{2j}(r=0)$, and $C_{2j}(r=0)$, corresponding to a given central value $\phi_1(r=0)$. As pointed out in [226], the frequency ω is determined by the coefficient $C_0(\infty)$ and is therefore called an output value [148].

Although the equations are non-linear, the Fourier series converges quickly, so a relatively small $j_{\max}$ usually suffices. However, it should be noted that $j_{\max}$ also affects the degree to which the Hamiltonian and momentum constraints are violated in the initial condition approximation. Only sufficiently high $j_{\max}$ values can ensure that these constraint

violations are minimized. For the practical application values of $j_{\max}$, refer to the appendix of [111].

The stability of Oscillatons is discussed in detail in [22]. In summary, the stability behavior of Oscillatons has many similarities with that of mini-boson stars.

3.6 Gravitational Cooling

Although we have found solutions for boson stars, this does not mean that such objects can actually form in the universe. This work was first studied in the work of E.Seidel and W.-M.Suen. In their study [199], they show that there is a dissipationless cooling mechanism which efficiently leads to the formation of compact bosonic objects. They refer to this mechanism as gravitational cooling.

The results for the evolution of a ***massive complex*** scalar field with mini-boson star potential (3.12) are shown in Figure 3.7. The initial configuration is a Gaussian distribution. Darker areas represent higher field strength. We observe that the field collapses and settles down into a bound state by ejecting part of itself with each bounce. The ejected "scalar radiation" appears as black strips in the upper right-hand corner. As time progresses, the ejection becomes less energetic, and the strips become more vertical as they are emitted with lower speed. By approximately $t = 4000\ m^{-1}$, the system settles into a perturbed boson star.

To contrast the formation process for a massive scalar field, Figure 3.8 shows the evolution of a ***massless complex*** scalar field with the same initial conditions. The field collapses, rebounds, and completely disperses to infinity. No nonsingular self-gravitating solitonic object can be formed with a massless Klein-Gordon scalar field. This implies that an initial collapse does not necessarily lead to the formation of a compact object.

Finally, Figure 3.9 shows the evolution of a ***real*** scalar field with similar initial data [4]. The gravitational cooling process is the same. The difference is that the final state has intrinsic oscillations, meaning it is an oscillaton instead of a boson star. For further discussions specifically on the formation of Axion stars, see [234].

Although these evolutions assumed spherical symmetry, which excludes important processes such as fragmentation or pancake formation, they demonstrate the feasibility of the formation mechanism. Scalar field clouds will collapse under their own self-gravity while shedding excess kinetic energy. The results also confirm the importance of the mass term in the potential. When the mass term is removed in simulations, the field collapses, rebounds, and completely disperses to infinity, preventing the formation of any compact object.

In subsequent studies, a similar gravitational cooling mechanism has been found in other types of boson stars, including Proca stars [83] and Fermion-boson stars [81].

[4] A subtle difference is that here $\dot{\phi} = 0$, whereas in the previous two examples $\dot{\phi} = 0.9i\phi$. For more details, see [199].

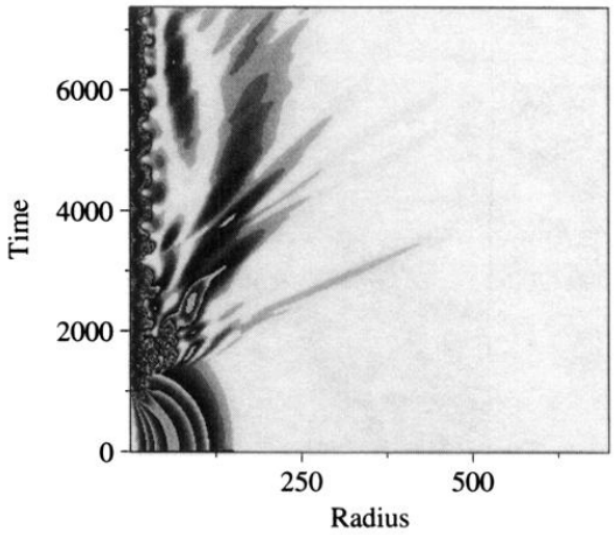

Fig. 3.7 The evolution of $r^2\rho$ for a ***massive***, self-gravitating ***complex*** scalar field is shown. Due to self-gravitation, the field rapidly collapses, forming a perturbed boson star at the center, settling down by gravitational cooling. Reproduced from [199], copyright by APS.

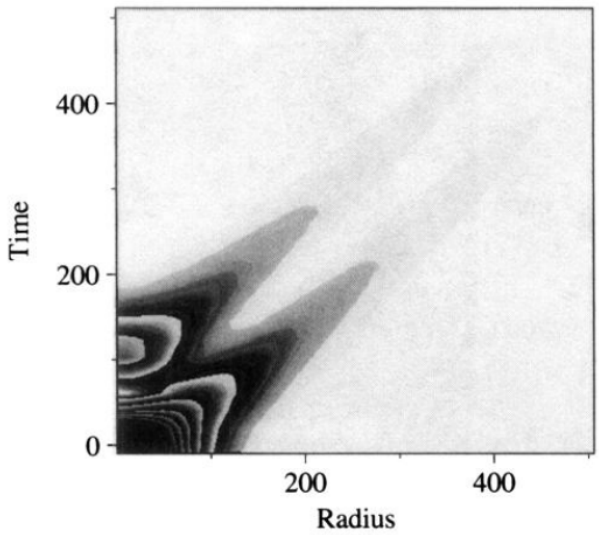

Fig. 3.8 The evolution of the energy density ρ for a ***massless***, self-gravitating ***complex*** scalar field is shown. For a massless field, no boson star can form. Reproduced from [199], copyright by APS.

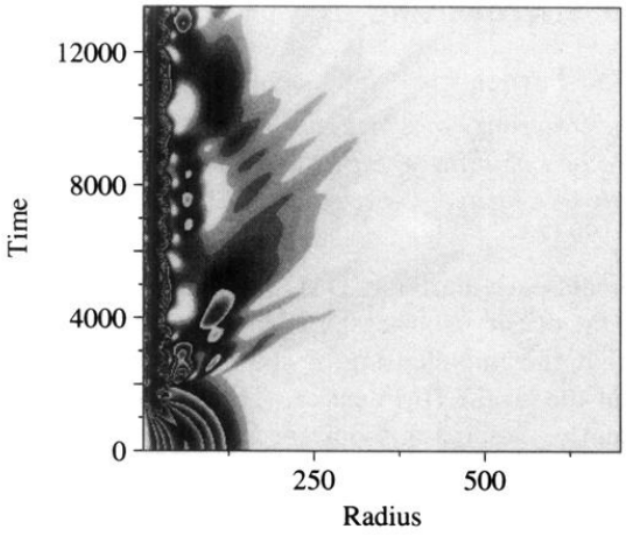

Fig. 3.9 The evolution of $r^2\rho$ for a ***massive***, self-gravitating ***real*** scalar field is shown. The results are similar to those obtained with a complex scalar field. Reproduced from [199], copyright by APS.

3.7 Critical Phenomena in Gravitational Collapse

Consider the initial energy distribution and observe its evolution: there are typically three possible outcomes [148].

1. If the gravitational influence of the energy is weak, it will disperse to increasingly larger distances.

2. If the form of the energy supports it, some of the energy will condense into a stationary state.

3. If the energy is substantial, it may concentrate and form a black hole.

For the case of black hole formation in the third point, adjust a parameter p of the initial data to the threshold of black hole formation, and compare the resulting spacetimes as a function of p. The following critical phenomena would be observed [102, 148]:

- Near the threshold, black holes with arbitrarily small masses can be created, and the black hole mass M scales as
$$M \propto (p - p_*)^\gamma,$$
where p parameterizes the initial data and black holes form for $p > p_*$.

- The critical exponent γ is universal with respect to initial data, meaning it is independent of the particular one-parameter family, although it depends on the type of collapsing matter.

- Similar to phase transitions, one can categorize two types of transitions: **Type II**, where the black hole mass varies ***continuously***, and **Type I**, where the black hole mass varies ***discontinuously***.

- In the region of large curvature before black hole formation, the spacetime approaches a self-similar solution, known as the critical solution, which is also universal with respect to initial data.

Critical phenomena were discovered by Choptuik. In his seminal work [68], Choptuik studied a real massless scalar field and numerically evolved various initial configurations, resulting in either dispersion or black hole formation. By parameterizing these initial configurations, for example by the amplitude of an initial pulse p, and tuning this parameter, he was able to study the threshold for black hole formation and identify critical behavior. His numerical work indicated that with continued tuning, it was possible to produce black holes of arbitrarily small mass. This behavior is similar to a Type II phase transition, where the black hole mass acts as an order parameter.

After that, Hawley and Choptuik [109] began their evolutions with boson star solutions and perturbed them both dynamically and gravitationally. They included a distinct, free, massless, real scalar field in their system that couples to the boson star purely through its gravity. The initial data consisted of a boson star surrounded by a distant shell of real scalar field, parameterized by the amplitude of the shell. For small perturbations, the boson star oscillated around an unstable boson star before settling into a low-mass, stable solution. For large perturbations, the real scalar field compressed the initial star, and after oscillating around an unstable boson star, the complex field collapsed into a black hole. By tuning the initial perturbation, they found a longer-lived unstable boson star, which served as the critical solution. The survival time τ follows a power law in terms of the distance from criticality $|p - p^*|$,

$$\tau \propto \gamma \ln |p - p^*| \tag{3.24}$$

where γ is a real constant that depends on the characteristic instability rate of the particular unstable boson star approached in the critical regime.

Jimenez-Vazquez and Alcubierre [126] investigated a system using a Gaussian pulse as initial data and found that increasing the pulse's initial width changed the system from Type II to Type I critical behavior. In similar research, Buchel et al. [61] showed that initial pulse width determines the system's fate, with unstable boson stars acting as critical solutions in the large-width, Type I regime, aligning with findings by Hawley and Choptuik [109].

Boson stars in axisymmetry were initially studied within conformally flat gravity by Rousseau [186] and later with adaptive mesh refinement by Lai [135] and Lai and Choptuik [136]. These studies suggested no additional unstable axisymmetric modes or very slow-growing modes.

Lai [135] also explored critical behavior by colliding boson stars, finding Type I critical behavior at the black hole formation threshold, and suggesting an unstable boson star as the critical solution. Similar findings were observed in neutron star collisions [127, 130].

Additionally, gauged stars in spherical symmetry also serve as critical solutions [69, 157].

3.8 Boson Stars in Astronomy

Gravitational Wave Sources

Gravitational wave astronomy allows us to explore the universe in new ways. We can now analyze these waves to learn more about boson stars. Key questions include whether current observations might be from pairs of boson stars instead of black holes, whether we can observe signals from boson stars, what templates we would need for detection, and if we can place tight bounds excluding the existence of boson stars [148].

Binary systems are the primary gravitational wave sources for boson stars. Early in the inspiral phase, the gravitational wave signals from binaries of neutron stars, black holes, and boson stars are similar [42]. However, during the late inspiral and merger phases, the internal structure and relative phase of boson stars become crucial in determining the gravitational wave signature [66, 170, 171].

Supermassive black holes could also be examined to see if they might actually be boson stars, with gravitational waves potentially distinguishing between the two [39].

Astrophysical Stellar Objects

Boson stars and neutron stars share similarities. For instance, in both types of stars, the central density plays a crucial role in determining their internal structure. Neutron stars are modeled using different equations of state, while boson stars are described by varying scalar field potentials. In practice, boson stars are often used in numerical simulations instead of neutron stars, as they are easier to evolve [148].

These similarities suggest that some objects classified as neutron stars might actually be boson stars. It is also possible that many observed stars contain a bosonic component, either from exotic matter at high densities or dark matter accretion [105]. This idea has gained interest, with studies attempting to constrain properties of dark matter particles by analyzing their effects within stars [134].

However, boson stars differ from neutron stars in significant ways. Neutron stars have a distinct surface where fluid density is discontinuous [101, 104], whereas boson stars have a smooth scalar field with no distinct surface. Instead, a radius is defined to include a certain percentage of the stellar mass. This difference could affect how matter accretes onto these stars.

Dark Matter Candidate

The existence of dark matter has been proposed to explain the galactic rotation curves in the outer regions of galaxies, where luminous matter is insufficient [187, 188]. Dark

matter is thought to consist of massive particles with low thermal velocities, known as Cold Dark Matter (CDM) [174, 50, 47, 169, 176]. Studies on colliding galaxy clusters support the presence of dark matter in spiral galaxies and galaxy clusters[71, 52]. The success of the Cold Dark Matter (CDM) model in explaining cosmic microwave background (CMB) anisotropies also supports this theory [146]. Promising candidates for CDM include Weakly Interacting Massive Particles (WIMPs) [40] and zero-momentum axions [177, 6, 84, 217, 114, 230]. For more information, see Refs. [92, 151].

However, several problems arise in CDM models when trying to reproduce observed properties of galaxies. These include the overabundance of small-scale structures (the "missing satellite" problem) [128, 133, 159], the presence of a central density cusp (the "cusp" problem) [164, 160, 168, 184], and too many massive dense subhalos compared to satellites around the Milky Way (the "too big to fail" problem) [51].

One proposed solution to the dark matter puzzle is that dark matter could consist of a coherent scalar field with long-range correlations, whose quanta are very light particles[116, 210, 125, 191, 137, 175].

Consider, for example, a mini-boson star with a Kaup mass [129]. The mass of such an object would be similar to that of a galaxy, $M_{\rm gal} \sim 10^{12} M_{\odot}$, if the boson mass is $\mu \sim 10^{-22}$eV. A complex scalar field with self-interaction has also been considered to explain the large-scale structure of galaxies [178], including the formation of a massive boson star [137]. The cosmology of complex scalar fields with self-interactions has been assessed, showing a better fit with data from the CMB and Big Bang nucleosynthesis [141, 142].

Studies suggest that if dark matter consists of bosonic particles, it may accumulate within neutron stars. These neutron stars would then contain both normal fermionic matter and a bosonic component. The accumulation of dark matter could potentially lead to the collapse of neutron stars into black holes [95]. However, this process can be stabilized through an effective gravitational cooling mechanism [59]. This mechanism explains why many old neutron stars are observed instead of black holes, thereby placing constraints on certain models that predict dark matter-induced collapse [88, 120, 53].

Further research indicates that the presence of dark matter can also be inferred from neutron stars in binary configurations. The accretion of dark matter around these neutron stars could produce an observable peak in the gravitational wave spectrum, differing from the features induced by the neutron components themselves [85, 86]. By examining these characteristic peaks in the gravitational wave spectrum, astronomers can indirectly detect and study dark matter, particularly bosonic dark matter.

Chapter 4

Binary Boson Star Initial Data and Gravitational Afterglow

This chapter comprises two articles. Section 4.1 contains **Malaise and Remedy of Binary Boson-Star Initial Data** [113], published in **Classical and Quantum Gravity**. Section 4.2 features **The Gravitational Afterglow of Boson Stars** [77], also published in **Classical and Quantum Gravity**. In both of these studies, my contribution involved using different codes to validate the results.

In the Section 4.1, we delve into the numerical simulations of boson-star head-on collisions to investigate the quality of binary initial data derived from the superposition of single-star spacetimes. Our findings reveal that evolutions commencing from a mere superposition of individual boosted boson-star spacetimes are susceptible to substantial unphysical artifacts. These issues can be mitigated by a simple amendment to the initial data as proposed in [110] for the collision of oscillatons. Although our attention is particularly on massive complex scalar field boson star models with a 6th-order-polynomial potential, we contend that this fragility is a universal feature observable in various types of exotic compact systems, thus necessitating further investigation [113].

In the Section 4.2, our study pivots to the enduring post-merger gravitational wave signature following a boson-star binary coalescence. Utilizing the full extent of numerical relativity, we simulate the post-merger epoch and monitor the gravitational afterglow over a prolonged duration. We incorporate recent advancements in binary initial data, which significantly curtail the spurious initial excitements of the scalar field profiles, along with a metric for the angular momentum that facilitates tracking the entire momentum of the spatial volume, inclusive of the curvature contribution. A critical discovery is that the afterglow persists well beyond the spin-down timescale, providing a sustained gravitational wave afterglow which emits a distinctive signal, potentially differentiating it from other astrophysical phenomena [77].

4.1 Malaise and Remedy of Binary Boson Star Initial Data

In this section, the first main goal is to highlight the significant risk of obtaining spurious physical results due to the use of overly simplistic initial data constructed by the plain superposition of single-boson star spacetimes. The second main goal is to demonstrate how a remarkably simple modification of the superposition procedure, first identified by Helfer et al. [110] for oscillatons, overcomes most of the issues associated with plain superposition. Our main findings are summarized as follows.

1. An adjustment of the superposition procedure, given by

$$\gamma_{ij} = \gamma^{\mathrm{A}}_{ij} + \gamma^{\mathrm{B}}_{ij} - \gamma^{\mathrm{B}}_{ij}\left(x^i_{\mathrm{A}}\right) = \gamma^{\mathrm{A}}_{ij} + \gamma^{\mathrm{B}}_{ij} - \gamma^{\mathrm{A}}_{ij}\left(x^i_{\mathrm{B}}\right), \tag{4.1}$$

   results in a significant reduction of the constraint violations inherent to the initial data; see Figure 4.2.

2. In the head-on collision of mini-boson star binaries with rather low compactness, we observe a significant drop of the radiated gravitational wave energy with increasing distance d if we use plain superposition. This physically unexpected dependence on the initial separation levels off only for rather large $d \gtrsim 150M$, where M denotes the Arnowitt-Deser-Misner (ADM) mass [29]. In contrast, the total radiated energy computed from the evolution of our adjusted initial data displays the expected behaviour over the entire studied range $75.5M \leq d \leq 176M$: a very mild increase in the radiated energy with d. In the limit of large $d \gtrsim 150M$, both types of simulations agree within numerical uncertainties; see upper panel in Figure 4.5.

3. In collisions of highly compact boson stars with solitonic potentials, the radiated energy is largely independent of the initial separations for both initial data types, but for plain superposition we consistently obtain $\sim 10\%$ more radiation than for the adjusted initial data; see bottom panel in Figure 4.5. Furthermore, we find plain superposition to result in a slightly faster infall. The most dramatic difference, however, is the collapse into individual black holes of both boson stars well before merger if we use plain superposition. No such collapse occurs if we use adjusted initial data. Rather, these lead to the expected near-constancy of the central scalar-field amplitude of the boson stars throughout most of the infall; see Figure 4.8.

4. We have verified through evolutions of single boosted boson stars that the premature collapse into a black hole is closely related to the spurious metric perturbation (4.3) that arises in the plain superposition procedure. Artificially adding the same perturbation to a single boson star spacetime induces an unphysical collapse of the

Model	$\sqrt{G}A_{\rm ctr}$	$\sqrt{G}\sigma$	$\mu M_{\rm BS}$	ω/μ	μr_{99}	$\max\frac{m(r)}{r}$
mini	0.0124	∞	0.395	0.971	22.31	0.0249
soli	0.17	0.2	0.713	0.439	3.98	0.222

Table 4.1 Parameters of the two single, spherically symmetric ground state boson star models employed for our simulations of head-on collisions. Up to the rescaling with the scalar mass μ, each boson star is determined by the central amplitude $A_{\rm ctr}$ of the scalar field and the potential parameter σ of Equation (3.20). The mass $M_{\rm BS}$ of the boson star, the scalar field frequency ω, the areal radius r_{99} containing 99 % of the total mass $M_{\rm BS}$ and the compactness, defined here as the maximal ratio of the mass function to radius, represent the main features of the stellar model.

boson star that is in qualitative and quantitative agreement with that observed in the binary evolution starting with plain superposition; see Figure 4.8.

Throughout this work, we use units where the speed of light and Planck's constant are set to unity, $c = \hbar = 1$. We denote spacetime indices by Greek letters running from 0 to 3 and spatial indices by Latin indices running from 1 to 3. The model parameters we use below are as shown in Table 4.1.

4.1.1 Boson Star Binary Initial Data

The single boson star models constructed according to the procedure of the previous section are exact solutions of the Einstein equations, affected only by a numerical error that we can control by increasing the resolution, the size of the computational domain and the degree of precision of the floating point variable type employed. The construction of binary initial data is conceptually more challenging due to the non-linear character of the Einstein equations; the superposition of two individual solutions will, in general, not constitute a new solution. Instead, such a superposition incurs some violation of the constraint equations (see Section 2.2). The purpose of this section is to illustrate how we can substantially reduce the degree of constraint violation with a relatively simple adjustment in the superposition. Before introducing this "trick", we first summarise the superposition as it is commonly used in numerical simulations.

Simple Superposition of Boson Stars

The most common configuration involving more than one boson star is a binary system, and this is the scenario we will describe here. We note, however, that the method generalises straightforwardly to any number of stars. Let us then consider two individual boson star solutions with their centres located at $x^i_{\rm A}$ and $x^i_{\rm B}$, velocities $v^i_{\rm A}$ and $v^i_{\rm B}$. The two boson star spacetimes are described by the 3+1 (ADM) variables $\gamma^{\rm A}_{ij}$, $\alpha_{\rm A}$, $\beta^i_{\rm A}$ and $K^{\rm A}_{ij}$, the scalar

field variables φ_{A} and Π_{A}, and likewise for star B. We can construct from these individual solutions an approximation for a binary boson star system via the pointwise superposition

$$\begin{aligned} \gamma_{ij} &= \gamma^{\mathrm{A}}_{ij} + \gamma^{\mathrm{B}}_{ij} - \delta_{ij}, \\ K_{ij} &= \gamma_{m(i}\left[K^{\mathrm{A}}_{j)n}\gamma^{nm}_{\mathrm{A}} + K^{\mathrm{B}}_{j)n}\gamma^{nm}_{\mathrm{B}}\right], \\ \varphi &= \varphi_{\mathrm{A}} + \varphi_{\mathrm{B}}, \\ \Pi &= \Pi_{\mathrm{A}} + \Pi_{\mathrm{B}}. \end{aligned} \tag{4.2}$$

One could similarly construct a superposition for the lapse α and shift vector β^i, but their values do not affect the physical content of the initial hypersurface. In our simulations we instead initialise them by $\alpha = \sqrt{\chi}$ and $\beta^i = 0$.

A simple superposition approach along the lines of Equation (4.2) has been used in numerous studies of boson star as well as black hole binaries including higher-dimensional black holes [171, 170, 204, 166, 172, 216]. For black holes and higher-dimensional spacetimes in particular, this leading-order approximation has proved remarkably successful and in some limits a simple superposition is exact, such as infinite initial separation, in Brill-Lindquist initial data for non-boosted black holes[7] [55] or in the superposition of Aichelburg-Sexl shockwaves [18] for head-on collisions of black holes at the speed of light. It has been noted in Helfer *et al.* [110], however, that this simple construction can result in spurious low-frequency amplitude modulations in the time evolution of binary oscillatons (real-scalar-field cousins of boson stars); cf. their Figure 7. Furthermore, they have proposed a straightforward remedy that essentially eliminates this spurious modulation. As we will see in the next section, the repercussions of the *simple superposition* according to Equations (4.2) can be even more dramatic for boson star binaries, but they can be cured in the same way as in the oscillaton case. We note in this context that boson stars may be more vulnerable to superposition artefacts near their centres due to the lack of a horizon and its potentially protective character in the superposition of black holes.

The key problem of the construction (4.2) is the equation for the spatial metric γ_{ij}. This is best illustrated by considering the centre x^i_{A} of star A. In the limit of infinite separation, the metric field of its companion star B becomes $\gamma^{\mathrm{B}}_{ij} \to \delta_{ij}$. This is, of course, precisely the contribution we subtract in the third term on the right-hand-side and all would be well. In practice, however, the boson stars start from initial positions x^i_{A} and x^i_{B} with finite

[7] Note that for Brill-Lindquist one superposes the conformal factor ψ rather than ψ^4 as in the method discussed here.

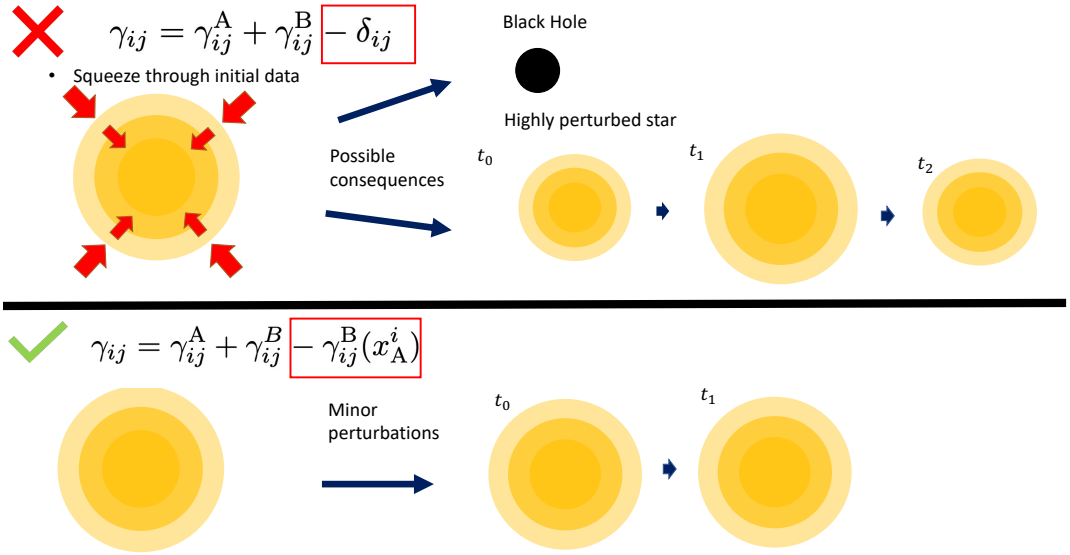

Fig. 4.1 Graphical illustration of the spurious dynamics that may be introduced by the simple superposition procedure (4.2). ***Upper panel***: The spurious increase in the volume element mimics a squeezing of the stellar core that effects a pulsation of the star or may even trigger gravitational collapse to a black hole. ***Lower panel***: No such squeezing occurs with the adjusted superposition (4.4), and the binary evolution starts with approximately unperturbed stars.

separation $d = ||x^i_{\mathrm{A}} - x^i_{\mathrm{B}}||$ and we consequently perturb the metric at star A's centre by

$$\delta\gamma_{ij} = \gamma^{\mathrm{B}}_{ij}(x^i_{\mathrm{A}}) - \delta_{ij} \tag{4.3}$$

away from its equilibrium value $\gamma^{\mathrm{A}}_{ij}(x^i_{\mathrm{A}})$. This metric perturbation can be interpreted as a distortion of the volume element $\sqrt{\gamma}$ at the centre of star A. More specifically, the volume element at star A's centre is enhanced by $\mathscr{O}(1)\,\%$ for initial separations $\mathscr{O}(100)\,M$ and likewise for the centre of star B (by symmetry); see appendix A of reference [110] for more details. The energy density ρ, on the other hand, is barely altered by the presence of the other star, because of the exponential fall-off of the scalar field. The leading-order error therefore consists in a small excess mass that has been added to each boson star's central region. We graphically illustrate this effect in the upper half of Figure 4.1 together with some of the possible consequences. As we will see, this qualitative interpretation is fully borne out by the phenomenology we observe in the binaries' time evolutions.

Finally, we would like to emphasise that, while evaluating the constraint violations is in general a good rule of thumb to check whether the field configuration is a solution of the system, it does not inform one whether it is the intended solution; a system with some constraint violation may have drifted closer to a different, unintended solution. In

the present case, in addition to the increased constraint violation, the constructed boson star solutions possess significant excitations. Thus, while applying a constraint damping system like conformal Z4 [38, 25] may eventually drive the system to a solution, it may no longer be what was originally intended to be the initial condition of an unexcited boson star.

Improved Superposition

The problem of the simple superposition is encapsulated by Equation (4.3) and the resulting deviation of the volume elements at the stars' centres away from their equilibrium values. At the same time, the equation presents us with a concrete recipe to mitigate this error: we merely need to replace in the simple superposition (4.2) the first relation $\gamma_{ij} = \gamma^{\mathrm{A}}_{ij} + \gamma^{B}_{ij} - \delta_{ij}$ by

$$\boxed{\gamma_{ij} = \gamma^{\mathrm{A}}_{ij} + \gamma^{\mathrm{B}}_{ij} - \gamma^{\mathrm{B}}_{ij}(x^i_{\mathrm{A}}) = \gamma^{\mathrm{A}}_{ij} + \gamma^{\mathrm{B}}_{ij} - \gamma^{\mathrm{A}}_{ij}(x^i_{\mathrm{B}})\,.} \tag{4.4}$$

The two expressions on the right-hand side are indeed equal thanks to the symmetry of our binary: its constituents have equal mass, no spin and their velocity components satisfy $v^i_{\mathrm{A}} v^j_{\mathrm{A}} = v^i_{\mathrm{B}} v^j_{\mathrm{B}}$ for all $i, j = 1, 2, 3$ in the centre-of-mass frame. Equation (4.4) manifestly ensures that at positions x^i_{A} and x^i_{B} we now recover the respective star's equilibrium metric and, hence, volume element. We graphically illustrate this improvement in the bottom panel of Figure 4.1.

A minor complication arises from the fact that the resulting spatial metric does not asymptote towards δ_{ij} as $R \to \infty$. We accordingly impose outgoing Sommerfeld boundary conditions on the asymptotic background metric $2\delta_{ij} - \gamma^{\mathrm{A}}_{ij}(x^i_{\mathrm{B}})$; in a set of test runs, however, we find this correction to result in very small changes well below the simulation's discretisation errors.

Finally, we note that the leading-order correction to the superposition as written in Equation (4.4) does not work for asymmetric configurations with unequal masses or spins. Generalising the method to arbitrary binaries requires the subtraction of a spatially varying term rather than a constant $\gamma^{\mathrm{B}}_{ij}(x^i_{\mathrm{A}}) = \gamma^{\mathrm{A}}_{ij}(x^i_{\mathrm{B}})$ or δ_{ij}. Such a generalisation may consist, for example, of a weighted sum of the terms $\gamma^{\mathrm{A}}_{ij}(x^i_{\mathrm{B}})$ and $\gamma^{\mathrm{B}}_{ij}(x^i_{\mathrm{A}})$. Leaving this generalisation for future work, we will focus on equal-mass systems in the remainder of this study and explore the degree of improvement achieved with Equation (4.4).

4.1.2 Models and Results

For our analysis of the two types of superposed initial data, we will now discuss time evolutions of binary boson star head-on collisions. A head-on collision is characterised by the two individual boson star models and three further parameters, the initial separation in

Table 4.2 The four types of boson star binary head-on collisions simulated in this study. The individual boson stars A and B are given either by the mini or solitonic model of Table 4.1, and start with initial velocity v directed towards each other. The initial data is constructed either by plain superposition (4.2) or by adjusting the superposed data according to Equation (4.4). For each type of binary, we perform five collisions with initial separations d listed in the final column.

Label	star A	star B	v	initial data	d/M
`mini`	mini	mini	0.1	plain	75.5, 101, 126, 151, 176
`+mini`	mini	mini	0.1	adjusted	75.5, 101, 126, 151, 176
`soli`	soli	soli	0.1	plain	16.7, 22.3, 27.9, 33.5, 39.1
`+soli`	soli	soli	0.1	adjusted	16.7, 22.3, 27.9, 33.5, 39.1

units of the ADM mass, d/M, and the initial velocities v_A and v_B of the boson stars. We perform all our simulations in the centre-of-mass frame, so that for equal-mass binaries, $v_A = -v_B =: v$. One additional parameter arises from the type of superposition used for the initial data construction: we either use the "plain" superposition of Equation (4.2) or the "adjusted" method (4.4).

For all our simulations, we set $v = 0.1$; this value allows us to cover a wide range of initial separations without the simulations becoming prohibitively long. The boson star binary configurations summarised in Table 4.2 then result in four sequences of head-on collisions labelled `mini`, `+mini`, `soli` and `+soli`, depending in the nature of the constituent boson stars and the superposition method. For each sequence, we vary the boson stars initial separation d to estimate the dependence of the outcome on d. First, however, we test our interpretation of the improved superposition (4.4) by computing the level of constraint violations in the initial data.

Initial Constraint Violations

As discussed in Section 4.1.1 and in Appendix A of reference [110], the main shortcoming of the plain superposition procedure consists in the distortion of the volume element near the individual boson stars' centres and the resulting perturbation of the mass-energy inside the stars away from their equilibrium values. If this interpretation is correct, we would expect this effect to manifest itself in an elevated level of violation of the Hamiltonian constraint which relates the energy density to the spacetime curvature. Put the other way round, we would expect our improved method (4.4) to reduce the Hamiltonian constraint violation. This is indeed the case as demonstrated in the upper panels of Figure 4.2 where we plot the Hamiltonian constraint violation of the initial data along the collision axis for the configurations `mini` and `+mini` with $d = 101M$ and the configurations `soli` and `+soli` with $d = 22.3M$.

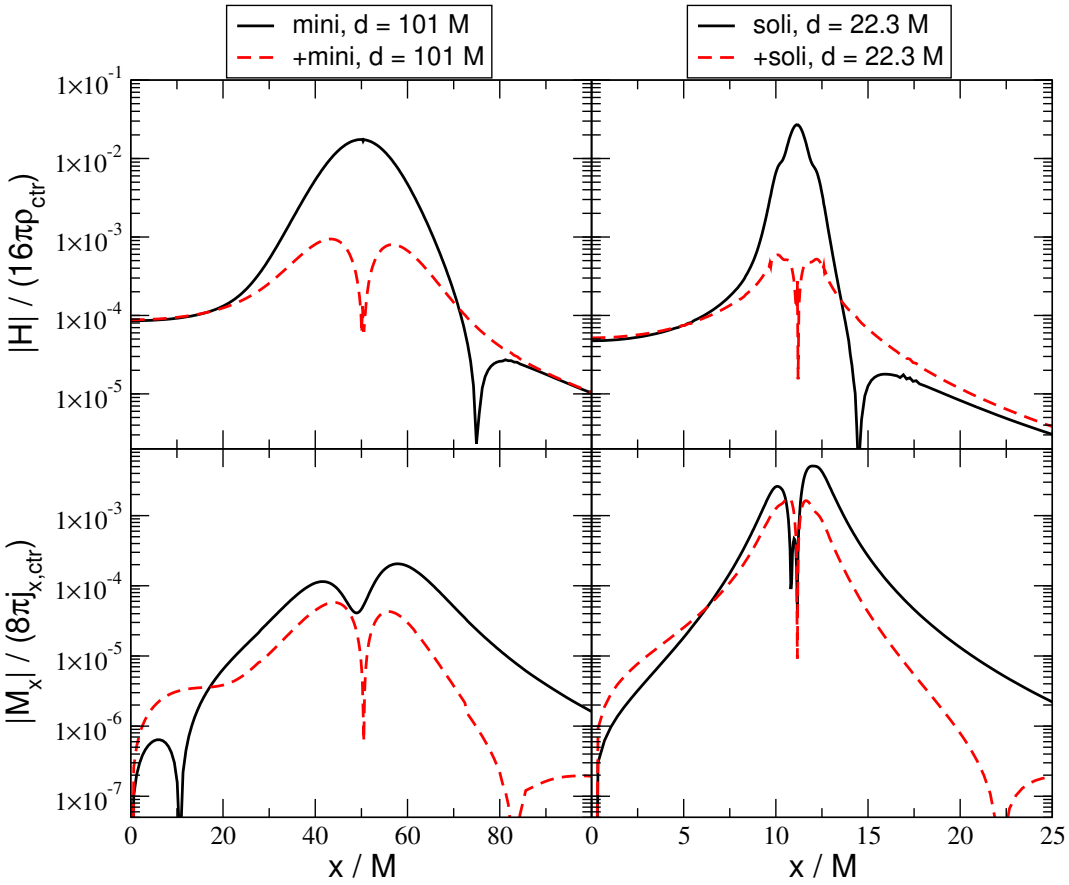

Fig. 4.2 Upper row: The Hamiltonian constraint violation $\mathscr{H}$ normalised by the respective boson star's central energy density $16\pi\rho_{\mathrm{ctr}}$ is plotted along the collision axis of the binary configurations `mini`, `+mini` with $d = 101M$ (left) and `soli`, `+soli` with $d = 22.3M$ (right). The degree of violations is substantially reduced in the boson star interior by using the improved superposition (4.4) for `+mini` and `+soli` relative to their plain counterparts; the maxima of $\mathscr{H}$ have dropped by over an order of magnitude in both cases. Bottom row: The same analysis for the momentum constraint $\mathscr{M}_x$ normalised by the central boson star's momentum density $8\pi j_x$. Here the improvement is less dramatic, but still yields a reduction by a factor of a few in the boson star core.

In the limit of zero boost velocity $v = 0$, this effect is even tractable through an analytic calculation which confirms that the improved superposition (4.4) ensures $\mathscr{H} = 0$ at the boson star's centres in isotropic coordinate; see [113] for more details.

Our adjustment (4.4) also leads to a reduction of the momentum constraint violations of the initial data, although the effect is less dramatic here. The bottom panels of Figure 4.2 display the momentum constraint $\mathscr{M}_x$ along the collision axis normalised by the momentum density $8\pi j_x$; we see a reduction by a factor of a few over large parts of the boson star interior for the modified data `+mini` and `+soli`.

The overall degree of initial constraint violations is rather small in all cases, well below 0.1 % for our adjusted data. These data should therefore also provide a significantly improved initial guess for a full constraint solving procedure. We leave such an analysis for future work and in the remainder of the work explore the impact of the adjustment (4.4) on the physical results obtained from the initial data's time evolutions.

Convergence and Numerical Uncertainties

In order to put any differences in the time evolutions into context, we need to understand the uncertainties inherent to our numerical simulations. For this purpose, we have studied the convergence of the gravitational wave radiation generated by the head-on collisions of mini and solitonic boson stars.

Figure 4.3 displays the convergence of the radiated energy E_{rad} as a function of time for the `+mini` configuration with $d = 101\,M$ of Table 4.1 obtained for grid resolutions $h_1 = M/6.35$, $h_2 = M/9.53$ and $h_3 = M/12.70$ on the innermost refinement level and corresponding grid spacings on the other levels. The functions $E_{\text{rad}}(t)$ and their differences are shown in the bottom and top panel, respectively, of Figure 4.3 together with an amplification of the high-resolution differences by the factor $Q_2 = 2.86$ for second-order convergence. The observation of second-order convergence is compatible with the second-order ingredients of the LEAN code, prolongation in time and the outgoing radiation boundary conditions. We believe that this dominance is mainly due to the smooth behaviour of the boson star centre as compared with the case of black holes [117]. By using the second-order Richardson extrapolated result, we determine the discretisation error of our energy estimates as 0.9 % for h_3 which is the resolution employed for all remaining mini-boson star collisions. We have performed the same convergence analysis for the plain-superposition counterpart `mini` and for the dominant $(\ell, m) = (2, 0)$ multipole of the Newman-Penrose scalar of both configurations and obtained the same convergence and very similar relative errors.

In Figure 4.4, we show the same convergence analysis for the solitonic collision `+soli` with $d = 22.3\,M$ and resolutions $h_1 = M/22.9$, $h_2 = M/45.9$, $h_3 = M/68.8$. We observe

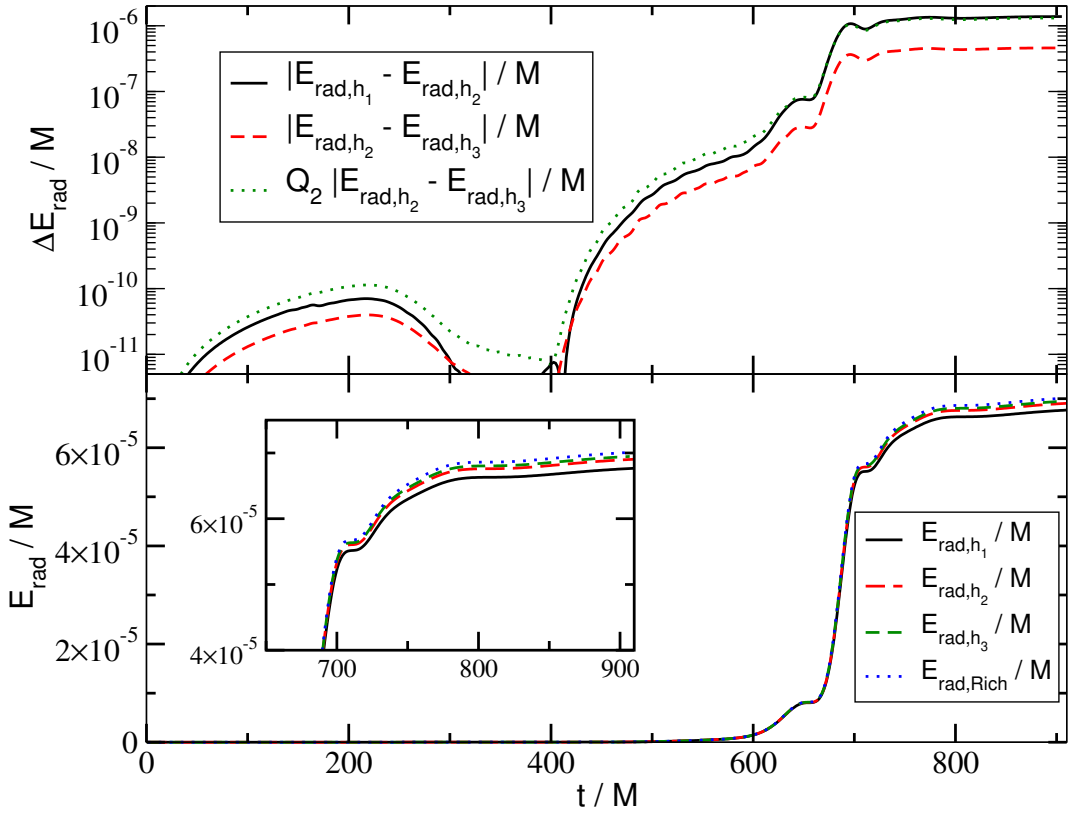

Fig. 4.3 Convergence analysis for the gravitational wave energy extracted at $R_{\rm ex} = 252$M from the head-on collision +mini of Table 1 with $d = 101M$. For the resolutions $h_1 = M/6.35, h_2 = M/9.53$ and $h_3 = M/12.70$ (on the innermost refinement level), we obtain convergence close to second order (upper panel). The numerical error, obtained by comparing our results with the second-order Richardson extrapolated values (bottom panel), is $0.9\%(1.6\%, 3.6\%)$ for our high (medium, coarse) resolutions.

second-order convergence during merger and ringdown and slightly higher convergence in the earlier infall phase. For the uncertainty estimate we conservatively use the second-order Richardson extrapolated result and obtain a discretisation error of about $0.07\,\%$ for our medium resolution h_2 which is the value we employ in our solitonic production runs. Again, we have repeated this analysis for the plain `soli` counterpart and the $(2,0)$ gravitational wave multipole observing the same order of convergence and similar uncertainties. Our error estimate for the solitonic configurations is rather small in comparison to the mini-boson star collisions and we cannot entirely rule out a fortuitous cancellation of errors in our simulations. From this point on, we therefore use a conservative discretisation error estimate of $1\,\%$ for all our boson star simulations.

A second source of uncertainty in our results is due to the extraction of the gravitational wave signal at finite radii rather than $\mathscr{I}^+$. We determine this error by extracting the signal at multiple radii, fitting the resulting data by the series expansion $f = f_0 + f_1/r$, and

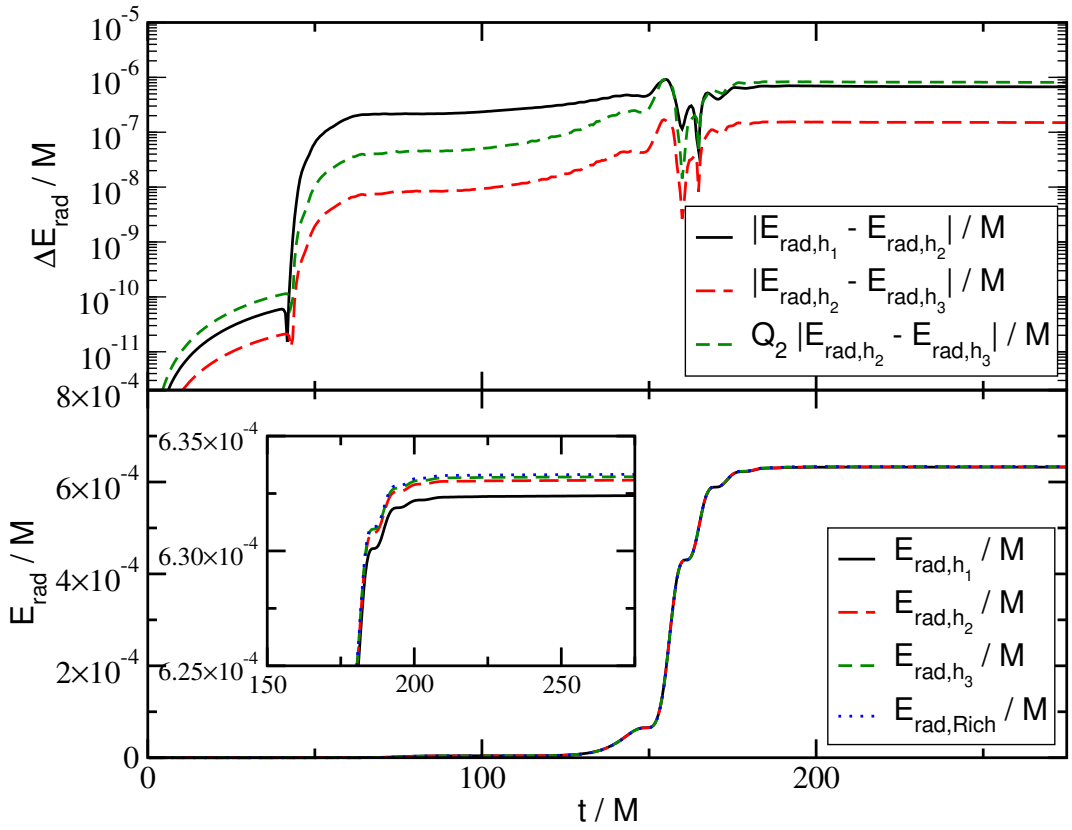

Fig. 4.4 Convergence analysis as in Figure 4.3 but for the configuration `+soli` of Table 4.1 with $d = 22.3M$ and resolutions $h_1 = M/22.9$, $h_2 = M/45.9$ and $h_3 = M/68.8$. The numerical error, obtained by comparing our results with the second-order Richardson extrapolated values (bottom panel), is 0.03 % (0.07 %, 0.6 %) for our high (medium, coarse) resolutions.

comparing the result at our outermost extraction radius with the limit f_0 [8]. This procedure results in errors in $E_{\rm rad}$ ranging between 0.5 % and 3 %. With the upper range, we arrive at a conservative total error budget for discretisation and extraction of about 4 %. As a final test, we have repeated the `mini` and `+mini` collisions for $d = 101M$ with the independent GRCHOMBO code [70, 27] using the BSSN/CCZ4 formulation [25] and obtain the same results within ≈ 1.5 %. Bearing in mind these tests and a 4 % error budget, we next study the dynamics of the boson star head-on collisions with and without our adjustment of the initial data.

[8] This is known as the **Peeling Theorem** (see [19] for details). Any wave at large r will have its first two terms as a constant f_0 term (the memory term, which can be zero) and an $\mathcal{O}(1/r)$ term. The next term is $\mathcal{O}(1/r^2)$, but it is typically too small to be significant.

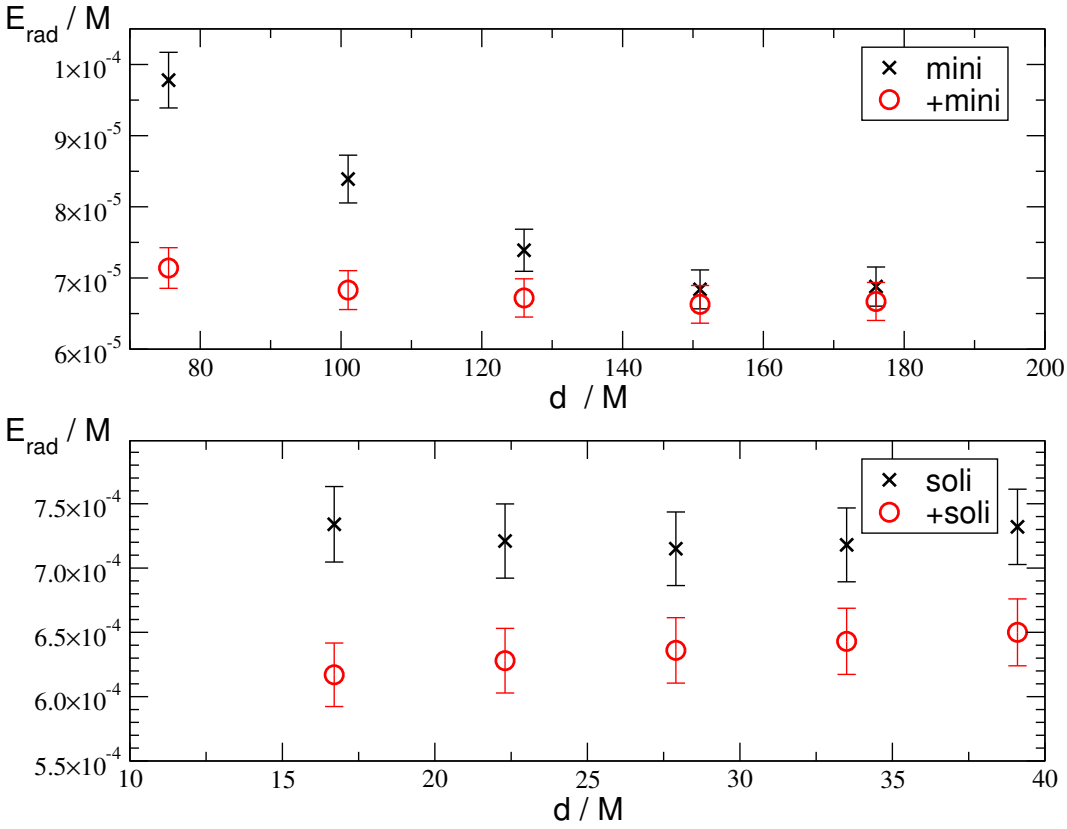

Fig. 4.5 The gravitational wave energy $E_{\rm rad}$ generated in the head-on collision of mini (upper panel) and solitonic (lower panel) boson star binaries starting with initial separation d and velocity $v = 0.1$ towards each other. For comparison, a non-spinning, equal-mass black hole binary colliding head-on with the same boost velocity $v = 0.1$ radiates $E_{\rm rad} = 6.0 \times 10^{-4} M$ [216].

Radiated Gravitational Wave Energy

For our first test, we compute the total radiated gravitational wave energy for all our head-on collisions focusing in particular on its dependence on the initial separation d of the boson star centres. In this estimate we exclude any spurious or "junk" radiation content of the initial data by starting the integration at $t = R_{\rm ex} + 40M$. Unless specified otherwise, all our results are extracted at $R_{\rm ex} = 300M$ for mini boson star collisions and $R_{\rm ex} = 84M$ for the solitonic binaries.

The main effect of increasing the initial separation is a reduction of the (negative) binding energy [9] of the binary and a corresponding increase of the collision velocity around merger. In the large d limit, however, this effect becomes negligible. For the comparatively large initial separations chosen in our collisions, we would therefore expect

[9] In this context, "binding energy" is an intuitive Newtonian concept, and therefore it lacks a unique mathematical definition in General Relativity. We use "binding energy" here to convey the idea that increasing the distance between the binary components makes them less gravitationally bound to each other.

the function $E_{\rm rad}$ to be approximately constant, possibly showing a mild increase with d. The mini-boson star collisions shown as black $\times$ symbols in the upper panel of Figure 4.5 exhibit a rather different behaviour: the radiated energy rapidly decreases with d and only levels off for $d \gtrsim 150\,M$. We have verified that the excess energy for smaller d is not due to an elevated level of junk radiation which consistently contribute well below $0.1\,\%$ of $E_{\rm rad}$ in all our mini-boson star collisions and has been excluded from the results of Figure 4.5 anyway. The `+mini` boson star collisions, in contrast, results in an approximately constant $E_{\rm rad}$ with a total variation approximately at the level of the numerical uncertainties. For $d \gtrsim 150\,M$, both types of initial data yield compatible results, as is expected. The key benefit of our adjusted initial data is that they provide reliable results even for smaller initial separations suitable for starting boson star inspirals.

The discrepancy is less pronounced for the head-on collisions of solitonic boson star collisions; both types of initial data result in approximately constant $E_{\rm rad}$. They differ, however, in the predicted amount of radiation at a level that is significant compared to the numerical uncertainties. As we will see below, this difference is accompanied by drastic differences in the boson star's dynamics during the long infall period. We furthermore note that the mild but steady increase obtained for the adjusted `+soli` agrees better with the physical expectations.

The differences in the total radiated gravitational wave energy also manifest themselves in different amplitudes of the $(2,0)$ multipole of the Newman-Penrose scalar Ψ_4. This is displayed in Figures 4.6 and 4.7 where we show the gravitational wave modes for the mini and solitonic collisions, respectively. The most prominent difference between the results for plain and adjusted initial data is the significant variation of the amplitude of the $(2,0)$ mode in the plain mini boson star collisions in the upper panel of Figure 4.6. In contrast, the differences in the amplitudes in Figure 4.7 for the solitonic collisions are very small. In fact, the differences in the radiated energy of the `soli` and `+soli` collisions mostly arise from a minor stretching of the signal for the `soli` case; this effect is barely perceptible in Figure 4.7 but is amplified by the integration in time when we calculate the energy. Finally, we note the different times of arrival of the main pulses in Figure 4.7; especially for larger initial separation, the merger occurs earlier for the `soli` configurations than for their adjusted counterparts `+soli`. We will discuss this effect together with the evolution of the scalar field amplitude in the next subsection.

Evolution of the Scalar Amplitude and Gravitational Collapse

The adjustment (4.4) in the superposition of oscillatons was originally developed in reference [110] to reduce spurious modulations in the scalar field amplitude; cf. their Figure 7. In our simulations, this effect manifests itself most dramatically in the collisions

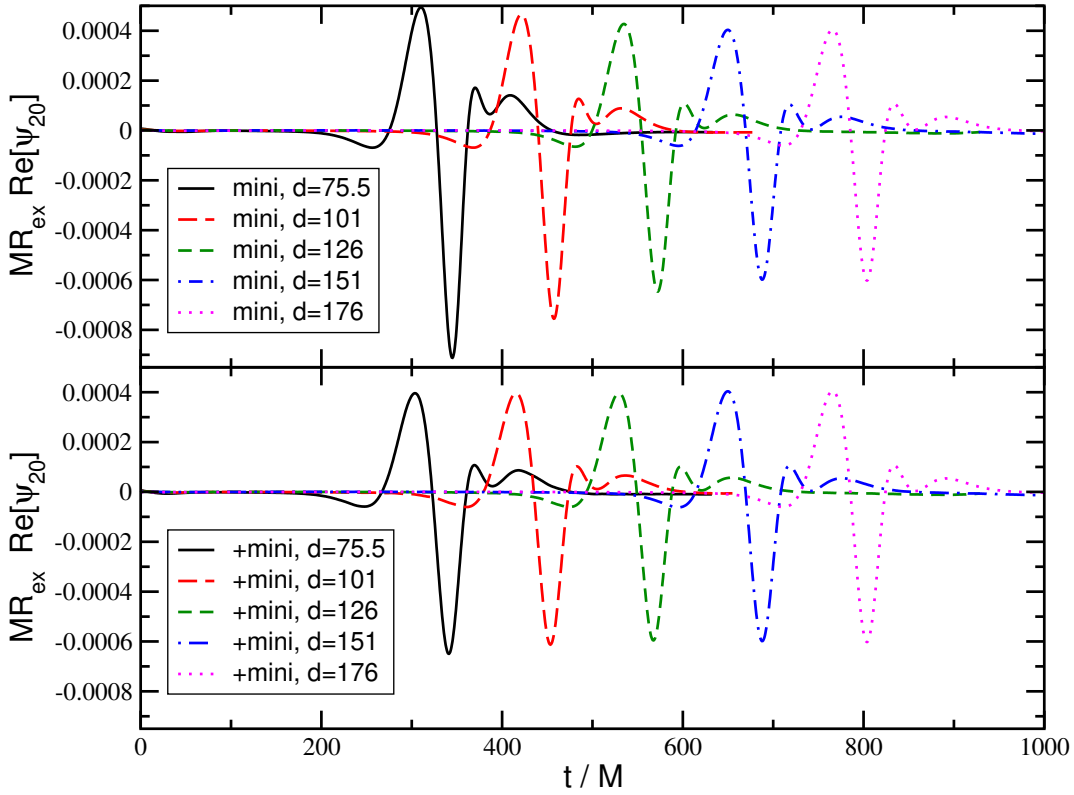

Fig. 4.6 The $(2,0)$ mode of the Newman-Penrose scalar for the mini boson star collisions of Table 1.

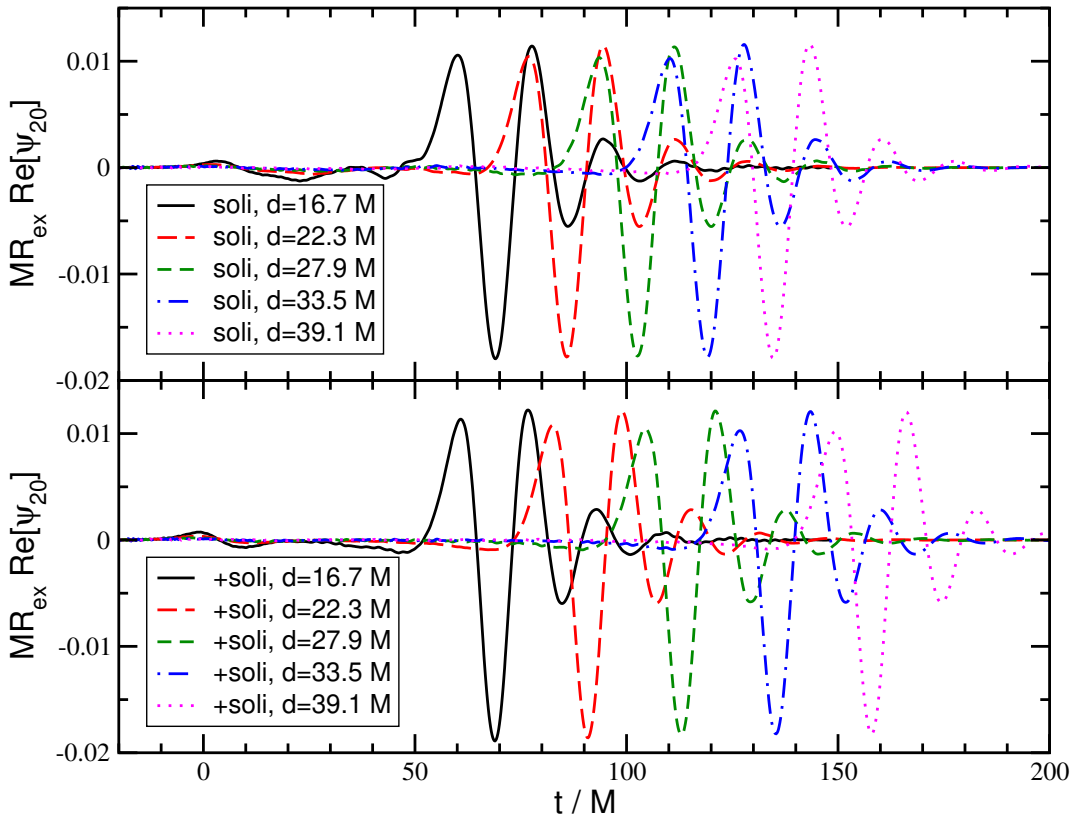

Fig. 4.7 The $(2,0)$ mode of the Newman-Penrose scalar for the solitonic boson star collisions of Table 4.1.

of our solitonic boson star configurations `soli` and `+soli`. We recall that the single-boson star constituents of these binaries are stable, but highly compact stars, located fairly close to the instability threshold. We would therefore expect them to be more sensitive to spurious modulations in their central energy density. This is exactly what we observe in all time evolutions of the `soli` configurations starting with plain-superposition initial data. As one example, we show in Figure 4.8 the scalar amplitude at the individual boson star centres and the boson star trajectories as functions of time for the `soli` and `+soli` configurations starting with initial separation $d = 22.3M$. Let us first consider the `soli` configuration using plain superposition displayed by the solid (black) curves. In the upper panel of Figure 4.8, we clearly see that the scalar amplitude steadily increases, reaching a maximum around $t \approx 30M$ and then rapidly drops to a near-zero level. Our interpretation of this behaviour as a collapse to a black hole is confirmed by the horizon finder which reports an apparent horizon of irreducible mass $m_{\rm irr} = 0.5M$ just before the scalar field amplitude collapses; the time of the first identification of an apparent horizon is marked by the vertical dotted black line at $t \approx 30M$. For reference we plot in the bottom panel the trajectory of the boson star centres along their collision (here the x) axis. In agreement with the horizon mass $m_{\rm irr} = 0.5M$, the trajectory clearly indicates that around $t \approx 30M$, the boson stars are still far away from merging into a single black hole; in units of the ADM mass, the individual boson star radius is $r_{99} = 2.78M$. We interpret this early black hole collapse as a spurious feature due to the use of plain superposition in the initial data construction. This behaviour is also seen in the case of the real scalar field oscillatons in [110].

We have tested this hypothesis with the evolution of the adjusted initial data. These exhibit a drastically different behaviour in the collision `+soli` displayed by the dashed (red) curves in Figure 4.8. Throughout most of the infall, the central scalar amplitude is constant, it increases mildly when the boson star trajectories meet near $x = 0$, and then rapidly drops to zero. Just as the maximum amplitude is reached, the horizon finder first computes an apparent horizon, now with $m_{\rm irr} = 0.99M$, as expected for a black hole resulting from the merger; see the vertical red line in the figure.

As a final test of our interpretation, we compare the behaviour of the binary constituents with that of single boson stars boosted with the same velocity $v = 0.1$. As expected, the scalar field amplitude at the centre of such a single boson star remains constant within high precision, about $\mathcal{O}(10^{-5})$, on the timescale of our collisions. We have then repeated the single boson star evolution by poisoning the initial data with the very same term (4.3) that is also added near a single boson star's centre by the plain-superposition procedure. The resulting scalar amplitude at the centre of this poisoned boson star is shown as the dash-dotted (blue) curve in Figure 4.8 and nearly overlaps with the corresponding curve of the `soli` binary. Furthermore, the poisoned single boson star collapses into a black hole after nearly the same amount of time as indicated by the vertical blue dotted curve

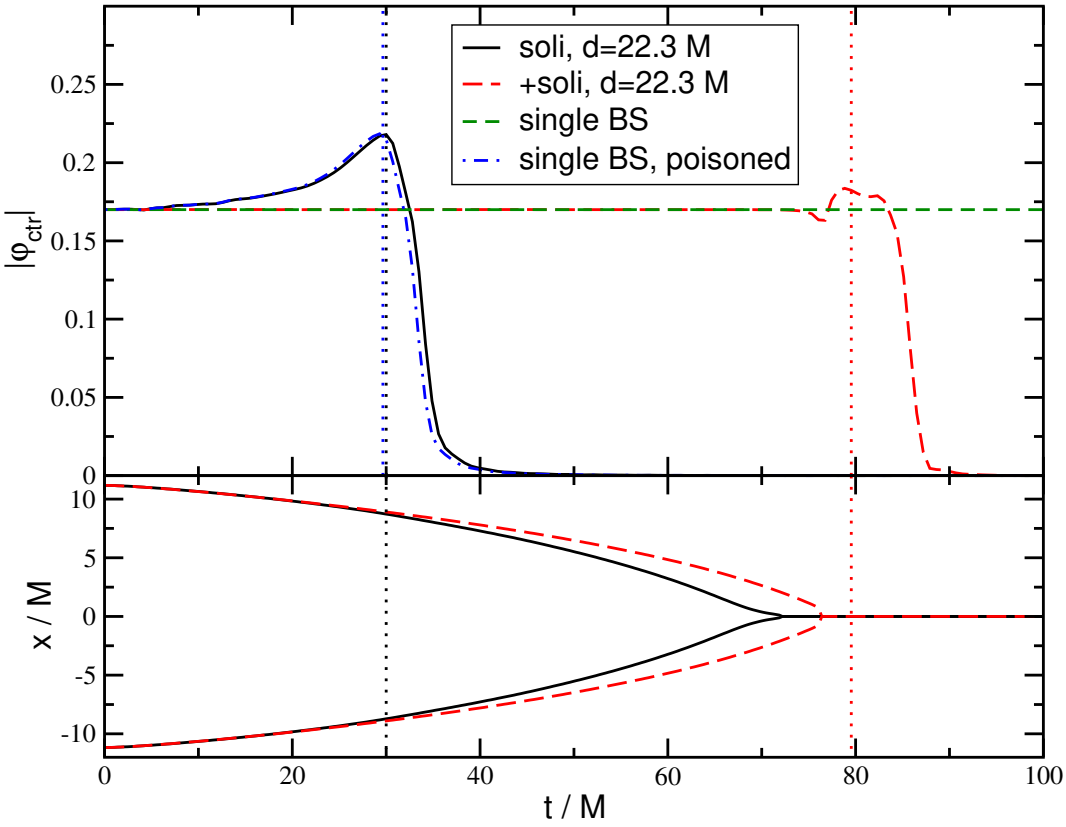

Fig. 4.8 The central scalar-field amplitude $|\varphi_{\rm ctr}|$ as a function of time for one boson star in the head-on collisions of solitonic boson stars with distance $d = 22.3M$ (black solid and red long-dashed) as well as a single boson star spacetime with the same parameters (green dashed) and the same single boson star spacetime "poisoned" with the metric perturbation (4.3) that would arise in a simple superposition (see text for details). The dotted vertical lines mark the first location of an apparent horizon in the simulation of the same colour; as expected, no horizon ever forms in the evolution of the unpoisoned single boson star. In the bottom panel, we show for reference the coordinate trajectories of the boson star centres as obtained from locally Gauss-fitting the scalar profile. Around merger this procedure becomes inaccurate, so that the values around $t \approx 70M$ should be regarded as qualitative measures, only.

in the figure. Clearly this behaviour of the single boosted boson star is unphysical, and strongly indicates that the plain superposition of initial data introduces the same unphysical behaviour to our `soli` binary constituents. We have repeated this analysis for our entire sequence of `soli` binaries with very similar results: the individual boson stars always collapse to distinct black holes about $\Delta t \approx 50M$ before the binary merger.

Finally, the trajectories in the bottom panel of Figure 4.8 indicate that the boson star merger occurs a bit later for the `+soli` case than its plain-superposition counterpart `soli`. This is indeed a systematic effect we see for all initial separations d and which agrees with the different arrival times of the peak gravitational wave signals that we have already noticed in Figure 4.7. We do not have a rigorous explanation of this effect, but note that the two trajectories in Figure 4.8 start diverging right at the time of spurious black hole formation in the `soli` binary. Perhaps some of the binding energy in boson star collisions is converted into deformation energy rather than simply kinetic energy of the stars' centres of mass, slowing down the infall compared to the black hole case. Another explanation may consider the generally repulsive character of the scalar field which endows it with support against gravitational collapse. When the infalling boson stars collapse to black holes, the scalar field essentially disappears as a potentially repulsive ingredient and the ensuing collision is sped up. Whatever ultimately generates this effect, the key observation of our study is that even rather mild imperfections in the initial data can drastically affect the physical outcome of the time evolution.

4.1.3 Conclusions

We have simulated head-on collisions of equal-mass, non-spinning boson stars and the gravitational wave radiation generated in the process. The main focus of our study is the construction of boson star binary initial data and the ensuing impact of systematic errors on the physical results of the simulations. In particular, we have contrasted the relatively common method of plain superposition according to Equation (4.2) with the adjusted procedure (4.4) first identified in reference [110] for oscillatons.

Our results demonstrate that the adjustment (4.4) in the construction of initial data leads to major improvements in the initial constraint violations and the time evolutions of binary boson star collisions. In contrast, we find that the use of plain superposition for boson star binary initial data may not only result in quantitatively wrong physical diagnostics but can even result in completely spurious physical behaviour such as premature gravitational collapse. In spite of the great simplicity of the adjustment (4.4) and its success in overcoming the most severe errors in the ensuing evolution, it is not free of shortcomings. (i) In its present form, the adjustment only works for a restricted class of binaries, namely equal-mass systems with no spin and velocity vectors satisfying $v^i_{\rm A} v^j_{\rm A} = v^i_{\rm B} v^j_{\rm B}$. (ii) Even

with the adjustment, the initial data contain some residual constraint violations; it should therefore primarily be regarded as an improved initial guess for a constraint solving procedure rather than the "real deal" in its own right. These shortcomings clearly point towards the most urgent generalisations of our work, overcoming the symmetry restrictions and adding a numerical constraint solver.

4.2 The Gravitational Afterglow of Boson Stars

The main focus of this section is the long-lived post-merger gravitational wave emission or **Afterglow** resulting from the merger of two boson stars into a single compact but horizon-free remnant; for first explorations of boson star coalescences including the relaxation into a non-rotating boson star or a hairy black hole see [170, 172, 193]. First indications of such an afterglow were noted in reference [110] in the case of a head-on collision resulting in a highly perturbed boson star. Here, we demonstrate that this afterglow can be very long lived, with barely any decay in amplitude following a transient burst during the merger phase itself. The characteristics of this post-merger afterglow contrast sharply with the corresponding gravitational wave signatures of most black hole or neutron star mergers, which, if resulting in black hole formation, are dominated by the exponential quasi-normal ringdown.

We illustrate and explore in detail the gravitational afterglow of boson stars for the case of the inspiral and merger of two equal-mass boson stars in a collision with a non-zero impact parameter [5]. For the moderate compactness of the initial binary constituents chosen in our simulations, the final state of the collision is a highly perturbed boson star with decreasing spin. Crucially, this spin-down occurs on a time scale *much longer* than a single gravitational wave oscillation time period. The associated long-lived gravitational wave afterglow may exhibit information about the post-merger dynamics of such systems. In particular, we find an intriguing correlation between the phases of different gravitational wave multipoles and the dynamical spin amplitude.

The results of this section suggest that using standard merger templates consisting mostly of the inspiral and merger contributions may be insufficient to capture fundamental dynamics of a boson-star merger event. Rather, comprehensive boson star searches likely require extended waveform templates which also capture the rich post-merger gravitational wave afterglow phenomenology.

Unless explicitly stated otherwise, we use units where the speed of light and Planck's constant are set to unity, $c = \hbar = 1$, and we express the gravitational constant in terms of the Planck mass $G = 1/M_{\rm Pl}^2$. Unless specified otherwise, Latin indices run from 1 to 3 while Greek ones run from 0 to 3.

[5] The **Impact Parameter** is defined as the perpendicular distance between the centers of the two bodies at their closest approach, assuming they continue along their respective straight-line trajectories without colliding. This distance is typically denoted as b. When $b = 0$, the two bodies are considered to be in a head-on collision.

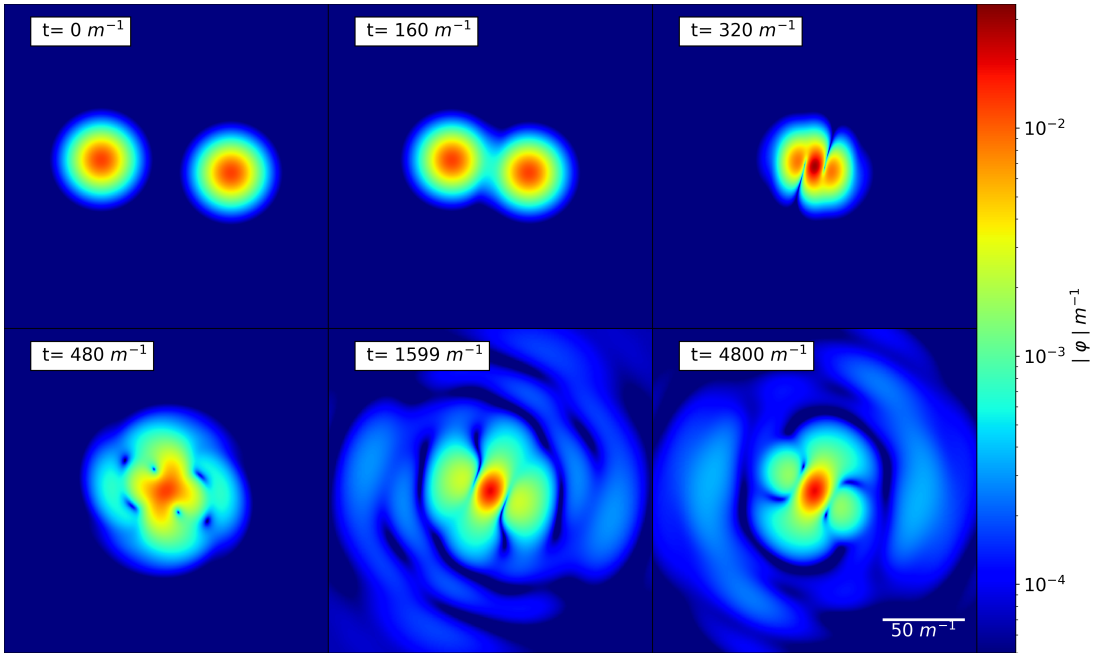

Fig. 4.9 Snapshots of the scalar field amplitude $|\varphi|$ in the orbital plane for a grazing collision of two boson stars of equal mass $M = 0.395\, M_{\rm Pl}^2 m^{-1}$ starting with initial horizontal distance $80\, m^{-1}$, impact parameter $b = 8\, m^{-1}$ (vertical center to center distance) and initial velocity $v = \pm 0.1$ in the x (horizontal) direction. A video of the merger can be found at https://youtu.be/JE5FRG7kgvU.

4.2.1 Simulation Set-Up

In this study, we employ the **Mini-Boson Stars** model outlined in Section 3.3. The construction of the boson-star binary initial data is broadly categorized into three steps.

1. Generate a stationary, non-rotating solution for a single boson star.
2. Apply a Lorentz boost to obtain a single star with linear momentum.
3. Superpose two such solutions according to the procedure described in Refs. [110, 113] which substantially reduces spurious initial oscillations of the individual boson stars as compared to the more common procedure of plain superposition.

Most of our results are obtained from simulating a grazing collision of two stable boson stars, each with mass[6] $M = 0.3950\, M_{\rm Pl}^2 m^{-1}$ and initial velocity $v = \mp(0.1, 0, 0)$.

[6]This mass is obtained for a central scalar-field amplitude $|\varphi(0)|/M_{\rm Pl} = 0.0124$ and results in a compactness estimate $C = 0.024$ in radial gauge. For comparison the Kaup limit configuration has $M = 0.633$ and $C = 0.12$.

The stars are initially located $d_{\rm init} = 80\ m^{-1}$ apart in the x direction and also offset by an impact parameter $b = 8\ m^{-1}$ perpendicular to this axis; it is through this offset (rather than a velocity component off the x direction) that the binary is endowed with initial orbital angular momentum. The Newtonian point-particle estimate for the angular momentum of this configuration,

$$L_{\rm N} = Mbv_x = 0.316\ M_{\rm Pl}^2/m^2 \tag{4.5}$$

agrees remarkably well with the relativistic measurement which only deviates by 1.1 %. A summary of this binary's initial data together with the main parameters of the numerical setup are given in Table 4.3. We have simulated numerous other binary configurations – different boson star masses, initial velocities v and impact parameters b – that display qualitatively the same behaviour. The main features of the binary dynamics that we will report in the following are thus *not* a consequence of any fine tuning of initial data.

For all simulations, we use a square box of width $D = 1024\ m^{-1}$, employing the adaptive mesh refinement (AMR) capabilities of GRChombo [181, 27, 70]. Besides the standard computation of the Newman-Penrose scalar whose implementation in GRChombo is described in detail in reference [181], we compute in our simulations two diagnostic quantities specific to the boson star systems under study.

First, we introduce the mass measure

$$M = \int_\Omega \rho \sqrt{\gamma} dV\ , \tag{4.6}$$

where $\rho = T_{\mu\nu} n^\mu n^\nu$ is the energy density as measured by observers moving along the normal vector n^μ to the spatial hypersurfaces. The second is a time-dependent measure, $\tilde{L}$, defined in reference [77] and also in reference [76], for the angular momentum contained inside a specified volume V. This quantity is obtained by adding to the initial angular momentum the time integrated rate of change due to the source of momentum that crucially includes contributions from the spacetime dynamics.

4.2.2 The Merger Remnant

When colliding two boson stars with angular momentum, we expect one of the following outcomes:

1. A toroidal spinning boson star [100, 239, 194, 207],
2. A spinning boson star [208],
3. A non-spinning boson star with perturbations carrying away the angularmomentum [154, 153, 240, 229],

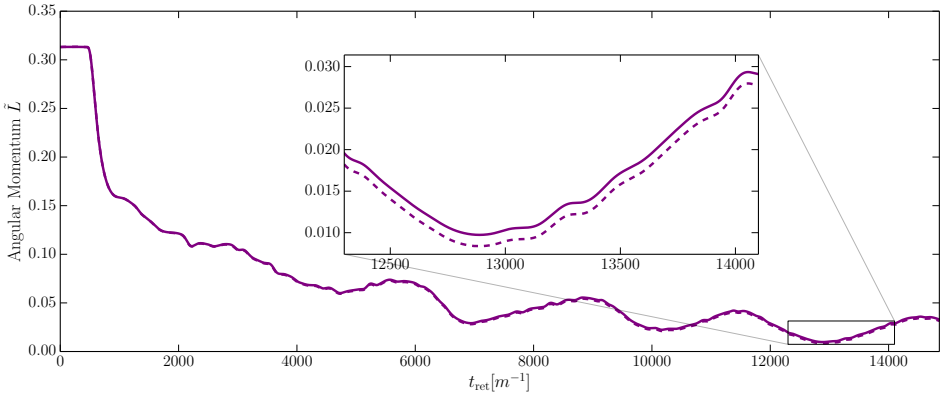

Fig. 4.10 **Angular momentum of the scalar field**: We show the angular momentum $\tilde{L}$ inside a coordinate sphere of radius 60 m^{-1} as a function of time. We compute $\tilde{L}$ in two ways, (i) via integrating the outgoing flux – solid lines – and (ii) as a volume-integral – dotted lines. This was plotted using run 2 of Table 4.3.

4. A black hole [110, 172, 42],

5. Total dispersion of all matter.

For sufficiently small compactness of the progenitors the merger does not form a black hole. While we have observed black-hole formation in some of our calibration runs starting with more compact boson stars, in the remainder of this paper we focus on the scenario where the merger results in a compact bosonic configuration without a horizon as shown in Figure 4.9. The scalar-amplitude profiles in this figure (nor at any other times during the evolution) display no signs of a toroidal structure and we therefore interpret the merger outcome as a perturbed non-spinning boson star corresponding to the second item in the above list; cf. also Refs. [172, 42].

In Figure 4.10, we display the angular momentum $\tilde{L}$ of the boson star configuration inside a coordinate sphere of radius 60 m^{-1} throughout inspiral, merger and the afterglow phase. Up to the time of merger around $t \approx 300\ m^{-1}$, the angular momentum remains approximately constant before rapidly decreasing in the post-merger phase. To leading order, the tail of the resulting curve $\tilde{L}(t)$ is approximated by an exponential decay with half-life $4 \times 10^3\ m^{-1}$, as obtained from an exponential fit to the data of Run 2 starting at $t = 2000\ m^{-1}$.

Translated into SI units, the half-life is

$$t_{\rm half} = 83 \text{ years} \left(\frac{10^{-21}\text{eV}}{m} \right) . \tag{4.7}$$

For a scalar mass $m = 10^{-14}$ eV, for example, the dominant frequency of the $\ell = 2$, $m = 0$ signal falls into the most sensitive region of the LISA noise curve (see (4.8) below) and we obtain a half-life of ~ 4 min. For scalar masses in or above this regime, this implies that a delayed formation of a black hole, should it occur, will result in a black hole with negligible spin. With regard to the possibility of the formation of a black-hole population through isolated boson star progenitors [111, 161], this implies that spinning black holes are unlikely to have formed this way unless the boson star progenitors are composed of ultra light scalar particles. More quantitatively, we see from Equation (4.7), that astrophysically large decay times for the angular momentum of order $\mathcal{O}(\mathrm{Myr})$ require ultra light scalars with mass[7] $m \lesssim 10^{-25}\,\mathrm{eV}$.

The rapid drop in the angular momentum of rotating scalar soliton stars has been noticed as early as the mid 1980s [138, 93], but we note that the post-merger evolution of our $\tilde{L}$, besides an approximately exponential drop, also exhibits significant oscillations on a time scale of about $2\,000\ m^{-1}$. We conjecture that these oscillations arise from the complex dynamics of the post-merger remnant and may carry memory of its formation process.

We also observe significant oscillations in the time evolution of the merger remnant's mass M as defined in Equation (4.6). As demonstrated in Figure 4.11, however, the mass evolution differs significantly from that of the angular momentum. First, the mass gradually levels off at $M \sim 0.57\ M_{\mathrm{Pl}}^2/m$ or ~ 72 % of the initial mass instead of decaying over time. Second, the oscillations occur on a much shorter time scale.

4.2.3 Gravitational Wave Signal

We now turn our attention to the gravitational wave signal generated by the boson star coalescence. We find this signal to be dominated by the $(l,m) = (2,\pm 2)$ and $(2,0)$ quadrupole modes which are displayed in Figure 4.12 for Run 2 using an extraction radius $220\ m^{-1}$. The large burst around merger at $t \approx 300\ m^{-1}$ (see the upper left inset of the figure) closely resembles the corresponding features regularly seen in the merger of black-hole binaries. The ensuing long-lived, semi-regular radiation clearly visible with barely any signs of diminuition up to the end of our simulation, however, drastically differs from the familiar ringdown of a merged black hole. This *afterglow* signal is the main result of our study. We emphasize that this signal is well resolved (rather than merely displaying numerical noise), and also persists with negligible variation under changes in the numerical resolution of our grid. As discussed in more detail in [77], we estimate the numerical uncertainty of the $r\Psi_4$ signal at about 7 % during the afterglow phase with most of this error budget being due to

[7] Note that candidates below $m \lesssim 10^{-22}\,\mathrm{eV}$ are ruled out as constituting 100% of the DM by structure formation constraints but may still form some proportion of the DM [155]

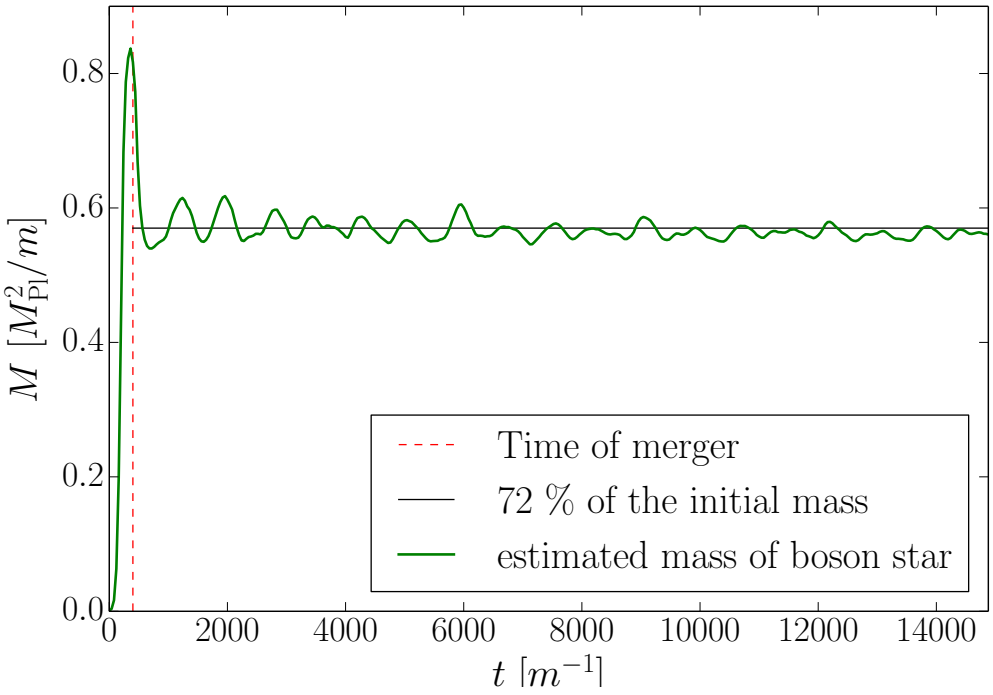

Fig. 4.11 **The estimated mass** using (4.6) contained inside a box Ω with side length $40\ m^{-1}$ as computed for the "medium" resolution run 2 of Table 4.3. Since the boson stars are not initially inside this box, the mass at $t = 0$ is close to zero. The small fluctuations after merger are due to the gauge-dependence of the measure.

the finite extraction radius. The gravitational wave signals of the higher-resolution Runs 3 and 4, if added to Figure 4.12, would almost overlap with that shown in the figure for Run[8] 2; cf. also Figure 4.13 below.

The afterglow signal (without the prodigious merger burst) is also shown in Figure 4.14 together with its Fourier spectrum. The frequency spectrum demonstrates contributions on many time scales, but also reveals a narrow dominant peak at $f_{\rm dom} \approx 0.6 \times 10^{-2}\ m$ which, translated into SI units, can be written as

$$f_{\rm dom} \sim 9.0 \cdot 10^{-2}\ \text{Hz} \left(\frac{m}{10^{-14}\ \text{eV}} \right) . \tag{4.8}$$

Both the time- and frequency-domain signals exhibit signature of beating effects: the amplitude of the rapid oscillations itself undergoes a modulation at lower frequency.

The prolonged afterglow furthermore accumulates a non-negligible amount of energy emitted in gravitational waves. By the end of our simulation at $t \approx 15\,000\ m^{-1}$, the radiated

[8] Run 2 is our longest simulation and therefore used for most of our analysis.

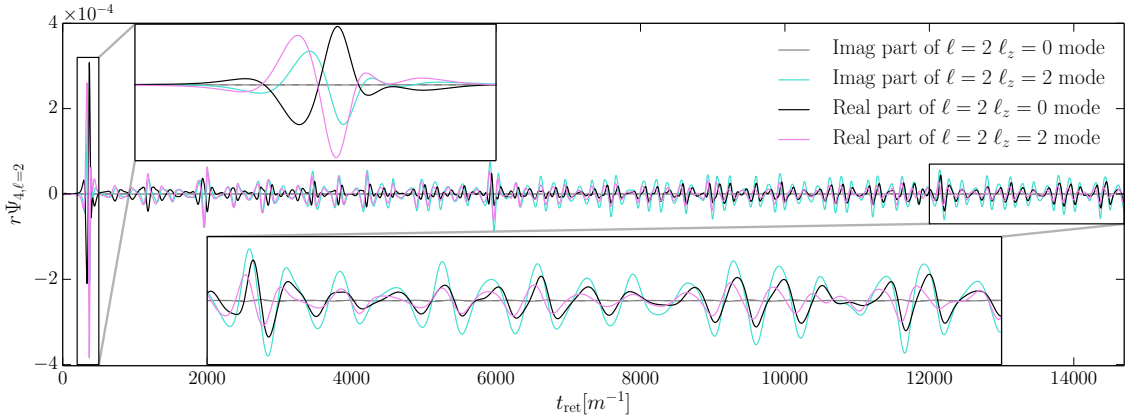

Fig. 4.12 **Gravitational wave afterglow** emission from the collision of two boson stars with non-zero impact parameter ("medium" run in 4.3). The Weyl scalar Ψ_4 is extracted at $r = 220\,m^{-1}$ and we only show the dominant $(\ell,\ell_z) = (2,2),(2,0)$ modes. The $(\ell,\ell_z) = (2,\pm 1)$ vanishes identically due to symmetry. There is a large initial burst at merger (first zoom-in box), followed by a long, but irregular signal produced by the excited remnant boson star. A video of the merger can be found at https://youtu.be/JE5FRG7kgvU.

energy computed according to

$$\frac{\mathrm{d}E}{\mathrm{d}t} = \lim_{r\to\infty} \frac{1}{16\pi} \sum_{\ell=2,m} \left| \int_{t_0}^{t} r\Psi_{4,\ell m}\, \mathrm{d}t' \right|^2 \tag{4.9}$$

including infall and merger has reached (0.04 ± 0.0014) % of the initial mass, corresponding to an average rate of $2.5\times 10^{-8} M_{\mathrm{init}}\, m$ (see dotted line in 4.15). The radiated energy and power are shown as functions of time in Figure 4.15 and clearly show an approximately linear increase in E_{GW} during the afterglow phase. This significant amount of post-merger gravitational wave emission in itself is a striking signature of exotic binary merger progenitors that distinguishes them from black hole binaries devoid of significant post-merger radiation beyond the quasi-normal ringdown. By using windowing of the gravitational wave signal, we find that the rate of radiation in the afterglow (excluding the merger peak) decreases by about 20% over the course of the simulation. Note that the decay in gravitational waves is much more protracted than the drop in the angular momentum displayed in Figure 4.10. Clearly, the system loses angular momentum much more rapidly than energy.

A more subtle feature in the post-merger signal is revealed in the multi-polar decomposition of the quadrupole signal; more specifically in the relative position of the local extrema in the $(\ell,\ell_z) = (2,2)$ and $(2,0)$ modes. As exhibited by the upper left inset of Figure 4.12, the amplitudes of the $(2,2)$ and $(2,0)$ modes are almost exactly in anti-phase

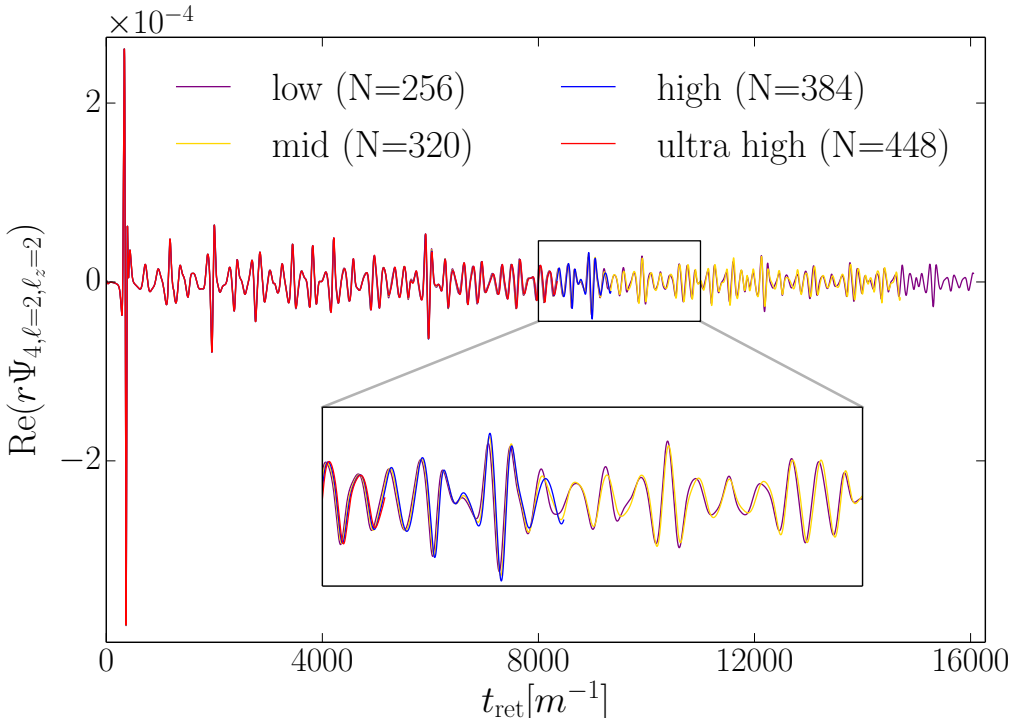

Fig. 4.13 **Convergence**: We display the $(2,2)$ multipole of the gravitational wave signal obtained for four different resolutions corresponding to runs 1 to 4 in 4.3. A quantitative analysis yields overall convergence at first order.

around merger and remain so in the early afterglow around $t \sim 1\,000\,m^{-1}$. At late times $t \gtrsim 3\,000\,m^{-1}$, however, the two modes are almost synchronized with their extrema in good overlap. The timing of this synchronization coincides remarkably well with the drop in angular momentum shown in Figure 4.10 and we hypothesize the two effects are causally related. This would imply a concrete observational signature of the boson star angular momentum in the emitted gravitational wave afterglow signal.

In physical terms, the gravitational wave afterglow is a direct consequence of the the presence of matter around the compact merger remnant and the resulting complex matter dynamics following the violent merger. A qualitatively similar behaviour may arise in the merger of neutron stars provided these do not promptly merge into a black hole. Two key differences between neutron-star and boson-star binaries, however, may aid considerably in the distinction between neutron-star and boson star signals. The first consists in the extremely long-lived nature of the boson star afterglow which we anticipate will last for much longer times than are presently within grasp of our numerical studies; cf. again Figure 4.12 and the barely perceptible drop in the gravitational wave signal. The second fundamental discriminator arises from the scale-free nature of the boson star

	Run	N	$d_{\rm init}\ [m^{-1}]$	$b\ [m^{-1}]$	v_x	$M\ [M_{\rm Pl}^2 m^{-1}]$
low	1	256	80	8	0.1	0.395(0)
medium	2	320	80	8	0.1	0.395(0)
high	3	384	80	8	0.1	0.395(0)
ultra-high	4	448	80	8	0.1	0.395(0)

Table 4.3 **Overview** of the simulations. Here, M is the individual mass of each boson star, v_x the initial velocity, b the impact parameter, $d_{\rm init}$ the initial distance in the x direction, b the vertical offset or *impact parameter* and N is the number of cells on the coarsest AMR Level (which sets the resolution of the respective runs). We allow for seven extra refinement levels. The data associated with these runs can be found here: https://github.com/ThomasHelfer/BosonStarAfterglow,

spacetimes; the scalar mass parameter m appears as a characteristic scale in all dimensional variables of the gravitational wave analysis. While neutron star masses are restricted to be below the Chandrasekhar limit of about $2M_\odot$, boson stars may theoretically exist across the entire mass spectrum and barring for a remarkable coincidence in the scalar mass value, will be distinguishable from their neutron-star counter parts by the frequency regime of their gravitational wave emission. Put the other way round, comprehensive observational searches for gravitational wave signatures from boson stars require scanning over a wide range of frequencies using vastly different detectors such as LIGO-Virgo-KAGRA, LISA, third-generation detectors but also high frequency gravitational wave observatories presently under development [17, 32].

4.2.4 Conclusion

In this section, we have shown that the inspiral and coalescence of boson star binaries into a non-black hole remnant can produce a long-lasting gravitational wave *afterglow*. This signature is salient, and markedly differs in duration and – possibly – also frequency from the gravitational wave signatures of more traditional astrophysical compact object mergers; it thus represents a distinct detection channel for exotic compact objects in compact-binary-coalescence and continuous-gravitational wave searches [3, 8, 9, 7, 16, 15, 14, 13].

There are several implications resulting from our findings. In terms of search strategies, as mentioned in the introduction, these signatures are likely to be missed if we focus exclusively on constructing pre-merger inspiral and merger waveform templates. The systematic construction of waveform templates for post-merger signatures of this type of binaries is in its infancy at present and an immediate challenge for further work consists in identifying an effective parameterization of the gravitational wave signatures. Our results furthermore demonstrate an efficient loss of angular momentum in boson star

mergers resulting in a horizon-less remnant, consistent with previous studies noticing that the spin of rotating boson stars decays with a fairly short half-life of $4 \times 10^3\ m^{-1}$ [192]. We also observe a remarkable correlation between the boson star remnant's spin-down in Figure 4.10 with a gradual synchronization of the local extrema in the gravitational wave amplitudes of the $(2,2)$ and $(2,0)$ modes; from near anti-alignment of the peaks around merger and shortly thereafter, the extrema gradually shift into approximate overlap over a time interval $\Delta t \approx 2\,000\ m^{-1}$ (see Figure 4.12), coinciding exactly with the time during which the angular momentum drops to a negligible level. We tentatively conclude that through this synchronization, the gravitational wave afterglow carries important information about the remnant's dynamical evolution.

Given the extraordinary length of the afterglow signal, one would expect the radiation from numerous boson star merger events – if they occur – to result in a stochastic background. Such a background could be searched for additionally to that expected from more traditional binary mergers [78]. Evidently, more exploration of the underlying boson star parameter space and the resulting afterglow phenomenology will be required to relate theoretical estimates of the gravitational wave background to hypothesized boson star populations. We reiterate, however, that nothing about our boson star configurations has been fine-tuned, so that we expect the afterglow to be a rather generic feature of boson star coalescences as long as these do not promptly form a black hole.

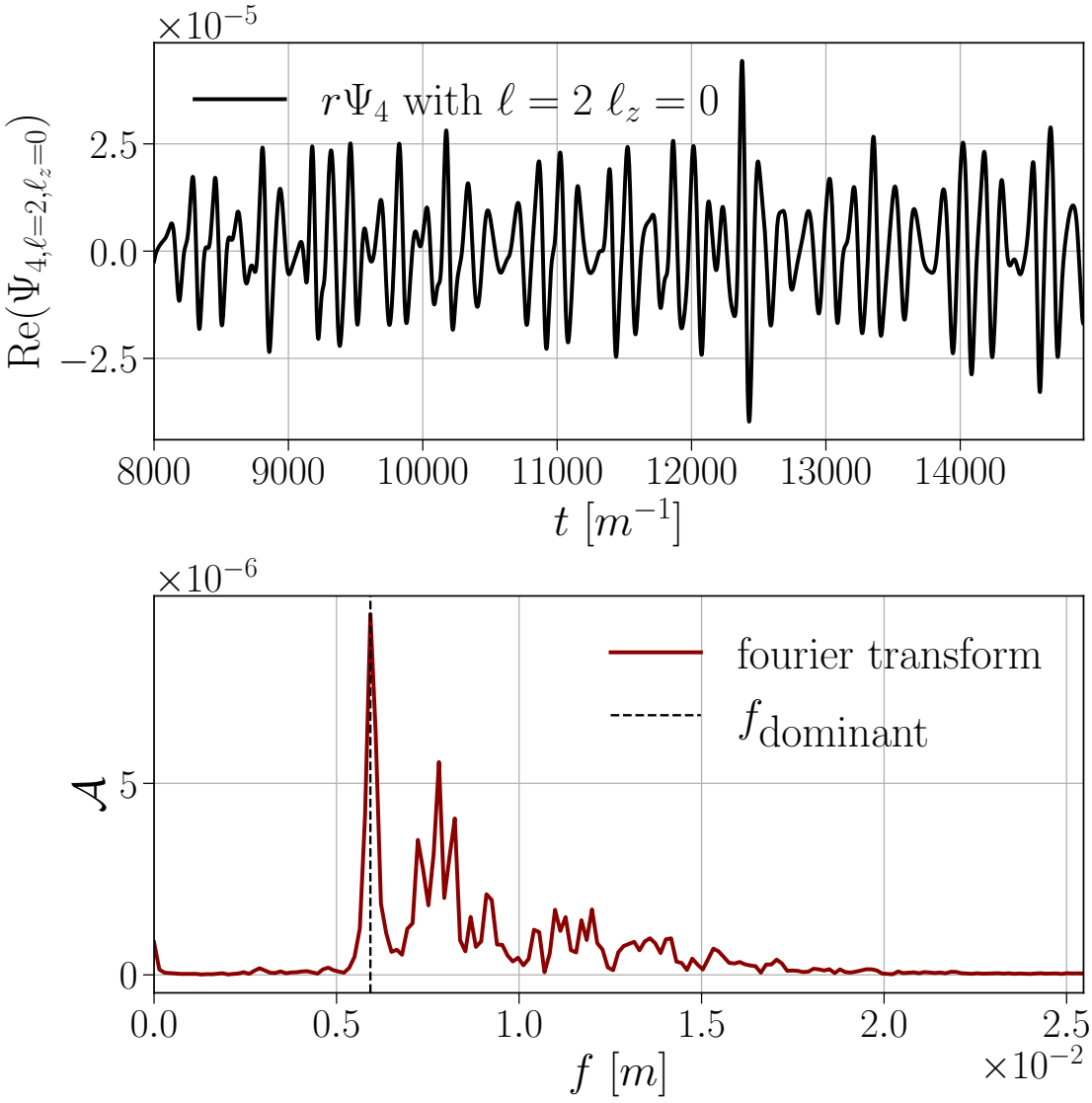

Fig. 4.14 **Time domain signal and Fourier transform of the** $(2,0)$ **mode of** $r\Psi_4$: We perform a Fourier transformation of the tail of the gravitational wave signal of the "medium" resolution run in 4.3. We find excellent agreement between the displayed spectrum for the $(2,0)$ mode and the corresponding Fourier transform of the $(2,2)$ mode; in particular, both yield the same peak frequency.

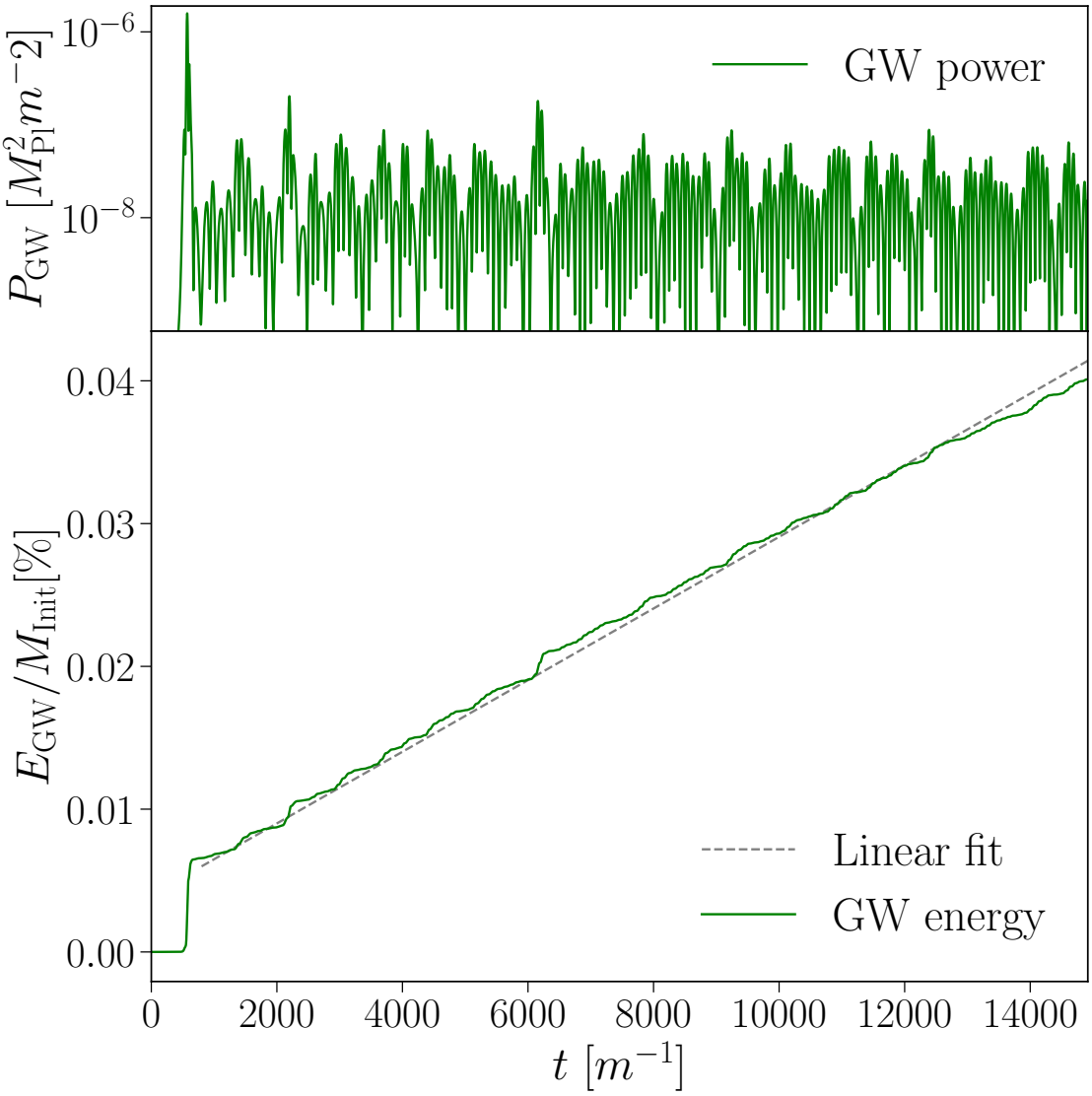

Fig. 4.15 **Radiated gravitational wave energy over time**: We calculate the energy and power radiated in gravitational waves from the "medium" resolution run of 4.3. We observe no significant reduction in the gravitational wave radiation over the simulation time, allowing us to estimate a lower bound on the half-life of the signal.

Chapter 5

Gravitational Wave from Phase Transitions of Boson Star Mergers

"Without freedom of criticism, there is no true praise."

In this chapter, we introduce our ongoing research. My contribution to this study includes the development of a 2D boson star code, which enhances the existing 2D framework. I applied this new code for evolutionary simulations and data processing. Our research explores the behavior of binary solitons in head-on collision models. Although numerous studies have already demonstrated a remarkably rich phenomenology in the merger dynamics and gravitational wave emission of boson star binaries [207, 192, 239, 156, 206, 79, 112, 77, 172, 31, 43, 87, 209, 41, 42, 110, 57, 193, 62, 208, 152], our current understanding remains largely confined to isolated points or patches in the boson star parameter space. This leaves systematic exploration of the complete parameter space as a key challenge for future complementary work. Specifically, we examine a two-dimensional hypersurface of the parameter space spanned by σ and the boson star compactness, controlled through the central scalar-field amplitude. Across this parameter range, we monitor the boson star dynamics during infall and merger, the remnant characteristics and the gravitational wave emission. The initial conditions were set using the novel superposition method, as introduced in the previous Chapter 4. We employed a more efficient two-dimensional code in this work, which significantly expedited the evolution process, compared to the previously used three-dimensional code.

Our findings indicate that **(1)** boson star collisions can be radiatively far more efficient than those of black holes, **(2)** discontinuities exist in the gravitational wave energy as a function of $A_{\rm ctr}$, **(3)** even away from these discontinuities, small initial configuration differences lead to significant gravitational wave emission variations, **(4)** for unstable

boson stars, the timescale for either migration to another boson star or collapse into a black hole is independent of perturbations, and **(5)** there appears to be a significant correlation between the radiated energy $E_{\rm GW}(A_{\rm ctr})$ and the mass function $M(A_{\rm ctr})$.

In our units, the speed of light and Planck's constant are set to unity, $c = \hbar = G = 1$, and the gravitational constant is expressed in terms of the Planck mass, $G = 1/M_{\rm Pl}^2$. Therefore, for the sake of brevity, the unit $M_{\rm Pl}$ will frequently be omitted when referring to σ and the central amplitude in this chapter. Additionally, in many of the ***evolution*** result figures, the x-axis is simply labeled as **Amplitude**, which refers to the **Initial Central Amplitude**. Unless otherwise stated, Latin indices range from 1 to 3, and Greek indices from 0 to 3.

5.1 Cartoon Method

5.1.1 Cartoon Method in 4-Dimenional Spacetime

Classical Approach to the Cartoon Method

Even if we use Cartesian coordinates for both the coordinate basis and grid point allocation, we can still simulate symmetric spacetimes by appropriately applying symmetry conditions. The **Cartoon Method** is based on this principle. This method, proposed by Alcubierre et al. in 1999 [23], was initially used for vacuum spacetime. Shortly thereafter, Shibata adopted the cartoon method for systems coupled with hydrodynamics and demonstrated its effectiveness in stably and accurately simulating the collapse of rotating stars [201]. The method was later extended to higher dimensions to address problems in higher-dimensional spacetime [205, 74]. In this work, we utilized the cartoon method to simplify a three-dimensional code into a two-dimensional code to improve computational efficiency.

The cartoon method allows for the efficient development of numerical relativity codes for symmetric spacetimes, even when a fully three-dimensional code in Cartesian coordinates (x,y,z) is already available. The computational cost of simulations using the cartoon method is comparable to that of codes using cylindrical coordinates. The main advantage of the Cartoon approach is that it entirely avoids the issue of coordinate singularities at the axis and origin, rendering the regularity problem irrelevant [19, 202].

After defining the computational domain, we designate the z-axis as the axis of symmetry. In the cartoon method, the evolution equations for geometric variables are solved only on the x-z plane at $y = 0$. Simulations are essentially performed on this two-dimensional subspace, similar to ordinary axisymmetric simulations.

Since a Cartesian grid is employed, all spatial derivatives must be evaluated in these coordinates. The derivatives associated with the x and z coordinates can be straightforwardly computed using finite differencing. However, since the evolution equations are solved only on the $y = 0$ plane, we do not explicitly evolve the data for $y \neq 0$ plane. Therefore, we utilize symmetry relations to evaluate the derivatives associated with the y-coordinate.

Specifically, we need several grid points in the neighborhood of $y = 0$ to evaluate the derivatives associated with the y-coordinate on the $y = 0$ plane using finite differencing. The number of necessary points depends on the chosen order of accuracy in the finite differencing. In our code, we use fourth-order finite differencing, which requires five grid points: $y = 0$, $y = \pm\Delta y$ and $y = \pm 2\Delta y$.

The next task is to assign the data at points where $y \neq 0$ using the axisymmetric relation. First, we define the cylindrical coordinates (ρ, φ, z), where the cylindrical radius ρ is given by $\rho = \sqrt{x^2 + y^2}$ for a point (x,y) with $y \neq 0$. Two points, (x,y) and $(\rho,0)$, are equivalent in axisymmetric spacetime (see Figure 5.1). For a scalar function (denoted by F), the z-

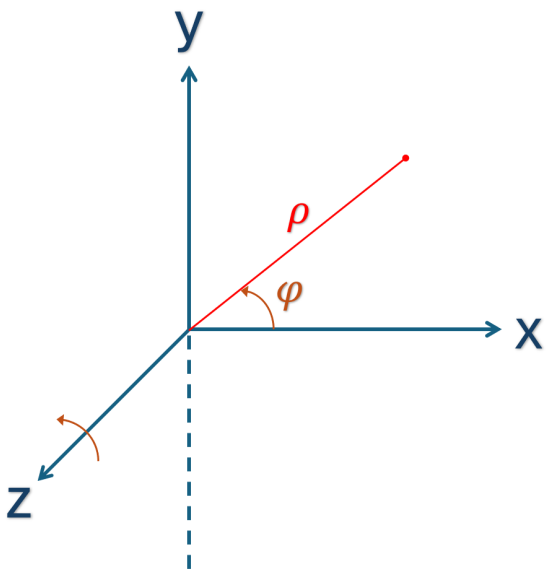

Fig. 5.1 This figure illustrates the cartoon method. We use Cartesian coordinates (x,y,z), with the z-axis as the axis of symmetry. In the x-y plane, we introduce polar coordinates (ρ,φ,z).

component of a vector function (denoted by V^z), and the zz-component of a tensor function (denoted by T^{zz}), the data at (x,y) are determined by the axisymmetric relation as follows:

$$\begin{aligned} F(x,y,z) &= F(\rho,0,z), \\ V^z(x,y,z) &= V^z(\rho,0,z), \\ T^{zz}(x,y,z) &= T^{zz}(\rho,0,z). \end{aligned} \tag{5.1}$$

It should be noted that not every grid point on the $y \neq 0$ plane has a corresponding grid point on the x-axis. For example, in Figure 5.2, grid point A on the $y \neq 0$ plane corresponds to grid point A' on the x-axis. However, the corresponding point B', associated with grid point B, does not lie on a grid point along the x-axis. Therefore, the values at these points must be determined using an interpolation scheme with the nearby grid points on the x-axis.

Here, we use a rank 2 tensor as an example to demonstrate this transformation process. Specifically, we consider the case of a rank 2 tensor, T_{ij}. Using the rotation matrix,

$$\Lambda(\varphi)^i{}_j = \begin{pmatrix} \cos\varphi & -\sin\varphi & 0 \\ \sin\varphi & \cos\varphi & 0 \\ 0 & 0 & 1 \end{pmatrix}. \tag{5.2}$$

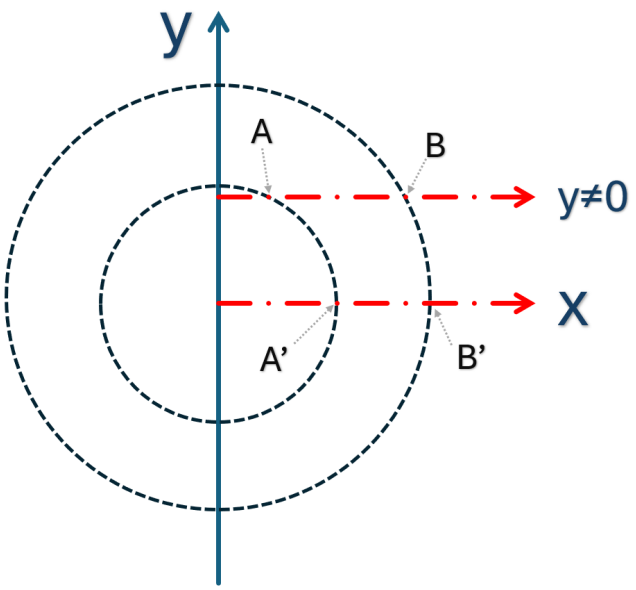

Fig. 5.2 This figure illustrates the relationship between points on the $y \neq 0$ plane and points on the $y = 0$ plane. The dots on the red line represent grid points in the actual numerical evolution. As shown, points A, A', and B lie on grid points, whereas B' does not. Therefore, an interpolation scheme is required to calculate the value at B'.

The tensor T_{ij} on the $y \neq 0$ plane can be written as

$$T_{ij}(\rho\cos\varphi, \rho\sin\varphi, z) = \Lambda(\varphi)^{k}{}_{i}\Lambda(\varphi)^{l}{}_{j}T_{kl}(\rho, 0, z). \tag{5.3}$$

Equation (5.3) successfully relates the points on the $y \neq 0$ plane to those on the $y = 0$ plane. Specifically, to determine the value of a rank-2 tensor at any point on the $y \neq 0$ plane, one simply needs to transform the corresponding Cartesian coordinates into cylindrical coordinates through a straightforward coordinate transformation, and then substitute the values of ρ, φ, and z into Equation (5.3).

$SO(3)$ Symmetry in 4-Dimensional Spacetime

Next, we will extend from axial symmetry $SO(2)$ to spherical symmetry $SO(3)$. Before doing so, we first need to make some adjustments to our notation to better accommodate the requirements of higher symmetry. We will change the rotation axis from the z-axis to the x-axis, establishing a polar coordinate (ρ, φ) in the y-z plane. The x-y plane will be selected as the plane for our actual evolution, while the z-axis will serve as the *redundant coordinate axis* (corresponding to the y-axis in the previous Section 5.1.1). This is also consistent with our actual 2D boson star code, as illustrated in Figure 5.5. Additionally, in

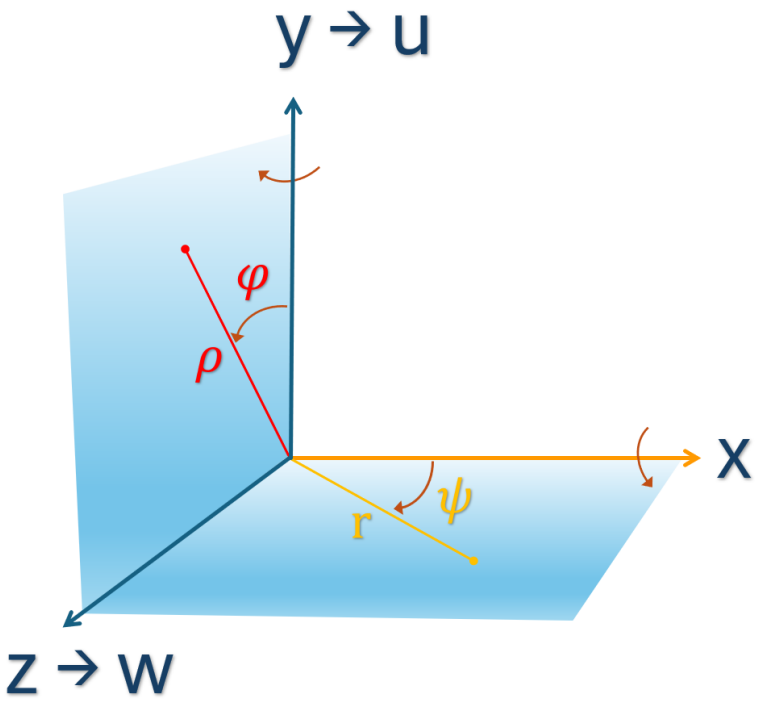

Fig. 5.3 This figure demonstrates the process of reconstructing three-dimensional space from one-dimensional evolution codes while accounting for $SO(3)$ symmetry. In higher-dimensional spacetime, to differentiate the actual evolution axis from the reduced redundant axes, we label all redundant axes as $w, u, \cdots$.

higher-dimensional cases, there may be several ***redundant*** axes. To further clarify which axis will be reduced, we label all the ***redundant*** coordinates as w (or u if needed).

One can prove that for the case of rotational symmetry in the φ direction, we can always choose coordinates such that the off-diagonal metric components $g_{\mu w}$ vanish [74]. Therefore, under axial symmetry $SO(2)$, the metric can be reduced to the following form:

$$\begin{pmatrix} g_{00} & g_{01} & g_{02} & g_{03} \\ g_{10} & g_{11} & g_{12} & g_{13} \\ g_{20} & g_{21} & g_{22} & g_{23} \\ g_{30} & g_{31} & g_{32} & g_{33} \end{pmatrix} \xrightarrow{SO(2)} \begin{pmatrix} g_{00} & g_{01} & g_{02} & 0 \\ g_{10} & g_{11} & g_{12} & 0 \\ g_{20} & g_{21} & g_{22} & 0 \\ 0 & 0 & 0 & g_{ww} \end{pmatrix}. \tag{5.4}$$

Note that in the new notation, since the z-axis is the axis being reduced, it is represented by "w" instead of "3".

Furthermore, we can apply a similar approach to consider $SO(3)$ symmetry, where we introduce an additional "redundant" axis, which we label as u, and establish the coordinate system as shown in Figure 5.3. Under $SO(3)$ symmetry, we only need to evolve the data along the x-axis and obtain the entire three-dimensional space through two rotations. Specifically, after obtaining the data on the x-axis, we first rotate it by $\frac{\pi}{2}$ in the x-y (or x-u)

plane along ψ to generate a sector. Then, we rotate it by 2π in the y-z (or u-w) plane along φ to obtain a hemisphere. By considering the portion of the x-axis where $x < 0$, we obtain the entire sphere.

Under such symmetry, the metric can be further reduced to the following form,

$$\begin{pmatrix} g_{00} & g_{01} & g_{02} & g_{03} \\ g_{10} & g_{11} & g_{12} & g_{13} \\ g_{20} & g_{21} & g_{22} & g_{23} \\ g_{30} & g_{31} & g_{32} & g_{33} \end{pmatrix} \xrightarrow{SO(3)} \begin{pmatrix} g_{00} & g_{01} & 0 & 0 \\ g_{10} & g_{11} & 0 & 0 \\ 0 & 0 & g_{uu} & 0 \\ 0 & 0 & 0 & g_{ww} \end{pmatrix}. \tag{5.5}$$

5.1.2 High-Dimensional Extensions of the Cartoon Method

The previous Section 5.1.1 introduced the cartoon method in 4-Dimensional spacetime. However, the cartoon method can essentially reduce the spacetime dimensions in D-dimensional spacetimes to $(d+1)$ dimensions by utilizing the $SO(D-d)$ symmetry[1]. This means that the ***spatial*** dimensions are reduced from $(D-1)$ to d dimensions, allowing the evolution to be performed using a 3D code. As a result, the computational cost is reduced by a factor of $N^{(D-1)-d}$.

Instead of using rotation matrices to obtain data, we introduce Killing vectors, which allow us to more effectively express the data on planes where the *redundant* coordinate axis is non-zero [74]. In our practical applications, we also employ this method. Below, we will introduce this approach in the context of $SO(D-3)$ symmetry in D-dimensional spacetime.

Coordinates and Notation

In higher-dimensional cases, we adopt the following notational conventions to enhance clarity and prevent misunderstandings or ambiguities.

We express a D-dimensional spacetime with Cartesian coordinates in the following form:

$$(t,\overbrace{x,y,z,\underbrace{w,u,v,\cdots,w^{D-1}}}^{\textbf{Uppercase}}) = (t,x,y,z,\overbrace{w^a}^{w,u,v,\cdots}). \tag{5.6}$$
$$\textbf{Lowercase}$$

Additionally, we make further conventions.

- None of the transformations involve the time coordinate, so in most cases, we can disregard t.
- The coordinate x is used to represent either x or y. Any result obtained for x applies equally to y after substituting x with y.
- z exclusively represents itself.
- w, u, and v denote distinct coordinates from the set $\{w^a\}$, meaning $w \neq u$, $u \neq v$, and $v \neq w$.
- ***Uppercase*** Latin indices range from 1 to $D-1$, ***lowercase early*** Latin indices range from 4 to $D-1$, and ***lowercase late*** Latin indices correspond to the x, y, and z directions.

[1]For example, consider a spacetime with $D = 11$ $(10+1)$ dimensions. When this spacetime has $SO(D-d=8)$ symmetry, the reduced spacetime will have $d+1=4$ dimensions. After performing a 3+1 decomposition on such a spacetime, it can be evolved using a 3-dimensional code.

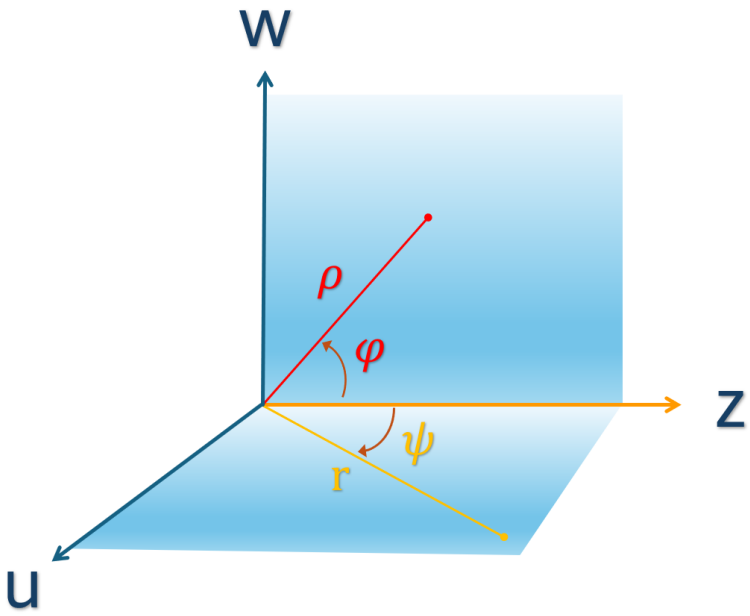

Fig. 5.4 This figure presents a diagram illustrating the transformation from Cartesian coordinates to polar coordinates. In this context, (ρ, φ) lies in the z-w plane, while (r, ψ) lies in the z-u plane.

With $SO(D-3)$ symmetry, which implies the presence of rotational Killing vectors in the planes spanned by z and w^a, or w^a and w^b, we consider coordinate transformations that replace two of the Cartesian coordinates (z, w^a) with polar coordinates, denoted by (ρ, φ).

Assuming that the transformation to polar coordinates involves z and a fixed w^n, the resulting polar coordinates are denoted by

$$x^{\bar{M}} = \left(t, x, y, \rho, w^4, \cdots, w^{n-1}, \varphi, w^{n+1}, \cdots, w^{D-1}\right), \tag{5.7}$$

where the ***bar*** indicates the transformed coordinates.

We use the aforementioned notational conventions to clearly express this coordinate transformation as follows:

$$x^A = (x, z, w, u, v) \quad \leftrightarrow \quad x^{\bar{M}} = (x, \rho, \varphi, u, v), \tag{5.8}$$

and similarly for the z-u or z-v planes (see Figures 5.4).

The coordinate transformations are given by

$$\begin{aligned} \rho &= \sqrt{z^2+w^2}, \\ \varphi &= \arctan\frac{w}{z}, \\ z &= \rho\cos\varphi, \\ w &= \rho\sin\varphi. \end{aligned} \tag{5.9}$$

and the Jacobian matrices by

$$\begin{pmatrix} \frac{\partial z}{\partial\rho} = \frac{z}{\rho} & \frac{\partial z}{\partial\varphi} = -w \\ \frac{\partial w}{\partial\rho} = \frac{w}{\rho} & \frac{\partial w}{\partial\varphi} = z \end{pmatrix}, \tag{5.10}$$

$$\begin{pmatrix} \frac{\partial\rho}{\partial z} = \frac{z}{\sqrt{w^2+z^2}} & \frac{\partial\rho}{\partial w} = \frac{w}{\sqrt{w^2+z^2}} \\ \frac{\partial\varphi}{\partial z} = -\frac{w}{z^2+w^2} & \frac{\partial\varphi}{\partial w} = \frac{z}{z^2+w^2} \end{pmatrix}. \tag{5.11}$$

Lie Derivatives and Spherical Symmetry

Spherical symmetry in N dimensions implies the existence of $N(N-1)/2$ rotational Killing vectors, one for each plane in the N dimensions. For Killing vector ξ, we have

$$\mathscr{L}_\xi g_{AB} = 0 \tag{5.12}$$

which also holds in the "barred" coordinate system, i.e.

$$\mathscr{L}_\xi g_{\bar{M}\bar{N}} = 0. \tag{5.13}$$

Specifically, for the rotational symmetry in the z-w plane,

$$\xi = \partial_\varphi \quad \Leftrightarrow \quad \xi^{\bar{M}} = \delta^{\bar{M}}{}_{\bar{n}}, \tag{5.14}$$

where $\bar{n}$ is the fixed index corresponding to the coordinate φ in the system $x^{\bar{M}}$ (see Equation (5.7)). Substituting this into the definition of the Lie derivative of the metric, we obtain

$$\mathscr{L}_\xi g_{\bar{M}\bar{N}} = \xi^{\bar{K}}\partial_{\bar{K}} g_{\bar{M}\bar{N}} + \left(\partial_{\bar{M}}\xi^{\bar{K}}\right) g_{\bar{K}\bar{N}} + \left(\partial_{\bar{N}}\xi^{\bar{K}}\right) g_{\bar{M}\bar{K}} = \partial_\varphi g_{\bar{M}\bar{N}} = 0. \tag{5.15}$$

This relation applies individually to each metric component. Furthermore, from

$$\partial_\varphi g^{\bar{A}\bar{B}} = -g^{\bar{A}\bar{M}} g^{\bar{B}\bar{N}} \partial_\varphi g_{\bar{M}\bar{N}} = 0, \tag{5.16}$$

we immediately obtain the same result for the inverse metric.

All ADM variables can be sequentially constructed from the metric, its derivative, and its inverse, using exclusively variables at each stage whose φ derivative has already been shown to vanish,

$$\begin{aligned} \gamma_{IM} &= g_{IM}, \\ \beta^I &= \gamma^{IM} g_{0M}, \\ \alpha &= \frac{1}{\sqrt{-g^{00}}}, \\ K_{IJ} &= -\frac{1}{2\alpha}\left(\partial_t \gamma_{IJ} - \beta^M \partial_M \gamma_{IJ} - \gamma_{MJ}\partial_I \beta^M - \gamma_{IM}\partial_J \beta^M\right). \end{aligned} \tag{5.17}$$

This construction is valid in any coordinates adapted to the spacetime decomposition, and we therefore omit the ***bars*** over the indices.

By also considering that ∂_φ commutes with all other partial derivative operators, and repeating the procedure from Equation (5.16) for the inverse spatial metric γ^{IJ}, we conclude that the φ derivative of all ADM variables vanishes.

Furthermore, all BSSN variables are constructed directly from the ADM variables, as well as the derivative of the spatial metric and its inverse,

$$\phi = \frac{1}{4(D-1)} \ln \gamma,$$

$$K = \gamma^{MN} K_{MN},$$

$$\tilde{\gamma}_{IJ} = e^{-4\phi}\gamma_{IJ} \quad \Leftrightarrow \quad \tilde{\gamma}^{IJ} = e^{4\phi}\gamma^{IJ}, \tag{5.18}$$

$$\tilde{A}_{IJ} = e^{-4\phi}\left(K_{IJ} - \frac{1}{D-1}\gamma_{IJ}K\right) \quad \Leftrightarrow \quad K_{IJ} = e^{4\phi}\left(\tilde{A}_{IJ} + \frac{1}{D-1}\tilde{\gamma}_{IJ}K\right),$$

$$\tilde{\Gamma}^I = \tilde{\gamma}^{MN}\tilde{\Gamma}^I_{MN} = \tilde{\gamma}^{MN}\tilde{\gamma}^{IK}\left(\partial_M \tilde{\gamma}_{NK} - \frac{1}{2}\partial_K \tilde{\gamma}_{MN}\right).$$

This construction is valid in any coordinate system adapted to the spacetime split. Notably, we have now established that the φ derivative of all BSSN variables vanishes.

To derive the relations imposed on the Cartesian components and derivatives of the BSSN variables, one additional detail is needed. For rotational symmetry in the φ direction, it is always possible to choose coordinates such that the off-diagonal metric components $g_{\bar{M}\varphi}$ vanish. This property extends to the BSSN variables $\tilde{\gamma}_{IJ}$ and $\tilde{A}_{IJ}$ in the same manner as described above for the φ derivatives.

The construction of the shift vector in Equation (5.17) implies that

$$\gamma^{\varphi M} = 0 \quad \Rightarrow \quad \beta^{\varphi} = 0. \tag{5.19}$$

Similarly, the vanishing of $\tilde{\gamma}^{\varphi K}$ in the construction of $\tilde{\Gamma}^{I}$ in Equation (5.18) implies that

$$\tilde{\gamma}^{\varphi K} = 0 \quad \Rightarrow \quad \tilde{\Gamma}^{\varphi} = 0. \tag{5.20}$$

Components and Derivatives

We shall illustrate, using the ww component of a tensor density of weight $\mathscr{W}$, how rotational symmetry leads to relations between different tensor components and their derivatives. We first note that a tensor density of weight $\mathscr{W}$ transforms under the coordinate transformation given by Equation (5.9) as follows,

$$T_{\bar{A}\bar{B}} = D^{\mathscr{W}} \frac{\partial x^M}{\partial x^{\bar{A}}} \frac{\partial x^N}{\partial x^{\bar{B}}} T_{MN}, \tag{5.21}$$

where

$$D \equiv \det\left(\frac{\partial x^M}{\partial x^{\bar{A}}}\right) = \begin{vmatrix} \frac{\partial z}{\partial \rho} & \frac{\partial z}{\partial \varphi} \\ \frac{\partial w}{\partial \rho} & \frac{\partial w}{\partial \varphi} \end{vmatrix} = \rho, \tag{5.22}$$

is the determinant of the Jacobian.

Our goal now is to replace derivatives in directions off the x-y-z hyperplane, such as derivatives with respect to w, u, v, and so on, with derivatives in the x, y, or z directions. The procedure to obtain such relations is similar for all types of variables, and we will illustrate it using the T_{ww} component as an example. For this purpose, we write

$$\partial_w T_{ww} = \frac{\partial \rho}{\partial w} \partial_\rho T_{ww} + \frac{\partial \varphi}{\partial w} \partial_\varphi T_{ww}, \tag{5.23}$$

and substitute for T_{ww} using

$$T_{ww} = D^{-\mathscr{W}} \Big(\frac{\partial \rho}{\partial w} \frac{\partial \rho}{\partial w} T_{\rho\rho} + 2 \frac{\partial \rho}{\partial w} \frac{\partial \varphi}{\partial w} \underbrace{T_{\rho\varphi}}_{=0} + \frac{\partial \varphi}{\partial w} \frac{\partial \varphi}{\partial w} T_{\varphi\varphi} \Big). \tag{5.24}$$

This is the first instance where we utilize a symmetry property: $T_{\rho\varphi} = 0$. Substituting Equation (5.24) into Equation (5.23) yields, among many other terms, derivatives of the $\rho\rho$ and $\varphi\varphi$ components of T with respect to the coordinates ρ and φ. The vanishing of the latter is the second point where rotational symmetry comes into play, while the ρ derivatives are obtained through the standard transformation.

$$\begin{aligned}
\partial_\rho T_{\rho\rho} &= \left(\frac{\partial z}{\partial \rho}\partial_z + \frac{\partial w}{\partial \rho}\partial_w\right)\left[D^{\mathscr{W}}\left(\frac{\partial z}{\partial \rho}\frac{\partial z}{\partial \rho}T_{zz} + 2\frac{\partial z}{\partial \rho}\frac{\partial w}{\partial \rho}T_{zw} + \frac{\partial w}{\partial \rho}\frac{\partial w}{\partial \rho}T_{ww}\right)\right], \\
\partial_\rho T_{\varphi\varphi} &= \left(\frac{\partial z}{\partial \rho}\partial_z + \frac{\partial w}{\partial \rho}\partial_w\right)\left[D^{\mathscr{W}}\left(\frac{\partial z}{\partial \varphi}\frac{\partial z}{\partial \varphi}T_{zz} + 2\frac{\partial z}{\partial \varphi}\frac{\partial w}{\partial \varphi}T_{zw} + \frac{\partial w}{\partial \varphi}\frac{\partial w}{\partial \varphi}T_{ww}\right)\right], \\
\partial_\varphi T_{\rho\rho} &= 0, \\
\partial_\varphi T_{\varphi\varphi} &= 0.
\end{aligned} \tag{5.25}$$

It is crucial that after the computation, the final step is to set $w = 0$ in the resulting expression, as we ultimately need the relations only in the computational domain, i.e., the x-y-z hyperplane. After substituting everything into Equation (5.23) and setting $w = 0$, we obtain $\partial_w T_{ww} = 0$. Additional Cartesian derivative operators can then be applied to the complete expression for $\partial_w T_{ww}$ (with $w = 0$ set only after taking the derivative), allowing us to derive the following relations,

$$\begin{aligned}
\partial_w T_{ww} = \partial_z \partial_w T_{ww} = \partial_x \partial_w T_{ww} = \partial_u \partial_w T_{ww} = 0, \\
\partial_w \partial_w T_{ww} = \frac{\partial_z T_{ww}}{z} + 2\frac{T_{zz} - T_{ww}}{z^2}.
\end{aligned} \tag{5.26}$$

We summarize the key details to be mindful of in the calculations, as they will be crucial for the subsequent computations.

- The derivatives of all BSSN variables along the Killing vectors vanish.
- The off-diagonal metric components $g_{\bar{M}\varphi}$ vanish.
- Set $w^a = 0$ in the resulting expression.

We still need to calculate the u derivative of T_{ww} to complete this analysis. To do so, we begin with Expression (5.24) for T_{ww} and substitute the following,

$$T_{\rho\rho} = D^{\mathscr{W}}\left(\frac{\partial z}{\partial \rho}\frac{\partial z}{\partial \rho}T_{zz} + 2\frac{\partial z}{\partial \rho}\frac{\partial w}{\partial \rho}T_{zw} + \frac{\partial w}{\partial \rho}\frac{\partial w}{\partial \rho}T_{ww}\right), \tag{5.27}$$

$$T_{\varphi\varphi} = D^{\not W}\left(\frac{\partial z}{\partial \varphi}\frac{\partial z}{\partial \varphi}T_{zz} + 2\frac{\partial z}{\partial \varphi}\frac{\partial w}{\partial \varphi}T_{zw} + \frac{\partial w}{\partial \varphi}\frac{\partial w}{\partial \varphi}T_{ww}\right). \tag{5.28}$$

This gives us an expression for T_{ww} exclusively in terms of Cartesian components and coordinates, constrained by the rotational symmetry in the z-w plane. Having obtained this expression, we can now disregard the coordinate system (ρ, φ).

Next, we consider a separate coordinate transformation to accommodate the rotation in the z-u plane (see Figures 5.4),

$$\begin{aligned} r &= \sqrt{z^2 + u^2}, \\ \psi &= \arctan\frac{u}{z}, \\ z &= r\cos\psi, \\ u &= r\sin\psi. \end{aligned} \tag{5.29}$$

The corresponding Jacobian matrix is given by

$$\begin{pmatrix} \frac{\partial z}{\partial r} = \frac{z}{r} & \frac{\partial z}{\partial \psi} = -u \\ \frac{\partial u}{\partial r} = \frac{u}{r} & \frac{\partial u}{\partial \psi} = z \end{pmatrix}, \tag{5.30}$$

$$\begin{pmatrix} \frac{\partial r}{\partial z} = \frac{z}{\sqrt{u^2+z^2}} & \frac{\partial r}{\partial u} = \frac{u}{\sqrt{u^2+z^2}} \\ \frac{\partial \psi}{\partial z} = -\frac{u}{z^2+u^2} & \frac{\partial \psi}{\partial u} = \frac{z}{z^2+u^2} \end{pmatrix}. \tag{5.31}$$

Note that rotational symmetry now implies that all ψ derivatives vanish, allowing us to write,

$$\partial_u T_{ww} = \frac{\partial r}{\partial u}\partial_r T_{ww} + \frac{\partial \psi}{\partial u}\underbrace{\partial_\psi T_{ww}}_{=0} = \frac{\partial r}{\partial u}\left(\frac{\partial u}{\partial r}\partial_u T_{ww} + \frac{\partial z}{\partial r}\partial_z T_{ww}\right). \tag{5.32}$$

Gathering all terms and setting $u = 0$ and $w = 0$, we find that $\partial_u T_{ww}$ vanishes. As before, we can directly take additional derivatives of $\partial_u T_{ww}$ and then set $u = w = 0$. This gives us,

$$\begin{aligned} \partial_u T_{ww} = \partial_v \partial_u T_{ww} = \partial_w \partial_u T_{ww} = \partial_x \partial_u T_{ww} = \partial_z \partial_u T_{ww} = 0, \\ \partial_u \partial_u T_{ww} = \frac{\partial_z T_{ww}}{z}. \end{aligned} \tag{5.33}$$

Equations (5.26) and (5.33) allow us to express all derivatives of T_{ww} outside the computational domain in terms of expressions within the x-y-z hyperplane. Consequently, we need to introduce additional grid functions, such as T_{ww}, but we do not need to extend the computational domain beyond the "$3+1$" case. It is also important to note that spherical symmetry imposes constraints on the components of T. In analogy to Equation (5.24), we

construct,

$$T_{zw} = D^{-\mathscr{W}} \left(\frac{\partial \rho}{\partial w} \frac{\partial \rho}{\partial z} T_{\rho\rho} + \frac{\partial \varphi}{\partial w} \frac{\partial \varphi}{\partial z} T_{\varphi\varphi} \right), \tag{5.34}$$

$$T_{zz} = D^{-\mathscr{W}} \left(\frac{\partial \rho}{\partial z} \frac{\partial \rho}{\partial z} T_{\rho\rho} + \frac{\partial \varphi}{\partial z} \frac{\partial \varphi}{\partial z} T_{\varphi\varphi} \right), \tag{5.35}$$

where we have used the fact that, due to rotational symmetry, $T_{\rho\varphi} = 0$. Substituting the expressions for $T_{\rho\rho}$ and $T_{\varphi\varphi}$ from Equations (5.27) and (5.28) into Equations (5.24), (5.34), and (5.35), and setting $w = 0$, we obtain $T_{zw} = 0$.

Instead of z, we could have chosen any other Cartesian coordinate that forms a rotationally symmetric plane with w, leading to the same result, $T_{uw} = 0$. For T_{ww} and T_{zz}, we merely obtain identities with no additional information, but it is worth noting that we can always rescale the Cartesian coordinates such that $T_{uu} = T_{ww}$.

Finally, we can write

$$T_{xw} = \frac{\partial \rho}{\partial w} T_{x\rho} + \frac{\partial \varphi}{\partial w} \underbrace{T_{x\varphi}}_{=0} = \frac{w}{\rho} T_{x\rho} \overset{w \to 0}{=} 0. \tag{5.36}$$

Summary of All Expressions

By applying the procedure described in the previous section to scalars, vectors, and rank-2 tensors or their corresponding densities, we obtain the following relations for derivatives in Cartesian coordinates.

Scalar

For a scalar function, we have

$$\begin{aligned} \partial_w \Psi =& \partial_x \partial_w \Psi = \partial_z \partial_w \Psi = \partial_u \partial_w \Psi = 0, \\ \partial_w \partial_w \Psi =& \frac{\partial_z \Psi}{z}. \end{aligned} \tag{5.37}$$

Vector

For a vector , we have

$$\begin{aligned} V^w &= \partial_x V^w = \partial_z V^w = \partial_u V^w = 0, \\ \partial_w V^w &= \frac{V^z}{z}, \\ \partial_w \partial_w V^w &= 2\frac{V^w}{z^2} + 2\frac{\partial_w V^z}{z} = 0 + 0 = 0, \\ \partial_u \partial_w V^w &= \frac{\partial_u V^z}{z} = 0, \\ \partial_x \partial_w V^w &= \frac{\partial_x V^z}{z}, \\ \partial_z \partial_w V^w &= \frac{\partial_z V^z}{z} - \frac{V^z}{z^2}, \\ \partial_w V^z &= \partial_x \partial_w V^z = \partial_z \partial_w V^z = \partial_u \partial_w V^z = 0, \\ \partial_w \partial_w V^z &= \frac{\partial_z V^z}{z} - \frac{V^z}{z^2}, \\ \partial_w V^x &= \partial_x \partial_w V^x = \partial_z \partial_w V^x = \partial_u \partial_w V^x = 0, \\ \partial_w \partial_w V^x &= \frac{\partial_z V^x}{z}. \end{aligned} \tag{5.38}$$

Rank-2 Tensor

For a rank-2 tensor , we have

$$
\begin{aligned}
T_{ww} &= T_{uu}, \\
T_{xw} &= T_{zw} = T_{uw} = 0, \\
\partial_w T_{ww} &= \partial_x \partial_w T_{ww} = \partial_z \partial_w T_{ww} = \partial_u \partial_w T_{ww} = 0, \\
\partial_w \partial_w T_{ww} &= 2\frac{T_{zz} - T_{ww}}{z^2} + \frac{\partial_z T_{ww}}{z}, \\
\partial_u T_{ww} &= \partial_x \partial_u T_{ww} = \partial_z \partial_u T_{ww} = \partial_w \partial_u T_{ww} = \partial_v \partial_u T_{ww} = 0, \\
\partial_u \partial_u T_{ww} &= \frac{\partial_z T_{ww}}{z}, \\
\partial_u T_{uw} &= \partial_x \partial_u T_{uw} = \partial_z \partial_u T_{uw} = \partial_u \partial_u T_{uw} = \partial_v \partial_u T_{uw} = 0, \\
\partial_u \partial_w T_{uw} &= \frac{\partial_u T_{zu}}{z} = \frac{T_{zz} - T_{ww}}{z^2}, \\
\partial_v T_{uw} &= \partial_x \partial_v T_{uw} = \partial_z \partial_v T_{uw} = \partial_{\tilde{v}} \partial_v T_{uw} = 0, \\
\partial_w T_{zw} &= \frac{T_{zz} - T_{ww}}{z}, \\
\partial_x \partial_w T_{zw} &= \frac{\partial_x T_{zz} - \partial_x T_{ww}}{z}, \\
\partial_z \partial_w T_{zw} &= -\frac{T_{zz} - T_{ww}}{z^2} + \frac{\partial_z T_{zz} - \partial_z T_{ww}}{z}, \\
\partial_w \partial_w T_{zw} &= 2\frac{\partial_w T_{zz}}{z} + 8\frac{T_{zw}}{z^2} - 2\frac{\partial_w T_{ww}}{z} = 0,
\end{aligned}
\tag{5.39}
$$

$$
\begin{aligned}
\partial_u \partial_w T_{zw} &= \frac{\partial_u T_{zz}}{z} - \frac{\partial_u T_{ww}}{z} = 0, \\
\partial_u T_{zw} &= \partial_x \partial_u T_{zw} = \partial_z \partial_u T_{zw} = \partial_u \partial_u T_{zw} = \partial_v \partial_u T_{zw} = 0, \\
\partial_w T_{zz} &= \partial_x \partial_w T_{zz} = \partial_z \partial_w T_{zz} = \partial_u \partial_w T_{zz} = 0, \\
\partial_w \partial_w T_{zz} &= -2\frac{T_{zz} - T_{ww}}{z^2} + \frac{\partial_z T_{zz}}{z}, \\
\partial_w T_{xz} &= \partial_x \partial_w T_{xz} = \partial_z \partial_w T_{xz} = \partial_u \partial_w T_{xz} = 0, \\
\partial_w \partial_w T_{xz} &= \frac{\partial_z T_{xz}}{z} - \frac{T_{xz}}{z^2}, \\
\partial_w T_{xw} &= \frac{T_{xz}}{z}, \\
\partial_x \partial_w T_{xw} &= \frac{\partial_x T_{xz}}{z}, \\
\partial_z \partial_w T_{xw} &= \frac{\partial_z T_{xz}}{z} - \frac{T_{xz}}{z^2}, \\
\partial_w \partial_w T_{xw} &= \frac{\partial_w T_{xz}}{z} + \frac{T_{xw}}{z^2} = 0, \\
\partial_u T_{xw} &= \partial_x \partial_u T_{xw} = \partial_z \partial_u T_{xw} = \partial_w \partial_u T_{xw} = \partial_u \partial_u T_{xw} = \partial_v \partial_u T_{xw} = 0, \\
\partial_w T_{xx} &= \partial_x \partial_x T_{xx} = \partial_z \partial_w T_{xx} = \partial_u \partial_w T_{xx} = 0, \\
\partial_w \partial_w T_{xx} &= \frac{\partial_z T_{xx}}{z}.
\end{aligned}
\tag{5.40}
$$

Concise Index Notation

We introduce the following notation: Late Latin indices $i, j, k, \cdots$ cover the x, y, and z directions as usual, i.e., they run from 1 to 3. Early Latin indices $a, b, c, \cdots$ cover the additional coordinates $w_1, w_2, w_3, \cdots$, running from 4 to $D-1$. Furthermore, we use the indices z and w to denote the quasiradial coordinate of the computational domain and a Cartesian coordinate off the hyperplane, respectively. It turns out that all components off the hyperplane are the same, and w represents the corresponding expressions. The z and w indices are therefore fixed and are not summed over when they appear repeatedly, as is done for other indices according to the Einstein summation convention. With this notation, we can reformulate the above as follows:

$$
\begin{aligned}
\partial_a \Psi &= 0, \\
\partial_i \partial_a \Psi &= 0, \\
\partial_a \partial_b \Psi &= \delta_{ab} \frac{\partial_z \Psi}{z}, \\
V^a &= 0, \\
\partial_i V^a &= 0, \\
\partial_a V^b &= \delta^b{}_a \frac{V^z}{z}, \\
\partial_i \partial_a V^b &= \delta^b{}_a \left(\frac{\partial_i V^z}{z} - \delta_{iz} \frac{V^z}{z^2} \right), \\
\partial_a \partial_b V^c &= 0, \\
\partial_a V^i &= 0, \\
\partial_a \partial_b V^i &= \delta_{ab} \left(\frac{\partial_z V^i}{z} - \delta^i_z \frac{V^z}{z^2} \right),
\end{aligned}
\tag{5.41}
$$

$$
\begin{aligned}
T_{ab} &= \delta_{ab} T_{ww}, \\
\partial_a T_{bc} &= 0, \\
\partial_a \partial_b T_{cd} &= (\delta_{ac}\delta_{bd} + \delta_{ad}\delta_{bc}) \frac{T_{zz} - T_{ww}}{z^2} + \delta_{ab}\delta_{cd} \frac{\partial_z T_{ww}}{z}, \\
\partial_i \partial_a T_{bc} &= 0, \\
T_{ia} &= 0, \\
\partial_a T_{ib} &= \delta_{ab} \frac{T_{iz} - \delta_{iz} T_{ww}}{z}, \\
\partial_a \partial_b T_{ic} &= 0, \\
\partial_i \partial_a T_{jb} &= \delta_{ab} \left(\frac{\partial_i T_{jz} - \delta_{jz} \partial_i T_{ww}}{z} - \delta_{iz} \frac{T_{jz} - \delta_{jz} T_{ww}}{z^2} \right), \\
\partial_a T_{ij} &= 0, \\
\partial_a \partial_b T_{ij} &= \delta_{ab} \left(\frac{\partial_z T_{ij}}{z} - \frac{\delta_{iz} T_{jz} + \delta_{jz} T_{iz} - 2\delta_{iz}\delta_{jz} T_{ww}}{z^2} \right), \\
\partial_i \partial_a T_{jk} &= 0.
\end{aligned}
\tag{5.42}
$$

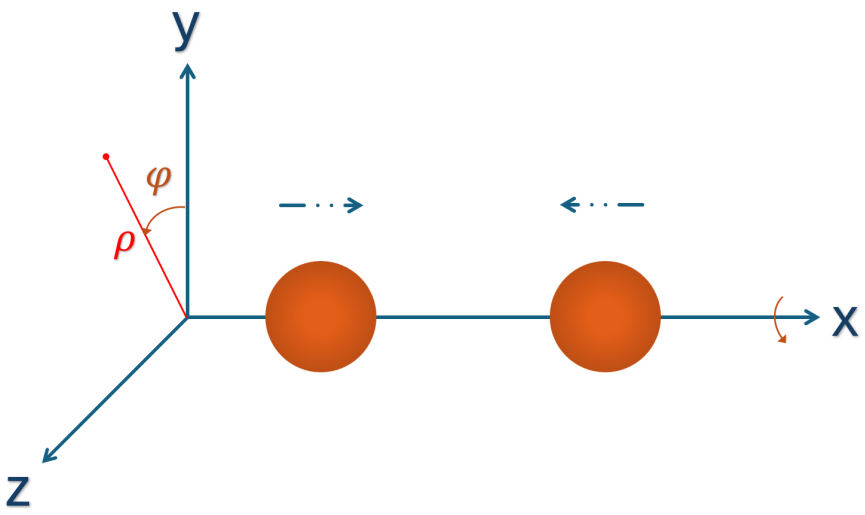

Fig. 5.5 This figure illustrates the evolution scheme used in the actual 2D boson stars code. The evolution is performed in Cartesian coordinates (x,y,z). In the figure, the two boson stars undergo a head-on collision in the region where $x > 0$. Unlike in Figure 5.1, the x-axis is chosen as the axis of symmetry in this setup.

5.2 2-Dimensional Boson Stars Code

In the previous section, we covered the fundamental concepts and techniques of the cartoon method. Here, we will outline the Cartoon strategy utilized in our work, followed by a description of the implementation of our 2D boson star code.

We use (x,y,z) to denote Cartesian coordinates and assume rotational symmetry about the x-axis. Then, we construct cylindrical coordinates (ρ,φ,x) as shown in Figure 5.5.

By evolving the data on the $z = 0, y \geq 0, x \geq 0$ plane, it is evident that the complete three-dimensional data can be obtained by rotating it around the φ direction. Thus, one only needs to define and evolve the initial conditions in this x-y plane[2].

The transformation between the two coordinate systems is as follows:

$$\begin{aligned} \varphi &= \arctan\frac{z}{y}, \\ y &= \rho\cos\varphi, \\ z &= \rho\sin\varphi, \\ \rho &= \sqrt{y^2+z^2}. \end{aligned} \tag{5.43}$$

[2]Since there is only one redundant axis in our code, it is unnecessary to use w^a as a label here.

We will use the following notation for tensor indices:

$$\begin{aligned} A,B,C,\cdots &= 0,1,2,3, \\ I,J,K,\cdots &= 1,2,3, \\ i,j,k,\cdots &= 1,2, \\ a,b,c,\cdots &= 3. \end{aligned} \tag{5.44}$$

In cylindrical coordinates, the Killing field is represented by $\xi = \partial_\varphi$, and the condition $\mathscr{L}_\xi g_{AB} = 0$ implies that $\partial_\varphi g_{AB} = 0$.

Next, we will apply the approach from the previous section to explore how $SO(2)$ symmetry causes many components of the tensor to vanish. We begin with the symmetric tensor T_{AB}. $SO(2)$ symmetry requires that $T_{i\varphi} = 0$. By applying the tensor transformation rules, we derive:

$$\begin{aligned} T_{i\varphi} &= \frac{\partial X^A}{\partial x^i}\frac{\partial X^B}{\partial \varphi}T_{AB} \\ &= \frac{\partial X^A}{\partial x^i}\left(\frac{\partial y}{\partial \varphi}T_{Ay} + \frac{\partial z}{\partial \varphi}T_{Az}\right) \\ &= -zT_{iy} + yT_{iz}. \end{aligned} \tag{5.45}$$

Thus, $T_{iz} = \frac{z}{y}T_{iy}$. Employing a comparable approach, we derive:

$$\begin{aligned} T_{\rho\varphi} &= \frac{\partial X^A}{\partial \rho}\frac{\partial X^B}{\partial \varphi}T_{AB} \\ &= \frac{\partial y}{\partial \rho}\frac{\partial y}{\partial \varphi}T_{yy} + \frac{\partial y}{\partial \rho}\frac{\partial z}{\partial \varphi}T_{yz} + \frac{\partial z}{\partial \rho}\frac{\partial y}{\partial \varphi}T_{zy} + \frac{\partial z}{\partial \rho}\frac{\partial z}{\partial \varphi}T_{zz} \\ &= -z\cos\varphi T_{yy} + y\cos\varphi T_{yz} - z\sin\varphi T_{zy} + y\sin\varphi T_{zz}. \end{aligned} \tag{5.46}$$

This yields:

$$\begin{aligned} \left(\frac{y^2}{\rho} - \frac{z^2}{\rho}\right)T_{yz} &= \frac{yz}{\rho}\left(T_{yy} - T_{zz}\right), \\ T_{yz} &= \frac{yz}{y^2+z^2}\left(T_{yy} - T_{zz}\right). \end{aligned} \tag{5.47}$$

Given our assumption of operating exclusively in the region where $z = 0$, the aforementioned Equations (5.45) (5.47) lead to the conclusion that $T_{iz} = 0$.

The Killing field can be represented as follows:

$$\xi^A = y\left(\frac{\partial}{\partial z}\right)^A - z\left(\frac{\partial}{\partial y}\right)^A. \tag{5.48}$$

Within the $z=0$ hyperplane, the Lie derivative is applied to T_{ia}:

$$\begin{aligned}
\mathscr{L}_\xi T_{ia} &= \xi^A \partial_A T_{ia} + T_{Aa}\partial_i \xi^A + T_{iA}\partial_a \xi^A \\
&= \left[y\left(\frac{\partial}{\partial z}\right)^A - z\left(\frac{\partial}{\partial y}\right)^A\right]\partial_A T_{ia} + T_{Aa}\partial_i\left[y\left(\frac{\partial}{\partial z}\right)^A - z\left(\frac{\partial}{\partial y}\right)^A\right] \\
&\quad + T_{iA}\partial_a\left[y\left(\frac{\partial}{\partial z}\right)^A - z\left(\frac{\partial}{\partial y}\right)^A\right] \\
&= y\partial_z T_{ia} - z\partial_y T_{ia} + T_{za}\delta_{iy} - T_{ya}\delta_{iz} + T_{iz}\delta_{ay} - T_{iy}\delta_{az}
\end{aligned} \tag{5.49}$$

(Taking into account the z=0 plane and the range of index values.)

$$= y\partial_z T_{ia} + T_{zz}\delta_{iy} - T_{iy}.$$

Given that $\mathscr{L}_\xi T_{ia} = 0$, it follows that: $\partial_z T_{iz} = \frac{T_{iy} - T_{zz}\delta_{iy}}{y}$.

By following a similar process, as in the previous section, we can derive higher-order tensor results and their corresponding derivatives. Detailed derivations and results can be found in reference [74]. Here, we present only the modified results relevant to our study.

$$\begin{aligned}
\partial_z \phi_{Re/Im} &= \partial_i \partial_z \phi_{Re/Im} = 0, \\
\partial_z^2 \phi_{Re/Im} &= \frac{\partial_y \phi_{Re/Im}}{y}, \\
V^z &= \partial_i V^z = \partial_z V^i = \partial_z^2 V^z = 0, \\
\partial_z V^z &= \frac{V^y}{y}, \\
\partial_i \partial_z V^z &= \left(\frac{\partial_i V^y}{y} - \delta_{iy}\frac{V^y}{y^2}\right), \\
\partial_z^2 V^i &= \left(\frac{\partial_y V^i}{y} - \delta^i_y \frac{V^y}{y^2}\right), \\
T_{iz} &= \partial_z T_{zz} = \partial_i \partial_z T_{zz} = \partial_z^2 T_{iz} = \partial_z T_{ij} = \partial_i \partial_z T_{jk} = 0.
\end{aligned} \tag{5.50}$$

Using these results, we can adapt the BSSN formalism and the evolution equations for matter to suit our two-dimensional problem. The BSSN results are also available in reference [74]. Below, we present the forms of the matter fields and the evolution equations relevant to our study.

$$\partial_t \phi_{Re} = \beta^k \partial_k \phi_{Re} - \alpha \Pi_{Re},$$

$$\partial_t \phi_{Im} = \beta^k \partial_k \phi_{Im} - \alpha \Pi_{Im},$$

$$\partial_t \Pi_{Re} = \beta^k \partial_R \Pi_{Re} - \psi \tilde{\gamma}^{ij} \partial_i \phi_{Re} \partial_j \alpha + \alpha \left(\chi \tilde{\Gamma}^k \partial_k \phi_{Re} + \frac{1}{2} \tilde{\gamma}^{lk} \partial_k \chi \partial_l \phi_{Re} - \psi \tilde{\gamma}^{zz} \frac{\partial_y \phi_{Re}}{y} + K \Pi_{Re} + V' \right),$$

$$\partial_t \Pi_{Im} = \beta^k \partial_R \Pi_{Im} - \psi \tilde{\gamma}^{ij} \partial_i \phi_{Im} \partial_j \alpha + \alpha \left(\chi \tilde{\Gamma}^k \partial_k \phi_{Im} + \frac{1}{2} \tilde{\gamma}^{lk} \partial_k \chi \partial_l \phi_{Im} - \psi \tilde{\gamma}^{zz} \frac{\partial_y \phi_{Im}}{y} + K \Pi_{Im} + V' \right),$$

$$S_{ij} = \partial_i \phi_{Re} \partial_j \phi_{Re} + \partial_i \phi_{Im} \partial_j \phi_{Im} - \frac{1}{2} \gamma_{ij} \left(\gamma^{kl} \partial_k \phi_{Re} \partial_l \phi_{Re} + \gamma^{kl} \partial_k \phi_{Im} \partial_l \phi_{Im} - \left(\Pi_{Re}^2 + \Pi_{Im}^2 \right) + V \right),$$

$$S_{zz} = -\frac{1}{2} \gamma_{zz} \left(\gamma^{kl} \partial_k \phi_{Re} \partial_l \phi_{Re} + \gamma^{kl} \partial_k \phi_{Im} \partial_l \phi_{Im} - \left(\Pi_{Re}^2 + \Pi_{Im}^2 \right) + V \right),$$

$$j_i = \Pi_{Re} \partial_i \phi_{Re} + \Pi_{Im} \partial_i \phi_{Im},$$

$$S = S_{ij} \gamma^{ij} + S_{zz} \gamma^{zz} = S_{ij} \gamma^{ij} + \frac{S_{zz}}{\gamma_{zz}}.$$

5.3 Gravitational Waves in 2D

To align with our 2D boson stars code, we require specific methods and coding techniques for computing gravitational waves in 2D. This section will detail the process of calculating gravitational waves in our study. The methods and notations described here, unlike those in Chapter 1, are in accordance with those employed in our actual code.

We follow the discussion of gravitational wave extraction in $d+1$ dimensions of reference [75] and apply it to our case of $2+1$ evolutions ($d=2$). The outgoing gravitational radiation is encoded in the the projections of the Weyl tensor C_{ABCD} onto a null tetrad $\{k^A, l^A, m^A, \bar{m}^A\}$

$$\Psi_4 = C_{ABCD} k^A \bar{m}^B k^C \bar{m}^D \tag{5.51}$$

here capital Latin indices run from 0 to d. In order to construct the null tetrad, we first define an orthonormal basis $\{e^A_{(0)}, e^A_{(1)}, e^A_{(2)}, e^A_{(3)}\}$, where $e^A_{(0)}$ is the unit normal to the spatial hypersurfaces, $e^A_{(1)}$ is the unit normal radial vector and $e^A_{(2)}, e^A_{(3)}$ are the angular vectors, which are typically constructed via Gram-Schmidt orthonormalisation. We then pick the tetrad consisting of ingoing and outgoing null vectors, k^A and l^A respectively, and a complex null vector m^A and its conjugate $\bar{m}^A$,

$$\begin{aligned} l^A &= \frac{1}{\sqrt{2}}\left(e^A_{(0)} + e^A_{(1)}\right), \\ k^A &= \frac{1}{\sqrt{2}}\left(e^A_{(0)} - e^A_{(1)}\right), \\ m^A &= \frac{1}{\sqrt{2}}\left(e^A_{(2)} + i e^A_{(3)}\right), \\ \bar{m}^A &= \frac{1}{\sqrt{2}}\left(e^A_{(2)} - i e^A_{(3)}\right). \end{aligned} \tag{5.52}$$

Following the notation and construction from reference [75], we denote the off-domain components with w, such that in $2+1$ dimensions, $e^A_{(3)}$ becomes $e^A_{(w)}$. Gravitational radiation is then re-expressed using an equivalent of Ψ_4, which we denote as Ω_{AB}. This quantity is purely real, as it is projected onto real tetrad elements and takes the following form,

$$\begin{aligned} \Omega_{(\alpha)(\beta)} = \frac{1}{4}(&R_{0B0D} e^B_{(\alpha)} e^D_{(\beta)} - R_{AB0D} e^A_{(1)} e^B_{(\alpha)} e^D_{(\beta)} \\ &- R_{0BCD} e^B_{(\alpha)} e^D_{(\beta)} e^C_{(1)} + R_{ABCD} e^A_{(1)} e^B_{(\alpha)} e^D_{(\beta)} e^C_{(1)}). \end{aligned}$$

Note that α, β here represent all angular directions. In 3D, these are (θ, ϕ), but in 2D, the only angular direction is θ, meaning the ϕ direction is outside the domain. In 2D Cartesian coordinates, the domain is parameterized by $\{x, y\}$, while z is outside the computational

domain. The system exhibits rotational symmetry about its axis, and tensor indices lying in the off-domain direction are commonly denoted by w, for example, Ω_{ww}, R_{0w0w}, etc. Assuming the stars collide along the x-axis, it is then convenient to define spherical coordinates as

$$\begin{aligned} x &= r\cos(\theta), \\ y &= r\sin(\theta)\cos(\phi), \\ z &= r\sin(\theta)\sin(\phi). \end{aligned} \tag{5.53}$$

In 2D, the stars are located in the $\phi = 0$ plane, which corresponds to $z = 0$.

Real Part of Ψ_4

Using the results from reference [75], we can express:

$$\begin{aligned} \mathrm{Re}(\Psi_4) =& \frac{1}{4} R_{ABCD}\left(e^A_{(0)} - e^A_{(1)}\right)\left(e^B_{(2)}e^D_{(2)} - e^B_{(3)}e^D_{(3)}\right)\left(e^C_{(0)} - e^C_{(1)}\right) \\ =& \frac{1}{4}\Big(R_{0B0D}e^B_{(2)}e^D_{(2)} - R_{0B0D}e^B_{(3)}e^D_{(3)} - R_{AB0D}e^A_{(1)}e^B_{(2)}e^D_{(2)} \\ &+ R_{AB0D}e^A_{(1)}e^B_{(3)}e^D_{(3)} + R_{ABCD}e^A_{(1)}e^B_{(2)}e^D_{(2)}e^C_{(1)} - R_{ABCD}e^A_{(1)}e^B_{(3)}e^D_{(3)}e^C_{(1)} \\ &- R_{0BCD}e^B_{(2)}e^D_{(2)}e^C_{(1)} + R_{0BCD}e^B_{(3)}e^D_{(3)}e^C_{(1)}\Big). \end{aligned} \tag{5.54}$$

Considering expression (5.53), we observe that:

$$\mathrm{Re}\left(\Psi_4\right) = \Omega_{22} - \Omega_{33}. \tag{5.55}$$

In 2D, the equation is reformulated as

$$\mathrm{Re}\left(\Psi_4\right) = \Omega_{22} - \Omega_{ww}. \tag{5.56}$$

Imaginary Part of Ψ_4

For the imaginary part, we have [75],

$$\begin{aligned}
\mathrm{Im}(\Psi_4) &= -\frac{1}{4} R_{ABCD}\left(e^A_{(0)} - e^A_{(1)}\right)\left(e^B_{(3)} e^D_{(2)} + e^B_{(2)} e^D_{(3)}\right)\left(e^C_{(0)} - e^C_{(1)}\right) \\
&= -\frac{1}{4}\Big(R_{0B0D} e^B_{(3)} e^D_{(2)} + R_{0B0D} e^B_{(2)} e^D_{(3)} - R_{AB0D} e^B_{(3)} e^D_{(2)} e^A_{(1)} \\
&\quad - R_{AB0D} e^A_{(1)} e^B_{(2)} e^D_{(3)} - R_{0BCD} e^B_{(3)} e^D_{(2)} e^C_{(1)} - R_{0BCD} e^B_{(2)} e^D_{(3)} e^C_{(1)} \\
&\quad + R_{ABCD} e^B_{(3)} e^D_{(2)} e^A_{(1)} e^C_{(1)} + R_{ABCD} e^A_{(1)} e^B_{(2)} e^D_{(3)} e^C_{(1)}\Big).
\end{aligned} \tag{5.57}$$

Applying equation (5.53), we obtain

$$\mathrm{Im}\,(\Psi_4) = -2\Omega_{23}. \tag{5.58}$$

In 2D, one can show that $\mathrm{Im}\,(\Psi_4) = 0$.

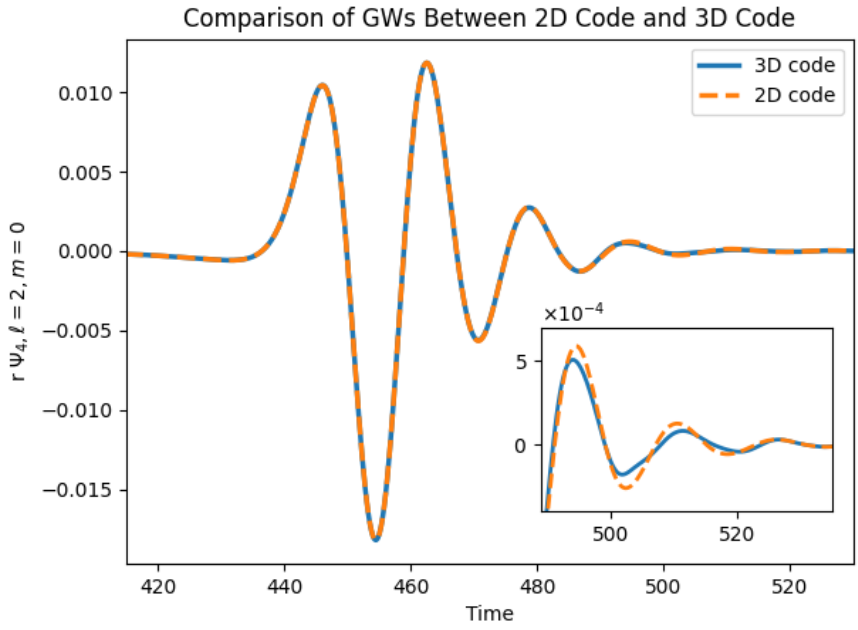

Fig. 5.6 This figure compares the $(2,0)$ mode of $r\Psi_4$ over time between our 2D code and our 3D code. The specific parameters are a distance of 80 m^{-1}, velocity of 0.1, $\sigma = 0.35$, and a central amplitude of 0.086 M_{Pl}.

2D vs. 3D Code Comparison

In Figure 5.6, we present a comparison between our 2D and 3D codes, focusing on a soliton as the model to compute gravitational waves generated in the head-on collision of two solitons. The figure illustrates that the results from the 2D code align perfectly with those from the 3D code. This consistency suggests that future simulations can be effectively conducted using our 2D code, which is expected to reduce computational time significantly, by more than an order of magnitude.

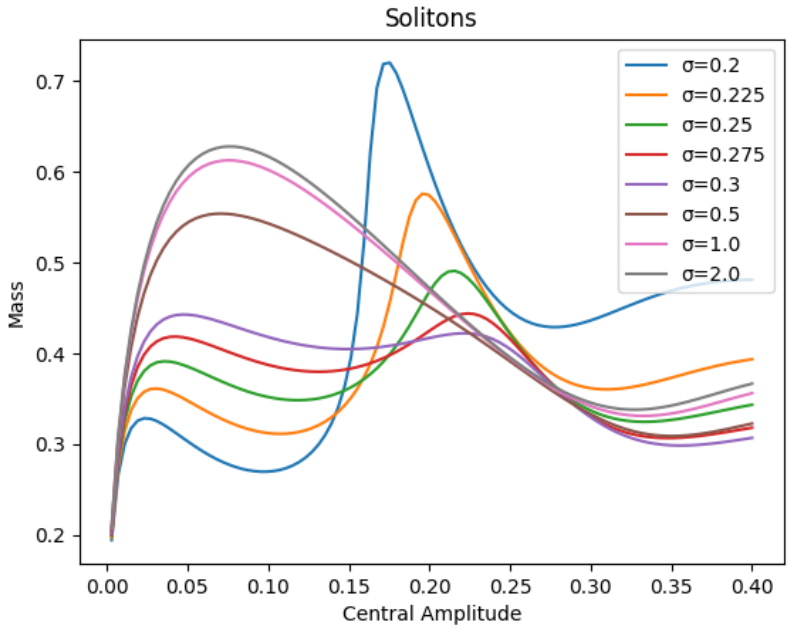

Fig. 5.7 This graph depicts the relationship between the central amplitude and mass of solitons.

5.4 Simulation Configuration

In our setup, we follow the method in Chapter 4 and expand the parameter space with a certain parameter. In our study, we only use the soliton model. Specifically, we show cases where σ is 0.2, 0.225, 0.25, 0.275, 0.3, 0.5, 1.0, 2.0 and expand the parameter space based on their central amplitude. Below are the soliton results we obtained using the initial solver based on LEAN [213].

The plots in Figure 5.7 shows the relationship between mass and central amplitude in a soliton. It can be seen that for σ values less than 0.3, there are two bumps. This is important because, as we find in later studies, novel phenomena always occur after the appearance of bumps, and they exhibit certain patterns.

The plots in Figure 5.8 shows the relationship between compactness and central amplitude. When compactness is high, we find that solitons collapse into black holes very quickly, especially when the central amplitude approaches 0.4, we are even unable to obtain valid initial data.

After obtaining the solution for a single soliton, we obtain the initial conditions for a double soliton using the superposition method described in [110]. We subsequently perform simulations of head-on collisions using the parameters specified in Table 5.1.

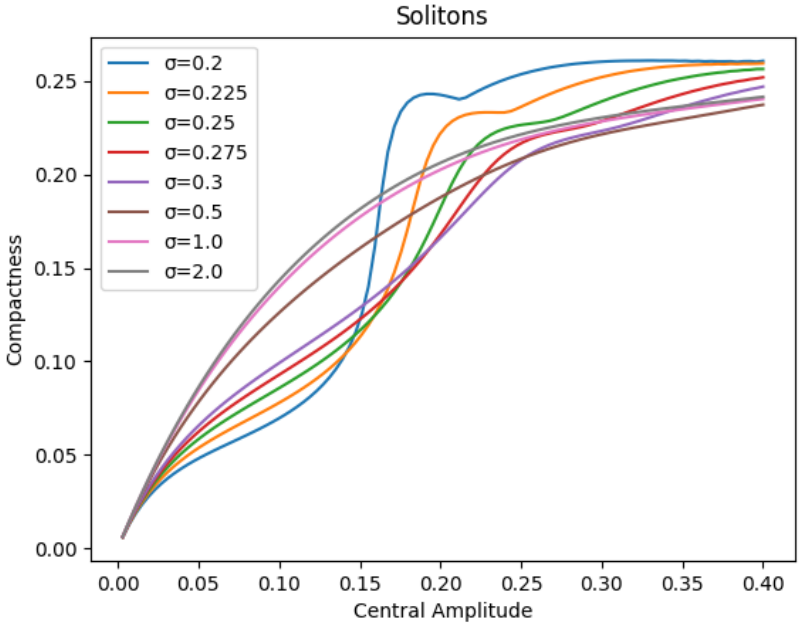

Fig. 5.8 This graph depicts the relationship between the central amplitude and compactness of solitons.

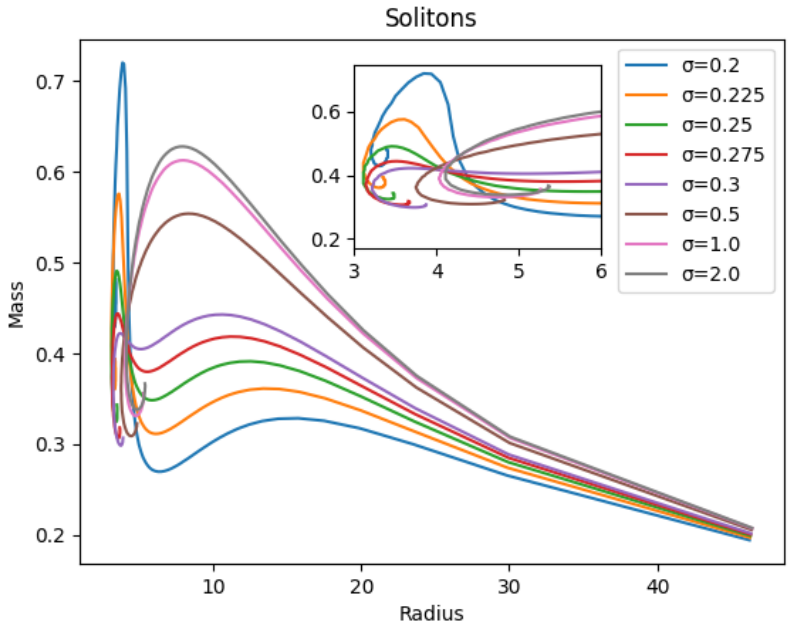

Fig. 5.9 This graph depicts the relationship between the radius and mass of solitons.

Parameter	Value
Distance	80
Velocity	0.1
Domain Size	512
Number of Grid Points	256
Max Level	6
Regridding Parameters	$\|\phi\|$ and χ
Regridding Threshold	0.3
Boundary Conditions	Static
dt Multiplier	0.25

Table 5.1 Simulation Parameters

- **Regridding Parameters** refer to the primary parameters considered during **Adaptive Mesh Refinement**.
- **Regridding Threshold** is the threshold required to trigger regridding.
- The **dt Multiplier** indirectly controls dx through the relationship $dt = dx \cdot dt_{multiplier}$.

For detailed explanations, please refer to [70, 27].

Here we present a list of physics units in Table 5.2, which will be utilized throughout this chapter.

Quantity	Unit
Length	m^{-1}
Time	m^{-1}
Mass	$M_{\mathrm{Pl}}^2 m^{-1}$
σ	M_{Pl}
Central Amplitude	M_{Pl}

Table 5.2 Simulation Unit

The results of the simulation can be summarized into three scenarios.

1. They merge and then form **another soliton**.
2. They merge and then form a **black hole**.
3. They collapse into black holes ***prior to*** merging, then merge into a single black hole.

In our research, we primarily focus on the second and third scenarios. Next, we will analyze the gravitational waves emitted by them, as well as the energy radiated by these gravitational waves.

5.5 Exploring the Stability of Boson Stars

Boson star equilibrium solutions can be parameterized using a single variable, such as the central amplitude of the scalar field $A_{\rm ctr}$, allowing us to express the mass as $M = M(A_{\rm ctr})$. Previous stability studies [54, 98, 196, 199, 34, 22] suggest that transitions between ***Stable (S)*** and ***Unstable (U)*** configurations occur only at critical points in the parameter space, characterized by

$$\frac{dM}{dA_{\rm ctr}} = 0. \tag{5.59}$$

These stability transitions are analogous to those observed in neutron stars [73, 94, 107, 219].

Under a small perturbation, a mini-boson star in the S branch oscillates and loses mass through the emission of relativistic bosons, to then relax in a stable configuration of smaller mass. Stars in the U branch would either collapse to form a black hole if accreted, or migrate to a stable configuration through wave emission. The critical value $\bar{A}_{\rm ctr}$, which demarcates ***Stable*** solutions with

$$A_{\rm ctr} \leq \bar{A}_{\rm ctr} \quad \text{namely} \quad \frac{dM}{dA_{\rm ctr}} \geq 0, \tag{5.60}$$

from ***Unstable*** ones with

$$A_{\rm ctr} > \bar{A}_{\rm ctr} \quad \text{namely} \quad \frac{dM}{dA_{\rm ctr}} < 0, \tag{5.61}$$

is identified as the point where (5.59) is satisfied. This critical value is pivotal in determining the behavior of boson stars against perturbations [22, 139, 97, 98, 121, 123, 122].

Solitons differ from mini-boson stars because they often have more than one point satisfying equation (5.59), making them relatively complex. Next, we will discuss these two types of boson stars separately.

It is important to clarify the criteria used in our simulations for determining black hole formation and migration to another boson star. For black hole formation, we monitored the conformal factor χ during the evolution and identified a black hole when χ dropped below **0.1**. Migration was determined by tracking the central amplitude of the boson star; when the central amplitude shifted by **0.1%** from its initial value, we considered the boson star to have migrated [3].

[3] It should be noted that we did not manually introduce any perturbations. Our "perturbations" arise from numerical errors in the initial conditions and errors caused by imperfections in the evolution process.

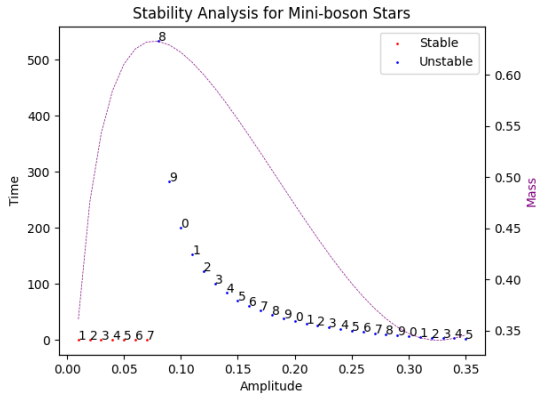

(a) The purple auxiliary coordinates represent the soliton mass.

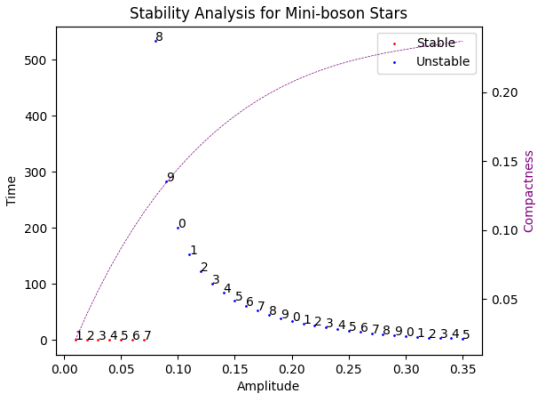

(b) The purple auxiliary coordinates represent the soliton compactness.

Fig. 5.10 The diagram illustrates the stability of the mini-boson star. The x-axis represents the central amplitude of the mini-boson star, while the left y-axis indicates the time it takes for the mini-boson star to collapse into a black hole. The red points represent mini-boson stars that remain stable, while the blue points denote mini-boson stars that collapse into black holes.

5.5.1 Mini-Boson Stars

Figure 5.10 shows the stability of mini-boson stars. Red points indicate that no black holes were found within our evolution time range ($t = 2000\ m^{-1}$), while blue points indicate the formation of black holes, with the corresponding y-axis showing the time of black hole formation for each point.

In both figures, we can see that when the central amplitude is less than 0.08, stable behavior is observed, while at a central amplitude greater than 0.08 (including 0.08), instability is shown. Moreover, the time it takes for them to collapse into black holes also becomes earlier with increasing central amplitude. Even at a central amplitude of 0.35, black holes form almost at the beginning of the evolution. It is worth mentioning that during the process of solving for a single boson star using the shooting method, the central amplitude can reach a value of 0.4. However, in actual evolution, we find that when the central amplitude exceeds 0.35, we are almost unable to generate effective initial conditions. Therefore, we only consider the situation of central amplitude up to 0.35.

In both figures, different auxiliary lines are used. Through Figure 5.10 (b), we can see that as compactness increases, mini-boson stars start to show instability, and become more unstable with increasing compactness. There might be a potential question here: Is it because our evolution time only goes up to $t = 2000\ m^{-1}$, therefore points before 0.07 do not show instability? To answer this question, we need to look at Figure 5.10 (a). In the auxiliary plot of Figure 5.10 (a), we find a mass bump around 0.08, which is the boundary

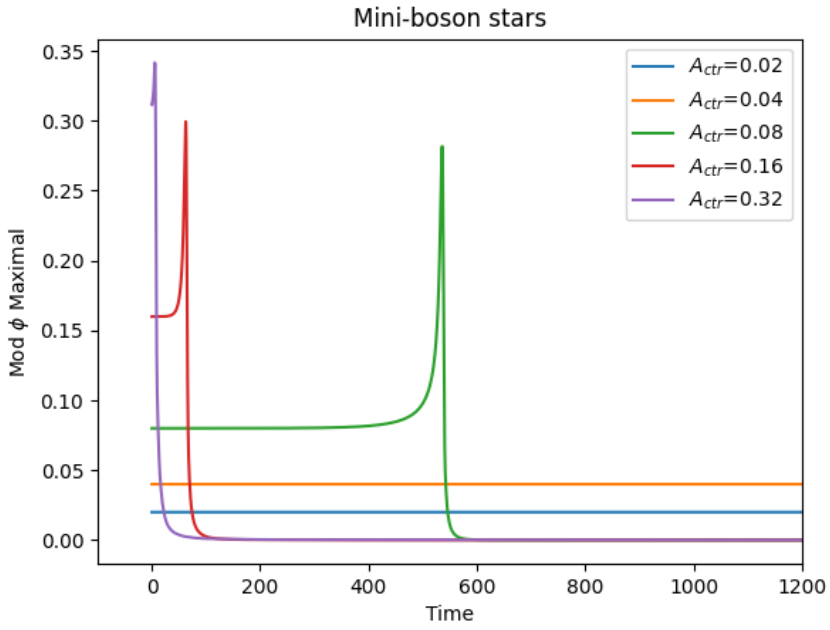

Fig. 5.11 This figure shows the maximum value of $\sqrt{|\phi|^2}$ as it changes over time. Here, A_{ctr} represents the initial central amplitude. We have simulated data from $t = 0\ m^{-1}$ to $t = 2000\ m^{-1}$. For better visual presentation, only data up to $t = 1200\ m^{-1}$ was selected.

of stability. On the left side of this bump $A_{\rm ctr} \leq \bar{A}_{\rm ctr}$, stability is shown, while on the right $A_{\rm ctr} > \bar{A}_{\rm ctr}$, instability is displayed. This is consistent with the results we argued before. Therefore, we can trust that $t = 2000\ m^{-1}$ is sufficient to illustrate the issue of stability.

Furthermore, we further explore the central amplitude of mini-boson stars in evolution to confirm their stability behavior is consistent with our expectations. Figure 5.11 shows the variation of the maximum value of $\sqrt{|\phi|^2}$ over time, as expected. For initial central amplitudes of 0.02 and 0.04, their evolution remains a constant value. For cases evolving into black holes, such as 0.08, 0.16, 0.32, their maximum values of $\sqrt{|\phi|^2}$ drop suddenly to 0 when they evolve into black holes.

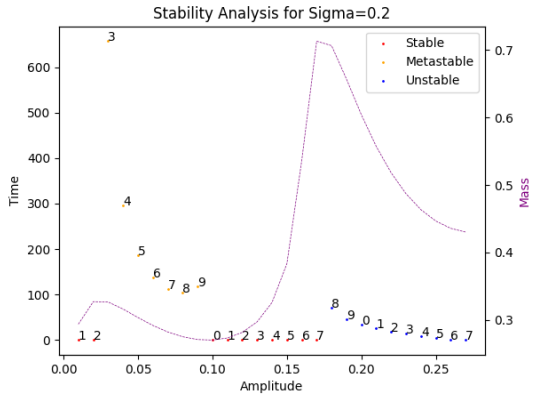

(a) The purple auxiliary coordinates represent the soliton mass.

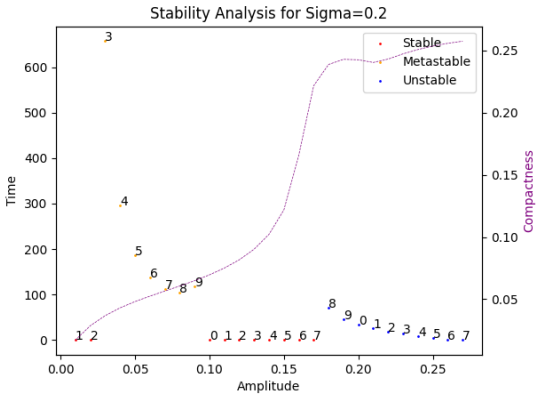

(b) The purple auxiliary coordinates represent the soliton compactness.

Fig. 5.12 The diagram illustrates the stability of the soliton with $\sigma = 0.2$. The x-axis represents the central amplitude of the soliton, while the left y-axis indicates the time it takes for the soliton to either collapse into a black hole or migrate to another soliton. The red points represent solitons that remain stable, the orange points indicate solitons that migrate to another soliton, and the blue points denote solitons that collapse into black holes.

5.5.2 Solitonic Boson Stars

We investigated the stability of solitons using methods similar to those used for mini-boson stars, referring to solitons corresponding to several values of σ. Surprisingly, when we studied their $\sqrt{|\phi|^2}$, we discovered a new phenomenon: unstable boson stars ***migrate*** to stable boson stars. In this work, we use **Metastable** to denote this kind of ***unstable*** boson star. This has also been mentioned in previous literature [148, 197].

According to Figures 5.12, 5.13, 5.14, 5.15, 5.16, and 5.17, the results are consistent across σ values of 0.2, 0.225, and 0.25. In regions where $\frac{dM}{dA_{\rm ctr}} > 0$, solitons demonstrate stable behavior. solitons are in a metastable state in the declining section ($\frac{dM}{dA_{\rm ctr}} < 0$) post the first bump. Following the declining section after the second bump, solitons are observed to collapse into black holes.

When σ increases to 0.275, we find that the first declining section further splits into two branches. For larger central amplitudes, such as 0.07, it remains in a metastable state, while for relatively smaller central amplitudes, such as 0.05, it collapses into a black hole (as in Figures 5.18 and 5.19 but for $\sigma = 0.275$).

σ equal to 0.28725 is a carefully selected example, where we specifically chose a case with two bumps that are exactly the same. We can see that for the first declining section, it is divided quite strictly into a metastable branch and a branch that collapses into a black hole (as in Figures 5.20 and 5.21 but for $\sigma = 0.28725$).

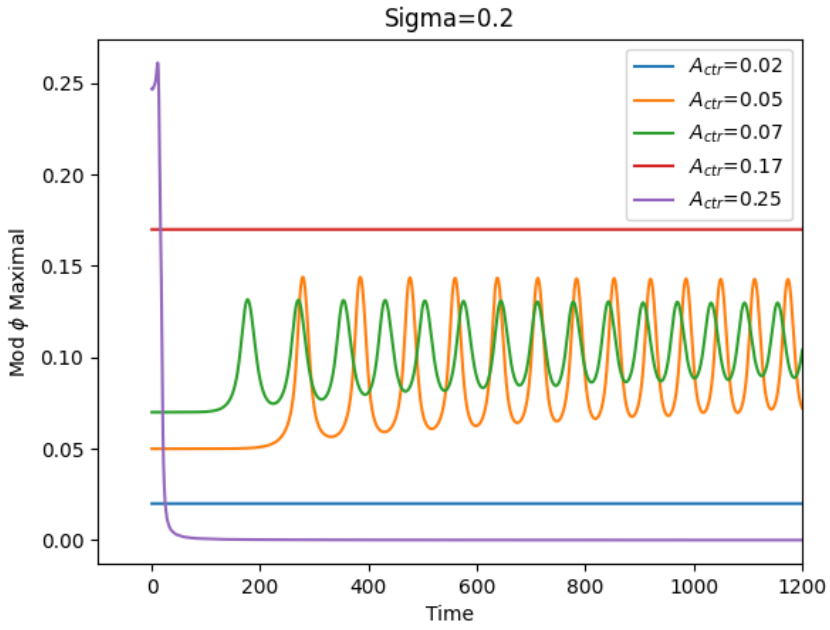

Fig. 5.13 This figure depicts the maximum value of $\sqrt{|\phi|^2}$ as it evolves over time. Here, A_{ctr} represents the initial central amplitude, with $\sigma = 0.2$. The simulation data spans from $t = 0\ m^{-1}$ to $t = 2000\ m^{-1}$. For clearer visualization, only data up to $t = 1200\ m^{-1}$ is presented.

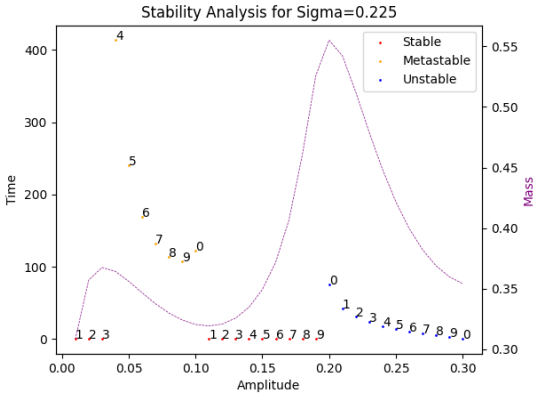

(a) The purple auxiliary coordinates represent the soliton mass.

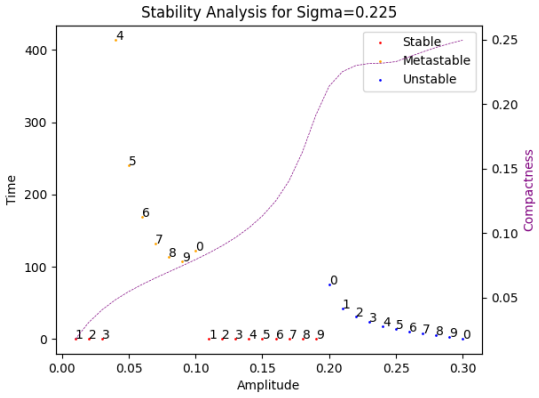

(b) The purple auxiliary coordinates represent the soliton compactness.

Fig. 5.14 The diagram illustrates the stability of the soliton with $\sigma = 0.225$. The x-axis represents the central amplitude of the soliton, while the left y-axis indicates the time it takes for the soliton to either collapse into a black hole or migrate to another soliton. The red points represent solitons that remain stable, the orange points indicate solitons that migrate to another soliton, and the blue points denote solitons that collapse into black holes.

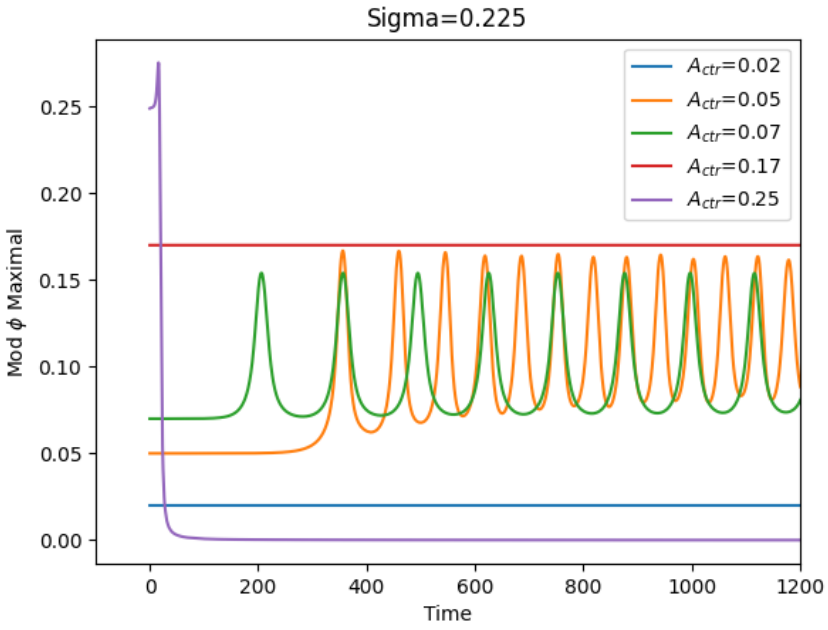

Fig. 5.15 This figure depicts the maximum value of $\sqrt{|\phi|^2}$ as it evolves over time. Here, A_{ctr} represents the initial central amplitude, with $\sigma = 0.225$. The simulation data spans from $t = 0\ m^{-1}$ to $t = 2000\ m^{-1}$. For clearer visualization, only data up to $t = 1200\ m^{-1}$ is presented.

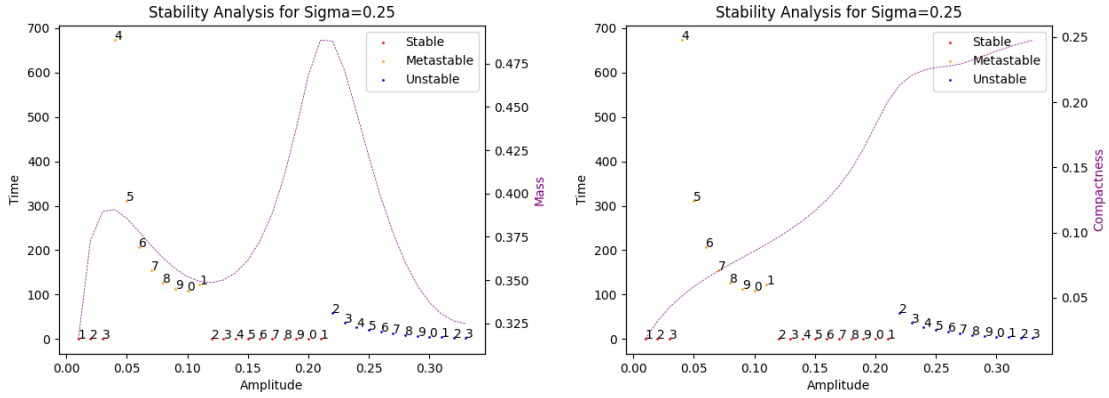

(a) The purple auxiliary coordinates represent the soliton mass.

(b) The purple auxiliary coordinates represent the soliton compactness.

Fig. 5.16 The diagram illustrates the stability of the soliton with $\sigma = 0.25$. The x-axis represents the central amplitude of the soliton, while the left y-axis indicates the time it takes for the soliton to either collapse into a black hole or migrate to another soliton. The red points represent solitons that remain stable, the orange points indicate solitons that migrate to another soliton, and the blue points denote solitons that collapse into black holes.

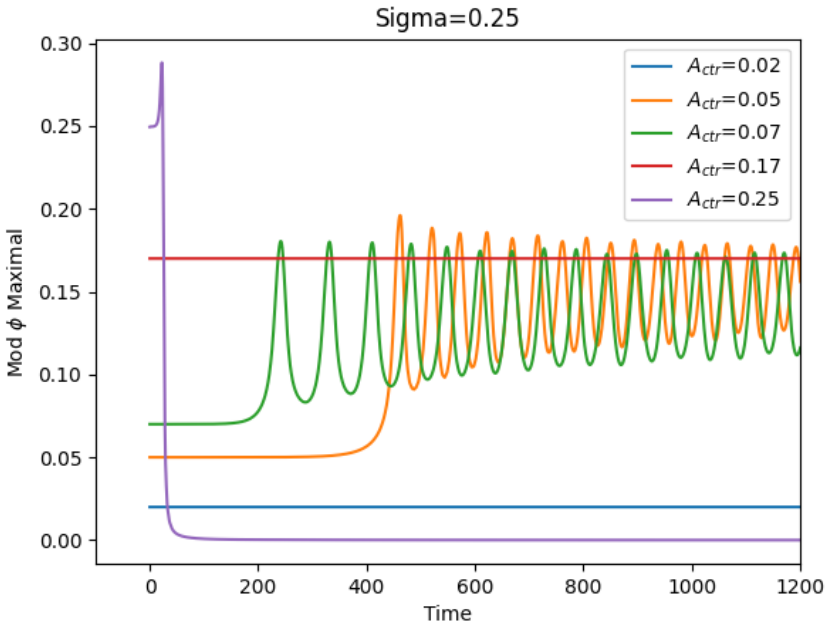

Fig. 5.17 This figure depicts the maximum value of $\sqrt{|\phi|^2}$ as it evolves over time. Here, A_{ctr} represents the initial central amplitude, with $\sigma = 0.25$. The simulation data spans from $t = 0\ m^{-1}$ to $t = 2000\ m^{-1}$. For clearer visualization, only data up to $t = 1200\ m^{-1}$ is presented.

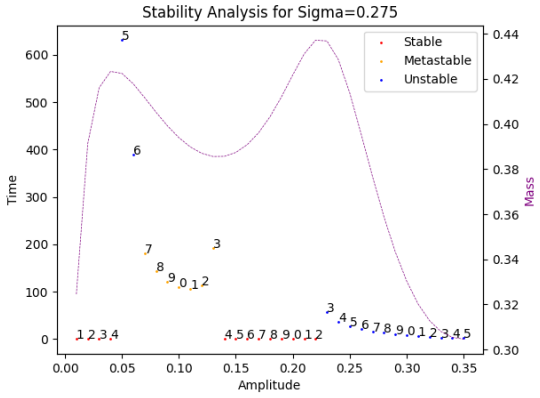

(a) The purple auxiliary coordinates represent the soliton mass.

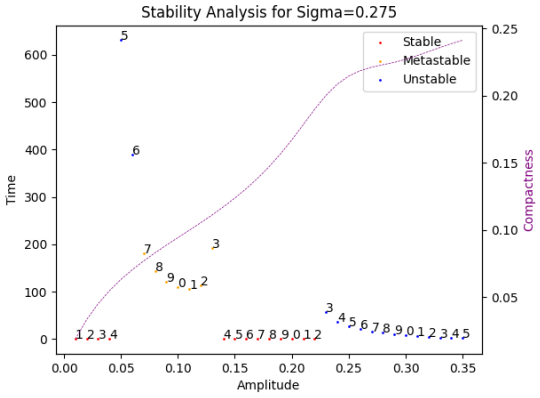

(b) The purple auxiliary coordinates represent the soliton compactness.

Fig. 5.18 The diagram illustrates the stability of the soliton with $\sigma = 0.275$. The x-axis represents the central amplitude of the soliton, while the left y-axis indicates the time it takes for the soliton to either collapse into a black hole or migrate to another soliton. The red points represent solitons that remain stable, the orange points indicate solitons that migrate to another soliton, and the blue points denote solitons that collapse into black holes.

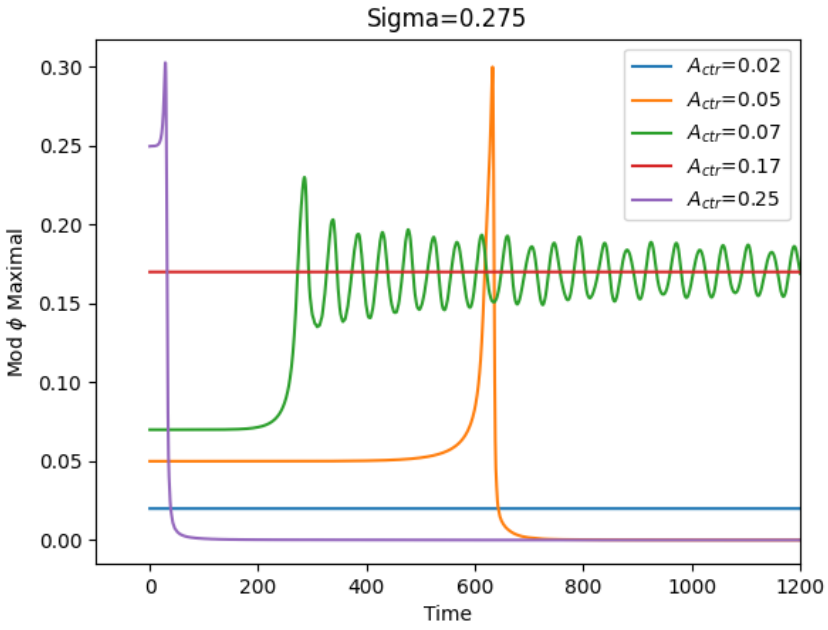

Fig. 5.19 This figure depicts the maximum value of $\sqrt{|\phi|^2}$ as it evolves over time. Here, A_{ctr} represents the initial central amplitude, with $\sigma = 0.275$. The simulation data spans from $t = 0\ m^{-1}$ to $t = 2000\ m^{-1}$. For clearer visualization, only data up to $t = 1200\ m^{-1}$ is presented.

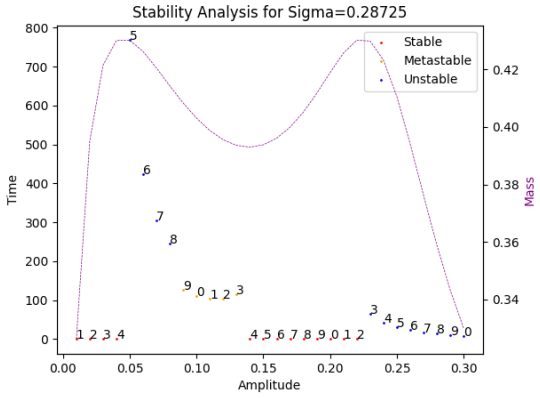

(a) The purple auxiliary coordinates represent the soliton mass.

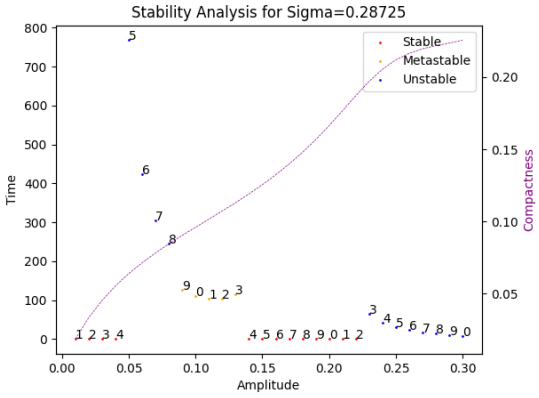

(b) The purple auxiliary coordinates represent the soliton compactness.

Fig. 5.20 The diagram illustrates the stability of the soliton with $\sigma = 0.28725$. The x-axis represents the central amplitude of the soliton, while the left y-axis indicates the time it takes for the soliton to either collapse into a black hole or migrate to another soliton. The red points represent solitons that remain stable, the orange points indicate solitons that migrate to another soliton, and the blue points denote solitons that collapse into black holes.

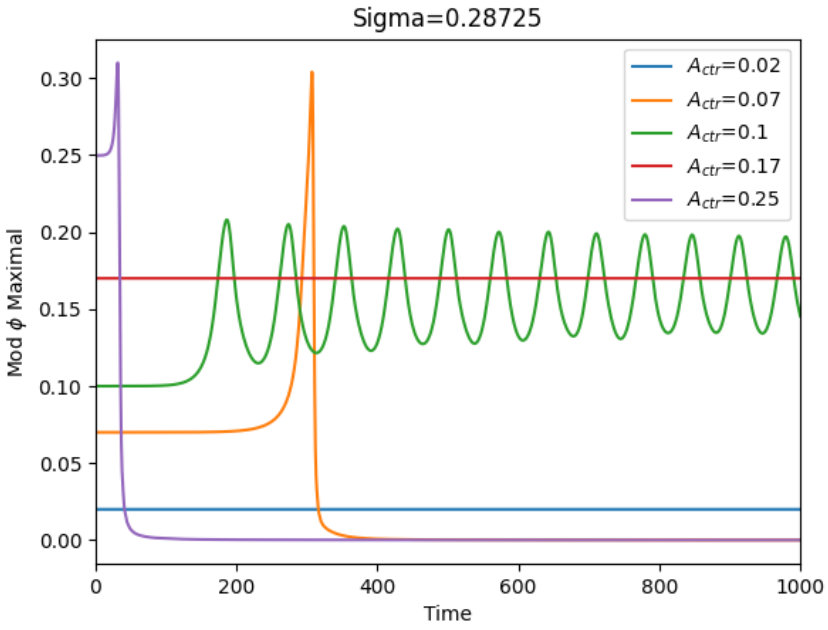

Fig. 5.21 This figure depicts the maximum value of $\sqrt{|\phi|^2}$ as it evolves over time. Here, A_{ctr} represents the initial central amplitude, with $\sigma = 0.28725$. The simulation data spans from $t = 0\ m^{-1}$ to $t = 2000\ m^{-1}$. For clearer visualization, only data up to $t = 1200\ m^{-1}$ is presented.

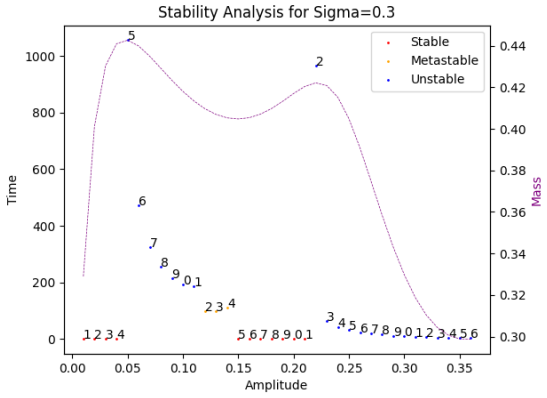

(a) The purple auxiliary coordinates represent the soliton mass.

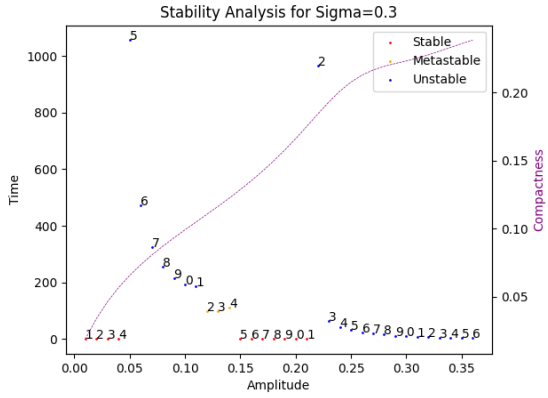

(b) The purple auxiliary coordinates represent the soliton compactness.

Fig. 5.22 The diagram illustrates the stability of the soliton with $\sigma = 0.3$. The x-axis represents the central amplitude of the soliton, while the left y-axis indicates the time it takes for the soliton to either collapse into a black hole or migrate to another soliton. The red points represent solitons that remain stable, the orange points indicate solitons that migrate to another soliton, and the blue points denote solitons that collapse into black holes.

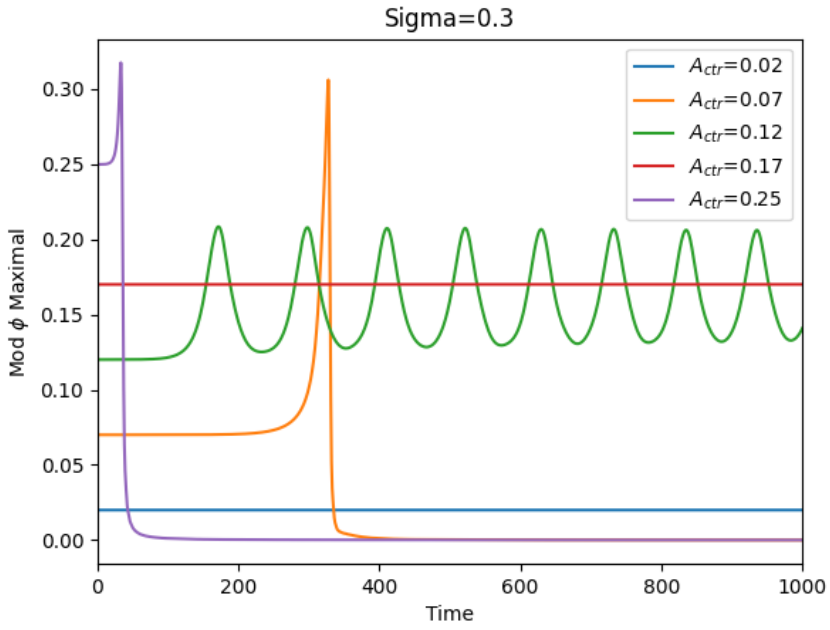

Fig. 5.23 This figure depicts the maximum value of $\sqrt{|\phi|^2}$ as it evolves over time. Here, A_{ctr} represents the initial central amplitude, with $\sigma = 0.3$. The simulation data spans from $t = 0\ m^{-1}$ to $t = 2000\ m^{-1}$. For clearer visualization, only data up to $t = 1200\ m^{-1}$ is presented.

When σ reaches 0.3, most of the solitons in the first declining section collapse into black holes. Only a few solitons remain in a metastable state (as in Figures 5.22 and 5.23 but for $\sigma = 0.3$).

For higher values of σ, such as $\sigma = 0.5$ (Figures 5.24 and 5.25), soliton behavior converges with that of mini-boson stars, offering limited additional insight.

Based on the detailed analysis of soliton stability, we can summarize the key findings as follows:

1. For single-bump cases (i.e., higher σ values), solitons collapse into black holes if $\frac{dM}{dA_{\text{ctr}}} < 0$. If $\frac{dM}{dA_{\text{ctr}}} > 0$, the soliton remains stable.
2. For two-bump cases, the region near the second bump follows the behavior seen in single-bump cases. Near the first bump, solitons remain stable when $\frac{dM}{dA_{\text{ctr}}} > 0$, but for $\frac{dM}{dA_{\text{ctr}}} < 0$, the outcome depends on the relative sizes of the two bumps. Figure 5.26 provides a summary of these results.

It is not surprising that solitons with higher initial central amplitudes collapse into black holes, as these solitons typically correspond to higher compactness. It is important

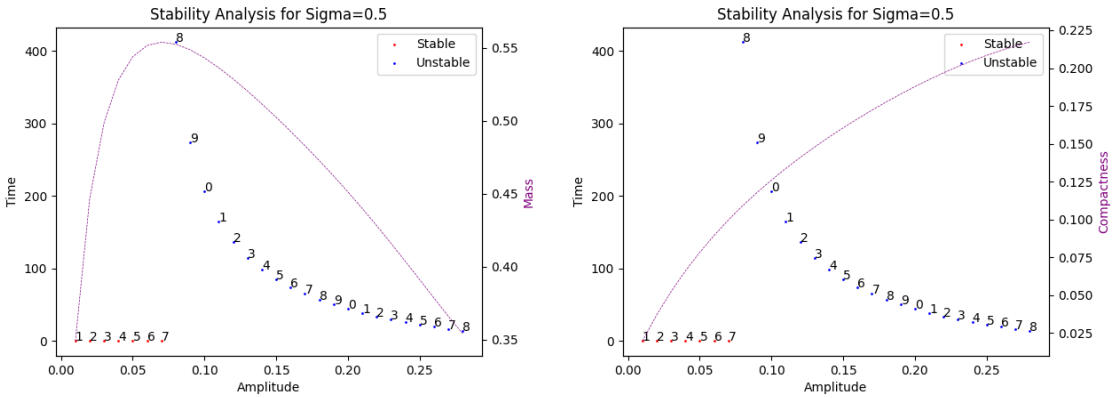

(a) The purple auxiliary coordinates represent the soliton mass.

(b) The purple auxiliary coordinates represent the soliton compactness.

Fig. 5.24 The diagram illustrates the stability of the soliton with $\sigma = 0.5$. The x-axis represents the central amplitude of the soliton, while the left y-axis indicates the time it takes for the soliton to collapse into a black hole. The red points represent solitons that remain stable, while the blue points denote solitons that collapse into black holes.

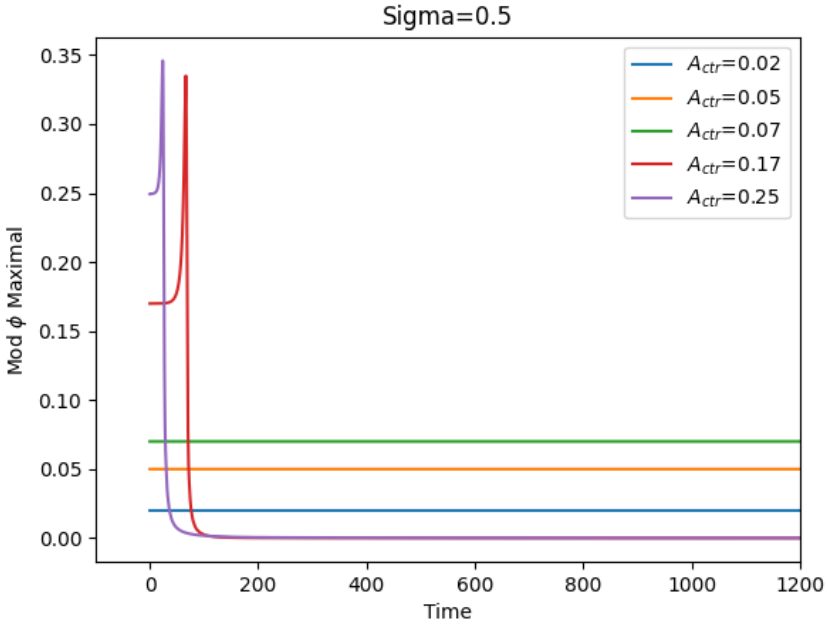

Fig. 5.25 This figure depicts the maximum value of $\sqrt{|\phi|^2}$ as it evolves over time. Here, A_{ctr} represents the initial central amplitude, with $\sigma = 0.5$. The simulation data spans from $t = 0\ m^{-1}$ to $t = 2000\ m^{-1}$. For clearer visualization, only data up to $t = 1200\ m^{-1}$ is presented.

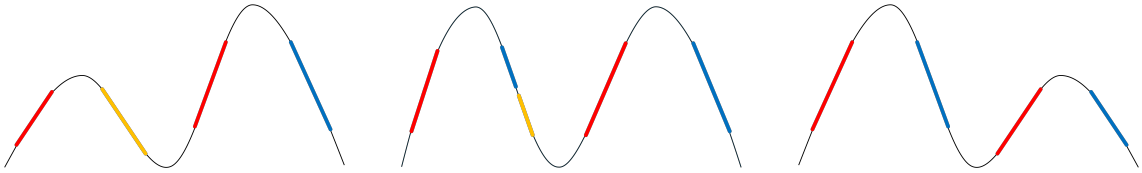

(a) The case where the first bump is lower than the second bump.

(b) The case where the first bump is (approximately)equal to the second bump.

(c) The case where the first bump is higher than the second bump.

Fig. 5.26 This diagram illustrates a schematic of stability. Here, red represents stable, blue represents unstable, and orange represents metastable.

to emphasize that metastable solitons tend to migrate to configurations with higher central amplitudes (lower mass) due to scalar radiation, which gradually reduces their mass [148, 197]. This can be seen from the potential energy curve of the soliton.

Finally, we consolidate all the obtained results, as shown in Figure 5.27. It can be observed that at high σ values, only two states exist, and the regions where the split occurs are similar (around an initial central amplitude of 0.07). The most complex scenario arises when σ is in the range of 0.3 to 0.275, where various types of solitons coexist and alternate. Notably, in this region, as σ decreases, the unstable region between central amplitudes of approximately 0.04 and 0.14 gradually shrinks (at lower σ values, it is eventually compressed until it disappears), while the metastable region expands. When σ decreases to around 0.25 to 0.2, the stable red region, representing central amplitudes between 0.14 and 0.21, begins to gradually *sink*.

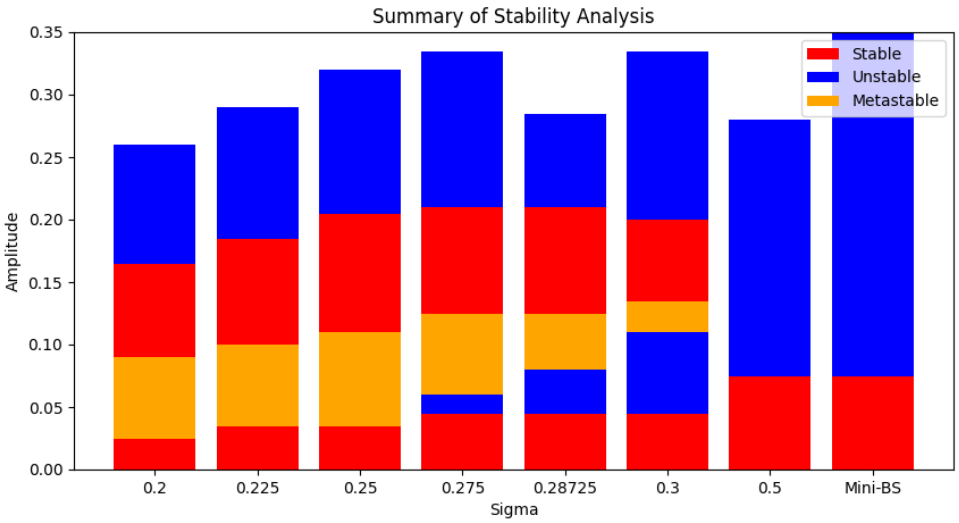

Fig. 5.27 This figure presents the stability results for various solitons and the mini-boson star. The red region represents solitons that are stable, the blue region indicates those that collapse into black holes, and the orange region represents solitons that migrate to another soliton. The x-axis corresponds to their σ values, with the rightmost bar representing the mini-boson star (which can be considered as σ approaching infinity). The y-axis corresponds to the initial central amplitude of these boson stars.

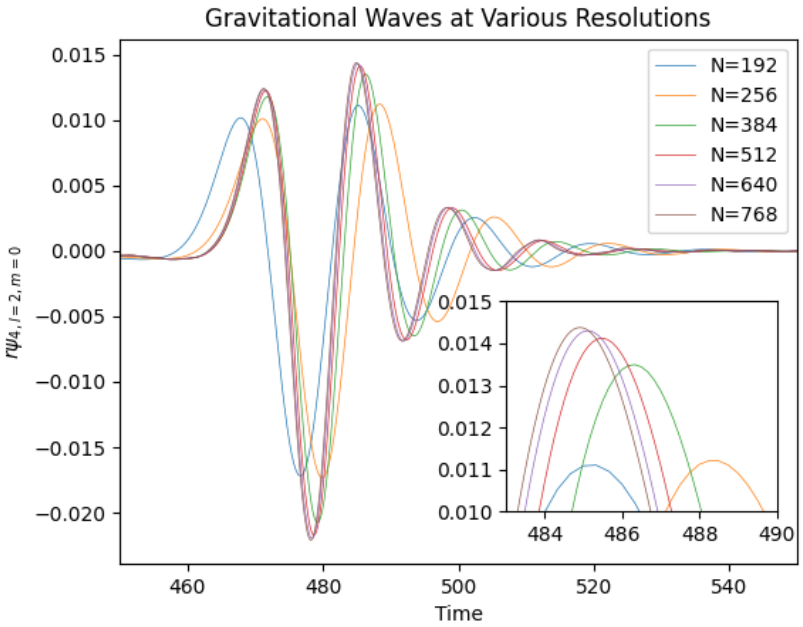

Fig. 5.28 In the figure, we present the Energy of gravitational wave $l = 2, m = 0$ mode, with the chosen model being $\sigma = 1.0$, central amplitude $= 0.25$.

5.6 Exploring Gravitational Waves and Energy Calculation

In this section, we first extract the gravitational waves and calculate the energy carried by these gravitational waves.

It is worth noting that although the 2D code is much more efficient than the 3D code, the need to perform numerous simulations still requires a significant amount of computational resources. Therefore, it is very important to carefully choose the resolution. Figure 5.28 shows the behavior of gravitational wave signals at different resolutions. In the magnified image in the bottom right corner, we can see that starting from $N = 256$, the gravitational wave signals begin to converge. This conclusion is particularly evident in Figure 5.29, where we can see that at $N = 192$, there is a trend of divergence in the energy of the gravitational waves towards the end. Therefore, we cautiously chose $N = 256$ as our evolution resolution. It should be mentioned that this is just one example, but we have referred to many samples with different parameters when choosing the resolution.

When calculating the energy of gravitational waves, we consider the contributions of $l = 2$, $l = 3$, and $l = 4$ (contributions from higher modes are almost negligible and can be ignored). Since different solitons usually correspond to different masses, it is necessary to normalize the energy. In our work, we have chosen two methods of normalization. The

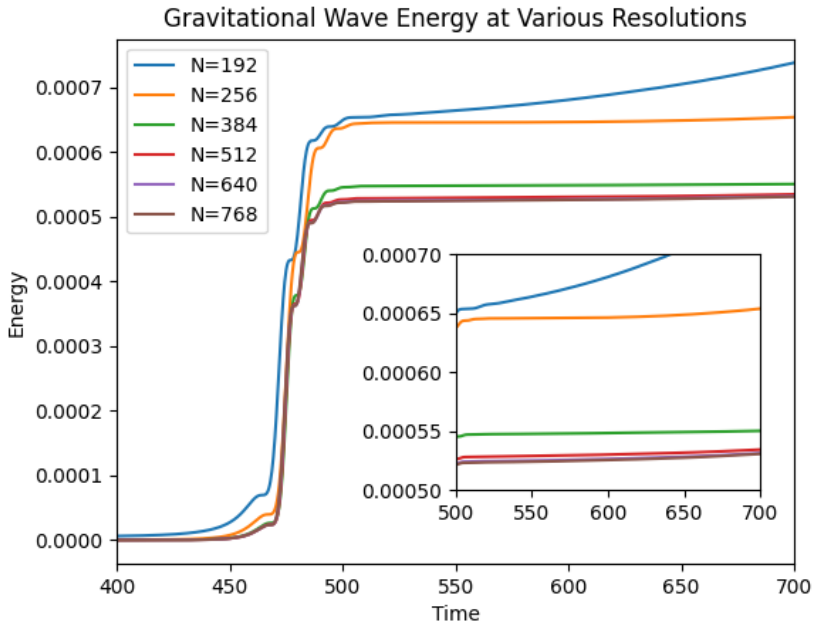

Fig. 5.29 In the figure, we present the gravitational wave $r\psi_{4,\ l=2,m=0}$, with the chosen model being $\sigma = 1.0$, central amplitude $= 0.25$.

first is based on the mass of the soliton in the initial conditions. The second method is based on the mass of the final state black hole, which is calculated using the Quasinormal mode (Here, we have used an implementation based on the code by Leo C. Stein [218].) from the Ringdown part of the gravitational wave signal. We will discuss our results in detail in the next section.

5.7 Results

In this section, we present the main results of our study. Specifically, we fix σ as a constant and expand the parameter space using the central amplitude as the x-axis. We examine the gravitational wave energy emitted during head-on soliton collisions at a fixed σ. In our discussions on stability, we noted that obtaining effective initial data can be challenging for solitons with very high central amplitudes, necessitating a cutoff in the parameter space. Additionally, we normalized all results using two types of mass measurements: the ***Initial Soliton*** mass and the ***Quasi-Normal Mode (QNM)*** mass.

To present our findings clearly, we classified our solitons into several categories. For solitons featuring two bumps, typically associated with lower sigma values, we have divided them into three distinct types, as illustrated in Figure 5.26: Type-A, Type-B, and Type-C. Solitons with a single bump, generally linked to higher sigma values, are discussed in conjunction with mini-boson stars.

For these three types, we briefly summarize as follows:

- Type-A: The scenario where the first bump is lower than the second bump is illustrated in Figure 5.26a. Our study includes cases with σ values of 0.2, 0.225, 0.25, and 0.275.
- Type-B: The scenario where the first bump is equal to the second bump is illustrated in Figure 5.26b. Our study includes cases with a σ value of 0.28725.
- Type-C: The scenario where the first bump is higher than the second bump is illustrated in Figure 5.26c. Our study includes cases with a σ value of 0.3.

Furthermore, we have divided the cases with two bumps into four regions, illustrated in schematic diagram 5.30.

Type-A

$\underline{\sigma = 0.2}$

We selected a minimum value of $\sigma = 0.2$, and from the data depicted in Figure 5.31, it is evident that in Region IV, the solitons initially collapse into black holes before colliding. This outcome aligns with our previous stability analysis and is therefore expected. In Region III, we observe that solitons with relatively low central amplitudes generate more gravitational wave energy. Furthermore, the normalization results using the initial soliton mass and Quasinormal Mode (QNM) mass are found to be comparable.

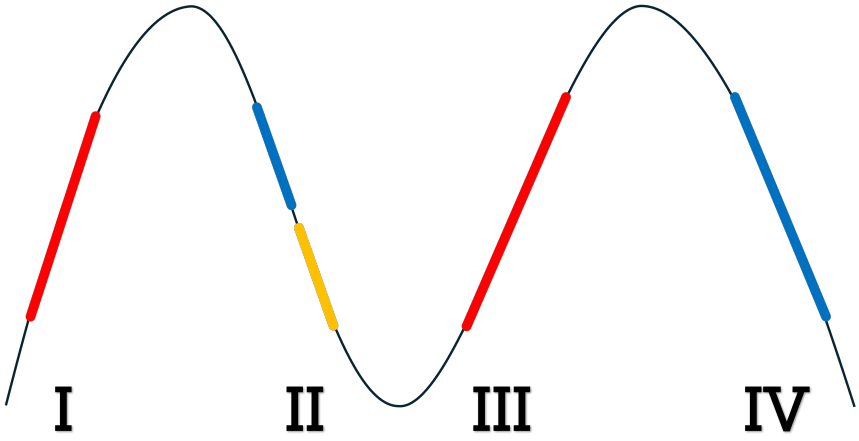

Fig. 5.30 Region I is the rising section located to the left of the first bump. Region II is the declining section to the right of the first bump. Region III mirrors Region I as another rising section to the left of the second bump. Region IV corresponds to Region II as the declining section to the right of the second bump. Here, a rising section signifies that the derivative of mass with respect to the central amplitude, dM/dA_{ctr}, is greater than zero, indicating an increase. Conversely, a declining section means that dM/dA_{ctr} is less than zero, indicating a decrease.

Additionally, we have noted that the transition from red dots to blue dots is discontinuous. While this discontinuity is not evident in Figure 5.31, it becomes clearly visible in Figure 5.32.

It is important to note that we have not addressed cases with central amplitudes below 0.13, as their eventual outcome tends to be another boson star rather than a black hole. These cases are outside the focus of our study.

$\sigma = 0.225$ $\sigma = 0.25$ $\sigma = 0.275$

Slightly increasing σ to 0.225 revealed unexpected results, as shown in Figure 5.33. In Region II, a complex yet regular structure appeared. Detailed observations from zoomed in Figure 5.34 reveal several fluctuations within this specific region. Notably, the amplitude of these fluctuations is not uniform, yet they demonstrate a clear regularity. Convergence tests on these results confirmed that these fluctuations are genuine phenomena, not noise or errors, indicating that these refined structures are indeed present.

Similar observations were made at σ values of 0.25 and 0.275, as shown in Figures 5.36 and 5.37 for $\sigma = 0.25$, and Figures 5.38 and 5.39 for $\sigma = 0.275$. The structural patterns at $\sigma = 0.25$ and $\sigma = 0.275$ are more pronounced compared to $\sigma = 0.225$. Notably, in Regions I and II, energy consistently oscillates upwards. Furthermore, the transition from red dots to blue dots remains discontinuous.

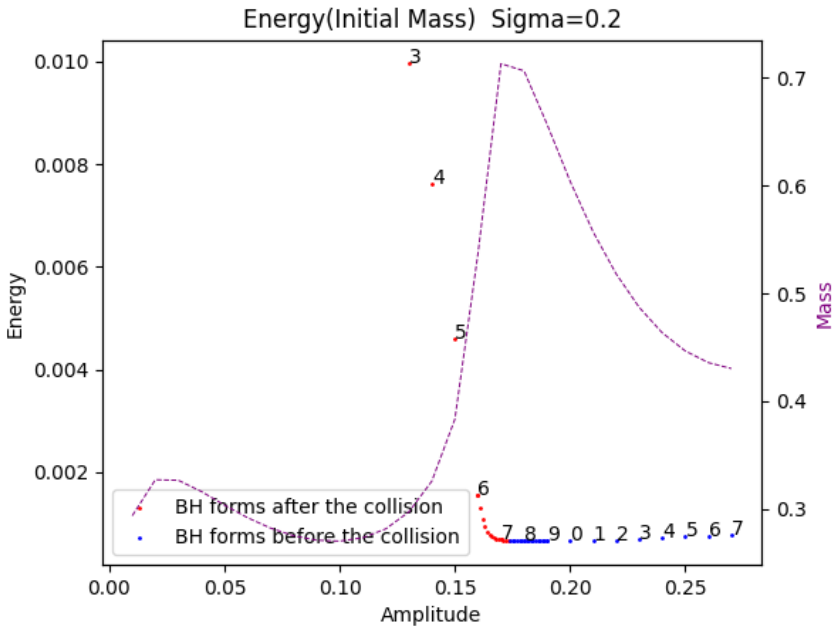

(a) The normalization method for this plot is based on the initial soliton mass.

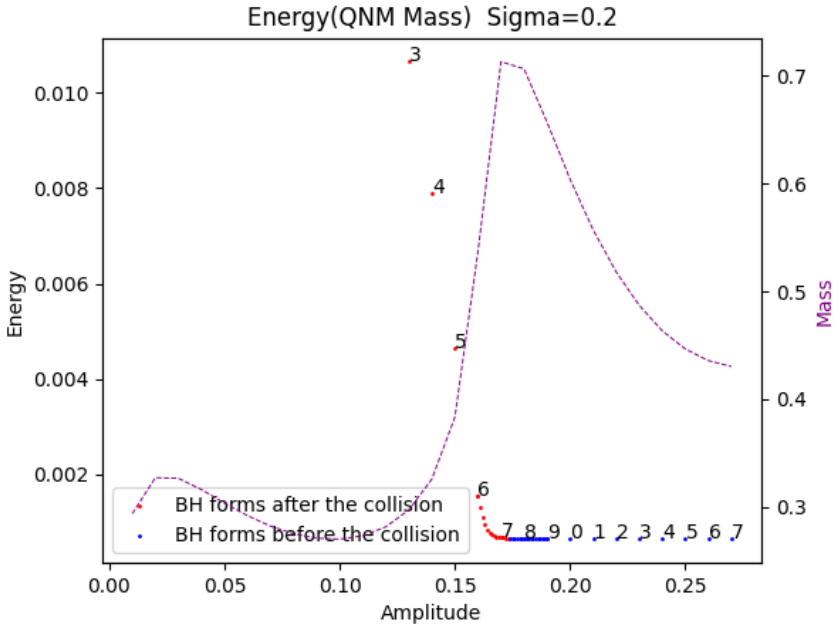

(b) The normalization method for this plot is based on the Quasinormal mode mass.

Fig. 5.31 This plot shows the energy of gravitational waves produced by head-on collisions with different central amplitude after a given $\sigma = 0.2$, where the purple auxiliary coordinates in both figures represent the initial soliton mass. In the plot, the red points represent two solitons colliding and eventually forming a black hole. The blue points represent two solitons that form black holes separately before colliding, and then form a new black hole after the collision.

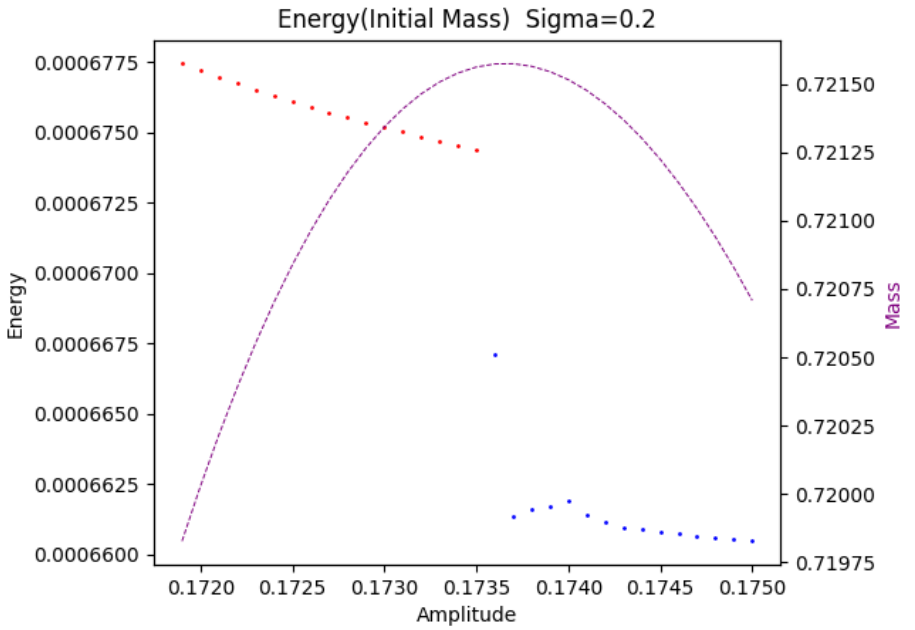

(a) The normalization method for this plot is based on the initial soliton mass.

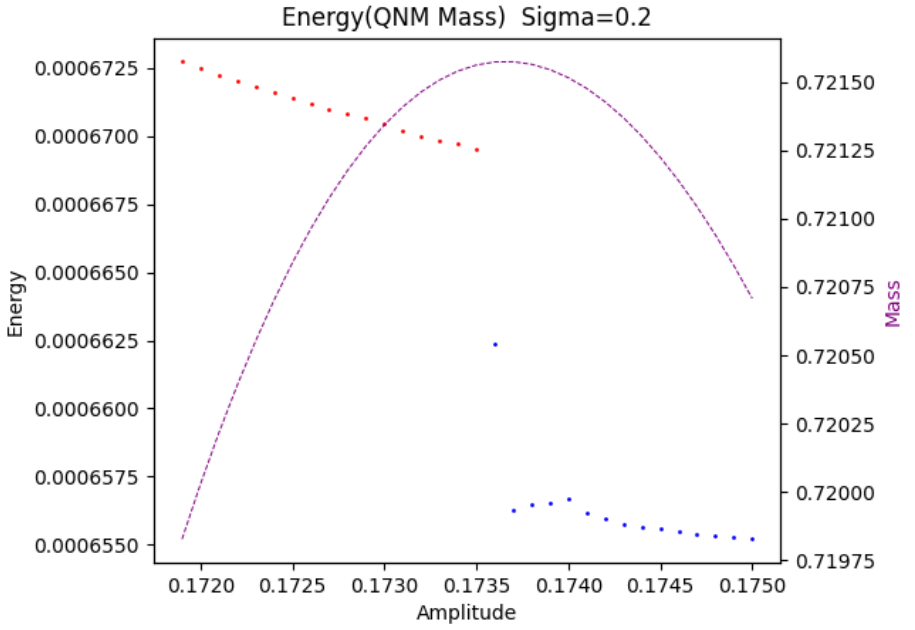

(b) The normalization method for this plot is based on the Quasinormal mode mass.

Fig. 5.32 This plot shows the energy of gravitational waves produced by head-on collisions with different central amplitude after a given $\sigma = 0.2$, where the purple auxiliary coordinates in both figures represent the initial soliton mass. In the plot, the red points represent two solitons colliding and eventually forming a black hole. The blue points represent two solitons that form black holes separately before colliding, and then form a new black hole after the collision.

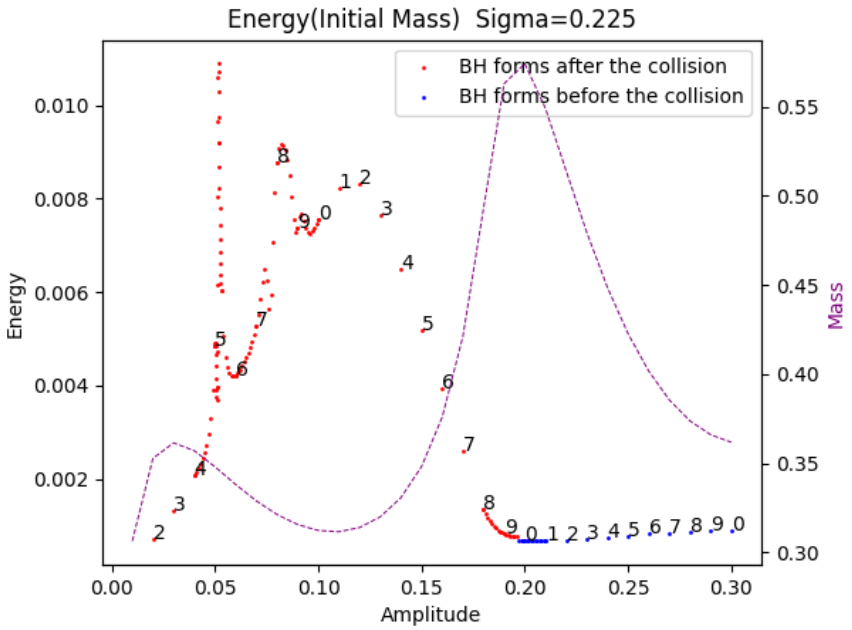

(a) The normalization method for this plot is based on the initial soliton mass.

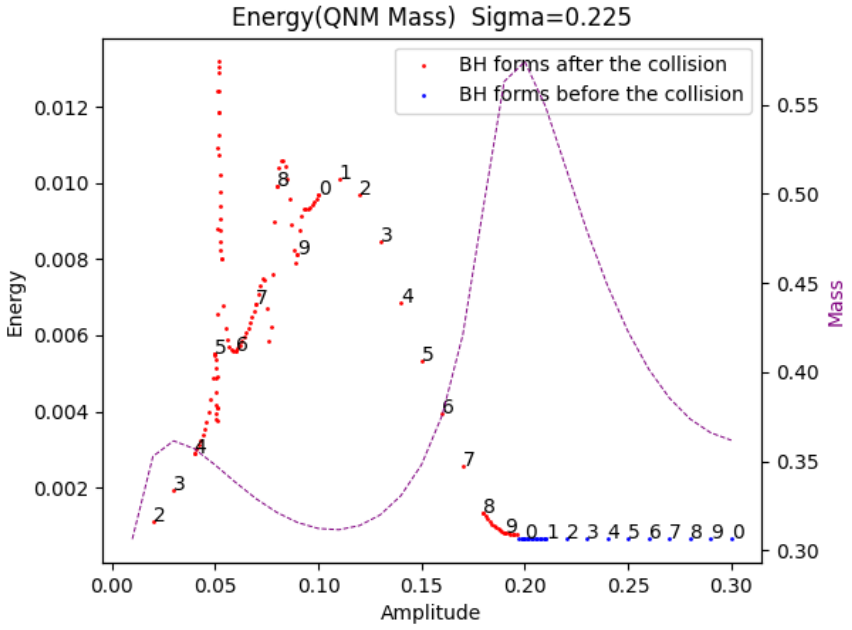

(b) The normalization method for this plot is based on the Quasinormal mode mass.

Fig. 5.33 This plot shows the energy of gravitational waves produced by head-on collisions with different central amplitude after a given $\sigma = 0.225$, where the purple auxiliary coordinates in both figures represent the initial soliton mass. In the plot, the red points represent two solitons colliding and eventually forming a black hole. The blue points represent two solitons that form black holes separately before colliding, and then form a new black hole after the collision.

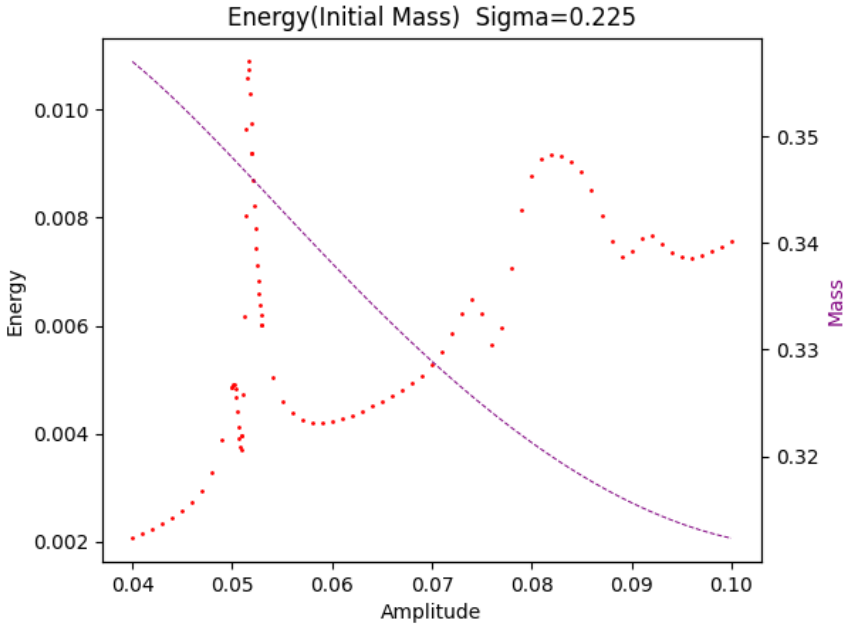

(a) The normalization method for this plot is based on the initial soliton mass.

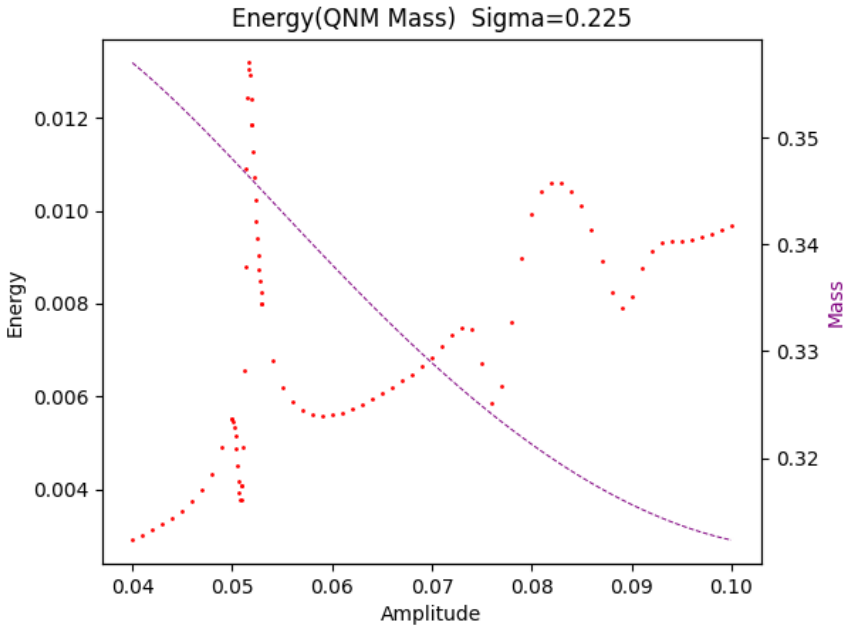

(b) The normalization method for this plot is based on the Quasinormal mode mass.

Fig. 5.34 This plot shows the energy of gravitational waves produced by head-on collisions with different central amplitude after a given $\sigma = 0.225$, where the purple auxiliary coordinates in both figures represent the initial soliton mass. In the plot, the red points represent two solitons colliding and eventually forming a black hole.

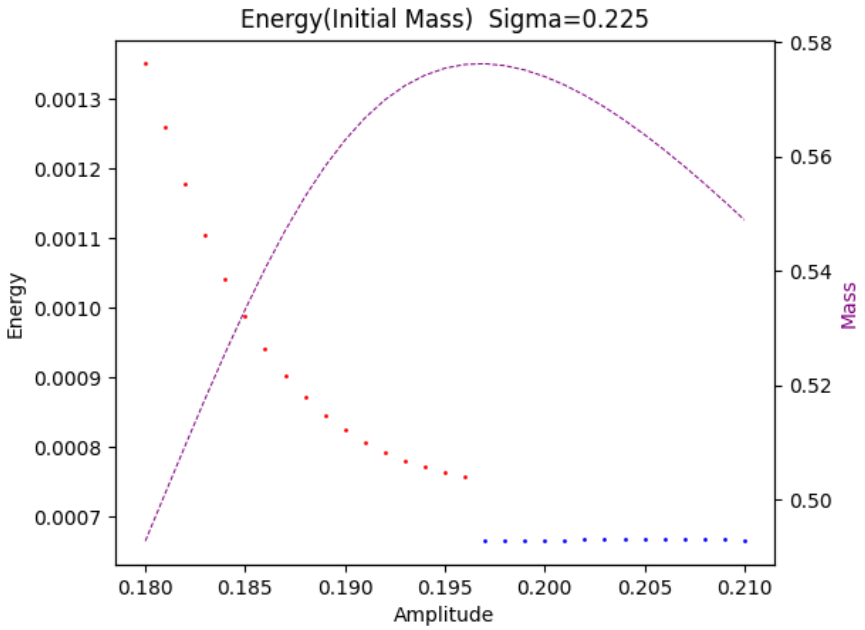

(a) The normalization method for this plot is based on the initial soliton mass.

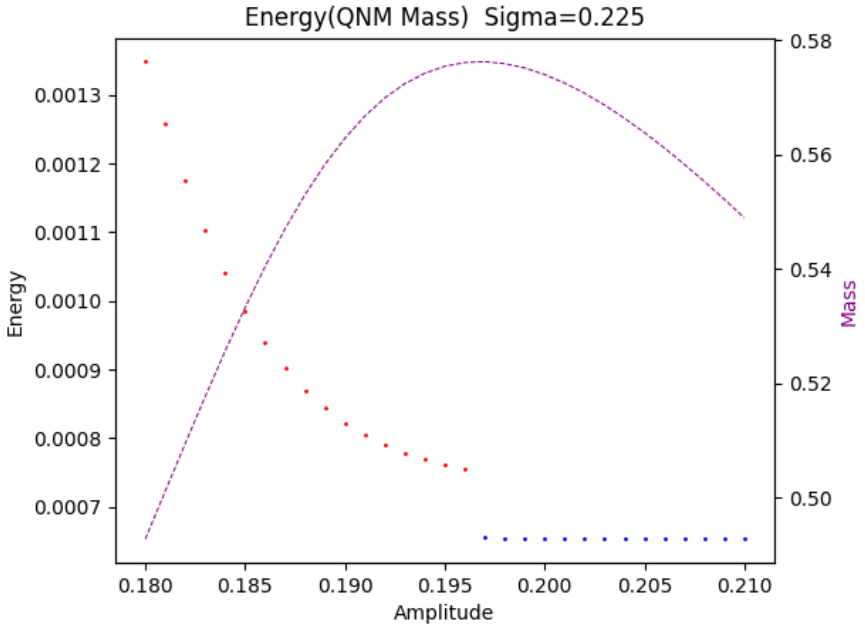

(b) The normalization method for this plot is based on the Quasinormal mode mass.

Fig. 5.35 This plot shows the energy of gravitational waves produced by head-on collisions with different central amplitude after a given $\sigma = 0.225$, where the purple auxiliary coordinates in both figures represent the initial soliton mass. In the plot, the red points represent two solitons colliding and eventually forming a black hole. The blue points represent two solitons that form black holes separately before colliding, and then form a new black hole after the collision.

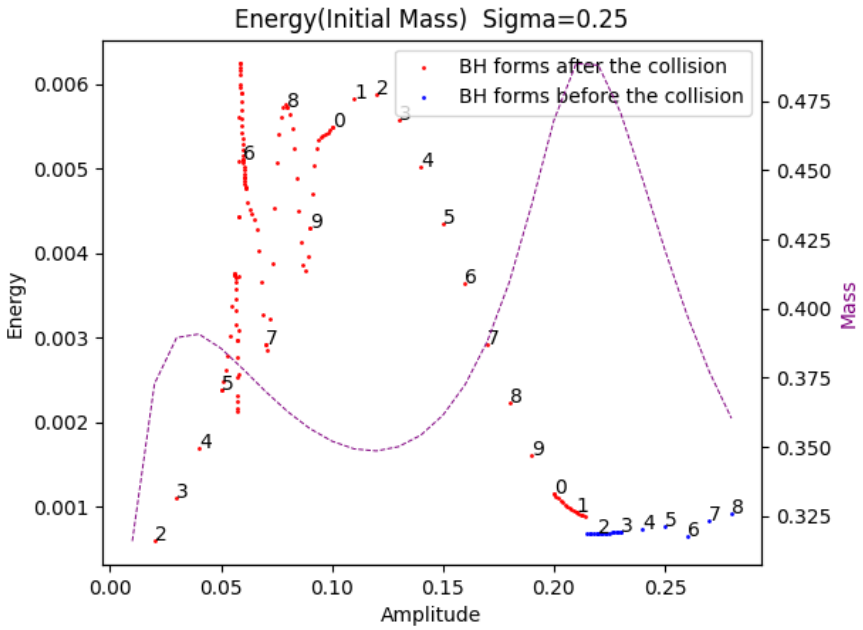

(a) The normalization method for this plot is based on the initial soliton mass.

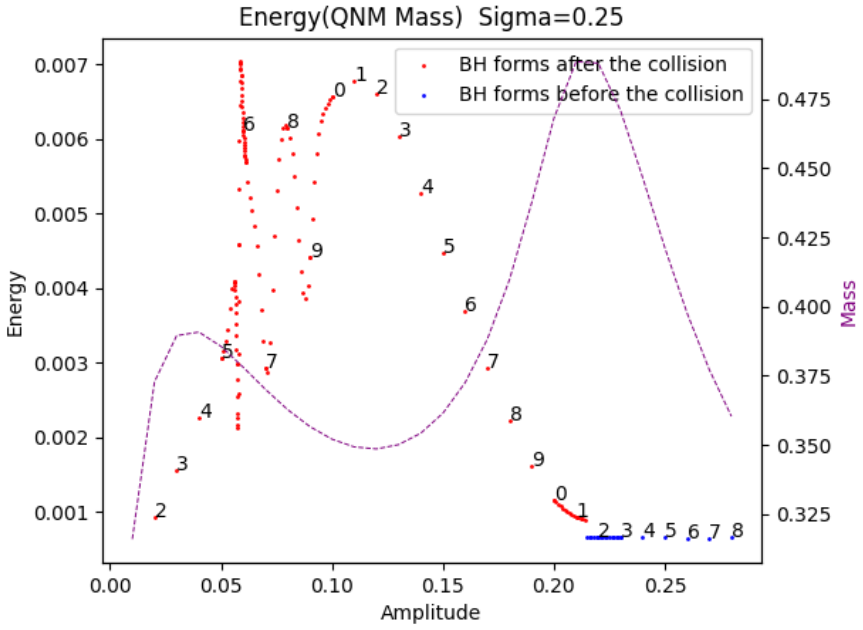

(b) The normalization method for this plot is based on the Quasinormal mode mass.

Fig. 5.36 This plot shows the energy of gravitational waves produced by head-on collisions with different central amplitude after a given $\sigma = 0.25$, where the purple auxiliary coordinates in both figures represent the initial soliton mass. In the plot, the red points represent two solitons colliding and eventually forming a black hole. The blue points represent two solitons that form black holes separately before colliding, and then form a new black hole after the collision.

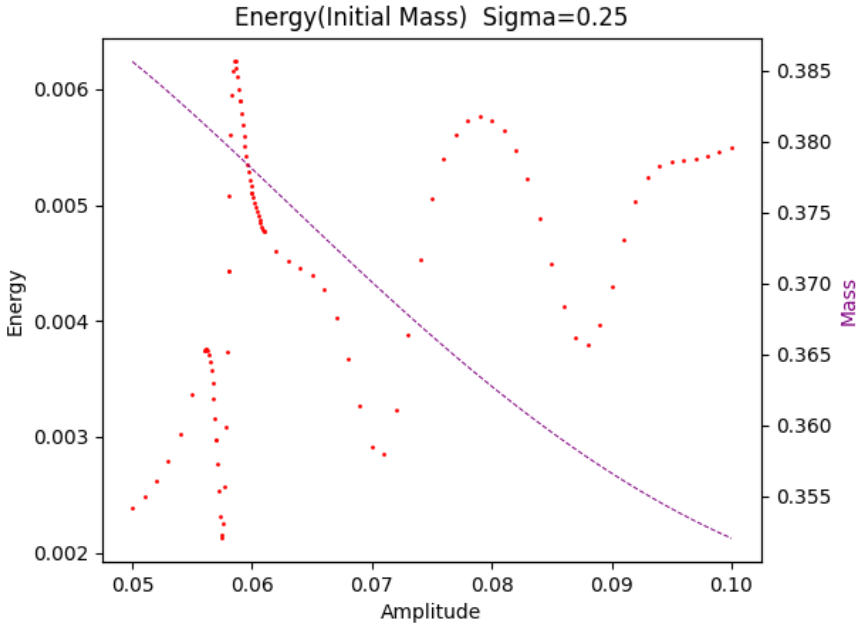

(a) The normalization method for this plot is based on the initial soliton mass.

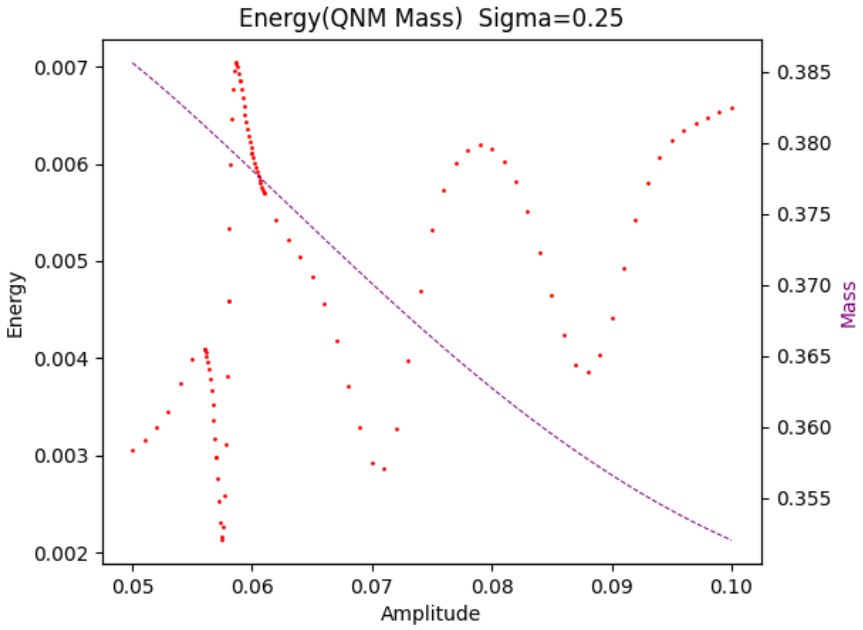

(b) The normalization method for this plot is based on the Quasinormal mode mass.

Fig. 5.37 This plot shows the energy of gravitational waves produced by head-on collisions with different central amplitude after a given $\sigma = 0.25$, where the purple auxiliary coordinates in both figures represent the initial soliton mass. In the plot, the red points represent two solitons colliding and eventually forming a black hole.

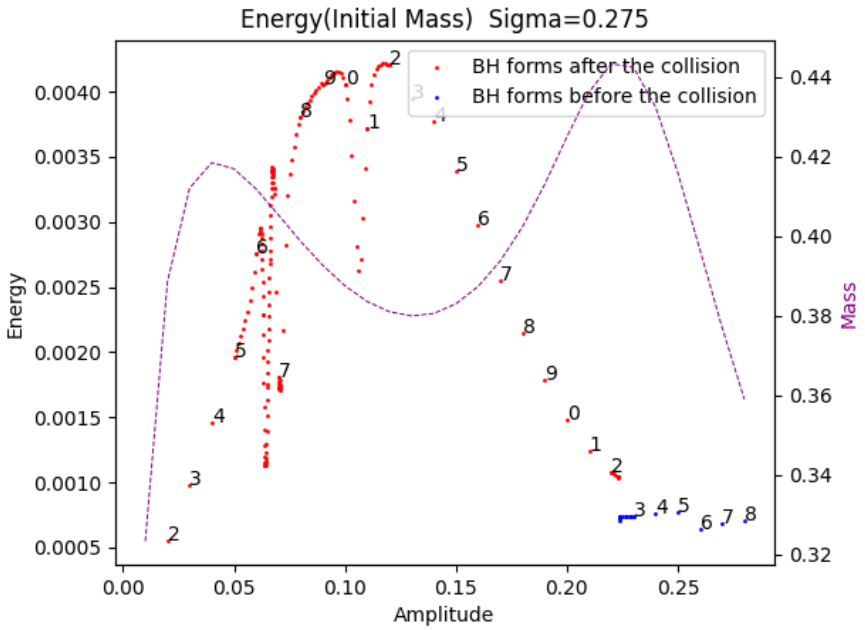

(a) The normalization method for this plot is based on the initial soliton mass.

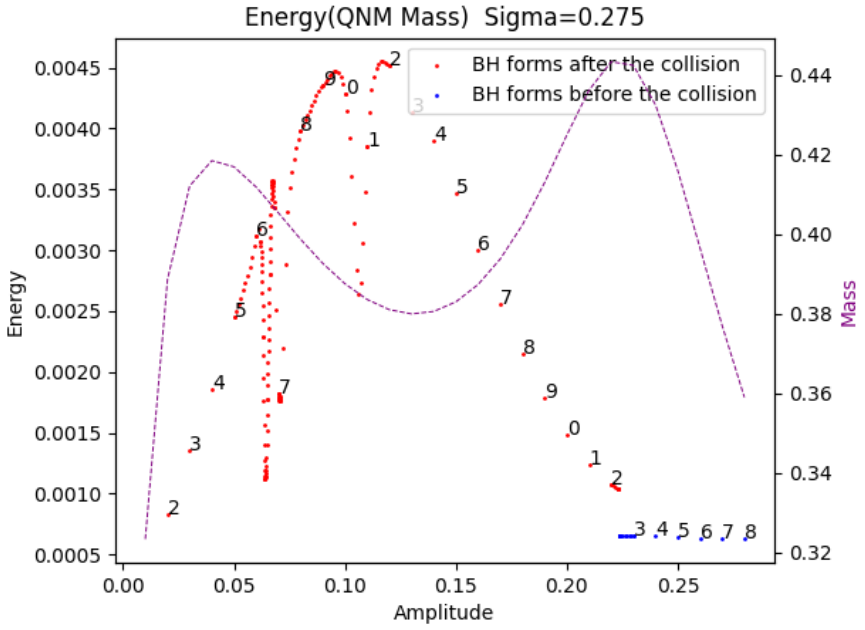

(b) The normalization method for this plot is based on the Quasinormal mode mass.

Fig. 5.38 This plot shows the energy of gravitational waves produced by head-on collisions with different central amplitude after a given $\sigma = 0.275$, where the purple auxiliary coordinates in both figures represent the initial soliton mass. In the plot, the red points represent two solitons colliding and eventually forming a black hole. The blue points represent two solitons that form black holes separately before colliding, and then form a new black hole after the collision.

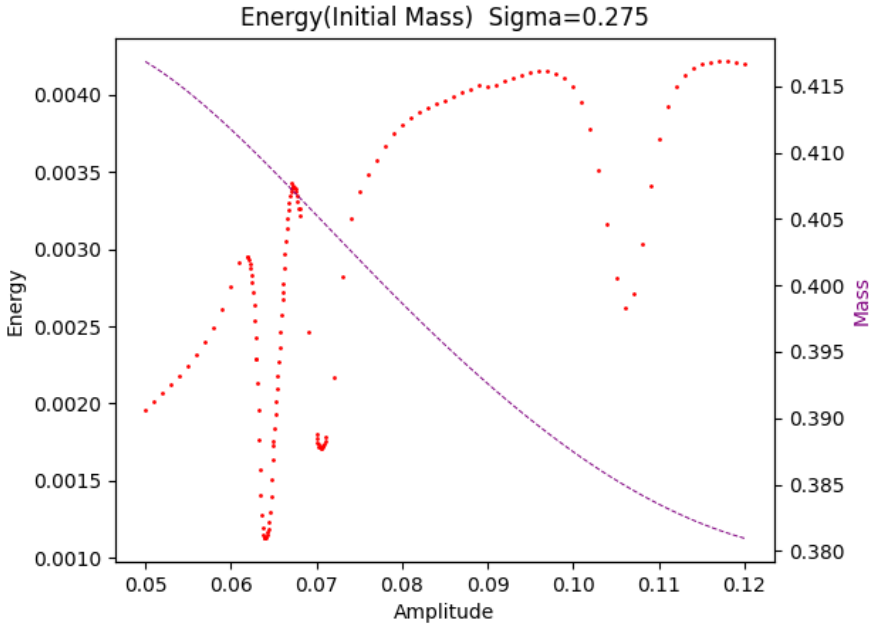

(a) The normalization method for this plot is based on the initial soliton mass.

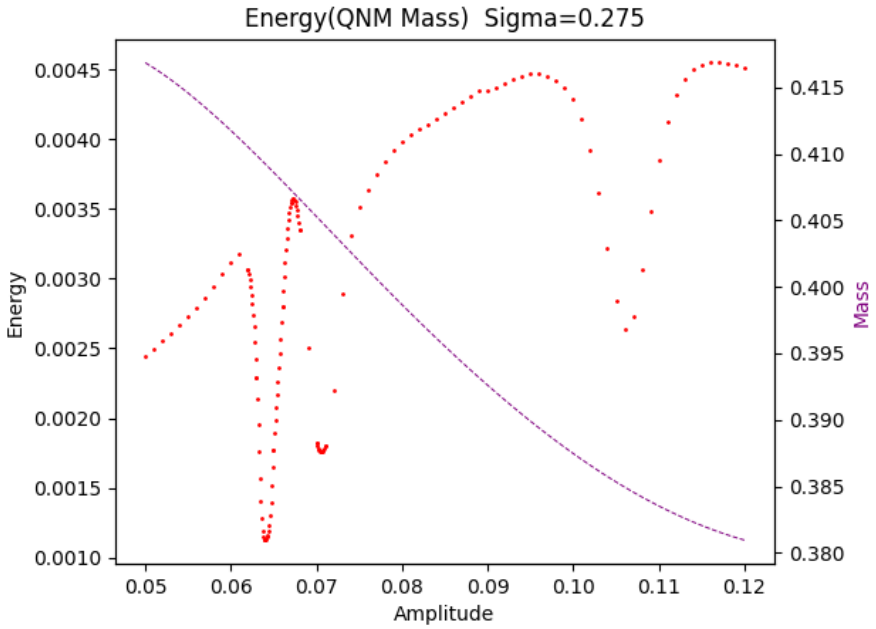

(b) The normalization method for this plot is based on the Quasinormal mode mass.

Fig. 5.39 This plot shows the energy of gravitational waves produced by head-on collisions with different central amplitude after a given $\sigma = 0.275$, where the purple auxiliary coordinates in both figures represent the initial soliton mass. In the plot, the red points represent two solitons colliding and eventually forming a black hole.

Combining these findings, we can summarize the following observations.

- Fine and intricate structures emerge after the first bump, located in the metastable region (see Figure 5.26a).
- The amplitudes of these structures vary, indicating a complex underlying dynamic.
- These fine structures begin to dissipate at the minima between the two bumps, suggesting a transition in stability.
- Following the second bump, which is also identified as the unstable section (refer to Figure 5.26a), solitons individually collapse into black holes prior to any collision.
- Energy consistently oscillates upwards in Regions I and II, reflecting continuous dynamic changes.
- In Region IV, the transition from red dots to blue dots is discontinuous.

Here, a clarification is necessary regarding stability discussions. Specifically, for $\sigma = 0.275$, we identified a few (two in our examples) solitons in Region II that were unstable. However, we did not observe them collapsing into black holes before their collision. This discrepancy arises because the collision time for these solitons is around $t = 315\ m^{-1}$, whereas their collapse into black holes happens significantly later (as in Figure 5.18).

Type-B

$\sigma = 0.28725$

In cases where the two bumps are equal, with the mass at 0.43018 $M_{\text{Pl}}^2 m^{-1}$ located at central amplitudes of 0.05 and 0.22, we observe two distinct branches in Region II: one continues to exhibit a fine structure, while the other demonstrates the phenomenon of *premature collapse into a black hole*. This bifurcation is consistent with the split observed in the corresponding section of Figure 5.26b (as in Figures 5.40 but for $\sigma = 0.28725$).

Furthermore, in Region II, the transition from red dots to blue dots is continuous, while the transition from blue dots back to red dots is discontinuous, as shown in the zoomed in Figure 5.41 but for $\sigma = 0.28725$. However, in Region IV, the transition from red dots to blue dots is discontinuous.

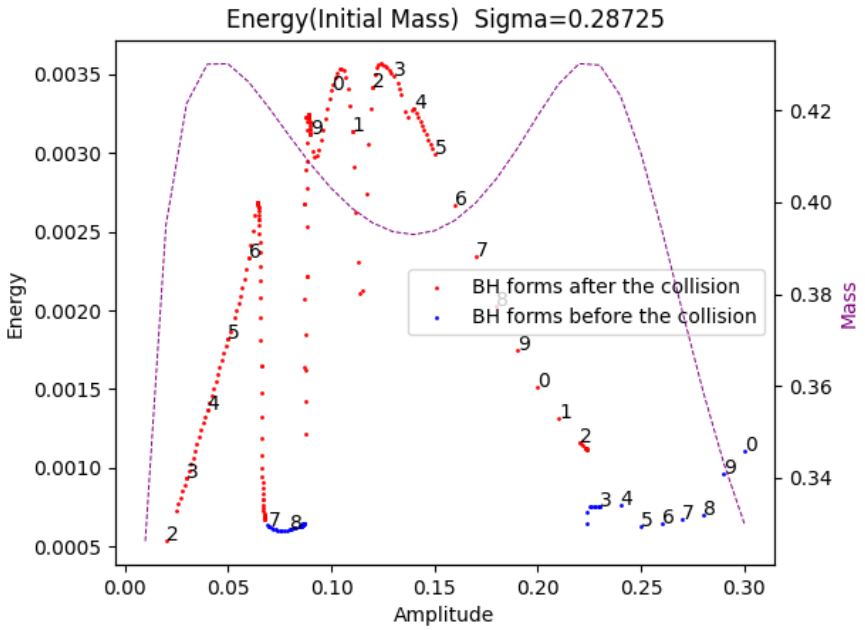

(a) The normalization method for this plot is based on the initial soliton mass.

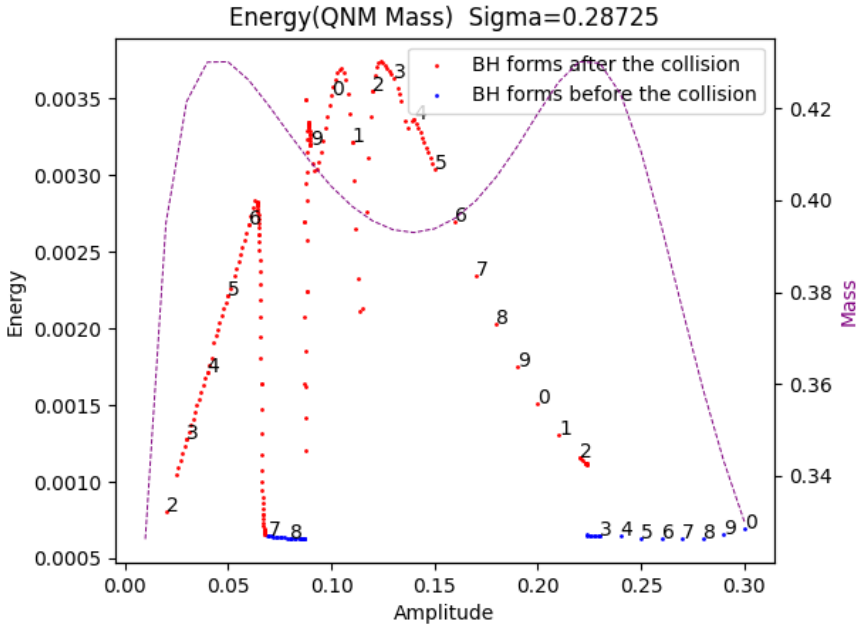

(b) The normalization method for this plot is based on the Quasinormal mode mass.

Fig. 5.40 This plot shows the energy of gravitational waves produced by head-on collisions with different central amplitude after a given $\sigma = 0.28725$, where the purple auxiliary coordinates in both figures represent the initial soliton mass. In the plot, the red points represent two solitons colliding and eventually forming a black hole. The blue points represent two solitons that form black holes separately before colliding, and then form a new black hole after the collision.

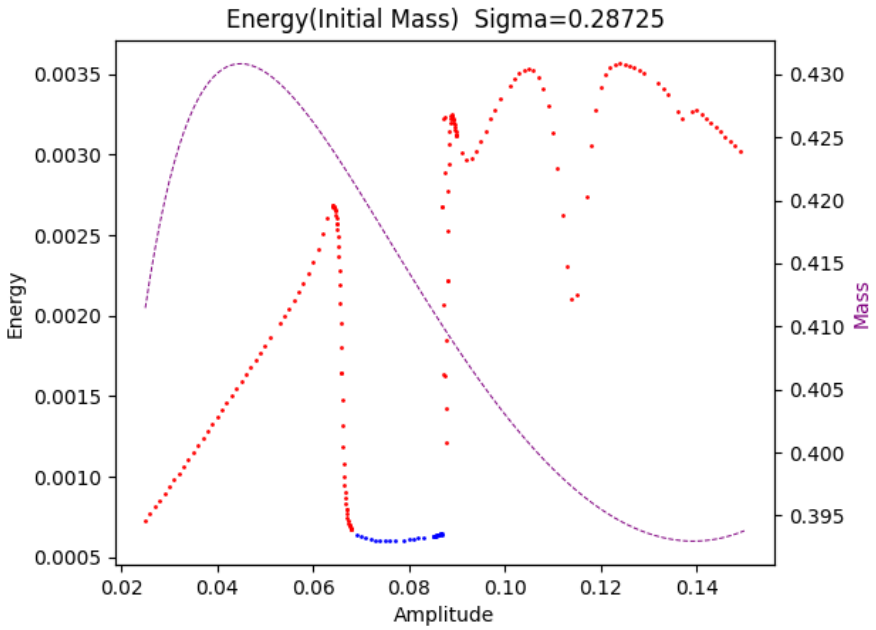

(a) The normalization method for this plot is based on the initial soliton mass.

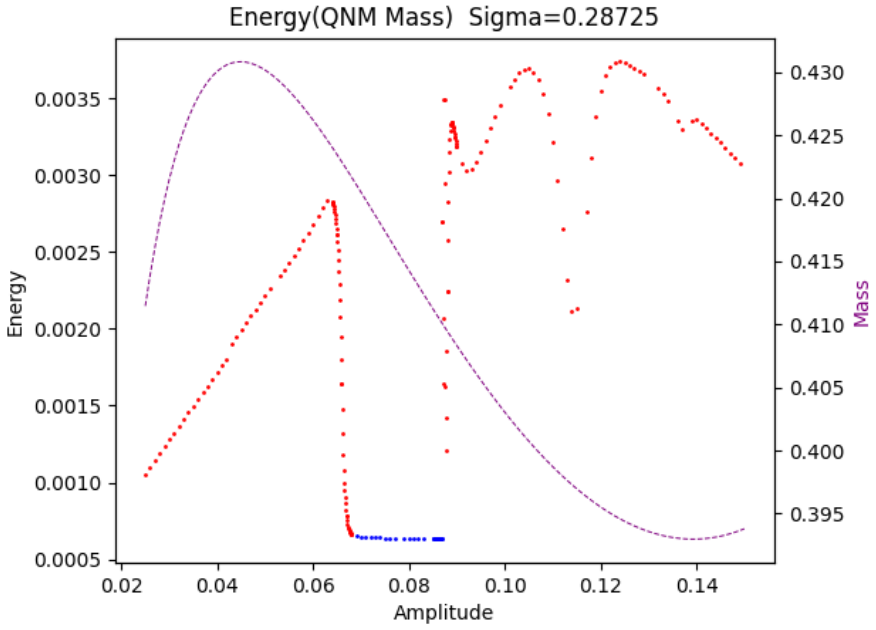

(b) The normalization method for this plot is based on the Quasinormal mode mass.

Fig. 5.41 This plot shows the energy of gravitational waves produced by head-on collisions with different central amplitude after a given $\sigma = 0.28725$, where the purple auxiliary coordinates in both figures represent the initial soliton mass. In the plot, the red points represent two solitons colliding and eventually forming a black hole. The blue points represent two solitons that form black holes separately before colliding, and then form a new black hole after the collision.

Type-C

$\sigma = 0.3$

When σ increases to 0.3, all fine structures in Region II vanish, replaced by the phenomenon of "premature collapse into a black hole" (as in Figure 5.42 but for $\sigma = 0.3$)[4]. This is consistent with what is shown in Figure 5.26c.

It is important to highlight that the transitions between blue dots and red dots in Region II are consistent with those observed at $\sigma = 0.28725$.

Higher σ

$\sigma = 0.5$

When σ reaches 0.5, we observe that their behavior closely resembles that of mini-boson stars, as illustrated in Figures 5.45 for $\sigma = 0.5$ and B.12 for mini-boson stars. However, their potential differs significantly, as detailed in Appendix B. These cases exhibit only one bump, and the transition from red dots to blue dots is continuous. For brevity, we only present the results for $\sigma = 0.5$ here. Detailed simulations for $\sigma = 1.0$, $\sigma = 2.0$, and mini-boson stars are available in Appendix B.

[4]In our analysis of stability for $\sigma = 0.3$, we observed that unstable solitons began to appear at a central amplitude of 0.05. However, because the time required for these solitons (with central amplitudes of 0.05 and 0.06) to collapse into black holes was significantly longer than $t = 315\ m^{-1}$, this delayed the appearance of the blue dots to a central amplitude of 0.07 (We have already encountered a similar situation in the example with $\sigma = 0.275$.

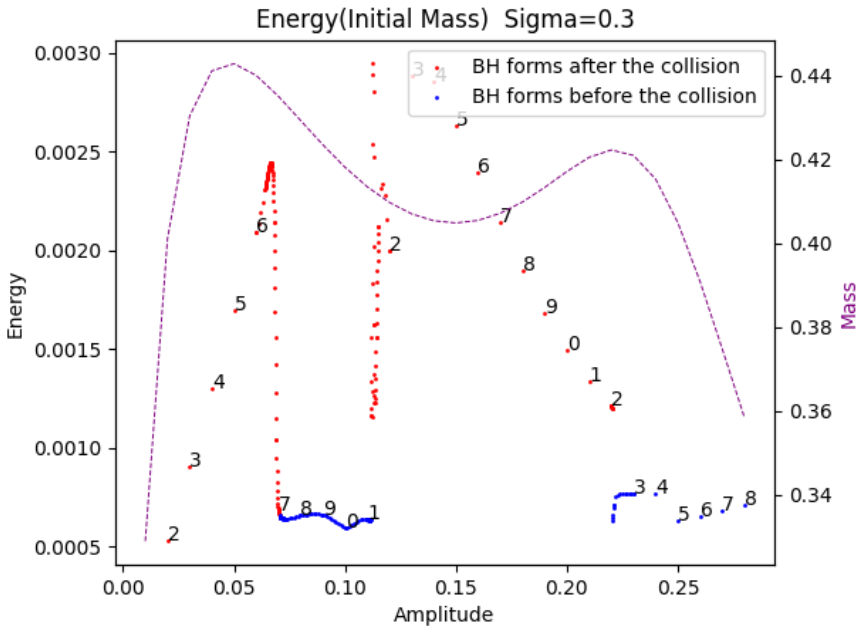

(a) The normalization method for this plot is based on the initial soliton mass.

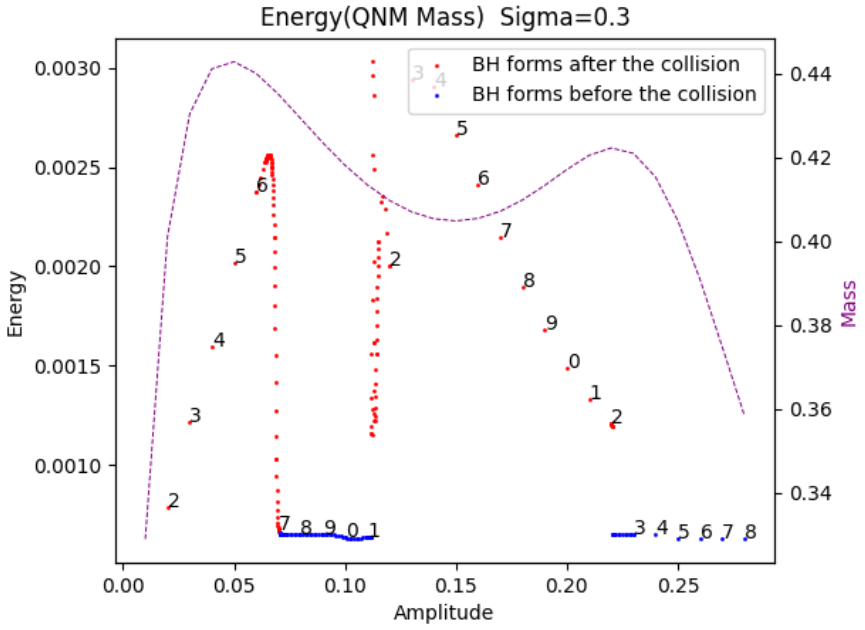

(b) The normalization method for this plot is based on the Quasinormal mode mass.

Fig. 5.42 This plot shows the energy of gravitational waves produced by head-on collisions with different central amplitude after a given $\sigma = 0.3$, where the purple auxiliary coordinates in both figures represent the initial soliton mass. In the plot, the red points represent two solitons colliding and eventually forming a black hole. The blue points represent two solitons that form black holes separately before colliding, and then form a new black hole after the collision.

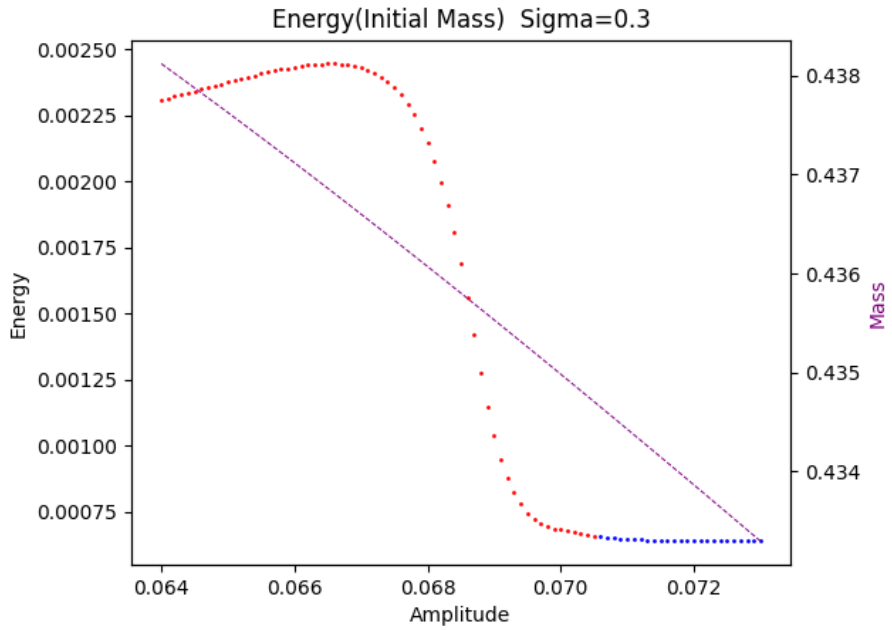

(a) The normalization method for this plot is based on the initial soliton mass.

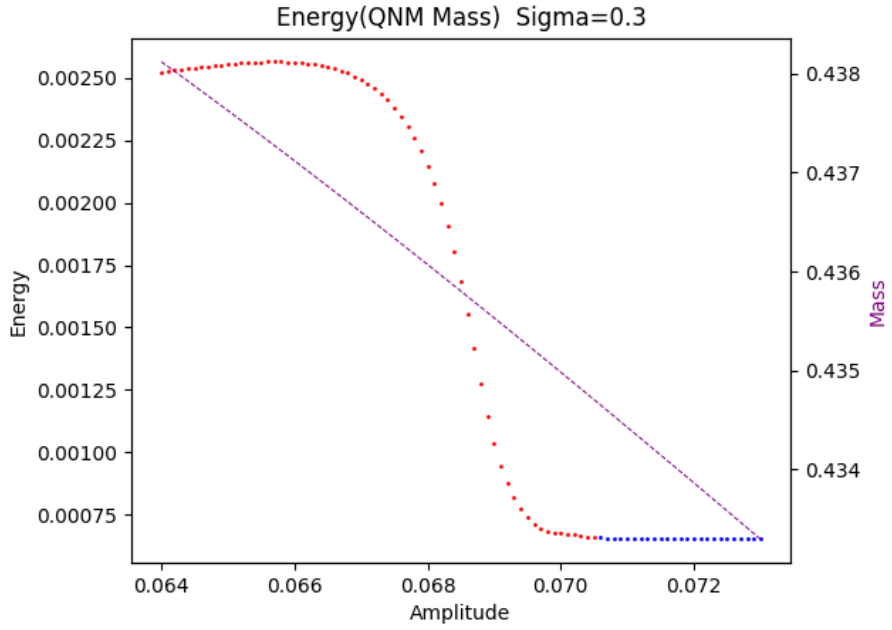

(b) The normalization method for this plot is based on the Quasinormal mode mass.

Fig. 5.43 This plot shows the energy of gravitational waves produced by head-on collisions with different central amplitude after a given $\sigma = 0.3$, where the purple auxiliary coordinates in both figures represent the initial soliton mass. In the plot, the red points represent two solitons colliding and eventually forming a black hole. The blue points represent two solitons that form black holes separately before colliding, and then form a new black hole after the collision.

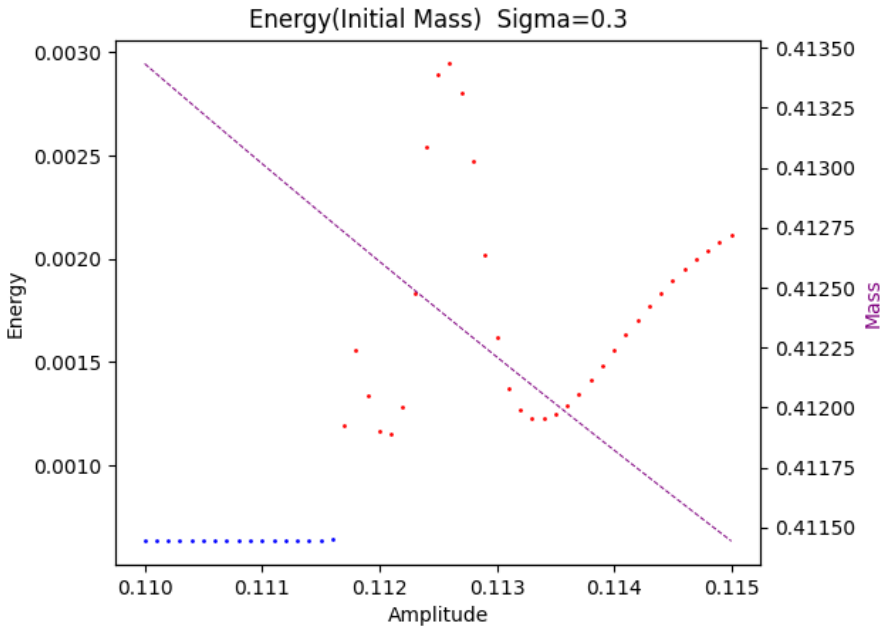

(a) The normalization method for this plot is based on the initial soliton mass.

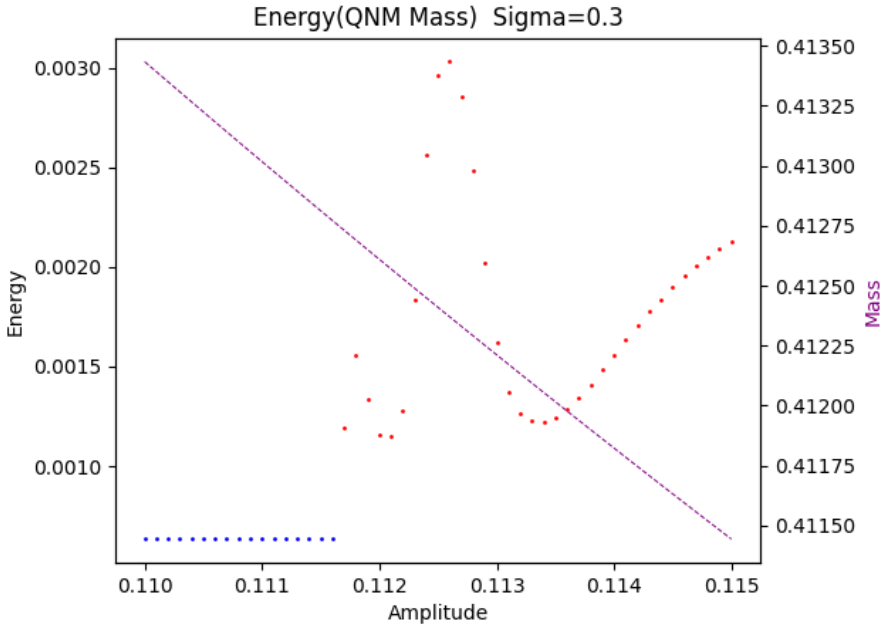

(b) The normalization method for this plot is based on the Quasinormal mode mass.

Fig. 5.44 This plot shows the energy of gravitational waves produced by head-on collisions with different central amplitude after a given $\sigma = 0.3$, where the purple auxiliary coordinates in both figures represent the initial soliton mass. In the plot, the red points represent two solitons colliding and eventually forming a black hole. The blue points represent two solitons that form black holes separately before colliding, and then form a new black hole after the collision.

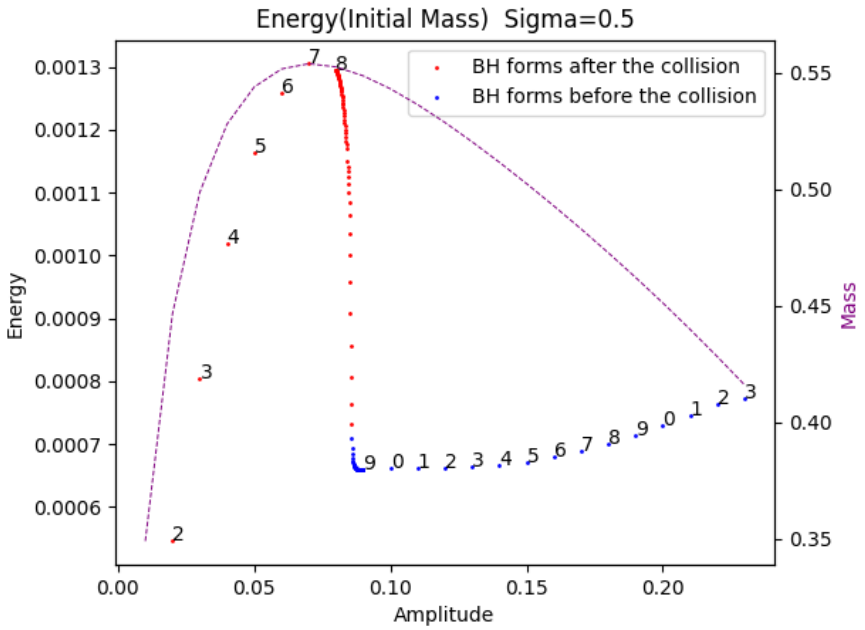

(a) The normalization method for this plot is based on the initial soliton mass.

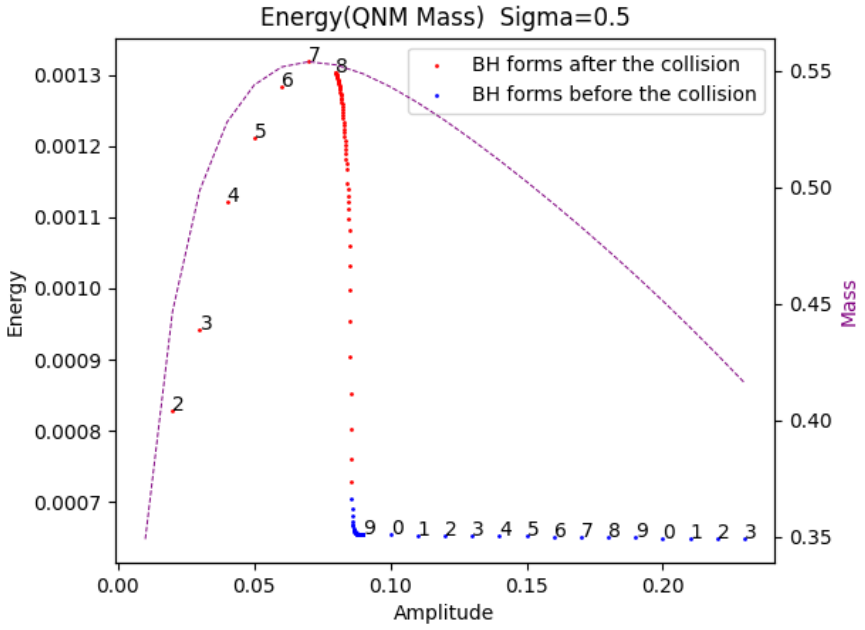

(b) The normalization method for this plot is based on the Quasinormal mode mass.

Fig. 5.45 This plot shows the energy of gravitational waves produced by head-on collisions with different central amplitude after a given $\sigma = 0.5$, where the purple auxiliary coordinates in both figures represent the initial soliton mass. In the plot, the red points represent two solitons colliding and eventually forming a black hole. The blue points represent two solitons that form black holes separately before colliding, and then form a new black hole after the collision.

Overall Results

Based on our findings, we summarize the following:

For lower σ, two mass bumps generally appear, exhibiting the following characteristics:

- In Region I, solitons are stable, and the energy of gravitational waves increases monotonically.
- In Region II, the state of solitons depends on the sizes of the two bumps. For metastable solitons, the energy of gravitational waves forms fine and regular structures, displaying an oscillatory upward trend. In contrast, unstable solitons collapse into black holes independently before colliding, with no significant changes in gravitational wave energy.
- In Region III, solitons are stable, and the energy of gravitational waves decreases monotonically.
- In Region IV, solitons are unstable; they collapse into black holes independently before any collision occurs, with no notable changes in gravitational wave energy.

For higher σ values, the pattern of gravitational wave energy resembles that of mini-boson stars, although in many instances, the potential of these solitons still significantly differs from that of mini-boson stars.

Notably, in Region II, the transition from red dots to blue dots appears continuous. However, as we will discuss later in Section 5.8, we expect this to become discontinuous with a larger initial separation distance. In contrast, the transition from blue dots back to red dots is discontinuous. Additionally, in Region IV, the transition from red dots to blue dots remains consistently discontinuous.

5.8 Exploring the Origins of Gravitational Wave Characteristics

We aim to determine if these fine and complex structures are inherent properties of the soliton and which specific characteristics of the soliton they reveal. To explore this, we intend to slightly modify the initial conditions of the simulation to assess whether these complex structures continue to exist and maintain stability.

Our investigation will concentrate on the scenario with $\sigma = 0.25$. We plan to adjust the initial separation distance from 80 m^{-1} to 60 m^{-1}, while maintaining all other parameters unchanged, and then reinitiate the evolution process.

The results, illustrated in Figure 5.46, reveal an unexpected finding: while the fine structures persist in Region II, their configurations are markedly different from those seen with an initial separation distance of 80 m^{-1} (see Figures 5.36 and 5.37). These structures are less intricate than those observed with the larger initial separation distance.

Given that a minor adjustment in the initial separation distance essentially alters the timing of their collisions, and linking this to the fact that solitons at $\sigma = 0.25$ in Region II are in a metastable state, we can reasonably hypothesize that this is related to the migration of these solitons. To test this hypothesis, it would be beneficial to select several points within Region II and continuously adjust their initial separation distances to explore the presence of any unique structural characteristics.

We selected examples in Region II with central amplitudes of 0.06, 0.07, and 0.08. For comparison, we also selected a case in Region I with a central amplitude of 0.03.

The results displayed in Figure 5.47 indicate that the stable soliton maintains relatively consistent gravitational wave energy as the initial separation distance varies, albeit with a gradual upward trend. In contrast, metastable solitons exhibit regular, fine structures.

The oscillatory-like structure brings to mind the maximum value of $\sqrt{|\phi|^2}$, as discussed in Section 5.5. This similarity prompted us to examine the relationship between the maximum value of $\sqrt{|\phi|^2}$ for a single soliton and that generated during the collision of binary solitons.

Figure 5.48 illustrates the scenario with an initial central amplitude of 0.08. It demonstrates that the merging of the binary system occurs while the solitons are in a metastable state. Consequently, solitons that merge at different times display markedly different gravitational wave energies.

On the other hand, Figure 5.49 illustrates the reason why decreasing the initial separation distance to 60 m^{-1} results in less complex fine structures in gravitational wave energies. This occurs because, at shorter initial separation distances, many solitons do not have sufficient time to reach a metastable state.

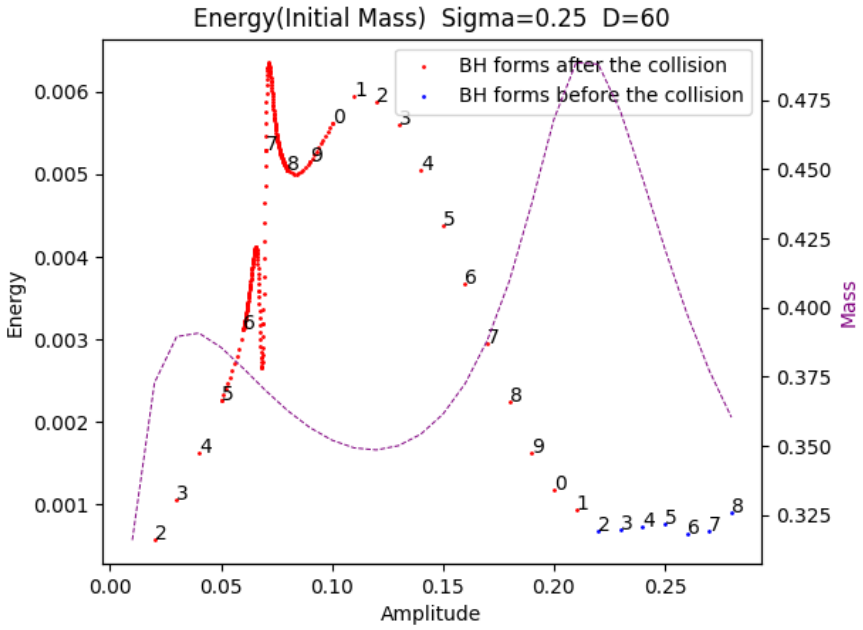

(a) The initial separation distance is set to 60 m^{-1}, and the normalization method employed is based on the initial soliton mass.

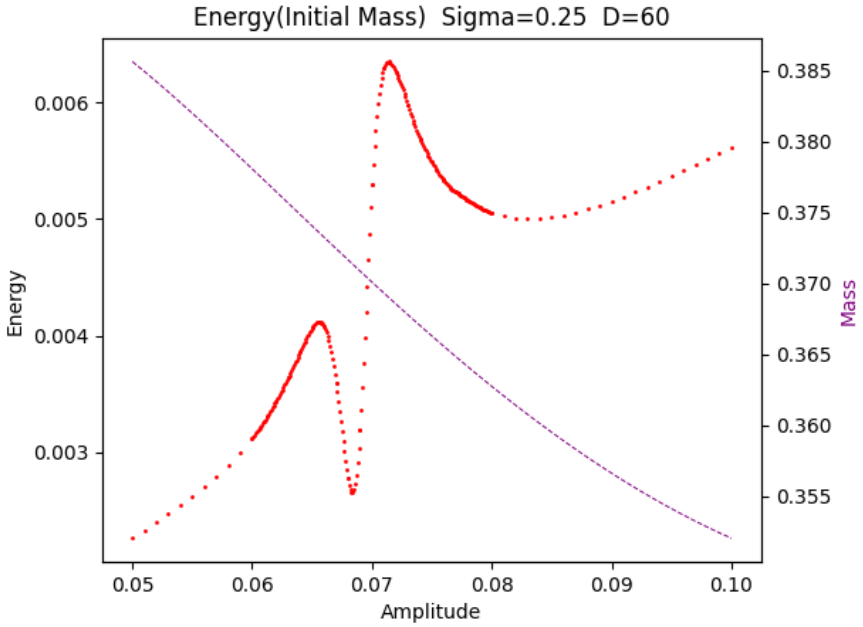

(b) The zoomed in view of the fine structure.

Fig. 5.46 This plot shows the energy of gravitational waves produced by head-on collisions with different central amplitude after a given $\sigma = 0.25$, where the purple auxiliary coordinates in both figures represent the initial soliton mass. In the plot, the red points represent two solitons colliding and eventually forming a black hole. The blue points represent two solitons that form black holes separately before colliding, and then form a new black hole after the collision.

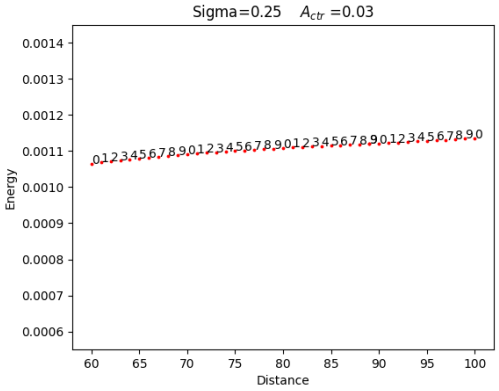

(a) $A_{ctr} = 0.03$ Stable

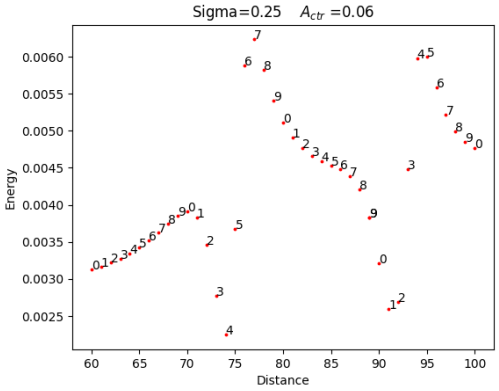

(b) $A_{ctr} = 0.06$ Metastable

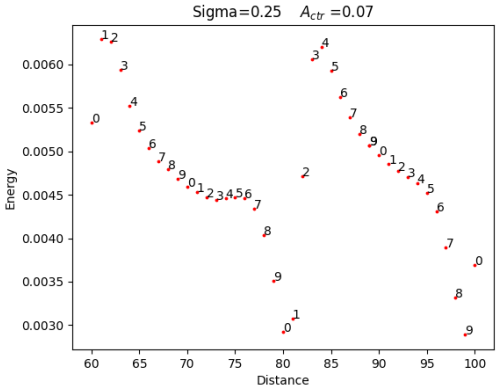

(c) $A_{ctr} = 0.07$ Metastable

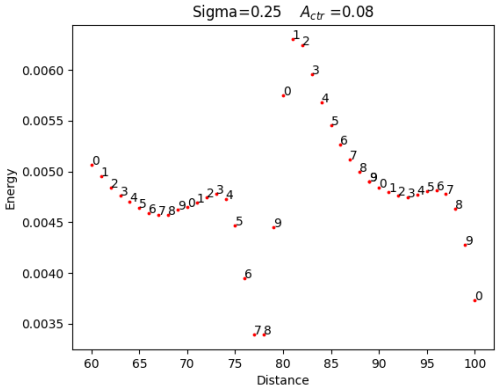

(d) $A_{ctr} = 0.08$ Metastable

Fig. 5.47 This figure illustrates the variation in gravitational wave energy as a function of initial separation distance.

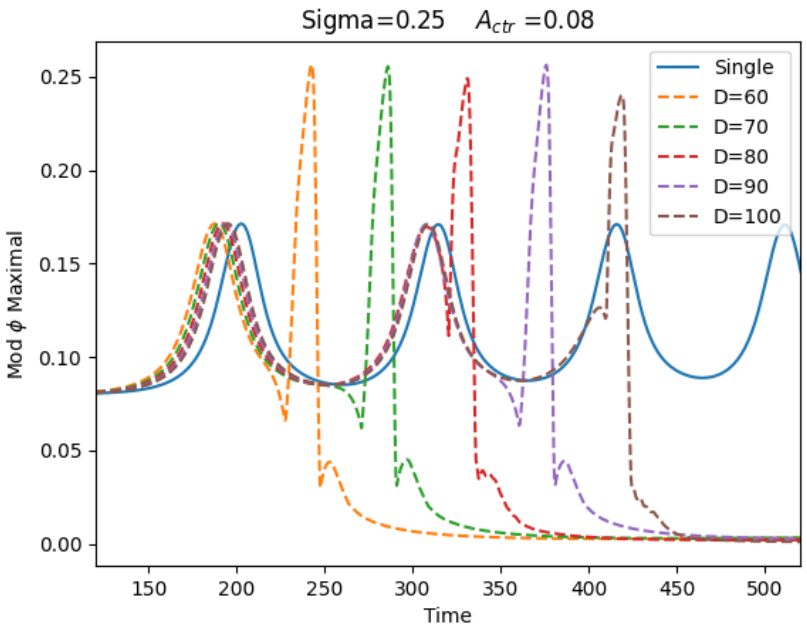

Fig. 5.48 This figure illustrates how the maximum value of $\sqrt{|\phi|^2}$ varies over time. In this context, $A_{ctr} = 0.08$ denotes the initial central amplitude, **Single** refers to an individual soliton, and **D** indicates the initial separation distance.

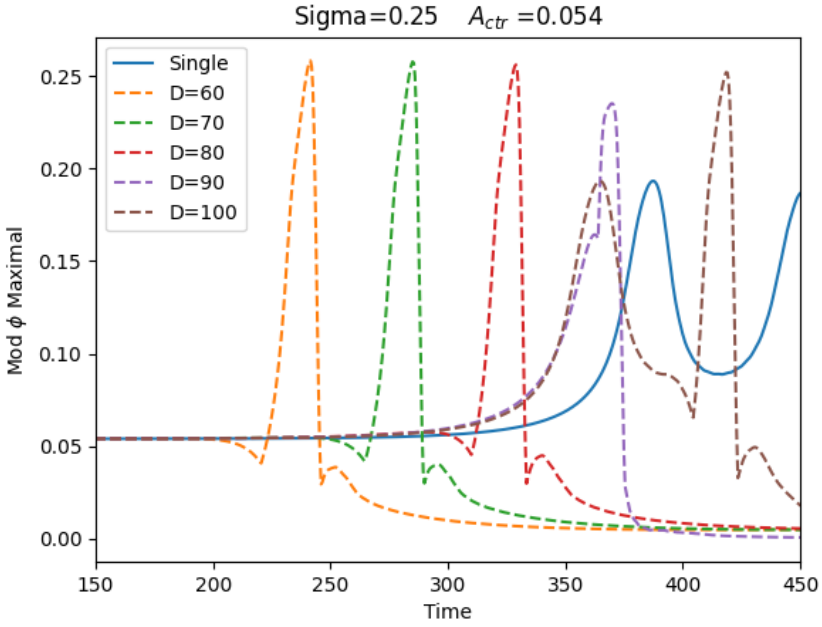

Fig. 5.49 This figure illustrates how the maximum value of $\sqrt{|\phi|^2}$ varies over time. In this context, $A_{ctr} = 0.054$ denotes the initial central amplitude, **Single** refers to an individual soliton, and **D** indicates the initial separation distance.

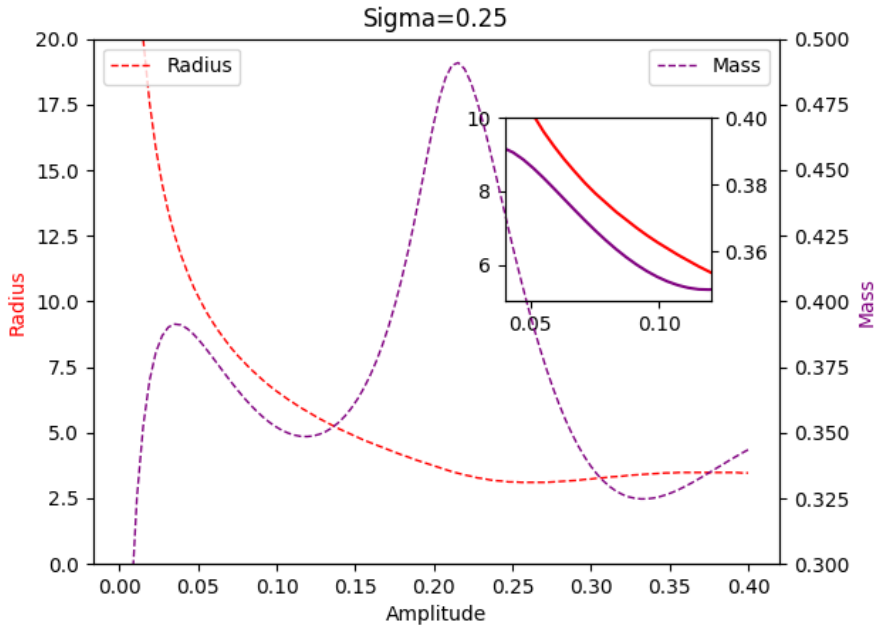

Fig. 5.50 Amplitude against Radius and Mass for $\sigma = 0.25$

We have also examined the correlation between the local maxima (or minima) of energy and the $\sqrt{|\phi|^2}$ of a single soliton. However, no definitive connection has been found. This may stem from the greater-than-expected differences between single soliton systems and binary systems. Numerous intrinsic factors within these systems could affect their $\sqrt{|\phi|^2}$. Consequently, we are limited to hypotheses. We speculate that in Region II, the variations in the solitons' radius are more pronounced than those in their mass, as illustrated in Figure 5.50. Thus, *fluffier* solitons may emit more gravitational wave energy, whereas the converse may be true for less fluffy ones. Unfortunately, this hypothesis remains unconfirmed as we still lack concrete evidence to substantiate it.

We understand the transitions between blue and red dots as follows: Our results show continuous transitions between red and blue dots near the $dM/dA = 0$ point in Region II. We hypothesize that this continuity may be misleading, potentially caused by **pseudo-red dots**. These are actually unstable solitons that appear similar to stable red dots because their collapse time exceeds their collision time. In truth, transitions between red dots and blue dots should all be discontinuous, as demonstrated when comparing the gravitational wave energies of actual red and blue dots. This explains why the apparent continuity is not observed in other areas, such as the transitions from blue dots to red dots in Region II and from red dots to blue dots in Region IV, where the collapse time of unstable solitons into black holes is significantly shorter than their collision time. Thus, pseudo-red dots in Region II obscure the true discontinuous nature of these transitions. If our initial separation

distance were sufficiently increased to allow each unstable soliton enough time to collapse into a black hole, then all transitions would be observed as discontinuous. This analysis also applies to scenarios involving a single bump.

5.9 Conclusion

In this section, we employ our **2D BosonStar Code** to systematically investigate the stability of single solitons and the gravitational wave energy emitted during the head-on collisions of solitons under varied conditions. We specifically focus on the parameters σ and central amplitude.

Our key findings regarding the gravitational wave energy emitted during the head-on collisions of solitons are summarized as follows:

1. In scenarios with a single bump, which are typically associated with higher σ values:
   - If the initial central amplitude results in $\frac{dM}{dA_{\text{ctr}}} < 0$, the soliton evolves into a black hole.
   - If the initial central amplitude results in $\frac{dM}{dA_{\text{ctr}}} > 0$, the soliton remains stable.
2. In scenarios with two bumps:
   - The area near the second bump consistently aligns with the conditions of the single bump.
   - Near the first bump, the soliton remains stable if $\frac{dM}{dA_{\text{ctr}}} > 0$. In regions where $\frac{dM}{dA_{\text{ctr}}} < 0$, the behavior depends on the size of the two bumps. Figure 5.26 provides a clear summary of these dynamics.

Our findings on the stability of solitons and gravitational wave energy across different σ levels are as follows:

1. For lower σ, two mass bumps generally manifest, with distinct behaviors in each region:
   - Region I: Solitons are stable (stable), and gravitational wave energy consistently increases.
   - Region II: The state of solitons varies with the size of the two bumps. Metastable solitons (metastable) show finely structured, oscillatory increases in gravitational wave energy. Unstable solitons (unstable) collapse into black holes independently before colliding, with no significant energy changes.
   - Region III: Solitons remain stable (stable), with a monotonic decrease in gravitational wave energy.
   - Region IV: Solitons are unstable (unstable); they independently collapse into black holes pre-collision, without significant energy changes.

2. For higher σ values, the gravitational wave energy pattern resembles that of mini-boson stars, though the potential of the solitons often significantly differs from that of mini-boson stars.

3. Significantly, transitions in gravitational wave energy in Region II from red dots to blue dots seem continuous. However, as discussed in Section 5.8, we expect this to become discontinuous with a larger initial separation distance. Conversely, the reverse transition is discontinuous. Moreover, in Region IV, the transition from red dots to blue dots is consistently discontinuous.

We are investigating whether the intricate structures observed in solitons are inherent and what characteristics they reflect. Specifically, we are adjusting the initial conditions of our simulation by reducing the separation distance from 80 m^{-1} to 60 m^{-1}, focusing on scenarios where $\sigma = 0.25$. This adjustment will help determine if these structures remain stable and retain their complexity.

The results from this adjusted setup, presented in Figure 5.46, show that while the fine structures persist in Region II, they are significantly simpler than those observed with a larger separation distance. This suggests that closer initial distance might inhibit the development of complex structures due to altered collision timing.

To further test this, we plan to continuously adjust the initial distances of selected points within Region II and monitor for any unique structural changes. Initial findings, as seen in Figure 5.47, reveal that stable solitons maintain consistent gravitational wave energy levels, showing a slight upward trend, while metastable solitons demonstrate distinct, regular patterns.

Additionally, our research examines the relationship between the maximum value of $\sqrt{|\phi|^2}$ and the gravitational wave energies produced during collisions. Despite the absence of a definitive connection, we conjecture that fluffier solitons might emit more gravitational wave energy. This hypothesis, while intriguing, still lacks concrete evidence.

Finally, we offer an explanation regarding the transitions. We believe that all transitions should be discontinuous. The continuity observed in Region II is due to pseudo-red dots.

Chapter 6

Conclusions

"Success is not final; failure is not fatal: it is the courage to continue that counts." — There is **no evidence** that this quote is attributed to Winston Churchill [1].

6.1 Summary

This thesis focuses on boson stars and their associated gravitational waves, encompassing an introduction to the relevant background and three related research studies.

In **Chapter** 1, we provide a brief introduction to the foundational concepts of General Relativity, covering Differential Geometry as the mathematical framework, the Einstein field equations as the core equation of the theory, and the primary focus of this thesis: Gravitational Waves.

Chapter 2 presents the core methodology of this thesis—Numerical Relativity. This includes the $3+1$ decomposition, the ADM formalism, the BSSN formalism, and the CCZ4 formalism, along with methods for generating initial conditions and selecting appropriate gauges.

In **Chapter** 3, we delve into the central topic of this thesis—boson stars. We begin by providing an overview of the methods used to solve the Einstein-Klein-Gordon system, followed by a discussion of several typical boson star models. Lastly, we briefly explore the formation of boson stars, their critical phenomena, and their significance in astronomy.

In the **First Section** of **Chapter** 4, we simulated head-on collisions of equal-mass, non-spinning boson stars and the accompanying gravitational wave radiation. Our study primarily focused on creating initial data for boson star binaries and assessing the impact

[1] Quotes Falsely Attributed To Winston Churchill (https://winstonchurchill.org/resources/quotes/quotes-falsely-attributed/).

of systematic errors on simulation results. We compared the usual method of plain superposition Equation (4.2) with a refined procedure Equation (4.4) from Ref. [110]. Our findings indicate that the refined procedure leads to significant improvements in initial constraint violations and binary boson star collision simulations. However, using plain superposition can lead to inaccurate results, including premature gravitational collapse. Despite its effectiveness, the refined method has limitations: it is suitable only for a specific class of equal-mass, non-spinning binaries, and it still leaves some residual constraint violations. Therefore, it is better viewed as an improved starting point for constraint-solving procedures. Future work will focus on overcoming these limitations and incorporating a numerical constraint solver.

In the **Second Section** of **Chapter** 4, we presented that the inspiral and coalescence of boson star binaries into a non-black hole remnant can produce a prolonged gravitational wave afterglow. This distinct signature, different in duration and possibly frequency from traditional compact object mergers, offers a unique detection channel in gravitational wave searches [3, 8, 9, 7, 16, 15, 14, 13]. Our findings imply several things. Regarding search strategies, these signatures might be missed by focusing only on pre-merger and merger waveforms. Developing waveform templates for post-merger boson star binaries is a current challenge, requiring effective parameterization of gravitational wave signatures. We also observed efficient angular momentum loss in boson star mergers, forming a horizon-less remnant, aligning with past studies on the spin decay of rotating boson stars [192]. A notable correlation between the spin-down of the boson star remnant and the synchronization of gravitational wave amplitude extrema across different modes was observed, suggesting that gravitational wave afterglows convey information about the remnant's evolution. Considering the length of the afterglow, we hypothesize that numerous boson star merger events could create a stochastic gravitational wave background, distinct from traditional binary mergers [78]. Further exploration of the boson star parameter space is necessary to link theoretical gravitational wave background estimates to hypothetical boson star populations. Our boson star configurations were not fine-tuned, indicating that the afterglow could be a common feature in boson star coalescences, as long as they do not immediately form a black hole.

In **Chapter** 5, the primary goal is to explore in depth the specific characteristics of gravitational wave emission from solitonic boson stars (soliton) in head-on collisions. Specifically, we consider a two-dimensional hypersurface of the parameter space spanned by σ and the boson star compactness, controlled through the central scalar-field amplitude A_{ctr}. Across this parameter range, we monitor the boson star dynamics during infall and merger, the nature of the remnant, and, most importantly, the resulting gravitational wave emission.

Several remarkable features are demonstrated in our results, with the case of $\sigma = 0.28725$ (see Figures 5.40 and 5.41) serving as an example to illustrate them.

1. **Boson star collisions can be radiatively way more efficient than those of black holes.**

   The gravitational wave energy released in the boson star collisions reaches values up to $E_{\rm GW}/M_{\rm tot} = 0.0035$, about [2] six times larger than the corresponding number 6×10^{-4} observed in head-on collisions of non-spinning equal-mass black holes; see e.g. Figure 4 in Ref. [216] and also compare with the blue dots in our Figure 5.40 where the boson stars have collapsed to black holes prior to merger. We will encounter yet larger energies when we discuss other σ values later on. This effect was first noted in Ref. [110] in the context of self-gravitating real-scalar-field oscillatons, suggesting that this is a generic effect for mergers of compact objects composed of fundamental fields.

2. **There are discontinuities in the gravitational wave energy viewed as a function of $A_{\rm ctr}$.**

   At $A_{\rm ctr} \gtrsim 0.08$, the energy $E_{\rm GW}$ abruptly jumps from the black hole value $E_{\rm GW}^{\rm BH} \approx 6\times10^{-4}\,M_{\rm tot}$ (blue dots) to about twice this value (the next right red dot). Between $A_{\rm ctr} = 0.22$ and $A_{\rm ctr} = 0.23$, the function $E_{\rm GW}(A_{\rm ctr})$ exhibits a further discontinuity; even though this jump is relatively small, it is well resolved by our numerics.

3. **Even away from these discontinuities, small differences in initial configurations lead to large $\mathcal{O}(1)$ differences in the gravitational wave emission.**

   The functional dependence of the gravitational wave energy on $A_{\rm ctr}$ exhibits sharp local extrema, most notably the local minimum at $A_{\rm ctr} \approx 0.115$. This effect suggests that it can be misleading to assume similar boson star collisions produce approximately equal output in gravitational waves.

4. **For unstable boson stars, the time scale for either migration to another boson star or collapse into a black hole is independent of perturbations**.

   This suggest that this timescale, which we dubbed *migration time* is a property of the equilibrium solutions, and not a function of initial conditions.

Additionally, there seems to be a significant correlation between the radiated energy $E_{\rm GW}(A_{\rm ctr})$ and the mass function $M(A_{\rm ctr})$—generally positive for small $A_{\rm ctr}$ and negative for large $A_{\rm ctr}$. However, this observation likely requires further research for confirmation.

[2] $M_{\rm tot}$ represents the total initial mass of the two boson stars.

6.2 Future Work

First, our findings from Chapter 5 will be discussed in greater detail and with more completeness in our forthcoming publication. Additionally, in Chapter 5, there are several issues that require further investigation. The first is related to metastable boson stars, where we aim to understand whether there is any correlation between their ***migration*** time and their central amplitude. The second issue concerns whether there is a correlation between the radiated energy and the mass function $M(A_{\rm ctr})$. Based on our current research, we seem to have found a possible connection, but further confirmation is needed. The third issue pertains to solitons with lower values of σ, where it is possible that three **bumps** could appear in the $M(A_{\rm ctr})$ function. We need to explore whether this leads to new results.

Our core task is to expand the parameter space. Although we have significantly improved the efficiency of numerical relativity with the 2D code, our computational resources are still insufficient for a comprehensive exploration of the parameter space. Therefore, the central question is how to generate more gravitational wave data using newer techniques based on our existing work. One promising approach is related to machine learning, where we could use machine learning to learn from and train on the existing gravitational wave data, and then generate new gravitational waves through machine learning [91, 152]. This could potentially be more efficient than pure 2D numerical relativity. This method, known as **Surrogate Modeling**, was first proposed in [91] and was later demonstrated to be effective in subsequent studies [44–46, 228]. More recently, [152] applied this approach to the Proca star system.

Additionally, since we need to run a large number of simulations, we cannot use very high resolutions. This means that our convergence and constraint violations may not be exceptional. However, in this case, the vast amount of existing data also opens the door for machine learning. One potential approach is to use deep convolutional neural networks to enhance the resolution and accuracy of numerical relativity simulations.

If the aforementioned work can be successfully accomplished, not only could we "perfectly" expand the parameter space for solitons, but we could also consider other models.

For example, our research in Chapter 5 primarily explores scenarios involving identical boson stars, as specified under the conditions in Equation 6.1, where $\varepsilon = 1$ and $\theta = 0$:

$$\phi = {}^{(1)}\phi_0(\mathbf{r_1})\, e^{i\omega t} + {}^{(2)}\phi_0(\mathbf{r_2})\, e^{i(\varepsilon\omega t+\theta)} \tag{6.1}$$

We are intrigued to explore whether such intricate structures are commonly found in other scenarios as well, including phase opposition ($\varepsilon = 1, \theta = \pi$), boson-anti-boson pairs ($\varepsilon = -1, \theta = 0$), or across various configurations with different θ values.

Similarly, any binary star model with $SO(2)$ symmetry can be explored using our code. In our research, we not only provide a framework for the 2D code but also offer an efficient, fully automated workflow script. This enables the simultaneous execution of 100 or even 10,000 simulations on a cluster (ideally), with parallelized scripts managing the processing and integration of the resulting data. We hope this marks the beginning of further research in the field, and we are prepared to open-source these codes to support the wider community. As mentioned when introducing the BSSN formalism, human progress is built on the selfless contributions of those who came before us. We are eager to make our own contribution to the community.

References

[1] (2021). The population of merging compact binaries inferred using gravitational waves through GWTC-3.

[2] Abbott, B. P. et al. (2016). Observation of Gravitational Waves from a Binary Black Hole Merger. *Phys. Rev. Lett.*, 116(6):061102.

[3] Abbott, B. P. et al. (2019a). All-sky search for continuous gravitational waves from isolated neutron stars using Advanced LIGO O2 data. *Phys. Rev. D*, 100(2):024004.

[4] Abbott, B. P. et al. (2019b). Binary Black Hole Population Properties Inferred from the First and Second Observing Runs of Advanced LIGO and Advanced Virgo. *Astrophys. J. Lett.*, 882(2):L24.

[5] Abbott, B. P. et al. (2019c). GWTC-1: A Gravitational-Wave Transient Catalog of Compact Binary Mergers Observed by LIGO and Virgo during the First and Second Observing Runs. *Phys. Rev. X*, 9(3):031040.

[6] Abbott, L. F. and Sikivie, P. (1983). Phys. lett. b. *Physics Letters B*, 120:133.

[7] Abbott, R. et al. (2021a). All-sky, all-frequency directional search for persistent gravitational-waves from Advanced LIGO's and Advanced Virgo's first three observing runs.

[8] Abbott, R. et al. (2021b). All-sky search for continuous gravitational waves from isolated neutron stars in the early O3 LIGO data. *Phys. Rev. D*, 104(8):082004.

[9] Abbott, R. et al. (2021c). All-sky search for gravitational wave emission from scalar boson clouds around spinning black holes in LIGO O3 data.

[10] Abbott, R. et al. (2021d). GWTC-2: Compact Binary Coalescences Observed by LIGO and Virgo During the First Half of the Third Observing Run. *Phys. Rev. X*, 11:021053.

[11] Abbott, R. et al. (2021e). GWTC-3: Compact Binary Coalescences Observed by LIGO and Virgo During the Second Part of the Third Observing Run.

[12] Abbott, R. et al. (2021f). Population Properties of Compact Objects from the Second LIGO-Virgo Gravitational-Wave Transient Catalog. *Astrophys. J. Lett.*, 913(1):L7.

[13] Abbott, R. et al. (2021g). Search for continuous gravitational waves from 20 accreting millisecond X-ray pulsars in O3 LIGO data.

[14] Abbott, R. et al. (2021h). Searches for Gravitational Waves from Known Pulsars at Two Harmonics in the Second and Third LIGO-Virgo Observing Runs.

[15] Abbott, R. et al. (2022a). All-sky search for continuous gravitational waves from isolated neutron stars using Advanced LIGO and Advanced Virgo O3 data.

[16] Abbott, R. et al. (2022b). Search for continuous gravitational wave emission from the Milky Way center in O3 LIGO–Virgo data.

[17] Aggarwal, N. et al. (2021). Challenges and opportunities of gravitational-wave searches at MHz to GHz frequencies. *Living Rev. Rel.*, 24(1):4.

[18] Aichelburg, P. C. and Sexl, R. U. (1971). On the Gravitational field of a massless particle. *Gen. Rel. Grav.*, 2:303–312.

[19] Alcubierre, M. (2008). *Introduction to 3+1 Numerical Relativity*. Oxford University Press.

[20] Alcubierre, M., Allen, G., Bruegmann, B., Seidel, E., and Suen, W.-M. (2000). Towards an understanding of the stability properties of the (3+1) evolution equations in General Relativity. *Phys. Rev. D*, 62:124011.

[21] Alcubierre, M., Barranco, J., Bernal, A., Degollado, J. C., Diez-Tejedor, A., Megevand, M., Nunez, D., and Sarbach, O. (2018). ℓ-Boson stars. *Class. Quant. Grav.*, 35(19):19LT01.

[22] Alcubierre, M., Becerril, R., Guzman, S. F., Matos, T., Nunez, D., and Urena-Lopez, L. A. (2003a). Numerical studies of Phi**2 oscillatons. *Class. Quant. Grav.*, 20:2883–2904.

[23] Alcubierre, M., Brandt, S., Bruegmann, B., Holz, D., Seidel, E., Takahashi, R., and Thornburg, J. (2001). Symmetry without symmetry: Numerical simulation of axisymmetric systems using Cartesian grids. *Int. J. Mod. Phys. D*, 10:273–290.

[24] Alcubierre, M., Bruegmann, B., Diener, P., Koppitz, M., Pollney, D., Seidel, E., and Takahashi, R. (2003b). Gauge conditions for long term numerical black hole evolutions without excision. *Phys. Rev. D*, 67:084023.

[25] Alic, D., Bona-Casas, C., Bona, C., Rezzolla, L., and Palenzuela, C. (2012). Conformal and covariant formulation of the Z4 system with constraint-violation damping. *Phys. Rev. D*, 85:064040.

[26] Alic, D., Kastaun, W., and Rezzolla, L. (2013). Constraint damping of the conformal and covariant formulation of the Z4 system in simulations of binary neutron stars. *Phys. Rev. D*, 88(6):064049.

[27] Andrade, T. et al. (2021). GRChombo: An adaptable numerical relativity code for fundamental physics. *J. Open Source Softw.*, 6(68):3703.

[28] Arkani-Hamed, N., Finkbeiner, D. P., Slatyer, T. R., and Weiner, N. (2009). A Theory of Dark Matter. *Phys. Rev. D*, 79:015014.

[29] Arnowitt, R., Deser, S., and Misner, C. W. (1962). The dynamics of general relativity. In Witten, L., editor, *Gravitation an introduction to current research*, pages 227–265. John Wiley, New York.

[30] Arvanitaki, A., Dimopoulos, S., Dubovsky, S., Kaloper, N., and March-Russell, J. (2010). String Axiverse. *Phys. Rev. D*, 81:123530.

[31] Atteneder, F., Rüter, H. R., Cors, D., Rosca-Mead, R., Hilditch, D., and Brügmann, B. (2024). Boson star head-on collisions with constraint-violating and constraint-satisfying initial data. *Phys. Rev. D*, 109(4):044058.

[32] Badurina, L. et al. (2020). AION: An Atom Interferometer Observatory and Network. *JCAP*, 05:011.

[33] Baker, J. G., Centrella, J., Choi, D.-I., Koppitz, M., and van Meter, J. (2006). Gravitational wave extraction from an inspiraling configuration of merging black holes. *Phys. Rev. Lett.*, 96:111102.

[34] Balakrishna, J., Seidel, E., and Suen, W.-M. (1998). Dynamical evolution of boson stars. 2. Excited states and selfinteracting fields. *Phys. Rev. D*, 58:104004.

[35] Barack, L. et al. (2019). Black holes, gravitational waves and fundamental physics: a roadmap. *Class. Quant. Grav.*, 36(14):143001.

[36] Baumgarte, T. W. and Shapiro, S. L. (1998). On the numerical integration of Einstein's field equations. *Phys. Rev. D*, 59:024007.

[37] Baumgarte, T. W. and Shapiro, S. L. (2021). *Numerical Relativity: Starting from Scratch*. Cambridge University Press.

[38] Bernuzzi, S. and Hilditch, D. (2010). Constraint violation in free evolution schemes: Comparing BSSNOK with a conformal decomposition of Z4. *Phys. Rev. D*, 81:084003.

[39] Berti, E. and Cardoso, V. (2006). Supermassive black holes or boson stars? Hair counting with gravitational wave detectors. *Int. J. Mod. Phys. D*, 15:2209–2216.

[40] Bertone, G., Hooper, D., and Silk, J. (2005). Particle dark matter: Evidence, candidates and constraints. *Phys. Rept.*, 405:279–390.

[41] Bezares, M., Bošković, M., Liebling, S., Palenzuela, C., Pani, P., and Barausse, E. (2022). Gravitational waves and kicks from the merger of unequal mass, highly compact boson stars. *Phys. Rev. D*, 105(6):064067.

[42] Bezares, M. and Palenzuela, C. (2018). Gravitational Waves from Dark Boson Star binary mergers. *Class. Quant. Grav.*, 35(23):234002.

[43] Bezares, M., Palenzuela, C., and Bona, C. (2017). Final fate of compact boson star mergers. *Phys. Rev. D*, 95(12):124005.

[44] Blackman, J., Field, S. E., Galley, C. R., Szilágyi, B., Scheel, M. A., Tiglio, M., and Hemberger, D. A. (2015). Fast and Accurate Prediction of Numerical Relativity Waveforms from Binary Black Hole Coalescences Using Surrogate Models. *Phys. Rev. Lett.*, 115(12):121102.

[45] Blackman, J., Field, S. E., Scheel, M. A., Galley, C. R., Hemberger, D. A., Schmidt, P., and Smith, R. (2017a). A Surrogate Model of Gravitational Waveforms from Numerical Relativity Simulations of Precessing Binary Black Hole Mergers. *Phys. Rev. D*, 95(10):104023.

[46] Blackman, J., Field, S. E., Scheel, M. A., Galley, C. R., Ott, C. D., Boyle, M., Kidder, L. E., Pfeiffer, H. P., and Szilágyi, B. (2017b). Numerical relativity waveform surrogate model for generically precessing binary black hole mergers. *Phys. Rev. D*, 96(2):024058.

[47] Blumenthal, G. R., Pagels, H., and Primack, J. R. (1982). Nature. *Nature*, 299:37.

[48] Bona, C., Ledvinka, T., Palenzuela, C., and Zacek, M. (2003). General covariant evolution formalism for numerical relativity. *Phys. Rev. D*, 67:104005.

[49] Bona, C., Masso, J., Seidel, E., and Stela, J. (1995). A New formalism for numerical relativity. *Phys. Rev. Lett.*, 75:600–603.

[50] Bond, J. R., Szalay, A. S., and Turner, M. S. (1982). Phys. rev. lett. *Physical Review Letters*, 48:1636.

[51] Boylan-Kolchin, M., Bullock, J. S., and Kaplinghat, M. (2011). Too big to fail? The puzzling darkness of massive Milky Way subhaloes. *Mon. Not. Roy. Astron. Soc.*, 415:L40.

[52] Bradac, M., Allen, S. W., Treu, T., Ebeling, H., Massey, R., Morris, R. G., von der Linden, A., and Applegate, D. (2008). Revealing the properties of dark matter in the merging cluster MACSJ0025.4-1222. *Astrophys. J.*, 687:959.

[53] Bramante, J., Fukushima, K., and Kumar, J. (2013). Constraints on bosonic dark matter from observation of old neutron stars. *Phys. Rev. D*, 87(5):055012.

[54] Breit, J. D., Gupta, S., and Zaks, A. (1984). COLD BOSE STARS. *Phys. Lett. B*, 140:329–332.

[55] Brill, D. R. and Lindquist, R. W. (1963). Interaction Energy in Geometrostatics. *Phys. Rev.*, 131:471–476.

[56] Brito, R., Cardoso, V., Herdeiro, C. A. R., and Radu, E. (2016a). Proca stars: Gravitating Bose–Einstein condensates of massive spin 1 particles. *Phys. Lett. B*, 752:291–295.

[57] Brito, R., Cardoso, V., Macedo, C. F. B., Okawa, H., and Palenzuela, C. (2016b). Interaction between bosonic dark matter and stars. *Phys. Rev. D*, 93(4):044045.

[58] Brito, R., Cardoso, V., and Pani, P. (2015). Superradiance. *Lect. Notes Phys.*, 906:pp.1–237.

[59] Brito, R. P. (2016). *Fundamental fields around compact objects: Massive spin-2 fields, Superradiant instabilities and Stars with dark matter cores*. PhD thesis, Lisbon U.

[60] Bruegmann, B., Gonzalez, J. A., Hannam, M., Husa, S., Sperhake, U., and Tichy, W. (2008). Calibration of Moving Puncture Simulations. *Phys. Rev. D*, 77:024027.

[61] Buchel, A., Liebling, S. L., and Lehner, L. (2013). Boson stars in AdS spacetime. *Phys. Rev. D*, 87(12):123006.

[62] Calderón Bustillo, J., Sanchis-Gual, N., Torres-Forné, A., Font, J. A., Vajpeyi, A., Smith, R., Herdeiro, C., Radu, E., and Leong, S. H. W. (2021). GW190521 as a Merger of Proca Stars: A Potential New Vector Boson of 8.7×10^{-13} eV. *Phys. Rev. Lett.*, 126(8):081101.

[63] Campanelli, M., Lousto, C. O., Marronetti, P., and Zlochower, Y. (2006). Accurate evolutions of orbiting black-hole binaries without excision. *Phys. Rev. Lett.*, 96:111101.

[64] Cao, Z. (2021). The Basics of Numerical Relativity. *Lecture notes*.

[65] Cardoso, V., Gualtieri, L., Herdeiro, C., and Sperhake, U. (2015). Exploring New Physics Frontiers Through Numerical Relativity. *Living Rev. Relativity*, 18:1. arXiv:1409.0014 [gr-qc].

[66] Cardoso, V., Hopper, S., Macedo, C. F. B., Palenzuela, C., and Pani, P. (2016). Gravitational-wave signatures of exotic compact objects and of quantum corrections at the horizon scale. *Phys. Rev. D*, 94(8):084031.

[67] Choptuik, M., Masachs, R., and Way, B. (2019). Multioscillating Boson Stars. *Phys. Rev. Lett.*, 123(13):131101.

[68] Choptuik, M. W. (1993). Universality and scaling in gravitational collapse of a massless scalar field. *Phys. Rev. Lett.*, 70:9–12.

[69] Choptuik, M. W., Chmaj, T., and Bizon, P. (1996). Critical behavior in gravitational collapse of a Yang-Mills field. *Phys. Rev. Lett.*, 77:424–427.

[70] Clough, K., Figueras, P., Finkel, H., Kunesch, M., Lim, E. A., and Tunyasuvunakool, S. (2015). GRChombo : Numerical Relativity with Adaptive Mesh Refinement. *Class. Quant. Grav.*, 32(24):245011. arXiv:1503.03436 [gr-qc].

[71] Clowe, D., Bradac, M., Gonzalez, A. H., Markevitch, M., Randall, S. W., Jones, C., and Zaritsky, D. (2006). A direct empirical proof of the existence of dark matter. *Astrophys. J. Lett.*, 648:L109–L113.

[72] Colpi, M., Shapiro, S. L., and Wasserman, I. (1986). Boson Stars: Gravitational Equilibria of Selfinteracting Scalar Fields. *Phys. Rev. Lett.*, 57:2485–2488.

[73] Cook, G. B., Shapiro, S. L., and Teukolsky, S. A. (1994). Rapidly rotating neutron stars in general relativity: Realistic equations of state. *The Astrophysical Journal*, 424:823–845.

[74] Cook, W. G., Figueras, P., Kunesch, M., Sperhake, U., and Tunyasuvunakool, S. (2016). Dimensional reduction in numerical relativity: Modified cartoon formalism and regularization. *Int. J. Mod. Phys. D*, 25(09):1641013.

[75] Cook, W. G. and Sperhake, U. (2017). Extraction of gravitational-wave energy in higher dimensional numerical relativity using the Weyl tensor. *Class. Quant. Grav.*, 34(3):035010.

[76] Croft, R. (2023). Local continuity of angular momentum and noether charge for matter in general relativity. *Class. Quant. Grav.*, 40(10):105007.

[77] Croft, R., Helfer, T., Ge, B.-X., Radia, M., Evstafyeva, T., Lim, E. A., Sperhake, U., and Clough, K. (2023). The gravitational afterglow of boson stars. *Class. Quant. Grav.*, 40(6):065001.

[78] Croon, D., Gleiser, M., Mohapatra, S., and Sun, C. (2018). Gravitational Radiation Background from Boson Star Binaries. *Phys. Lett. B*, 783:158–162.

[79] Cunha, P. V. P., Berti, E., and Herdeiro, C. A. R. (2017). Light-Ring Stability for Ultracompact Objects. *Phys. Rev. Lett.*, 119(25):251102.

[80] Darmois, G. (1927). *Les équations de la gravitation einsteinienne*. Number 25 in Mémorial des sciences mathématiques. 58 p.

[81] Di Giovanni, F., Fakhry, S., Sanchis-Gual, N., Degollado, J. C., and Font, J. A. (2020a). Dynamical formation and stability of fermion-boson stars. *Phys. Rev. D*, 102(8):084063.

[82] Di Giovanni, F., Sanchis-Gual, N., Cerdá-Durán, P., Zilhão, M., Herdeiro, C., Font, J. A., and Radu, E. (2020b). Dynamical bar-mode instability in spinning bosonic stars. *Phys. Rev. D*, 102(12):124009.

[83] Di Giovanni, F., Sanchis-Gual, N., Herdeiro, C. A. R., and Font, J. A. (2018). Dynamical formation of Proca stars and quasistationary solitonic objects. *Phys. Rev. D*, 98(6):064044.

[84] Dine, M. and Fischler, W. (1983). Phys. lett. b. *Physics Letters B*, 120:137.

[85] Ellis, J., Hektor, A., Hütsi, G., Kannike, K., Marzola, L., Raidal, M., and Vaskonen, V. (2018a). Search for Dark Matter Effects on Gravitational Signals from Neutron Star Mergers. *Phys. Lett. B*, 781:607–610.

[86] Ellis, J., Hütsi, G., Kannike, K., Marzola, L., Raidal, M., and Vaskonen, V. (2018b). Dark Matter Effects On Neutron Star Properties. *Phys. Rev. D*, 97(12):123007.

[87] Evstafyeva, T., Sperhake, U., Helfer, T., Croft, R., Radia, M., Ge, B.-X., and Lim, E. A. (2023). Unequal-mass boson-star binaries: initial data and merger dynamics. *Class. Quant. Grav.*, 40(8):085009.

[88] Fan, Y.-z., Yang, R.-z., and Chang, J. (2012). Constraining Asymmetric Bosonic Non-interacting Dark Matter with Neutron Stars.

[89] Feinblum, D. A. and McKinley, W. A. (1968). Stable States of a Scalar Particle in Its Own Gravational Field. *Phys. Rev.*, 168(5):1445.

[90] Feng, J. L. (2010). Dark Matter Candidates from Particle Physics and Methods of Detection. *Ann. Rev. Astron. Astrophys.*, 48:495–545.

[91] Field, S. E., Galley, C. R., Hesthaven, J. S., Kaye, J., and Tiglio, M. (2014). Fast prediction and evaluation of gravitational waveforms using surrogate models. *Phys. Rev. X*, 4(3):031006.

[92] Freese, K. (2017). Status of Dark Matter in the Universe. *Int. J. Mod. Phys.*, 1(06):325–355.

[93] Friedberg, R., Lee, T. D., and Pang, Y. (1987). Scalar Soliton Stars and Black Holes. *Phys. Rev. D*, 35:3658.

[94] Friedman, J. L., Ipser, J. R., and Sorkin, R. D. (1988). Turning-point method for axisymmetric stability of rotating relativistic stars. *The Astrophysical Journal*, 325:722–724.

[95] Garani, R., Levkov, D., and Tinyakov, P. (2022). Solar mass black holes from neutron stars and bosonic dark matter. *Phys. Rev. D*, 105(6):063019.

[96] Garfinkle, D. (2002). Harmonic coordinate method for simulating generic singularities. *Phys. Rev. D*, 65:044029.

[97] Gleiser, M. (1988). Stability of Boson Stars. *Phys. Rev. D*, 38:2376. [Erratum: Phys.Rev.D 39, 1257 (1989)].

[98] Gleiser, M. and Watkins, R. (1989). Gravitational Stability of Scalar Matter. *Nucl. Phys. B*, 319:733–746.

[99] Gourgoulhon, E. (2012). *3+1 Formalism in General Relativity*. Lecture Notes in Physics. Springer.

[100] Grandclément, P., Somé, C., and Gourgoulhon, E. (2014). Models of rotating boson stars and geodesics around them: New type of orbits. *Phys. Rev. D*, 90:024068.

[101] Gundlach, C. and Leveque, R. J. (2011). Universality in the run-up of shock waves to the surface of a star. *J. Fluid Mech.*, 676:237–264.

[102] Gundlach, C. and Martin-Garcia, J. M. (2007). Critical phenomena in gravitational collapse. *Living Rev. Rel.*, 10:5.

[103] Gundlach, C., Martin-Garcia, J. M., Calabrese, G., and Hinder, I. (2005). Constraint damping in the Z4 formulation and harmonic gauge. *Class. Quant. Grav.*, 22:3767–3774.

[104] Gundlach, C. and Please, C. (2009). Generic behaviour of nonlinear sound waves near the surface of a star: smooth solutions. *Phys. Rev. D*, 79:067501. [Erratum: Phys.Rev.D 79, 089901 (2009)].

[105] Güver, T., Erkoca, A. E., Hall Reno, M., and Sarcevic, I. (2014). On the capture of dark matter by neutron stars. *JCAP*, 05:013.

[106] Hahn, S. G. and Lindquist, R. W. (1964). The two-body problem in geometrodynamics. *Annals of Physics*, 29:304–331.

[107] Harrison, B. K., Thorne, K. S., Wakano, M., and Wheeler, J. A. (1965). *Gravitation Theory and Gravitational Collapse*. University of Chicago Press, Chicago.

[108] Hartmann, B., Kleihaus, B., Kunz, J., and Schaffer, I. (2012). Compact Boson Stars. *Phys. Lett. B*, 714:120–126.

[109] Hawley, S. H. and Choptuik, M. W. (2000). Boson stars driven to the brink of black hole formation. *Phys. Rev. D*, 62:104024.

[110] Helfer, T., Lim, E. A., Garcia, M. A. G., and Amin, M. A. (2019). Gravitational Wave Emission from Collisions of Compact Scalar Solitons. *Phys. Rev. D*, 99(4):044046.

[111] Helfer, T., Marsh, D. J. E., Clough, K., Fairbairn, M., Lim, E. A., and Becerril, R. (2017). Black hole formation from axion stars. *JCAP*, 03:055.

[112] Helfer, T., Sperhake, U., Croft, R., Radia, M., Ge, B.-X., and Lim, E. A. (2021). Malaise and remedy of binary boson-star initial data.

[113] Helfer, T., Sperhake, U., Croft, R., Radia, M., Ge, B.-X., and Lim, E. A. (2022). Malaise and remedy of binary boson-star initial data. *Class. Quant. Grav.*, 39(7):074001.

[114] Hertzberg, M. P., Tegmark, M., and Wilczek, F. (2008). Axion Cosmology and the Energy Scale of Inflation. *Phys. Rev. D*, 78:083507.

[115] Hilditch, D., Bernuzzi, S., Thierfelder, M., Cao, Z., Tichy, W., and Bruegmann, B. (2013). Compact binary evolutions with the Z4c formulation. *Phys. Rev. D*, 88:084057.

[116] Hu, W., Barkana, R., and Gruzinov, A. (2000). Cold and fuzzy dark matter. *Phys. Rev. Lett.*, 85:1158–1161.

[117] Husa, S., González, J. A., Hannam, M. D., Brügmann, B., and Sperhake, U. (2008). Reducing phase error in long numerical binary black hole evolutions with sixth order finite differencing. *Class. Quant. Grav.*, 25:105006. arXiv:0706.0740 [gr-qc].

[118] Isaacson, R. A. (1968a). Gravitational Radiation in the Limit of High Frequency. I. The Linear Approximation and Geometrical Optics. *Phys. Rev.*, 166:1263–1271.

[119] Isaacson, R. A. (1968b). Gravitational Radiation in the Limit of High Frequency. II. Nonlinear Terms and the Ef fective Stress Tensor. *Phys. Rev.*, 166:1272–1279.

[120] Jamison, A. O. (2013). Effects of gravitational confinement on bosonic asymmetric dark matter in stars. *Phys. Rev. D*, 88:035004.

[121] Jetzer, P. (1989a). Dynamical Instability of Bosonic Stellar Configurations. *Nucl. Phys. B*, 316:411–428.

[122] Jetzer, P. (1989b). Stability of Excited Bosonic Stellar Configurations. *Phys. Lett. B*, 222:447–452.

[123] Jetzer, P. (1990). STABILITY OF EXCITED BOSE STARS. *Nucl. Phys. B Proc. Suppl.*, 14:265–272.

[124] Jetzer, P. (1992). Boson stars. *Phys. Rept.*, 220:163–227.

[125] Ji, S. U. and Sin, S. J. (1994). Late time phase transition and the galactic halo as a bose liquid: 2. The Effect of visible matter. *Phys. Rev. D*, 50:3655–3659.

[126] Jimenez-Vazquez, E. and Alcubierre, M. (2022). Critical gravitational collapse of a massive complex scalar field. *Phys. Rev. D*, 106(4):044071.

[127] Jin, K.-J. and Suen, W.-M. (2007). Critical phenomena in head-on collisions of neutron stars. *Phys. Rev. Lett.*, 98:131101.

[128] Kauffmann, G., White, S. D. M., and Guiderdoni, B. (1993). Mon. not. roy. astron. soc. *Monthly Notices of the Royal Astronomical Society*, 264:201.

[129] Kaup, D. J. (1968). Klein-Gordon Geon. *Phys. Rev.*, 172:1331–1342.

[130] Kellermann, T., Rezzolla, L., and Radice, D. (2010). Critical Phenomena in Neutron Stars II: Head-on Collisions. *Class. Quant. Grav.*, 27:235016.

[131] Kidder, L. E., Scheel, M. A., and Teukolsky, S. A. (2001). Extending the lifetime of 3-D black hole computations with a new hyperbolic system of evolution equations. *Phys. Rev. D*, 64:064017.

[132] Kim, J. E. (1987). Light Pseudoscalars, Particle Physics and Cosmology. *Phys. Rept.*, 150:1–177.

[133] Klypin, A. A., Kravtsov, A. V., Valenzuela, O., and Prada, F. (1999). Where are the missing Galactic satellites? *Astrophys. J.*, 522:82–92.

[134] Kouvaris, C. and Tinyakov, P. (2010). Can Neutron stars constrain Dark Matter? *Phys. Rev. D*, 82:063531.

[135] Lai, C.-W. (2004). *A Numerical study of boson stars*. Other thesis, The University of British Columbia.

[136] Lai, C. W. and Choptuik, M. W. (2007). Final fate of subcritical evolutions of boson stars.

[137] Lee, J.-w. and Koh, I.-g. (1996). Galactic halos as boson stars. *Phys. Rev. D*, 53:2236–2239.

[138] Lee, T. D. (1987). Soliton Stars and the Critical Masses of Black Holes. *Phys. Rev. D*, 35:3637.

[139] Lee, T. D. and Pang, Y. (1989). Stability of Mini - Boson Stars. *Nucl. Phys. B*, 315:477.

[140] Lee, T. D. and Pang, Y. (1992). Nontopological solitons. *Phys. Rept.*, 221:251–350.

[141] Li, B., Rindler-Daller, T., and Shapiro, P. R. (2014). Cosmological Constraints on Bose-Einstein-Condensed Scalar Field Dark Matter. *Phys. Rev. D*, 89(8):083536.

[142] Li, B., Shapiro, P. R., and Rindler-Daller, T. (2017). Bose-Einstein-condensed scalar field dark matter and the gravitational wave background from inflation: new cosmological constraints and its detectability by LIGO. *Phys. Rev. D*, 96(6):063505.

[143] Liang, C. and Zhou, B. (2009). *Differential Geometry and General Relativity: Volume 2*.

[144] Liang, C. and Zhou, B. (2023). *Differential Geometry and General Relativity: Volume 1*. Springer.

[145] Lichnerowicz, A. (1944). L'intégration des équations de la gravitation relativiste et le problème des n corps. *Journal de Mathématiques Pures et Appliquées*, 23:37–63.

[146] Liddle, A. R. and Lyth, D. H. (1993). The Cold dark matter density perturbation. *Phys. Rept.*, 231:1–105.

[147] Liddle, A. R. and Madsen, M. S. (1992). The Structure and formation of boson stars. *Int. J. Mod. Phys. D*, 1:101–144.

[148] Liebling, S. L. and Palenzuela, C. (2023). Dynamical boson stars. *Living Rev. Rel.*, 26(1):1.

[149] Lim, E. A. (2019). General Relativity. *Lecture notes*.

[150] Lindblom, L., Scheel, M. A., Kidder, L. E., Owen, R., and Rinne, O. (2006). A New generalized harmonic evolution system. *Class. Quant. Grav.*, 23:S447–S462.

[151] Lisanti, M. (2017). Lectures on Dark Matter Physics. In *Theoretical Advanced Study Institute in Elementary Particle Physics: New Frontiers in Fields and Strings*, pages 399–446.

[152] Luna, R., Llorens-Monteagudo, M., Lorenzo-Medina, A., Calderón Bustillo, J., Sanchis-Gual, N., Torres-Forné, A., Font, J. A., Herdeiro, C. A. R., and Radu, E. (2024). Numerical relativity surrogate waveform models for exotic compact objects: The case of head-on mergers of equal-mass Proca stars. *Phys. Rev. D*, 110(2):024004.

[153] Macedo, C. F. B., Cardoso, V., Crispino, L. C. B., and Pani, P. (2016). Quasinormal modes of relativistic stars and interacting fields. *Phys. Rev. D*, 93(6):064053.

[154] Macedo, C. F. B., Pani, P., Cardoso, V., and Crispino, L. C. B. (2013). Astrophysical signatures of boson stars: quasinormal modes and inspiral resonances. *Phys. Rev. D*, 88(6):064046.

[155] Marsh, D. J. E. (2016). Axion Cosmology. *Phys. Rept.*, 643:1–79.

[156] Mielke, E. W. (2016). Rotating Boson Stars. *Fundam. Theor. Phys.*, 183:115–131.

[157] Millward, R. S. and Hirschmann, E. W. (2003). Critical behavior of gravitating sphalerons. *Phys. Rev. D*, 68:024017.

[158] Misner, C., Thorne, K., and Wheeler, J. (1973). *Gravitation*. W H Freeman and Company, San Francisco.

[159] Moore, B., Ghigna, S., Governato, F., Lake, G., Quinn, T. R., Stadel, J., and Tozzi, P. (1999a). Dark matter substructure within galactic halos. *Astrophys. J. Lett.*, 524:L19–L22.

[160] Moore, B., Quinn, T. R., Governato, F., Stadel, J., and Lake, G. (1999b). Cold collapse and the core catastrophe. *Mon. Not. Roy. Astron. Soc.*, 310:1147–1152.

[161] Muia, F., Cicoli, M., Clough, K., Pedro, F., Quevedo, F., and Vacca, G. P. (2019). The Fate of Dense Scalar Stars. *JCAP*, 07:044.

[162] Nagy, G., Ortiz, O. E., and Reula, O. A. (2004). Strongly hyperbolic second order Einstein's evolution equations. *Phys. Rev. D*, 70:044012.

[163] Nakamura, T., Oohara, K., and Kojima, Y. (1987). General Relativistic Collapse to Black Holes and Gravitational Waves from Black Holes. *Prog. Theor. Phys. Suppl.*, 90:1–218.

[164] Navarro, J. F., Frenk, C. S., and White, S. D. M. (1997). A Universal density profile from hierarchical clustering. *Astrophys. J.*, 490:493–508.

[165] Newman, E. and Penrose, R. (1962). An Approach to gravitational radiation by a method of spin coefficients. *J. Math. Phys.*, 3:566–578.

[166] Okawa, H., Nakao, K.-i., and Shibata, M. (2011). Is super-Planckian physics visible? Scattering of black holes in 5 dimensions. *Phys. Rev. D*, 83:121501(R). arXiv:1105.3331 [gr-qc].

[167] Oppenheimer, J. R. and Volkoff, G. M. (1939). On massive neutron cores. *Phys. Rev.*, 55:374–381.

[168] Ostriker, J. P. and Steinhardt, P. J. (2003). New light on dark matter. *Science*, 300:1909–1913.

[169] Padmanabhan, T. (2003). Cosmological constant: The Weight of the vacuum. *Phys. Rept.*, 380:235–320.

[170] Palenzuela, C., Lehner, L., and Liebling, S. L. (2008). Orbital Dynamics of Binary Boson Star Systems. *Phys. Rev. D*, 77:044036.

[171] Palenzuela, C., Olabarrieta, I., Lehner, L., and Liebling, S. L. (2007). Head-on collisions of boson stars. *Phys. Rev. D*, 75:064005.

[172] Palenzuela, C., Pani, P., Bezares, M., Cardoso, V., Lehner, L., and Liebling, S. (2017). Gravitational Wave Signatures of Highly Compact Boson Star Binaries. *Phys. Rev. D*, 96(10):104058.

[173] Peccei, R. D. and Quinn, H. R. (1977). CP Conservation in the Presence of Instantons. *Phys. Rev. Lett.*, 38:1440–1443.

[174] Peebles, P. J. E. (1982). Astrophys. j. lett. *Astrophysical Journal Letters*, 263:L1.

[175] Peebles, P. J. E. (2000). Fluid dark matter. *Astrophys. J. Lett.*, 534:L127.

[176] Peebles, P. J. E. and Ratra, B. (2003). The Cosmological Constant and Dark Energy. *Rev. Mod. Phys.*, 75:559–606.

[177] Preskill, J., Wise, M. B., and Wilczek, F. (1983). Phys. lett. b. *Physics Letters B*, 120:127.

[178] Press, W. H., Ryden, B. S., and Spergel, D. N. (1990). Phys. rev. lett. *Physical Review Letters*, 64:1084.

[179] Pretorius, F. (2005a). Evolution of binary black hole spacetimes. *Phys. Rev. Lett.*, 95:121101.

[180] Pretorius, F. (2005b). Numerical relativity using a generalized harmonic decomposition. *Class. Quant. Grav.*, 22:425–452.

[181] Radia, M., Sperhake, U., Drew, A., Clough, K., Lim, E. A., Ripley, J. L., Aurrekoetxea, J. C., França, T., and Helfer, T. (2021). Lessons for adaptive mesh refinement in numerical relativity.

[182] Radia, M. R. (2023). *Numerical modelling of gravitational wave sources in general relativity*. PhD thesis, Department of Applied Mathematics And Theoretical Physics, Cambridge U., University of Cambridge.

[183] Ringwald, A. (2014). Searching for axions and ALPs from string theory. *J. Phys. Conf. Ser.*, 485:012013.

[184] Romanowsky, A. J., Douglas, N. D., Arnaboldi, M., Kuijken, K., Merrifield, M. R., Napolitano, N. R., Capaccioli, M., and Freeman, K. C. (2003). A dearth of dark matter in ordinary elliptical galaxies. *Science*, 301:1696–1698.

[185] Rosato, N., Healy, J., and Lousto, C. O. (2021). Adapted gauge to small mass ratio binary black hole evolutions. *Phys. Rev. D*, 103(10):104068.

[186] Rousseau, B. (2003). *Axisymmetric boson stars in the conformally flat approximation*. PhD thesis, The University of British Columbia, Vancouver. http://laplace.physics.ubc.ca/Members/matt/Doc/Theses/.

[187] Rubin, V. C., Ford, J., K., W., Thonnard, N., Roberts, M. S., and Graham, J. A. (1976a). Astrophys. j. *Astrophysical Journal*, 81:687.

[188] Rubin, V. C., Thonnard, N., J. Ford, W. K., and Roberts, M. S. (1976b). Astrophys. j. *Astrophysical Journal*, 81:719.

[189] Ruffini, R. and Bonazzola, S. (1969). Systems of selfgravitating particles in general relativity and the concept of an equation of state. *Phys. Rev.*, 187:1767–1783.

[190] Sachs, R. and Wu, H. (2012). *General Relativity for Mathematicians*. Graduate Texts in Mathematics. Springer New York.

[191] Sahni, V. and Wang, L.-M. (2000). A New cosmological model of quintessence and dark matter. *Phys. Rev. D*, 62:103517.

[192] Sanchis-Gual, N., Di Giovanni, F., Zilhão, M., Herdeiro, C., Cerdá-Durán, P., Font, J., and Radu, E. (2019a). Nonlinear Dynamics of Spinning Bosonic Stars: Formation and Stability. *Phys. Rev. Lett.*, 123(22):221101.

[193] Sanchis-Gual, N., Herdeiro, C., Font, J. A., Radu, E., and Di Giovanni, F. (2019b). Head-on collisions and orbital mergers of Proca stars. *Phys. Rev. D*, 99(2):024017.

[194] Schunck, F. E. and Mielke, E. W. (1996). Rotating boson stars. In *Relativity and Scientific Computing. Computer Algebra, Numerics, Visualization*, pages 138–151.

[195] Schunck, F. E. and Torres, D. F. (2000). Boson stars with generic selfinteractions. *Int. J. Mod. Phys. D*, 9:601–618.

[196] Seidel, E. and Suen, W.-M. (1990a). Dynamical Evolution of Boson Stars. 1. Perturbing the Ground State. *Phys. Rev. D*, 42:384–403.

[197] Seidel, E. and Suen, W.-M. (1990b). Dynamical evolution of boson stars: Perturbing the ground state. *Physical Review D*, 42(2):384.

[198] Seidel, E. and Suen, W. M. (1991). Oscillating soliton stars. *Phys. Rev. Lett.*, 66:1659–1662.

[199] Seidel, E. and Suen, W.-M. (1994). Formation of solitonic stars through gravitational cooling. *Phys. Rev. Lett.*, 72:2516–2519.

[200] Sennett, N., Hinderer, T., Steinhoff, J., Buonanno, A., and Ossokine, S. (2017). Distinguishing Boson Stars from Black Holes and Neutron Stars from Tidal Interactions in Inspiraling Binary Systems. *Phys. Rev. D*, 96(2):024002.

[201] Shibata, M. (2000). Axisymmetric simulations of rotating stellar collapse in full general relativity: Criteria for prompt collapse to black holes. *Prog. Theor. Phys.*, 104:325–358.

[202] Shibata, M. (2015). *100 Years of General Relativity: Volume 1 Numerical Relativity*. World Scientific.

[203] Shibata, M. and Nakamura, T. (1995). Evolution of three-dimensional gravitational waves: Harmonic slicing case. *Phys. Rev. D*, 52:5428–5444.

[204] Shibata, M., Okawa, H., and Yamamoto, T. (2008). High-velocity collisions of two black holes. *Phys. Rev. D*, 78:101501(R). arXiv:0810.4735 [gr-qc].

[205] Shibata, M. and Yoshino, H. (2010). Bar-mode instability of rapidly spinning black hole in higher dimensions: Numerical simulation in general relativity. *Phys. Rev. D*, 81:104035.

[206] Siemonsen, N. (2024). Nonlinear Treatment of a Black Hole Mimicker Ringdown. *Phys. Rev. Lett.*, 133(3):031401.

[207] Siemonsen, N. and East, W. E. (2021). Stability of rotating scalar boson stars with nonlinear interactions. *Phys. Rev. D*, 103(4):044022.

[208] Siemonsen, N. and East, W. E. (2023a). Binary boson stars: Merger dynamics and formation of rotating remnant stars. *Phys. Rev. D*, 107(12):124018.

[209] Siemonsen, N. and East, W. E. (2023b). Generic initial data for binary boson stars. *Phys. Rev. D*, 108(12):124015.

[210] Sin, S.-J. (1994). Late time cosmological phase transition and galactic halo as Bose liquid. *Phys. Rev. D*, 50:3650–3654.

[211] Smarr, L. and York, Jr., J. W. (1978a). Kinematical conditions in the construction of space-time. *Phys. Rev. D*, 17:2529–2551.

[212] Smarr, L. and York, Jr., J. W. (1978b). Radiation gauge in general relativity. *Phys. Rev. D*, 17(8):1945–1956.

[213] Sperhake, U. (2007). Binary black-hole evolutions of excision and puncture data. *Phys. Rev. D*, 76:104015. gr-qc/0606079.

[214] Sperhake, U. (2015). The numerical relativity breakthrough for binary black holes. *Class. Quant. Grav.*, 32(12):124011.

[215] Sperhake, U. (2024). Gravitational Waves and Numerical Relativity. *Lecture notes*.

[216] Sperhake, U., Cook, W., and Wang, D. (2020). The high-energy collision of black holes in higher dimensions. *Phys. Rev. D*, 100(10):104046.

[217] Stecker, F. W. and Shafi, Q. (1983). Phys. rev. lett. *Physical Review Letters*, 50:928.

[218] Stein, L. C. (2019). qnm: A Python package for calculating Kerr quasinormal modes, separation constants, and spherical-spheroidal mixing coefficients. *J. Open Source Softw.*, 4(42):1683.

[219] Straumann, N. (1984). *General Relativity and Relativistic Astrophysics*. Springer, Berlin; New York.

[220] Svrcek, P. and Witten, E. (2006). Axions In String Theory. *JHEP*, 06:051.

[221] Synge, J. L. (1960). *Relativity: The General Theory*. North-Holland Publishing Company, Amsterdam.

[222] Synge, J. L. (1964). *Introduction to General Relativity*. Blackie and Son Limited, London.

[223] Thomas W. Baumgarte, S. L. S. (2010). *Numerical Relativity: Solving Einstein's Equations on the Computer*. Cambridge University Press, Cambridge. Online publication date: March 2013.

[224] Tolman, R. C. (1939). Static solutions of Einstein's field equations for spheres of fluid. *Phys. Rev.*, 55:364–373.

[225] Toubiana, A., Babak, S., Barausse, E., and Lehner, L. (2021). Modeling gravitational waves from exotic compact objects. *Phys. Rev. D*, 103(6):064042.

[226] Urena-Lopez, L. A., Matos, T., and Becerril, R. (2002). Inside oscillatons. *Class. Quant. Grav.*, 19:6259–6277.

[227] van Meter, J. R., Baker, J. G., Koppitz, M., and Choi, D.-I. (2006). How to move a black hole without excision: Gauge conditions for the numerical evolution of a moving puncture. *Phys. Rev. D*, 73:124011.

[228] Varma, V., Field, S. E., Scheel, M. A., Blackman, J., Gerosa, D., Stein, L. C., Kidder, L. E., and Pfeiffer, H. P. (2019). Surrogate models for precessing binary black hole simulations with unequal masses. *Phys. Rev. Research.*, 1:033015.

[229] Vásquez Flores, C., Parisi, A., Chen, C.-S., and Lugones, G. (2019). Fundamental oscillation modes of self-interacting bosonic dark stars. *JCAP*, 06:051.

[230] Visinelli, L. and Gondolo, P. (2009). Dark Matter Axions Revisited. *Phys. Rev. D*, 80:035024.

[231] Wald, R. M. (1984). *General Relativity*. Chicago Univ. Pr., Chicago, USA.

[232] Weinberg, S. (1978). A New Light Boson? *Phys. Rev. Lett.*, 40:223–226.

[233] Wheeler, J. A. (1955). Geons. *Phys. Rev.*, 97:511–536.

[234] Widdicombe, J. Y., Helfer, T., Marsh, D. J. E., and Lim, E. A. (2018). Formation of Relativistic Axion Stars. *JCAP*, 10:005.

[235] Wilczek, F. (1978). Problem of Strong P and T Invariance in the Presence of Instantons. *Phys. Rev. Lett.*, 40:279–282.

[236] York, J. W. (1971). Gravitational degrees of freedom and the initial-value problem. *Phys. Rev. Lett.*, 26:1656–1658.

[237] York, J. W. (1972). Role of conformal three-geometry in the dynamics of gravitation. *Phys. Rev. Lett.*, 28:1082–1085.

[238] York, Jr., J. W. (1978). Kinematics and Dynamics of General Relativity. In *Workshop on Sources of Gravitational Radiation*, pages 83–126.

[239] Yoshida, S. and Eriguchi, Y. (1997). Rotating boson stars in general relativity. *Phys. Rev. D*, 56:762–771.

[240] Yoshida, S., Eriguchi, Y., and Futamase, T. (1994). Quasinormal modes of boson stars. *Phys. Rev. D*, 50:6235–6246.

Appendix A

Additional Details on the Derivation

In this Appendix, we will provide the derivation details of several equations from Chapter 2.

A.1 Detailed Derivation of the ADM Formalism

Gauss-Codazzi Equation

The Gauss-Codazzi equation is as follows:

$$\gamma_\alpha{}^\delta \gamma_\beta{}^\kappa \gamma_\mu{}^\lambda \gamma_\nu{}^\sigma R_{\delta\kappa\lambda\sigma} = {}^{(3)}R_{\alpha\beta\mu\nu} + K_{\alpha\mu}K_{\beta\nu} - K_{\alpha\nu}K_{\beta\mu}. \tag{A.1}$$

The detailed derivation process is as follows:

Accroding to the definition of spatial derivative, we have $D_\beta \omega_\mu = \gamma_\mu{}^\rho \gamma_\beta{}^\alpha \nabla_\alpha \omega_\rho$. Then, we have

$$
\begin{aligned}
&D_\alpha D_\beta \omega_\mu \\
&= D_\alpha \left(\gamma_\mu{}^\rho \gamma_\beta{}^\alpha \nabla_\alpha \omega_\rho\right) = \gamma_\mu{}^\lambda \gamma_\beta{}^\sigma \gamma_\alpha{}^\varepsilon \nabla_\varepsilon \left(\gamma_\lambda{}^\rho \gamma_\sigma{}^\kappa \nabla_\kappa \omega_\rho\right) \\
&= \gamma_\mu{}^\lambda \gamma_\beta{}^\sigma \gamma_\alpha{}^\varepsilon \left[\gamma_\lambda{}^\rho \gamma_\sigma{}^\kappa \nabla_\varepsilon \nabla_\kappa \omega_\rho + \left(\nabla_\kappa \omega_\rho\right) \nabla_\varepsilon \left(\gamma_\lambda{}^\rho \gamma_\sigma{}^\kappa\right)\right] \\
&= \gamma_\mu{}^\rho \gamma_\beta{}^\kappa \gamma_\alpha{}^\varepsilon \nabla_\varepsilon \nabla_\kappa \omega_\rho + \gamma_\mu{}^\lambda \gamma_\beta{}^\sigma \gamma_\alpha{}^\varepsilon \left[\gamma_\lambda{}^\rho \left(\nabla_\kappa \omega_\rho\right) \nabla_\varepsilon \gamma_\sigma{}^\kappa + \gamma_\sigma{}^\kappa \left(\nabla_\kappa \omega_\rho\right) \nabla_\varepsilon \gamma_\lambda{}^\rho\right] \\
&= \gamma_\mu{}^\rho \gamma_\beta{}^\kappa \gamma_\alpha{}^\varepsilon \nabla_\varepsilon \nabla_\kappa \omega_\rho + \gamma_\mu{}^\rho \gamma_\beta{}^\sigma \gamma_\alpha{}^\varepsilon \left(\nabla_\kappa \omega_\rho\right) \nabla_\varepsilon \left(\delta_\sigma^\kappa + n^\kappa n_\sigma\right) + \gamma_\mu{}^\lambda \gamma_\beta{}^\kappa \gamma_\alpha{}^\varepsilon \left(\nabla_\kappa \omega_\rho\right) \nabla_\varepsilon \left(\delta_\lambda{}^\rho + n^\rho n_\lambda\right) \\
&= \gamma_\mu{}^\rho \gamma_\beta{}^\kappa \gamma_\alpha{}^\varepsilon \nabla_\varepsilon \nabla_\kappa \omega_\rho + \gamma_\mu{}^\rho \gamma_\beta{}^\sigma \gamma_\alpha{}^\varepsilon n^\kappa \left(\nabla_\kappa \omega_\rho\right) \nabla_\varepsilon n_\sigma + \gamma_\mu{}^\lambda \gamma_\beta{}^\kappa \gamma_\alpha{}^\varepsilon n^\rho \left(\nabla_\kappa \omega_\rho\right) \nabla_\varepsilon n_\lambda \\
&= \gamma_\mu{}^\rho \gamma_\beta{}^\kappa \gamma_\alpha{}^\varepsilon \nabla_\varepsilon \nabla_\kappa \omega_\rho - \gamma_\mu{}^\rho K_{\alpha\beta} n^\kappa \nabla_\kappa \omega_\rho + \gamma_\mu{}^\lambda \gamma_\beta{}^\kappa K_{\alpha\lambda} \omega_\rho \nabla_\kappa n^\rho \\
&= \gamma_\mu{}^\rho \gamma_\alpha{}^\varepsilon \gamma_\beta{}^\kappa \nabla_\varepsilon \nabla_\kappa \omega_\rho - \gamma_\mu{}^\rho n^\kappa K_{\alpha\beta} \nabla_\kappa \omega_\rho - K_{\alpha\mu} K_\beta{}^\rho \omega_\rho .
\end{aligned}
\tag{A.2}
$$

Taking the antisymmetric part, we have:

$$
\begin{aligned}
&2D_{[\alpha} D_{\beta]} \omega_\mu \\
&= 2\gamma_\mu{}^\rho \gamma_{[\alpha}{}^\varepsilon \gamma_{\beta]}{}^\kappa \nabla_\varepsilon \nabla_\kappa \omega_\rho - 2\gamma_\mu{}^\rho n^\kappa K_{[\alpha\beta]} \nabla_\kappa \omega_\rho - 2K_{\mu[\alpha} K_{\beta]}{}^\rho \omega_\rho \\
&= 2\gamma_\mu{}^\rho \gamma_\alpha{}^\varepsilon \gamma_\beta{}^\kappa \nabla_{[\varepsilon} \nabla_{\kappa]} \omega_\rho - 2K_{\mu[\alpha} K_{\beta]}{}^\rho \omega_\rho .
\end{aligned}
\tag{A.3}
$$

We know that $\nabla_{[\varepsilon}\nabla_{\kappa]}$ is related to the 4-dimensional Riemann curvature tensor, and $D_{[\alpha}D_{\beta]}$ is related to the 3-dimensional Riemann tensor. Therefore, we can associate them together,

$$
{}^{(3)}R_{\alpha\beta\mu}{}^\nu \omega_\nu = \gamma_\mu{}^\rho \gamma_\alpha{}^\varepsilon \gamma_\beta{}^\kappa \gamma_\sigma{}^\nu R_{\varepsilon\kappa\rho}{}^\sigma \omega_\nu - 2K_{\mu[\alpha} K_{\beta]}{}^\nu \omega_\nu . \tag{A.4}
$$

Therefore, it is not difficult to derive the following equation:

$$
{}^{(3)}R_{\alpha\beta\mu}{}^\nu \omega_\nu = \gamma_\alpha{}^\varepsilon \gamma_\beta{}^\kappa \gamma_\mu{}^\rho \gamma_\sigma{}^\nu R_{\varepsilon\kappa\rho}{}^\sigma - 2K_{\mu[\alpha} K_{\beta]}{}^\nu . \tag{A.5}
$$

Further

$$
{}^{(3)}R_{\alpha\beta\mu\nu} = \gamma_\alpha{}^\varepsilon \gamma_\beta{}^\kappa \gamma_\mu{}^\rho \gamma_\nu{}^\sigma R_{\varepsilon\kappa\rho\sigma} - 2K_{\mu[\alpha} K_{\beta]\nu} . \tag{A.6}
$$

And this happens to be:

$$
\gamma_\alpha{}^\varepsilon \gamma_\beta{}^\kappa \gamma_\mu{}^\rho \gamma_\nu{}^\sigma R_{\varepsilon\kappa\rho\sigma} = {}^{(3)}R_{\alpha\beta\mu\nu} + K_{\alpha\mu} K_{\beta\nu} - K_{\alpha\nu} K_{\beta\mu} , \tag{A.7}
$$

and this is exactly what we were aiming for.

Codazzi-Mainardi Equation

The Codazzi-Mainardi equation is as follows:

$$\gamma_\alpha{}^\delta \gamma_\beta{}^\kappa \gamma_\mu{}^\lambda n^\nu R_{\delta\kappa\lambda\nu} = D_\beta K_{\alpha\mu} - D_\alpha K_{\beta\mu}. \tag{A.8}$$

The detailed derivation process is as follows:

We will begin deriving from the right-hand side of the equation, as it is simpler and clearer.

$$\begin{aligned}
&D_\lambda K_{\mu\nu} - D_\mu K_{\lambda\nu} \\
=&\gamma_\mu{}^\alpha \gamma_\nu{}^\beta \gamma_\lambda{}^\sigma \nabla_\sigma K_{\alpha\beta} - \gamma_\lambda{}^\alpha \gamma_\nu{}^\beta \gamma_\mu{}^\sigma \nabla_\sigma K_{\alpha\beta} \\
=&-\gamma_\mu{}^\alpha \gamma_\nu{}^\beta \gamma_\lambda{}^\sigma \nabla_\sigma \left(\gamma_\alpha{}^\rho \nabla_\rho n_\beta\right) + \gamma_\lambda{}^\alpha \gamma_\nu{}^\beta \gamma_\mu{}^\sigma \nabla_\sigma \left(\gamma_\alpha{}^\rho \nabla_\rho n_\beta\right) \\
=&-\gamma_\mu{}^\rho \gamma_\nu{}^\beta \gamma_\lambda{}^\sigma \nabla_\sigma \nabla_\rho n_\beta - \gamma_\mu{}^\alpha \gamma_\nu{}^\beta \gamma_\lambda{}^\sigma \left(\nabla_\rho n_\beta\right) \nabla_\sigma \left(\delta_\alpha{}^\rho + n_\alpha n^\rho\right) + \gamma_\lambda{}^\rho \gamma_\nu{}^\beta \gamma_\mu{}^\sigma \nabla_\sigma \nabla_\rho n_\beta \\
&+\gamma_\lambda{}^\alpha \gamma_\nu{}^\beta \gamma_\mu{}^\sigma \left(\nabla_\rho n_\beta\right) \nabla_\sigma \left(\delta_\alpha{}^\rho + n_\alpha n^\rho\right) \\
=&-\gamma_\mu{}^\rho \gamma_\nu{}^\beta \gamma_\lambda{}^\sigma \nabla_\sigma \nabla_\rho n_\beta - \gamma_\mu{}^\alpha \gamma_\nu{}^\beta \gamma_\lambda{}^\sigma n^\rho \left(\nabla_\rho n_\beta\right) \nabla_\sigma n_\alpha \\
&+\gamma_\lambda{}^\rho \gamma_\nu{}^\beta \gamma_\mu{}^\sigma \nabla_\sigma \nabla_\rho n_\beta + \gamma_\lambda{}^\alpha \gamma_\nu{}^\beta \gamma_\mu{}^\sigma n^\rho \left(\nabla_\rho n_\beta\right) \nabla_\sigma n_\alpha \\
=&-\gamma_\mu{}^\rho \gamma_\nu{}^\beta \gamma_\lambda{}^\sigma \nabla_\sigma \nabla_\rho n_\beta + \gamma_\nu{}^\beta n^\rho \left(\nabla_\rho n_\beta\right) K_{\lambda\mu} + \gamma_\lambda{}^\rho \gamma_\nu{}^\beta \gamma_\mu{}^\sigma \nabla_\sigma \nabla_\rho n_\beta - \gamma_\nu{}^\beta n^\rho \left(\nabla_\rho n_\beta\right) K_{\mu\lambda} \\
=&-\gamma_\mu{}^\rho \gamma_\nu{}^\beta \gamma_\lambda{}^\sigma \nabla_\sigma \nabla_\rho n_\beta + \gamma_\lambda{}^\sigma \gamma_\nu{}^\beta \gamma_\mu{}^\rho \nabla_\rho \nabla_\sigma n_\beta \\
=&\gamma_\mu{}^\rho \gamma_\lambda{}^\sigma \gamma_\nu{}^\beta R_{\rho\sigma\beta\alpha} n^\alpha.
\end{aligned} \tag{A.9}$$

Ricci Equation

The Ricci equation is as follows:

$$\gamma_\mu{}^\delta \gamma_\nu{}^\kappa n^\lambda n^\sigma R_{\delta\lambda\kappa\sigma} = \mathscr{L}_{\vec{n}} K_{\mu\nu} + K_{\mu\lambda} K_\nu{}^\lambda + \frac{1}{\alpha} D_\mu D_\nu \alpha. \tag{A.10}$$

The detailed derivation process is as follows:

$$
\begin{aligned}
&\gamma^{\alpha}{}_{\mu}\gamma^{\beta}{}_{\nu}n^{\sigma}n^{\rho}R_{\rho\alpha\sigma\beta} \\
&= -\gamma^{\alpha}{}_{\mu}\gamma^{\beta}{}_{\nu}n^{\sigma}R_{\sigma\beta\alpha}{}^{\rho}n_{\rho} = -\gamma^{\alpha}{}_{\mu}\gamma^{\beta}{}_{\nu}n^{\sigma}(\nabla_{\sigma}\nabla_{\beta}-\nabla_{\beta}\nabla_{\sigma})n_{\alpha} \\
&= -[n^{\sigma}\nabla_{\sigma}(\gamma^{\alpha}{}_{\mu}\gamma^{\beta}{}_{\nu}\nabla_{\beta}n_{\alpha}) - n^{\sigma}(\nabla_{\beta}n_{\alpha})\nabla_{\sigma}(\gamma^{\alpha}{}_{\mu}\gamma^{\beta}{}_{\nu})] + [\gamma^{\alpha}{}_{\mu}\gamma^{\beta}{}_{\nu}\nabla_{\beta}(n^{\sigma}\nabla_{\sigma}n_{\alpha}) \\
&\quad - \gamma^{\alpha}{}_{\mu}\gamma^{\beta}{}_{\nu}(\nabla_{\beta}n^{\sigma})\nabla_{\sigma}n_{\alpha}] \\
&= n^{\sigma}\nabla_{\sigma}K_{\nu\mu} + n^{\sigma}(\nabla_{\beta}n_{\alpha})\gamma^{\alpha}{}_{\mu}\nabla_{\sigma}(\delta^{\beta}{}_{\nu}+n^{\beta}n_{\nu}) + n^{\sigma}(\nabla_{\beta}n_{\alpha})\gamma^{\beta}{}_{\nu}\nabla_{\sigma}(\delta^{\alpha}{}_{\mu}+n^{\alpha}n_{\mu}) + \gamma^{\alpha}{}_{\mu}\gamma^{\beta}{}_{\nu}\nabla_{\beta}a_{\alpha} \\
&\quad - K^{\sigma}{}_{\nu}K_{\sigma\mu} \\
&= n^{\sigma}\nabla_{\sigma}K_{\nu\mu} + a_{\mu}a_{\nu} + \gamma^{\alpha}{}_{\mu}(\gamma^{\sigma}{}_{\nu}-\delta^{\sigma}{}_{\nu})(\nabla_{\beta}n_{\alpha})\nabla_{\sigma}n^{\beta} + \gamma^{\beta}{}_{\nu}(\gamma^{\sigma}{}_{\mu}-\delta^{\sigma}{}_{\mu})(\nabla_{\beta}n_{\alpha})\nabla_{\sigma}n^{\alpha} + D_{\nu}a_{\mu} \\
&\quad - K^{\sigma}{}_{\nu}K_{\sigma\mu} \\
&= n^{\sigma}\nabla_{\sigma}K_{\nu\mu} + a_{\mu}a_{\nu} + K^{\beta}{}_{\nu}K_{\beta\mu} - (\nabla_{\beta}n_{\mu})\nabla_{\nu}n^{\beta} + K_{\nu\alpha}K^{\alpha}{}_{\mu} + K_{\nu\alpha}\nabla_{\mu}n^{\alpha} + D_{\nu}a_{\mu} - K^{\sigma}{}_{\nu}K_{\sigma\mu} \\
&= n^{\sigma}\nabla_{\sigma}K_{\nu\mu} + a_{\mu}a_{\nu} + K_{\beta\mu}\nabla_{\nu}n^{\beta} + K_{\nu\alpha}K^{\alpha}{}_{\mu} + K_{\nu\alpha}\nabla_{\mu}n^{\alpha} + D_{\nu}a_{\mu} \\
&= n^{\sigma}\nabla_{\sigma}K_{\nu\mu} + K_{\beta\mu}\nabla_{\nu}n^{\beta} + K_{\nu\alpha}\nabla_{\mu}n^{\alpha} + K_{\nu\alpha}K^{\alpha}{}_{\mu} + \frac{1}{\alpha^{2}}(D_{\mu}\alpha)D_{\nu}\alpha + [\frac{1}{\alpha}D_{\nu}D_{\mu}\alpha \\
&\quad - \frac{1}{\alpha^{2}}(D_{\nu}\alpha)D_{\mu}\alpha] \\
&= \mathscr{L}_{\vec{n}}K_{\nu\mu} + K_{\nu\alpha}K^{\alpha}{}_{\mu} + \frac{1}{\alpha}D_{\nu}D_{\mu}\alpha.
\end{aligned}
$$

Claim:

$$
R_{\mu\nu} = 8\pi\left(T_{\mu\nu} - \frac{1}{2}T g_{\mu\nu}\right). \tag{A.11}
$$

Proof.

$$
\begin{aligned}
&\because\ R_{\mu\nu} - \tfrac{1}{2}R g_{\mu\nu} = 8\pi T_{\mu\nu}, \\
&\therefore\ g^{\mu\nu}\left(R_{\mu\nu} - \tfrac{1}{2}R g_{\mu\nu}\right) = 8\pi T_{\mu\nu}g^{\mu\nu}, \\
&\therefore\ R = -8\pi T, \\
&\therefore\ R_{\mu\nu} = 8\pi\left(T_{\mu\nu} - \tfrac{1}{2}T g_{\mu\nu}\right).
\end{aligned} \tag{A.12}
$$

□

Claim:

$$-\gamma_\mu{}^\delta \gamma_\nu{}^\kappa R_{\delta\kappa} = 4\pi \left[\gamma_{\mu\nu}(S-\rho) - 2S_{\mu\nu}\right]. \tag{A.13}$$

Proof.

$$\begin{aligned}
-\gamma_\mu{}^\delta \gamma_\nu{}^\kappa R_{\delta\kappa} &= -\gamma_\mu{}^\delta \gamma_\nu{}^\kappa \left[8\pi\left(T_{\delta\kappa} - \frac{1}{2} T g_{\delta\kappa}\right)\right] \\
&= 4\pi\left(\gamma_{\mu\nu} T - 2\gamma_\mu{}^\delta \gamma_\nu{}^\kappa T_{\delta\kappa}\right) \\
&= 4\pi\left(\gamma_{\mu\nu} g^{\alpha\beta} T_{\alpha\beta} - 2\gamma_\mu{}^\delta \gamma_\nu{}^\kappa T_{\delta\kappa}\right) \\
&= 4\pi\left[\gamma_{\mu\nu}\left(g^{\delta\kappa}\gamma_\delta{}^\alpha \gamma_\kappa{}^\beta T_{\alpha\beta} - n^\alpha n^\beta T_{\alpha\beta}\right) - 2\gamma_\mu{}^\delta \gamma_\nu{}^\kappa T_{\delta\kappa}\right] \\
&= 4\pi\left[\gamma_{\mu\nu}(S-\rho) - 2S_{\mu\nu}\right]
\end{aligned} \tag{A.14}$$

where $S_{\mu\nu} \equiv \gamma_\mu^\delta \gamma_\nu^\kappa T_{\delta\kappa}, S \equiv g^{\mu\nu} S_{\mu\nu}$ and $\rho \equiv n^\alpha n^\beta T_{\alpha\beta}$. □

A.2 Detailed Derivation of the BSSN Formalism

Claim:

$$\partial_t \tilde{\gamma}^{ij} - \mathscr{L}_{\vec{\beta}} \tilde{\gamma}^{ij} = 2\alpha \widetilde{A}^{ij}. \tag{A.15}$$

Proof.

$$\begin{aligned}
(\partial_t - \mathscr{L}_{\vec{\beta}})\tilde{\gamma}_{kl} &= -2\alpha \widetilde{A}_{kl} \\
\tilde{\gamma}^{ik}\tilde{\gamma}^{jl}(\partial_t - \mathscr{L}_{\vec{\beta}})\tilde{\gamma}_{kl} &= -2\alpha \tilde{\gamma}^{ik}\tilde{\gamma}^{jl}\widetilde{A}_{kl} \\
\tilde{\gamma}^{ik}[(\partial_t - \mathscr{L}_{\vec{\beta}})\tilde{\gamma}^{jl}\tilde{\gamma}_{kl} - \tilde{\gamma}_{kl}(\partial_t - \mathscr{L}_{\vec{\beta}})\tilde{\gamma}^{jl}] &= -2\alpha \widetilde{A}^{ij} \\
-\delta^i_l(\partial_t - \mathscr{L}_{\vec{\beta}})\tilde{\gamma}^{jl} &= -2\alpha \widetilde{A}^{ij} \\
(\partial_t - \mathscr{L}_{\vec{\beta}})\tilde{\gamma}^{ij} &= 2\alpha \widetilde{A}^{ij}.
\end{aligned}$$

□

Claim:

Momentum constraints written out in terms of conformally transformed quantities:

$$\partial_j \widetilde{A}^{ij} + \widetilde{\Gamma}^i{}_{jk}\widetilde{A}^{jk} + 6\widetilde{A}^{ij}\partial_j \phi - \frac{2}{3}\tilde{\gamma}^{ij}\partial_j K = 8\pi \tilde{j}^i \tag{A.16}$$

where $\tilde{j}^i \equiv e^{4\phi} j^i$.

Proof.

$$
\begin{aligned}
D_j(K^{ij} - \gamma^{ij}K) &= 8\pi j^i \\
D_j(A^{ij} + \frac{1}{3}\gamma^{ij}K) - \gamma^{ij}D_jK &= 8\pi j^i \\
D_jA^{ij} - \frac{2}{3}\gamma^{ij}D_jK &= 8\pi j^i \\
(\partial_jA^{ij} + \Gamma^i{}_{jk}A^{kj} + \Gamma^j{}_{jk}A^{ik}) - \frac{2}{3}\gamma^{ij}D_jK &= 8\pi j^i \\
(e^{-4\phi}\partial_j\widetilde{A}^{ij} + \widetilde{A}^{ij}\partial_je^{-4\phi}) + \Gamma^i{}_{jk}(e^{-4\phi}\widetilde{A}^{kj}) + \Gamma^j{}_{jk}(e^{-4\phi}\widetilde{A}^{ik}) - \frac{2}{3}e^{-4\phi}\tilde{\gamma}^{ij}\partial_jK &= 8\pi j^i \\
e^{-4\phi}(\partial_j\widetilde{A}^{ij} - 4\widetilde{A}^{ij}\partial_j\phi + \Gamma^i{}_{jk}\widetilde{A}^{kj} + \Gamma^j{}_{jk}\widetilde{A}^{ik} - \frac{2}{3}\tilde{\gamma}^{ij}\partial_jK) &= 8\pi j^i \\
\partial_j\widetilde{A}^{ij} - 4\widetilde{A}^{ij}\partial_j\phi + \widetilde{A}^{kj}[\tilde{\Gamma}^i{}_{jk} + 2(\delta^i{}_j\partial_k\phi + \delta^i{}_k\partial_j\phi - \gamma_{jk}\gamma^{il}\partial_l\phi)] + 6\widetilde{A}^{ik}\partial_k\phi - \frac{2}{3}\tilde{\gamma}^{ij}\partial_jK &= 8\pi\tilde{j}^i \\
\partial_j\widetilde{A}^{ij} - 4\widetilde{A}^{ij}\partial_j\phi + \widetilde{A}^{kj}\tilde{\Gamma}^i{}_{jk} + 2(\widetilde{A}^{ki}\partial_k\phi + \widetilde{A}^{ij}\partial_j\phi) + 6\widetilde{A}^{ik}\partial_k\phi - \frac{2}{3}\tilde{\gamma}^{ij}\partial_jK &= 8\pi\tilde{j}^i \\
\partial_j\widetilde{A}^{ij} + \widetilde{A}^{kj}\tilde{\Gamma}^i{}_{jk} + 6\widetilde{A}^{ik}\partial_k\phi - \frac{2}{3}\tilde{\gamma}^{ij}\partial_jK &= 8\pi\tilde{j}^i.
\end{aligned}
$$

□

Claim:

$$\widetilde{R}_{ij} = -\frac{1}{2}\tilde{\gamma}^{lm}\partial_l\partial_m\tilde{\gamma}_{ij} + \tilde{\gamma}_{k(i}\partial_{j)}\widetilde{\Gamma}^k + \widetilde{\Gamma}^k\widetilde{\Gamma}_{(ij)k} + \tilde{\gamma}^{lm}(2\widetilde{\Gamma}^k{}_{l(i}\widetilde{\Gamma}_{j)km} + \widetilde{\Gamma}^k{}_{im}\widetilde{\Gamma}_{klj}). \tag{A.17}$$

Proof.

$$\widetilde{R}_{ij} = \partial_k\widetilde{\Gamma}^k{}_{ij} - \partial_j\widetilde{\Gamma}^k{}_{ik} + \widetilde{\Gamma}^k{}_{ij}\widetilde{\Gamma}^l{}_{kl} - \widetilde{\Gamma}^k{}_{il}\widetilde{\Gamma}^l{}_{kj} = \partial_k\widetilde{\Gamma}^k{}_{ij} - \widetilde{\Gamma}^k{}_{il}\widetilde{\Gamma}^l{}_{kj}. \tag{A.18}$$

For the first term on the right-hand side $\partial_k \widetilde{\Gamma}^k{}_{ij}$:

$$\begin{aligned}
\partial_k \widetilde{\Gamma}^k{}_{ij} &= \partial_k [\frac{1}{2}\tilde{\gamma}^{kl}(\partial_i \tilde{\gamma}_{jl} + \partial_j \tilde{\gamma}_{il} - \partial_l \tilde{\gamma}_{ij})] = \frac{1}{2}\partial_k(-\tilde{\gamma}_{jl}\partial_i \tilde{\gamma}^{kl} - \tilde{\gamma}_{il}\partial_j \tilde{\gamma}^{kl} - \tilde{\gamma}^{kl}\partial_l \tilde{\gamma}_{ij}) \\
&= \frac{1}{2}[-\tilde{\gamma}_{jl}\partial_k\partial_i \tilde{\gamma}^{kl} - (\partial_k \tilde{\gamma}_{jl})\partial_i \tilde{\gamma}^{kl} - \tilde{\gamma}_{il}\partial_k\partial_j \tilde{\gamma}^{kl} - (\partial_k \tilde{\gamma}_{il})\partial_j \tilde{\gamma}^{kl} - \tilde{\gamma}^{kl}\partial_k\partial_l \tilde{\gamma}_{ij} \\
&\quad - (\partial_k \tilde{\gamma}^{kl})\partial_l \tilde{\gamma}^{ij}] \\
&= \frac{1}{2}[\tilde{\gamma}_{jl}\partial_i \widetilde{\Gamma}^l - (\partial_k \tilde{\gamma}_{jl})\partial_i \tilde{\gamma}^{kl} + \tilde{\gamma}_{il}\partial_j \widetilde{\Gamma}^l - (\partial_k \tilde{\gamma}_{il})\partial_j \tilde{\gamma}^{kl} - \tilde{\gamma}^{kl}\partial_k\partial_l \tilde{\gamma}_{ij} + \widetilde{\Gamma}^l \partial_l \tilde{\gamma}_{ij}] \\
&= -\frac{1}{2}\tilde{\gamma}^{kl}\partial_k\partial_l \tilde{\gamma}_{ij} + \tilde{\gamma}_{l(i}\partial_{j)}\widetilde{\Gamma}^l + \widetilde{\Gamma}^l \widetilde{\Gamma}_{(ij)l} - \frac{1}{2}(\partial_k \tilde{\gamma}_{jl})\partial_i \tilde{\gamma}^{kl} - \frac{1}{2}(\partial_k \tilde{\gamma}_{il})\partial_j \tilde{\gamma}^{kl}.
\end{aligned}$$

In the above expression, we utilized the following two equations:

$$\widetilde{\Gamma}_{klj} = \tilde{\gamma}_{nk}\widetilde{\Gamma}^n{}_{lj} = \frac{1}{2}\delta^{\bar{m}}{}_k(\partial_l \tilde{\gamma}_{j\bar{m}} + \partial_j \tilde{\gamma}_{l\bar{m}} - \partial_{\bar{m}} \tilde{\gamma}_{lj}) = \frac{1}{2}(\partial_l \tilde{\gamma}_{jk} + \partial_j \tilde{\gamma}_{lk} - \partial_k \tilde{\gamma}_{lj}), \tag{A.19}$$

and

$$\begin{aligned}
\widetilde{\Gamma}^k \widetilde{\Gamma}_{(ij)k} &= \frac{1}{2}\widetilde{\Gamma}^k(\widetilde{\Gamma}_{ijk} + \widetilde{\Gamma}_{jik}) = \frac{1}{2}\widetilde{\Gamma}^k[\frac{1}{2}(\partial_j \tilde{\gamma}_{ki} + \partial_k \tilde{\gamma}_{ji} - \partial_i \tilde{\gamma}_{jk}) + \frac{1}{2}(\partial_i \tilde{\gamma}_{kj} + \partial_k \tilde{\gamma}_{ij} - \partial_j \tilde{\gamma}_{ik})] \\
&= \frac{1}{2}\widetilde{\Gamma}^k \partial_k \tilde{\gamma}_{ij}.
\end{aligned} \tag{A.20}$$

For the second term on the right-hand side $-\widetilde{\Gamma}^k{}_{il}\widetilde{\Gamma}^l{}_{kj}$.

We first look at $-\widetilde{\Gamma}^k{}_{il}\widetilde{\Gamma}^l{}_{kj} - \tilde{\gamma}^{lm}\widetilde{\Gamma}^k{}_{im}\widetilde{\Gamma}_{klj}$:

$$\begin{aligned}
&-\widetilde{\Gamma}^k{}_{il}\widetilde{\Gamma}^l{}_{kj} - \tilde{\gamma}^{lm}\widetilde{\Gamma}^k{}_{im}\widetilde{\Gamma}_{klj} \\
&= \widetilde{\Gamma}^k{}_{im}(-\widetilde{\Gamma}^m{}_{kj} - \tilde{\gamma}^{lm}\widetilde{\Gamma}_{klj}) \\
&= \widetilde{\Gamma}^k{}_{im}[\frac{1}{2}\tilde{\gamma}^{mn}(\partial_n \tilde{\gamma}_{kj} - \partial_k \tilde{\gamma}_{jn} - \partial_j \tilde{\gamma}_{kn}) - \frac{1}{2}\tilde{\gamma}^{nm}(\partial_n \tilde{\gamma}_{jk} + \partial_j \tilde{\gamma}_{nk} - \partial_k \tilde{\gamma}_{nj})] \\
&= \widetilde{\Gamma}^k{}_{im}(-\tilde{\gamma}^{mn}\partial_j \tilde{\gamma}_{kn}) = \frac{1}{2}\tilde{\gamma}^{kp}(\partial_i \tilde{\gamma}_{mp} + \partial_m \tilde{\gamma}_{ip} - \partial_p \tilde{\gamma}_{im})(\tilde{\gamma}_{kn}\partial_j \tilde{\gamma}^{mn}) \\
&= \frac{1}{2}(\partial_i \tilde{\gamma}_{mn} + \partial_m \tilde{\gamma}_{in} - \partial_n \tilde{\gamma}_{im})\partial_j \tilde{\gamma}^{mn} = \frac{1}{2}(\partial_i \tilde{\gamma}_{mn})\partial_j \tilde{\gamma}^{mn}.
\end{aligned}$$

This implies:

$$-\widetilde{\Gamma}^k{}_{il}\widetilde{\Gamma}^l{}_{kj} = \tilde{\gamma}^{lm}\widetilde{\Gamma}^k{}_{im}\widetilde{\Gamma}_{klj} + \frac{1}{2}(\partial_i \tilde{\gamma}_{mn})\partial_j \tilde{\gamma}^{mn}. \tag{A.21}$$

Now, we will focus on the expression $\frac{1}{2}(\partial_i \tilde{\gamma}_{mn})\,\partial_j \tilde{\gamma}^{mn}$.

Starting with $\tilde{\gamma}^{lm}\widetilde{\Gamma}^k{}_{li}\widetilde{\Gamma}_{jkm}$:

$$
\begin{aligned}
&\tilde{\gamma}^{lm}\widetilde{\Gamma}^k{}_{li}\widetilde{\Gamma}_{jkm} \\
&= \tilde{\gamma}^{lm}\frac{1}{2}\tilde{\gamma}^{k\bar{m}}(\partial_l \tilde{\gamma}_{i\bar{m}} + \partial_i \tilde{\gamma}_{l\bar{m}} - \partial_{\bar{m}} \tilde{\gamma}_{li})\widetilde{\Gamma}_{jkm} \\
&= \frac{1}{2}[\tilde{\gamma}^{lm}\tilde{\gamma}^{k\bar{m}}\partial_l \tilde{\gamma}_{i\bar{m}} + \tilde{\gamma}^{k\bar{m}}(-\tilde{\gamma}_{l\bar{m}}\partial_i \tilde{\gamma}^{lm}) - \tilde{\gamma}^{lm}\tilde{\gamma}^{k\bar{m}}\partial_{\bar{m}} \tilde{\gamma}_{li}]\widetilde{\Gamma}_{jkm} \\
&= \frac{1}{2}(\tilde{\gamma}^{lm}\tilde{\gamma}^{k\bar{m}}\partial_l \tilde{\gamma}_{i\bar{m}} - \partial_i \tilde{\gamma}^{km} - \tilde{\gamma}^{lm}\tilde{\gamma}^{k\bar{m}}\partial_{\bar{m}} \tilde{\gamma}_{li}) \times \frac{1}{2}(\partial_k \tilde{\gamma}_{mj} + \partial_m \tilde{\gamma}_{kj} - \partial_j \tilde{\gamma}_{km}) \\
&= -\frac{1}{4}\partial_i \tilde{\gamma}^{km}(\partial_k \tilde{\gamma}_{mj} + \partial_m \tilde{\gamma}_{kj} - \partial_j \tilde{\gamma}_{km}) \\
&= -\frac{1}{2}(\partial_i \tilde{\gamma}^{km})\partial_k \tilde{\gamma}_{mj} + \frac{1}{4}(\partial_i \tilde{\gamma}^{km})\partial_j \tilde{\gamma}_{km}.
\end{aligned}
$$

To obtain $\frac{1}{2}(\partial_i \tilde{\gamma}_{mn})\,\partial_j \tilde{\gamma}^{mn}$, simply symmetrize the indices i and j in the previous expression,

$$
\begin{aligned}
&2\tilde{\gamma}^{lm}\widetilde{\Gamma}^k{}_{l(i}\widetilde{\Gamma}_{j)km} \\
&= \tilde{\gamma}^{lm}(\widetilde{\Gamma}^k{}_{li}\widetilde{\Gamma}_{jkm} + \widetilde{\Gamma}^k{}_{lj}\widetilde{\Gamma}_{ikm}) = -\frac{1}{2}(\partial_i \tilde{\gamma}^{km})\partial_k \tilde{\gamma}_{mj} - \frac{1}{2}(\partial_j \tilde{\gamma}^{km})\partial_k \tilde{\gamma}_{mi} + \frac{1}{2}(\partial_i \tilde{\gamma}^{km})\partial_j \tilde{\gamma}_{km}.
\end{aligned}
\tag{A.22}
$$

Thus,

$$
\frac{1}{2}(\partial_i \tilde{\gamma}^{km})\partial_j \tilde{\gamma}_{km} = 2\tilde{\gamma}^{lm}\widetilde{\Gamma}^k{}_{l(i}\widetilde{\Gamma}_{j)km} + \frac{1}{2}(\partial_i \tilde{\gamma}^{km})\partial_k \tilde{\gamma}_{mj} + \frac{1}{2}(\partial_j \tilde{\gamma}^{km})\partial_k \tilde{\gamma}_{mi}. \tag{A.23}
$$

Now we have the expression for $-\widetilde{\Gamma}^k{}_{il}\widetilde{\Gamma}^l{}_{kj}$,

$$
-\widetilde{\Gamma}^k{}_{il}\widetilde{\Gamma}^l{}_{kj} = \tilde{\gamma}^{lm}\widetilde{\Gamma}^k{}_{im}\widetilde{\Gamma}_{klj} + 2\tilde{\gamma}^{lm}\widetilde{\Gamma}^k{}_{l(i}\widetilde{\Gamma}_{j)km} + \frac{1}{2}(\partial_i \tilde{\gamma}^{km})\partial_k \tilde{\gamma}_{mj} + \frac{1}{2}(\partial_j \tilde{\gamma}^{km})\partial_k \tilde{\gamma}_{mi}. \tag{A.24}
$$

By substituting equations A.20 and A.24 into equation A.18, we obtain equation A.17.

□

Appendix B

Supplementary Data

In this Appendix, we will present some supplementary material. Including this content in the main text may be overly redundant.

B.1 Comparative Analysis of Mass, Radius, Compactness and Potential

As a supplement to the data on boson stars, we have listed comparative data on the mass, radius, and potential energy of specifically selected solitons in Chapter 5.

Overall Comparison of Solitons with $\sigma = 0.2$

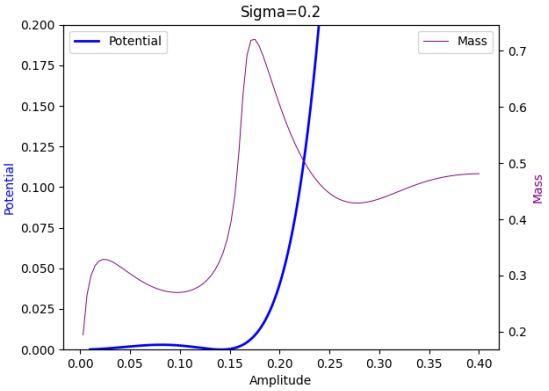

(a) Amplitude against Potential and Mass

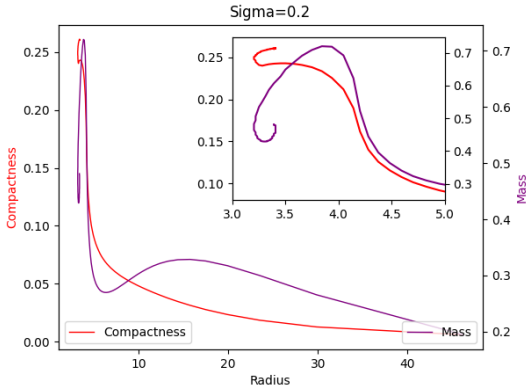

(b) Radius against Compactness and Mass

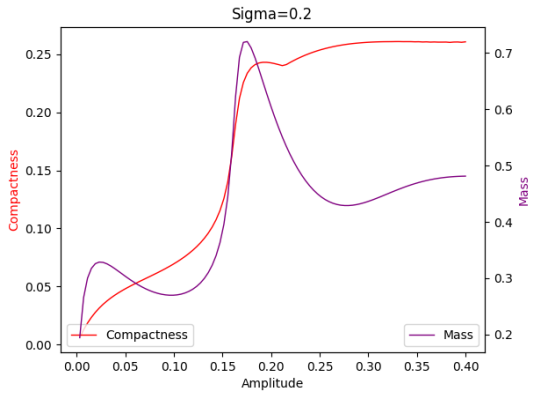

(c) Amplitude against Compactness and Mass

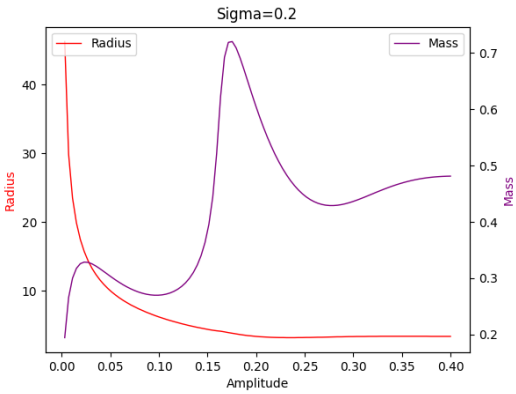

(d) Amplitude against Radius and Mass

Fig. B.1 As a supplement to the data on boson stars, we have listed comparative data on the mass, radius, and potential energy of specifically selected solitons in Chapter 5.

Overall Comparison of Solitons with $\sigma = 0.225$

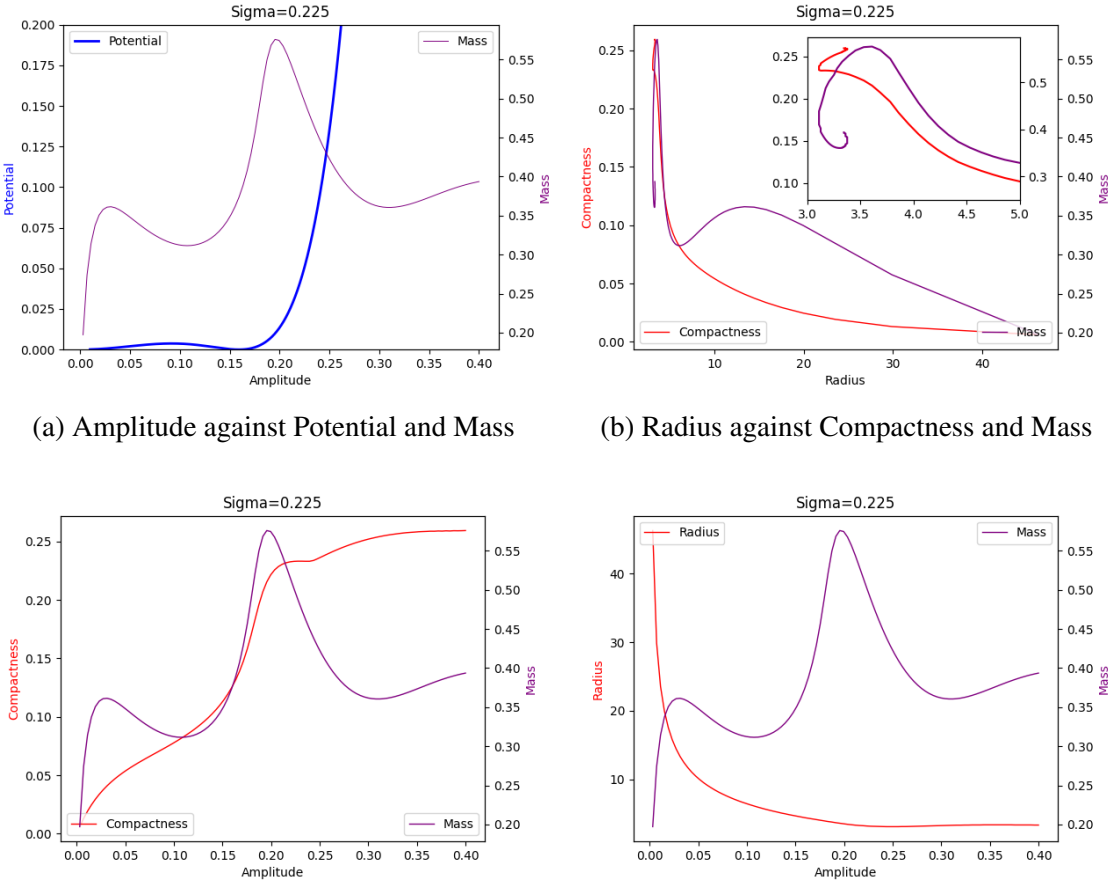

(a) Amplitude against Potential and Mass

(b) Radius against Compactness and Mass

(c) Amplitude against Compactness and Mass

(d) Amplitude against Radius and Mass

Fig. B.2 As a supplement to the data on boson stars, we have listed comparative data on the mass, radius, and potential energy of specifically selected solitons in Chapter 5.

Overall Comparison of Solitons with $\sigma = 0.25$

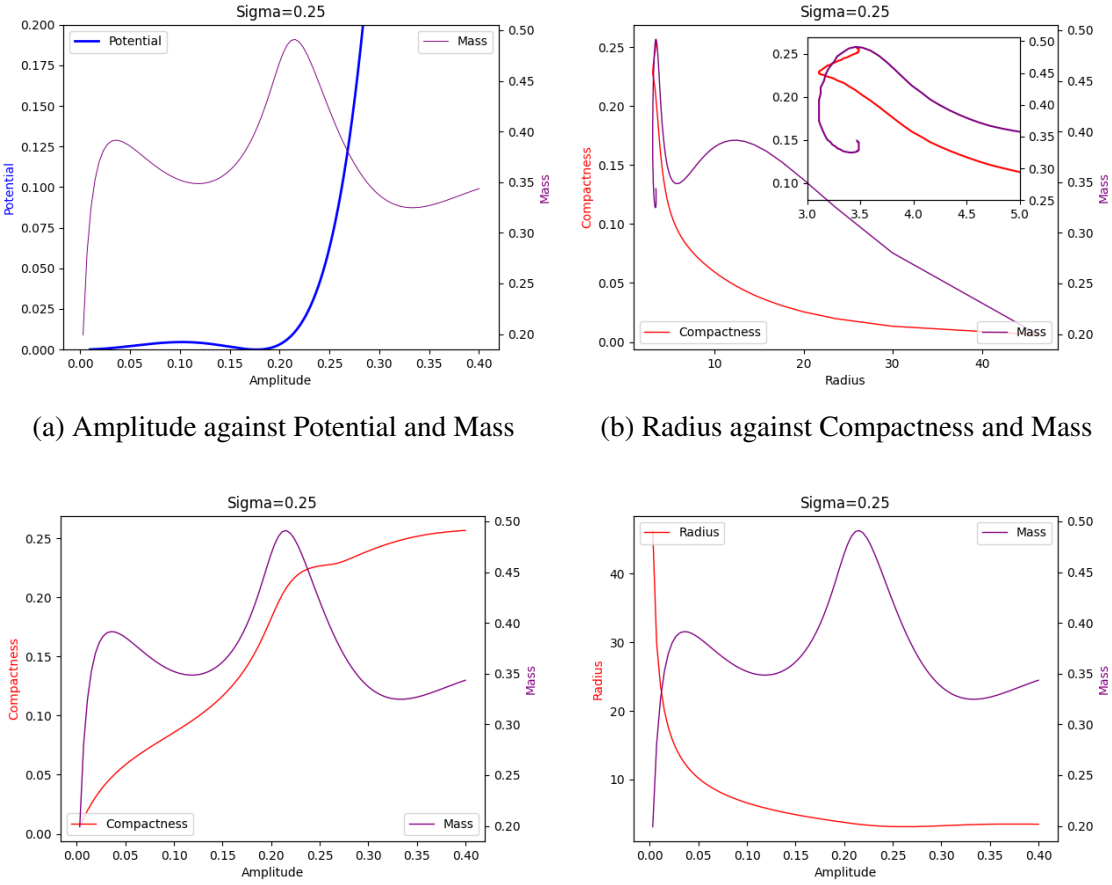

(a) Amplitude against Potential and Mass

(b) Radius against Compactness and Mass

(c) Amplitude against Compactness and Mass

(d) Amplitude against Radius and Mass

Fig. B.3 As a supplement to the data on boson stars, we have listed comparative data on the mass, radius, and potential energy of specifically selected solitons in Chapter 5.

Overall Comparison of Solitons with $\sigma = 0.275$

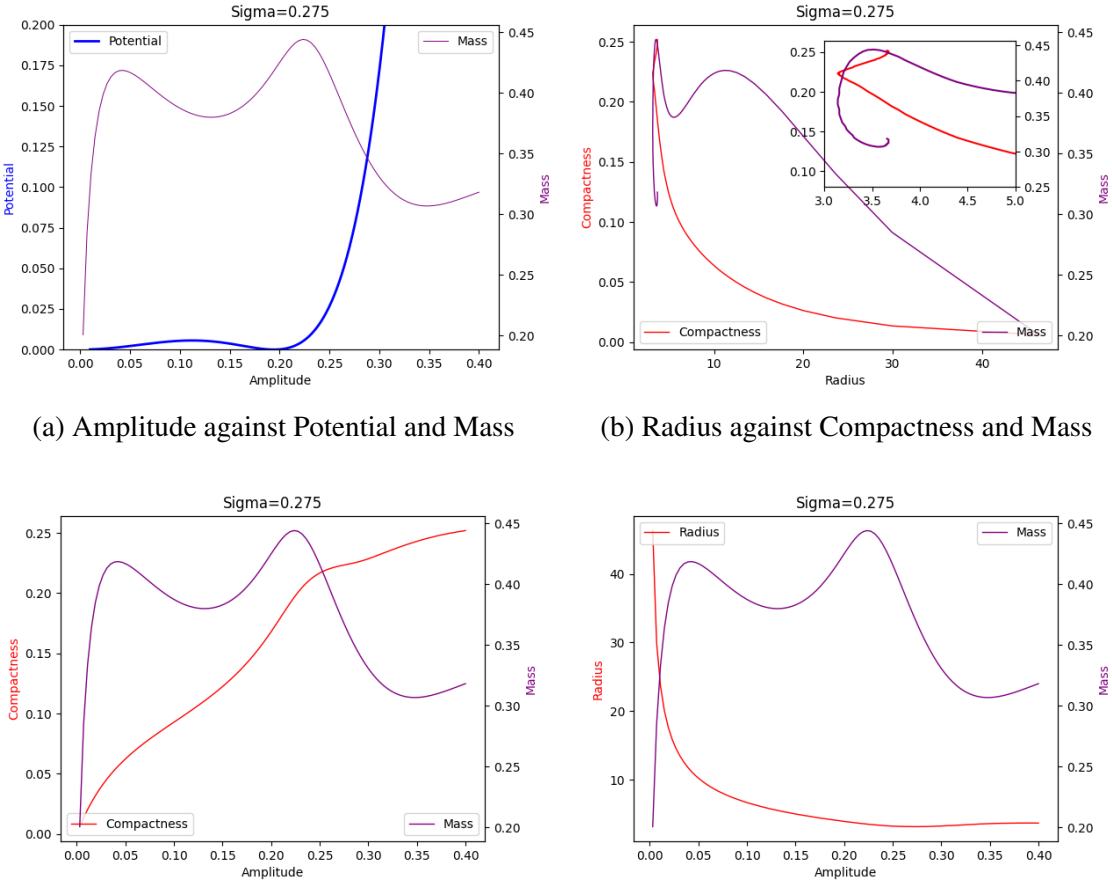

(a) Amplitude against Potential and Mass

(b) Radius against Compactness and Mass

(c) Amplitude against Compactness and Mass

(d) Amplitude against Radius and Mass

Fig. B.4 As a supplement to the data on boson stars, we have listed comparative data on the mass, radius, and potential energy of specifically selected solitons in Chapter 5.

Overall Comparison of Solitons with $\sigma = 0.28725$

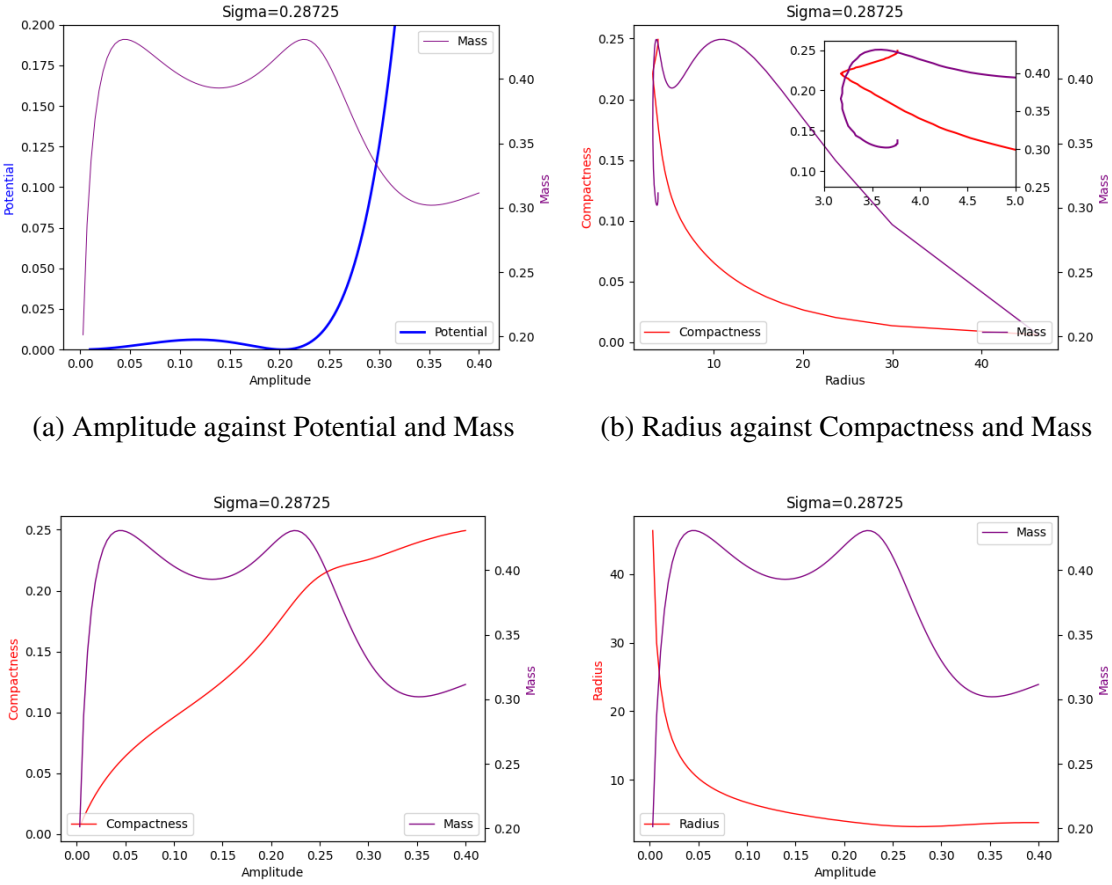

(a) Amplitude against Potential and Mass

(b) Radius against Compactness and Mass

(c) Amplitude against Compactness and Mass

(d) Amplitude against Radius and Mass

Fig. B.5 As a supplement to the data on boson stars, we have listed comparative data on the mass, radius, and potential energy of specifically selected solitons in Chapter 5.

Overall Comparison of Solitons with $\sigma = 0.3$

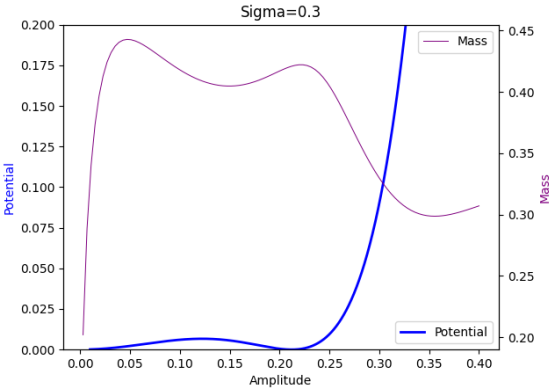

(a) Amplitude against Potential and Mass

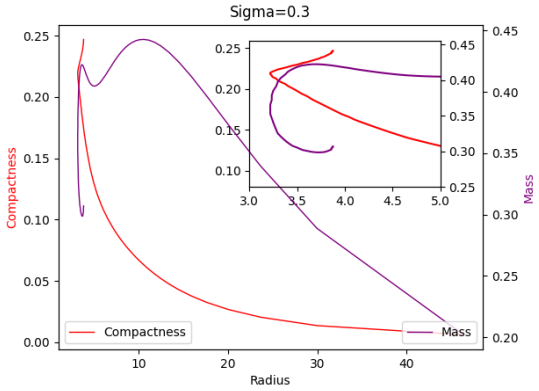

(b) Radius against Compactness and Mass

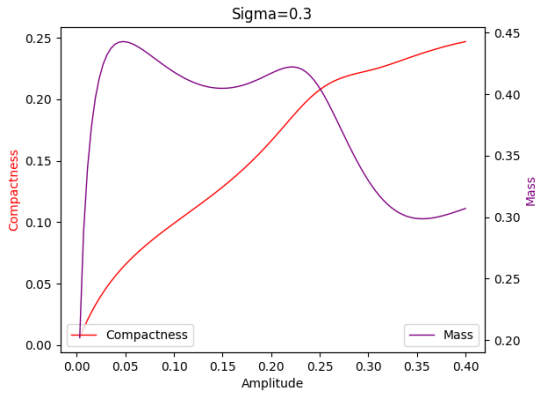

(c) Amplitude against Compactness and Mass

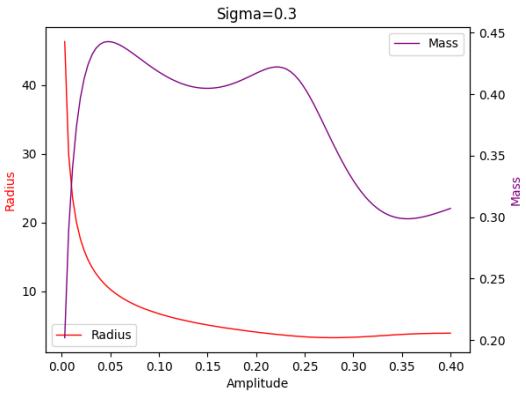

(d) Amplitude against Radius and Mass

Fig. B.6 As a supplement to the data on boson stars, we have listed comparative data on the mass, radius, and potential energy of specifically selected solitons in Chapter 5.

Overall Comparison of Solitons with $\sigma = 0.5$

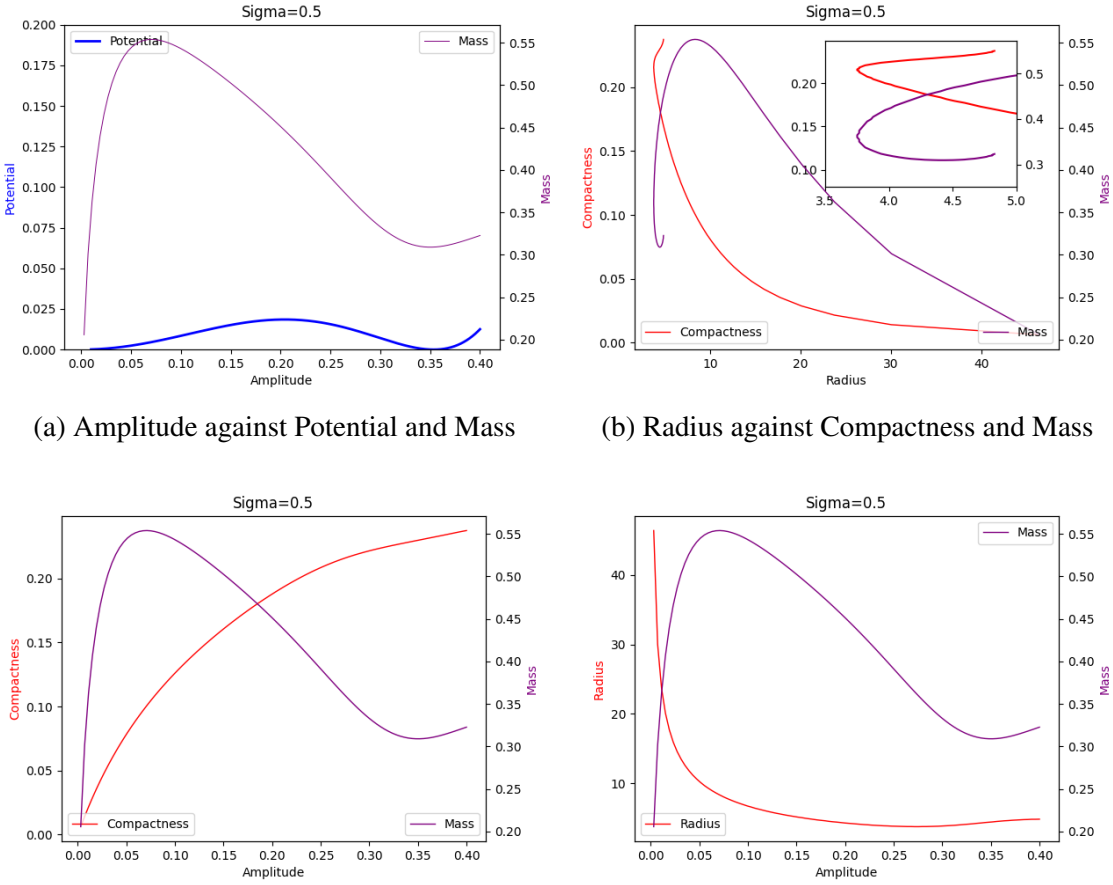

(a) Amplitude against Potential and Mass

(b) Radius against Compactness and Mass

(c) Amplitude against Compactness and Mass

(d) Amplitude against Radius and Mass

Fig. B.7 As a supplement to the data on boson stars, we have listed comparative data on the mass, radius, and potential energy of specifically selected solitons in Chapter 5.

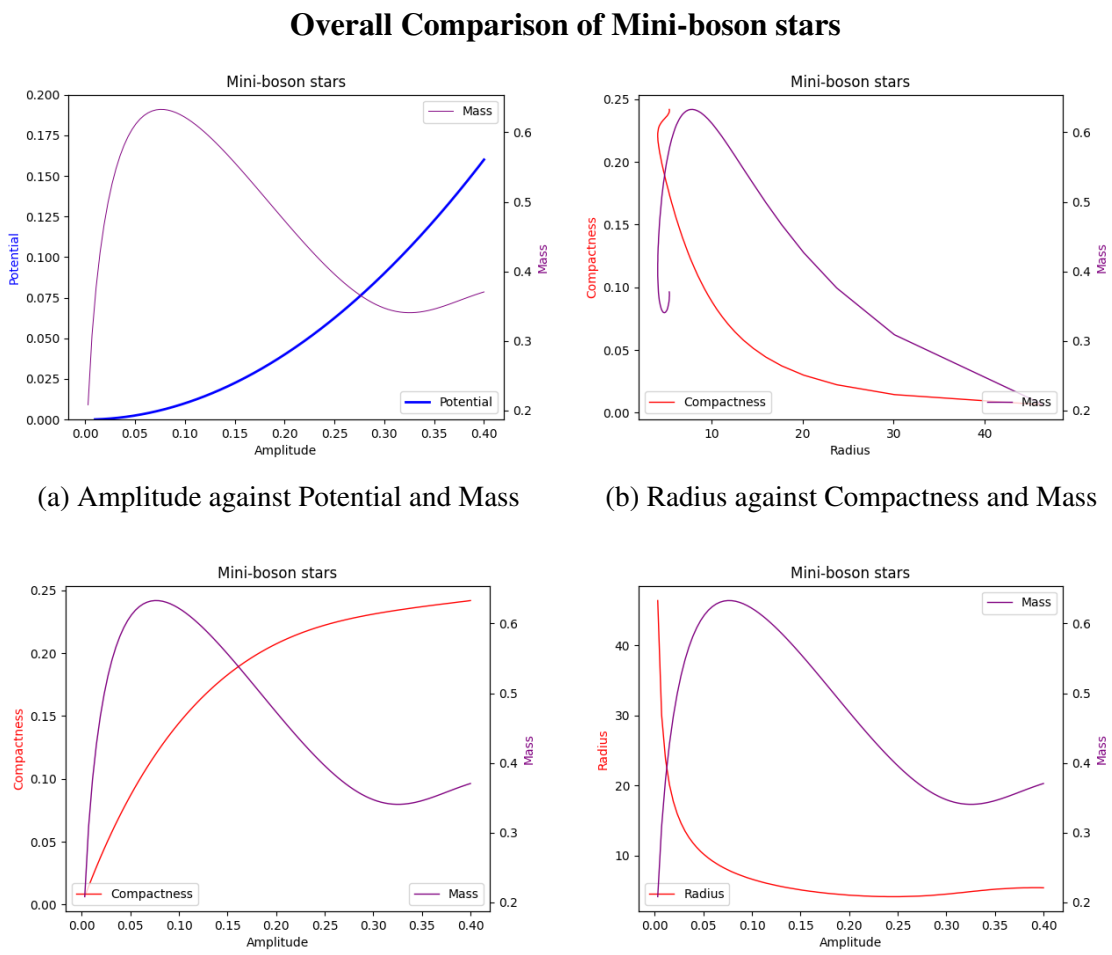

(a) Amplitude against Potential and Mass

(b) Radius against Compactness and Mass

(c) Amplitude against Compactness and Mass

(d) Amplitude against Radius and Mass

Fig. B.8 As a supplement to the data on boson stars, we have listed comparative data on the mass, radius, and potential energy of specifically selected solitons in Chapter 5.

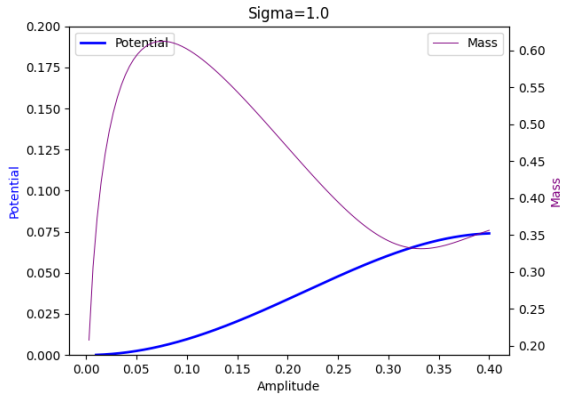

(a) Amplitude against Potential and Mass for $\sigma = 1.0$

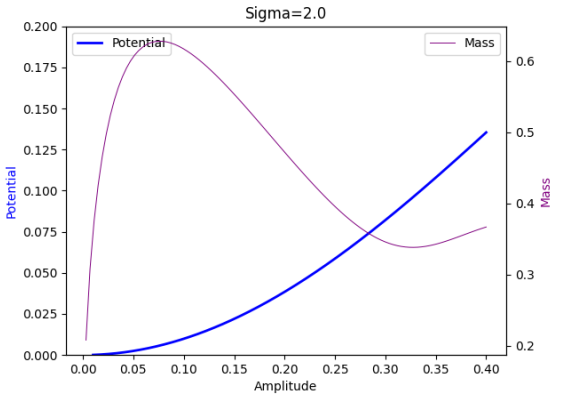

(b) Amplitude against Potential and Mass for $\sigma = 2.0$

B.2 Results for $\sigma = 1.0, 2.0$ and Mini-Boson Stars

In this section, we supplement the results for σ equal to 1.0, 2.0 and mini-boson stars. It is evident that for σ values of 1.0 and 2.0, the results closely resemble those of mini-boson stars. Importantly, the transition from "red dots" to "blue dots" is discontinuous. Furthermore, we note a significant difference in the results when using QNM for normalization compared to using the initial mass of boson stars.

Another detail to mention is that for cases where σ is higher than 0.5, their data on mass, compactness, radius, and other parameters are very similar to those of mini-boson stars. Even their gravitational wave energy is similar, but their potential shows differences.

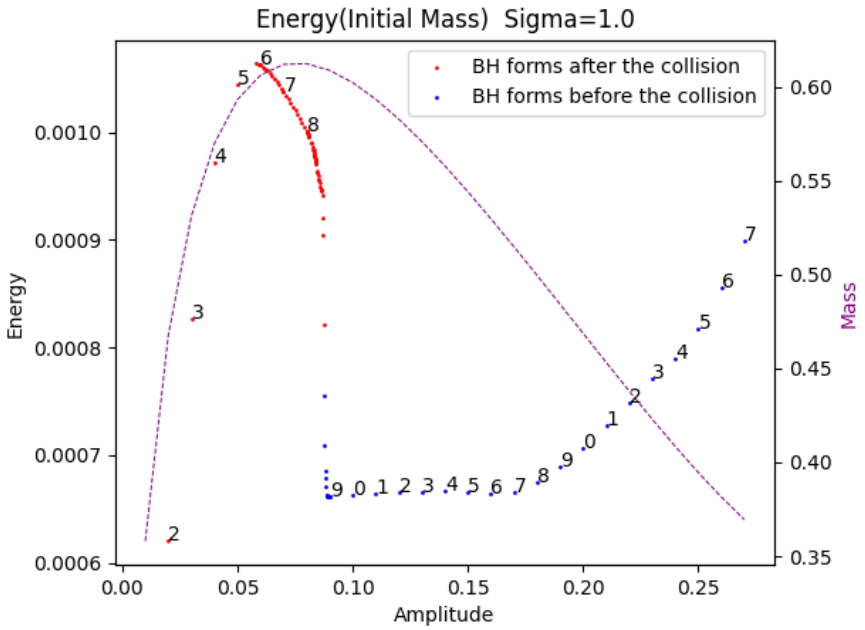

(a) The normalization method for this plot is based on the initial soliton mass.

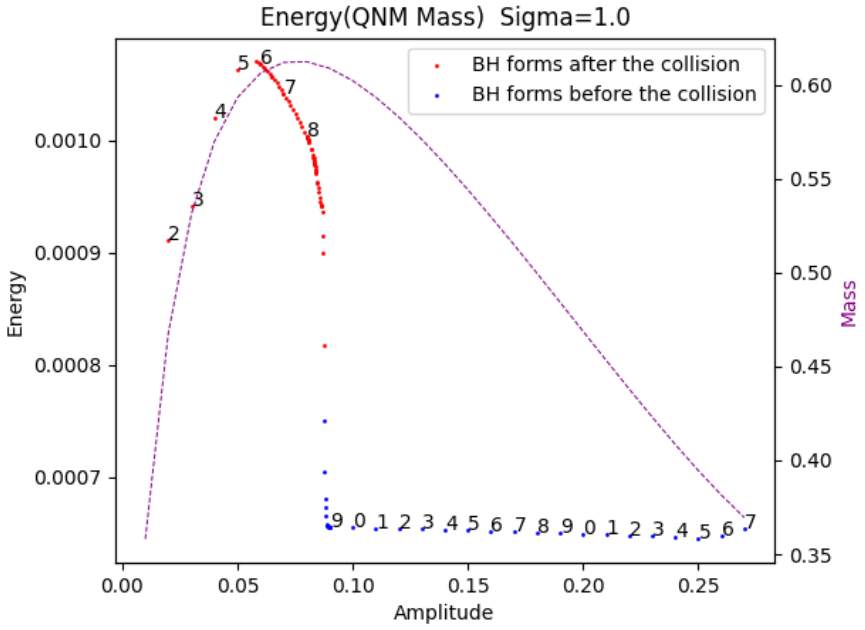

(b) The normalization method for this plot is based on the Quasinormal mode mass.

Fig. B.10 This plot shows the energy of gravitational waves produced by head-on collisions with different central amplitudes after a given $\sigma = 1.0$, where the purple auxiliary coordinates in both figures represent the initial soliton mass. In the plot, the red points represent two solitons colliding and eventually forming a black hole. The blue points represent two solitons that form black holes separately before colliding, and then form a new black hole after the collision.

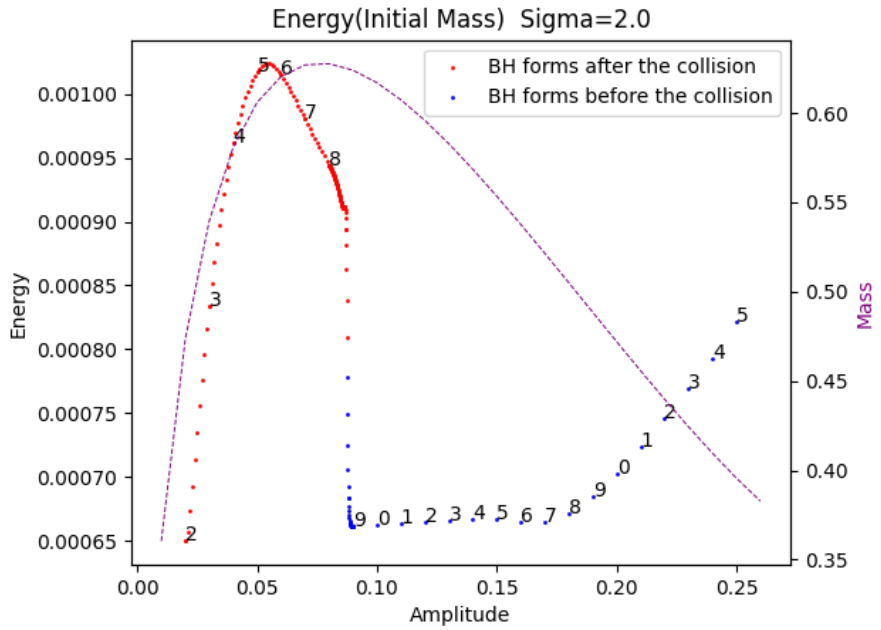

(a) The normalization method for this plot is based on the initial soliton mass.

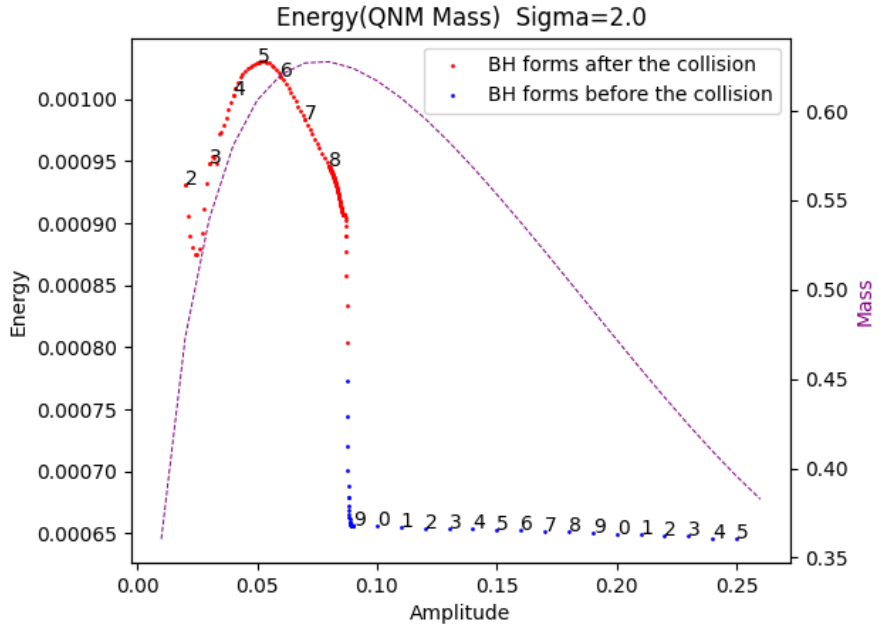

(b) The normalization method for this plot is based on the Quasinormal mode mass.

Fig. B.11 This plot shows the energy of gravitational waves produced by head-on collisions with different central amplitudes after a given $\sigma = 2.0$, where the purple auxiliary coordinates in both figures represent the initial soliton mass. In the plot, the red points represent two solitons colliding and eventually forming a black hole. The blue points represent two solitons that form black holes separately before colliding, and then form a new black hole after the collision.

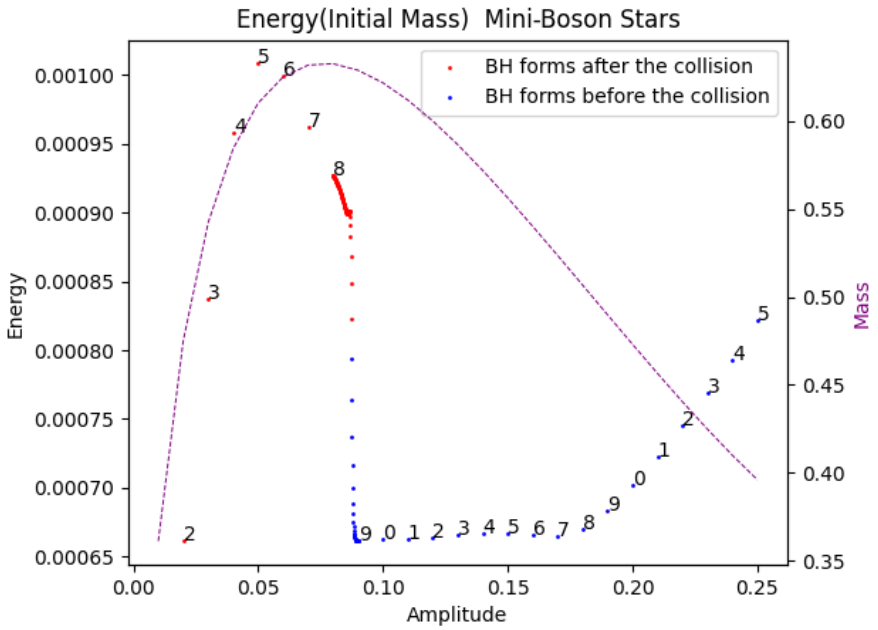

(a) The normalization method for this plot is based on the initial mini-boson star mass.

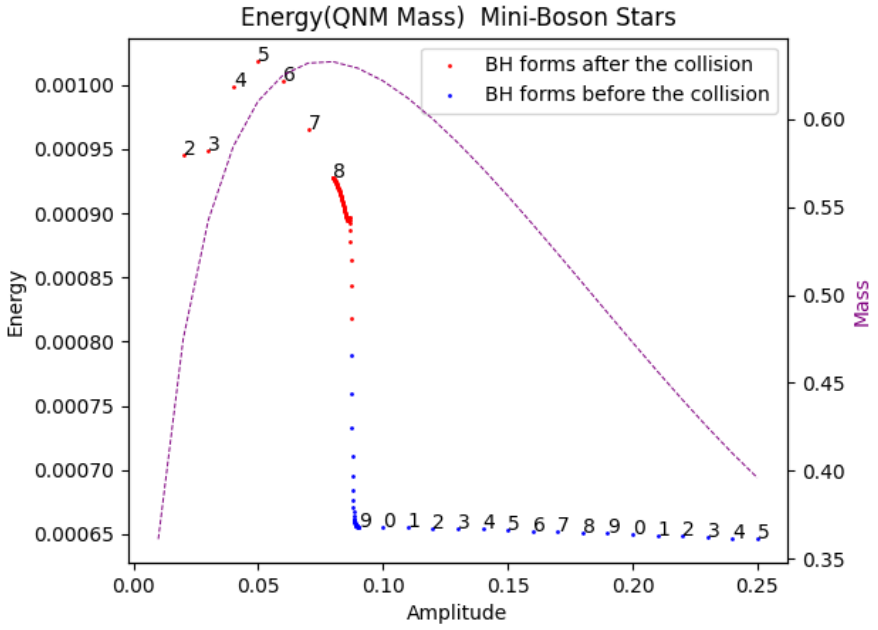

(b) The normalization method for this plot is based on the Quasinormal mode mass.

Fig. B.12 This plot shows the energy of gravitational waves produced by head-on collisions with different central amplitudes for mini-boson stars, where the purple auxiliary coordinates in both figures represent the initial soliton mass. In the plot, the red points represent two solitons colliding and eventually forming a black hole. The blue points represent two solitons that form black holes separately before colliding, and then form a new black hole after the collision.

Appendix C

Constraints and Convergence Tests

In this appendix, we present the constraint violations and convergence tests related to Chapter 5. This is crucial to our confidence that the results we obtained are not merely noise, but represent real physical phenomena. Throughout our research, we conducted numerous similar tests, and here we showcase a selection of these for $\sigma = 0.25$. We believe these tests are sufficient to demonstrate the validity of our results.

It is important to note that N in the legend represents the resolution of the numerical simulation. For example, $N = 256$ indicates that 256 grid points were selected in a single direction. The term **Central Amplitude**, which frequently appears in the subfigures, refers to the ***initial*** central amplitude of the boson star.

Figure C.1 illustrates the constraint violations in head-on collisions of two solitons with varying central amplitudes. Figure C.1a corresponds to the collision of stable solitons, Figure C.1b to metastable solitons, and Figure C.1c to unstable solitons that collapse prematurely into black holes.

Figure C.2 depicts the gravitational wave energy generated during the collision, considering three different resolutions. The blue curve corresponds to the resolution that we used in practice.

Figure C.3 displays the maximum value of $\sqrt{|\phi|^2}$ over time for a single soliton. The two examples shown in this figure are both unstable solitons that collapse into black holes.

Figure C.4 displays the maximum value of $\sqrt{|\phi|^2}$ over time for a single soliton. The two examples shown here are both metastable solitons that, during their evolution, migrate to other soliton states.

Figure C.5 presents the results of the minimum value of χ over time. Subfigure C.5a corresponds to a metastable soliton, while subfigure C.5b corresponds to an unstable soliton that collapses into a black hole.

Figure C.6 presents the results for a stable soliton. Subfigure C.6a illustrates the maximum value of $\sqrt{|\phi|^2}$ over time, while subfigure C.6b depicts the minimum value of χ over time.

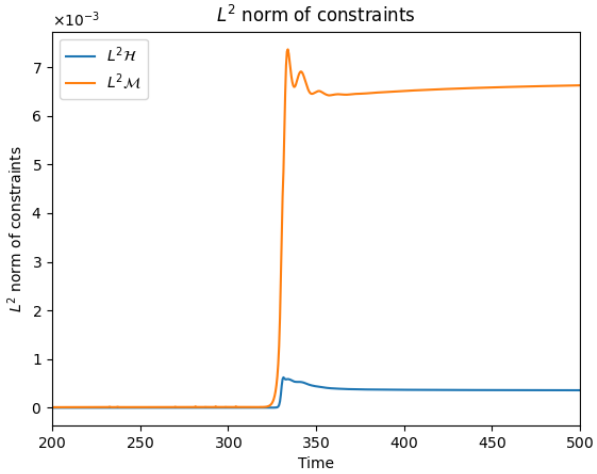

(a) Central Amplitude = 0.05.

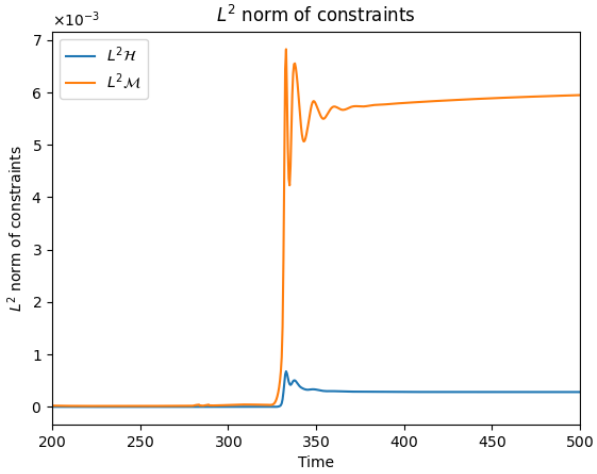

(b) Central Amplitude = 0.08.

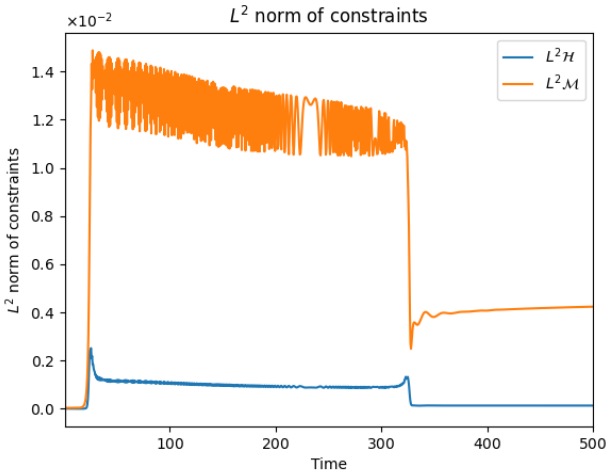

(c) Central Amplitude = 0.25.

Fig. C.1 Constraint violations for varying central amplitudes in head-on collisions.

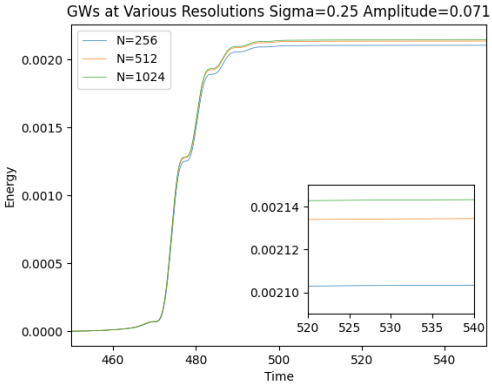

(a) Central Amplitude = 0.071

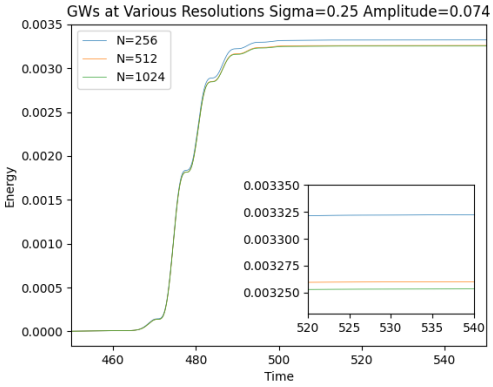

(b) Central Amplitude = 0.05

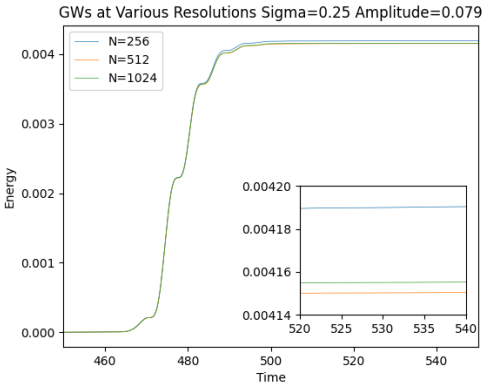

(c) Central Amplitude = 0.079

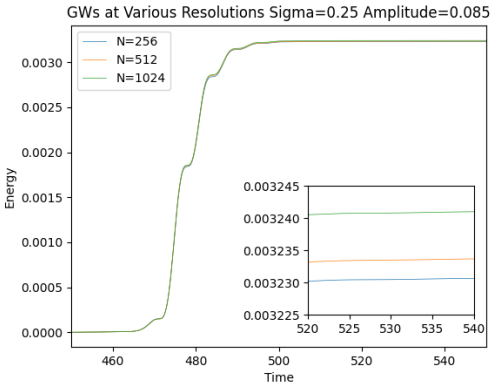

(d) Central Amplitude = 0.085

Fig. C.2 This figure displays the energy of gravitational waves versus time for $\sigma = 0.25$, specifically considering cases with central amplitudes of 0.071, 0.074, 0.079, and 0.085. The blue line ($N = 256$) corresponds to the actual resolution used in our simulations. For comparison, we also considered higher resolutions ($N = 512$) and even higher resolutions ($N = 1024$).

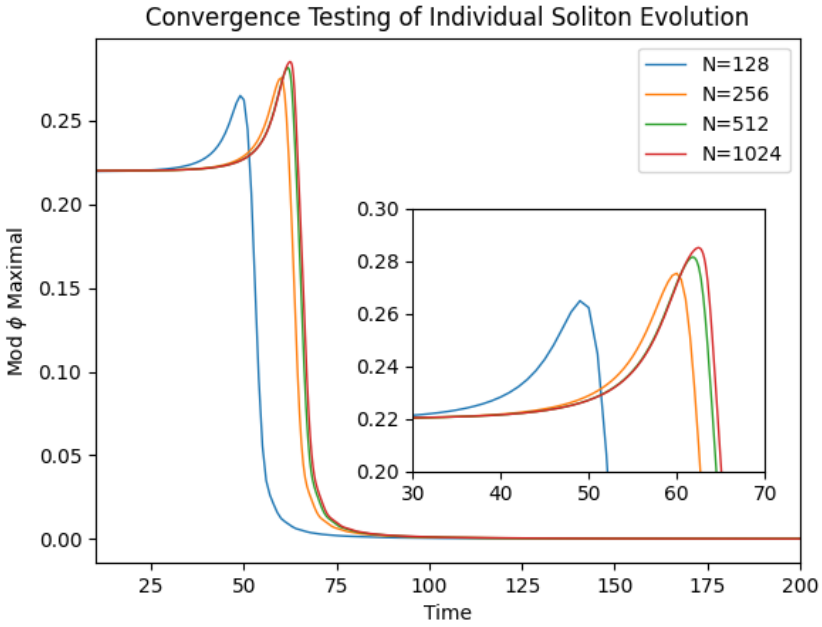

(a) Central Amplitude = 0.22

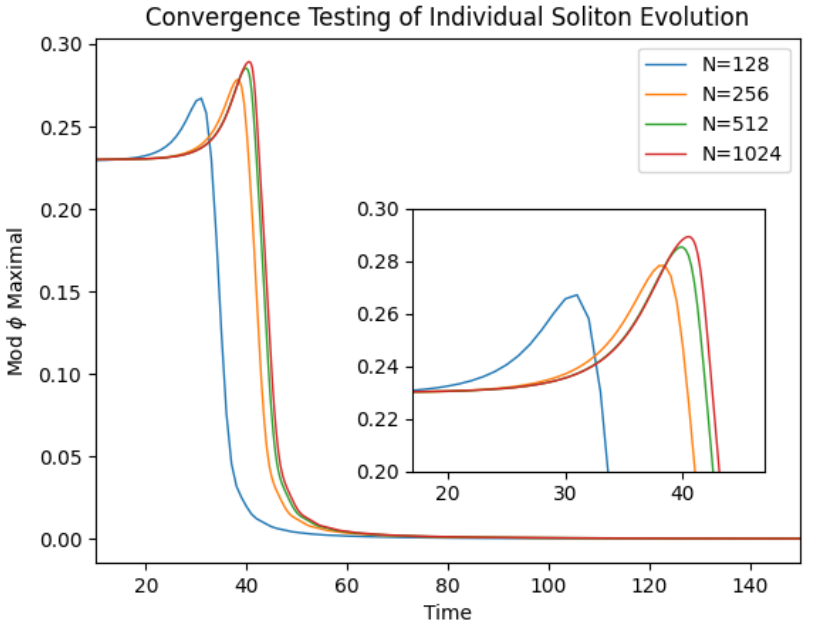

(b) Central Amplitude = 0.23

Fig. C.3 This figure presents the numerical results of the maximum value of $\sqrt{|\phi|^2}$ over time at different resolutions. The resolution $N = 256$ is the one we used in practice. Specifically, the two results selected here both correspond to unstable solitons.

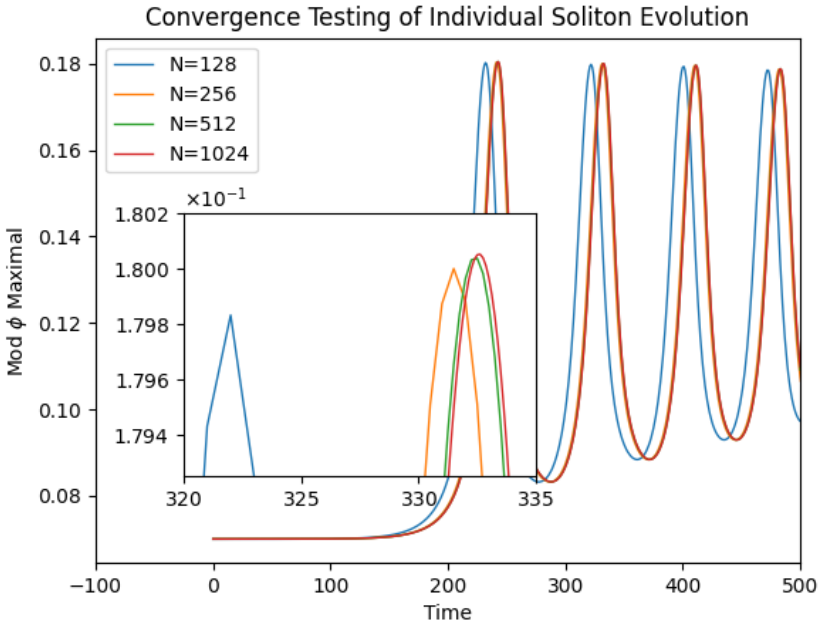

(a) Central Amplitude = 0.07

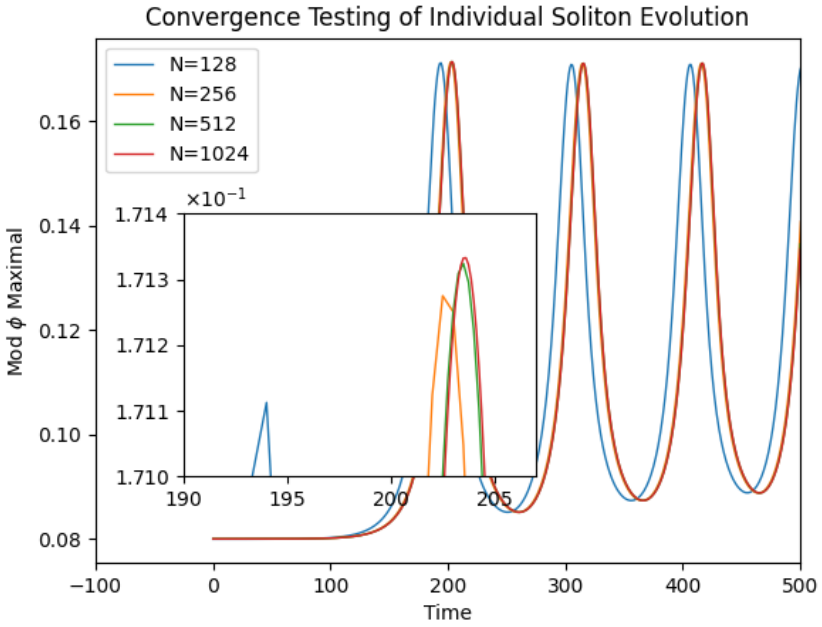

(b) Central Amplitude = 0.08

Fig. C.4 This figure presents the numerical results of the maximum value of $\sqrt{|\phi|^2}$ over time at different resolutions. The resolution $N = 256$ is the one we used in practice. Specifically, the two results selected here both correspond to metastable solitons.

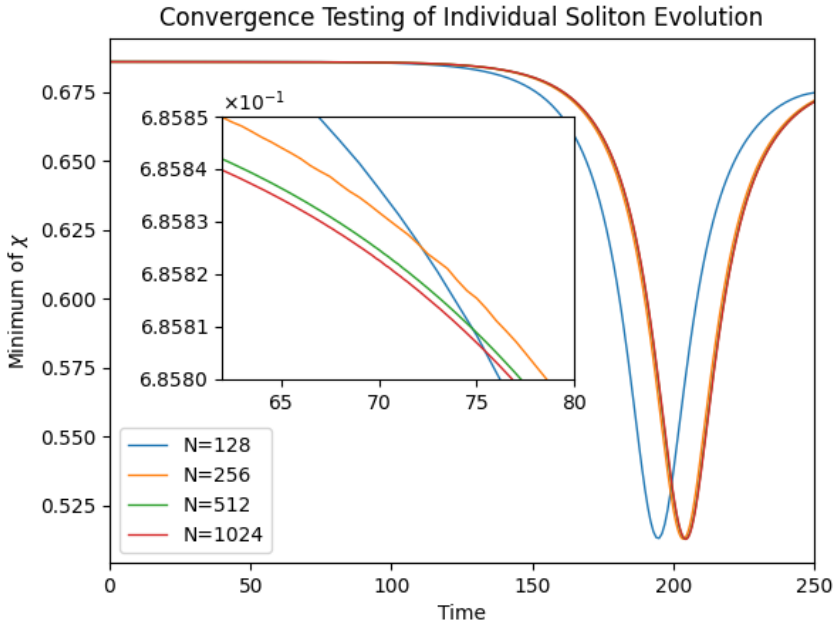

(a) Central Amplitude = 0.08

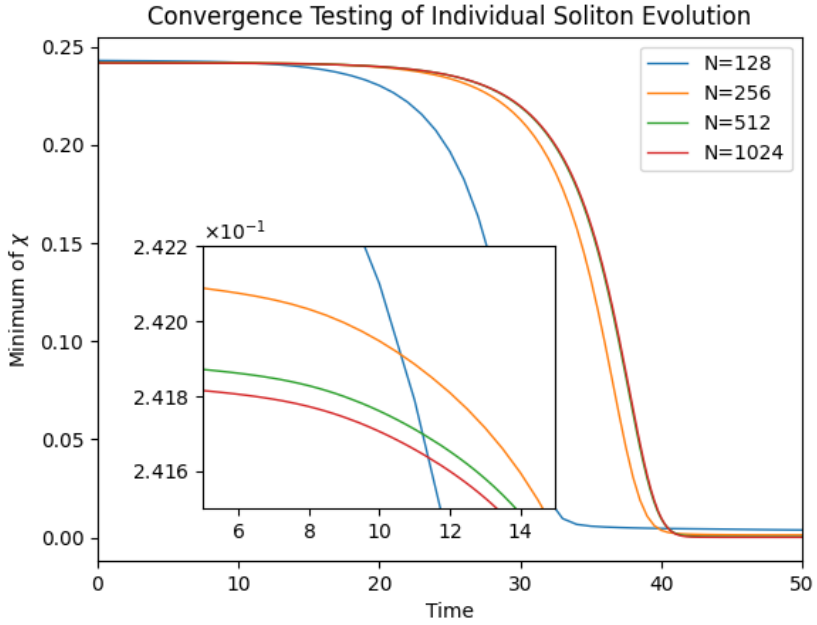

(b) Central Amplitude = 0.23

Fig. C.5 This figure presents the numerical results of the minimum value of χ over time at different resolutions. The resolution $N = 256$ is the one we used in practice.

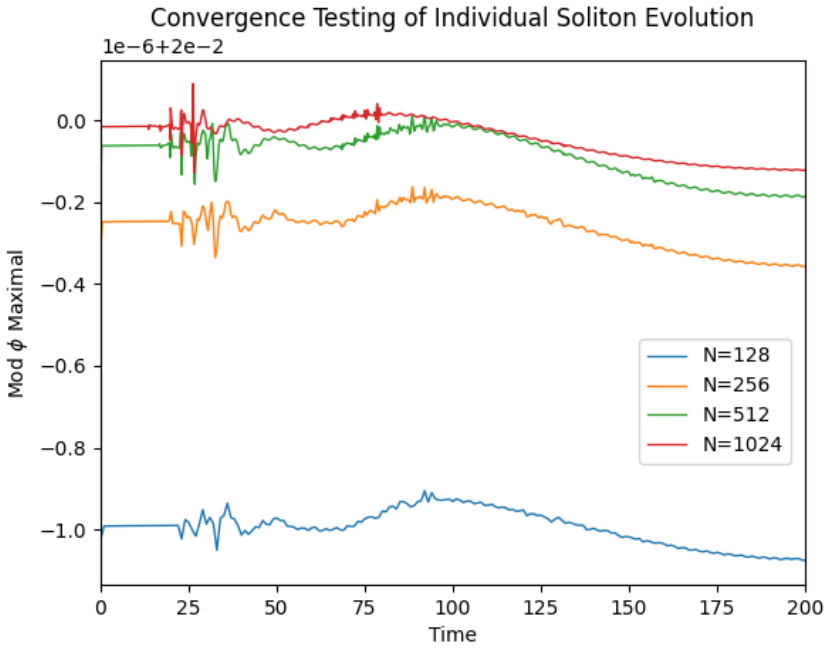

(a) Maximum of $\sqrt{|\phi|^2}$

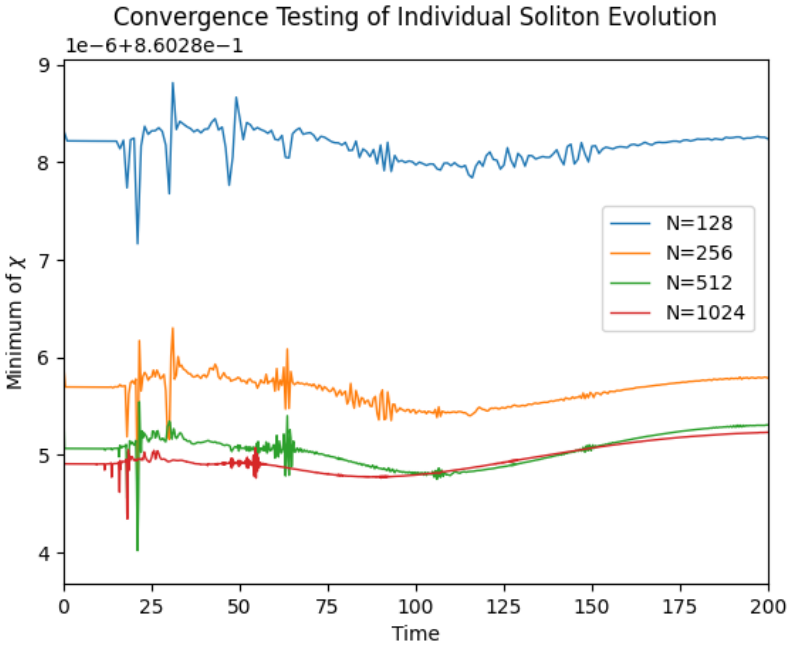

(b) Minimum of χ

Fig. C.6 This figure presents the numerical results for the maximum value of $\sqrt{|\phi|^2}$ and the minimum value of χ for a central amplitude of 0.02 over time at different resolutions. The resolution $N = 256$ is the one used in our simulations.